

# SMART SENSORS FOR UTILITY ASSETS

A Thesis  
Presented to  
The Academic Faculty

by

Rohit Moghe

In Partial Fulfillment  
Of the Requirements for the Degree  
Doctor of Philosophy in  
Electrical and Computer Engineering

School of Electrical and Computer Engineering  
Georgia Institute of Technology  
August 2012

# SMART SENSORS FOR UTILITY ASSETS

Approved by:

Professor Deepak M. Divan, Advisor  
School of Electrical and Computer  
Engineering  
*Georgia Institute of Technology*

Professor Manos M. Tentzeris  
School of Electrical and Computer  
Engineering  
*Georgia Institute of Technology*

Professor Ronald G. Harley  
School of Electrical and Computer  
Engineering  
*Georgia Institute of Technology*

Professor J. Rhett Mayor  
School of Mechanical Engineering  
*Georgia Institute of Technology*

Professor Carlos S. Grijalva  
School of Electrical and Computer  
Engineering  
*Georgia Institute of Technology*

Date Approved: May 04, 2012

*Dedicated to my beloved grandmother  
Leela Golwalkar (Aai)  
and my parents,  
Ravindra and Chitra Moghe  
for their selfless love and support*

## ACKNOWLEDGEMENTS

My journey as a PhD student has been the most fruitful time of my life till now. During this journey, my PhD advisor, Dr. Deepak Divan, has been instrumental in nurturing the right attitude within me. He has helped me not just learn how to solve problems, but to understand the importance of asking the right questions. The guidance that he gave in the form of prompt suggestions, immaculate solutions, and his out-of-the box thinking has been awe-inspiring. The skill of constructive argumentation, the concept of conservation of sorrows and the *wif-me* factor are some of the pragmatic ideas that I take away with me from my rewarding experience as his student. I have great respect and deep gratitude for him.

Further, I would also like to express my acknowledgements to my committee members, Dr. Grijalva, Dr. Harley, Dr. Tentzeris, and Dr. Mayor for taking time out of their busy schedules and helping me by reviewing my thesis and providing their valuable suggestions.

Particularly, I would like to thank Dr. Grijalva for being a mentor and guiding me from a non-academic perspective through the energy club. His support and passion instilled confidence within me which helped me to work with an open mind.

Apart from my committee members, I am also grateful to Frank Lambert whose wealth of practical knowledge helped me gain more insight into the different projects on which I worked with him. His cheerful attitude is particularly inspiring. My many thanks go to NEETRAC and its advisors for their valuable suggestions in shaping the design requirements of the sensor, filling the survey forms, and allowing me to perform experiments at their facility.

I would also like to thank James Steinberg in helping me build the various prototypes that I have built during the course of my PhD.



I thank Deborah King for being prompt with ordering material, clearing payments and taking the burden of accounts always with a smile on her face.

Furthermore, I am thankful to Prasad, Amrit, Jorge and Andrew for the long discussions on various academic pursuits, their unrelenting hard work and support during deadlines; Frank and Anish for being inspirational; Yi for being a mentor; Dustin and Diogenes for the philosophical coffee sessions; Siwei and Jiaqi for their help in courses; and Debrup and Harjeet for their support.

Finally, I also thank all my close friends who served almost like family away from home, Akanksha, Advait, Ahmad, Naveen, Vijay, Kartick, Prabhakar, Satyan, Tejas, Uday and Mayank. I thank all for the extended discussions that gave me confidence to keep moving forward and achieve my dreams. In addition, I thank my adorable sister Gargi for providing me motivation and always believing in me.

Without the support from my advisor, committee members, staff, fellow students, friends and family, it would have been very difficult to complete my doctorate. I also extend many thanks to all who have helped and supported me in any possible way during my PhD.

# TABLE OF CONTENTS

|   |             |
|---|-------------|
| <b>ACKNOWLEDGEMENTS .....</b>                               | <b>IV</b>   |
| <b>LIST OF TABLES.....</b>                                  | <b>XIII</b> |
| <b>LIST OF FIGURES.....</b>                                 | <b>XV</b>   |
| <b>SUMMARY.....</b>   | <b>XXV</b>  |
| <b>CHAPTER 1 INTRODUCTION .....</b>                         | <b>1</b>    |
| <b>1.1 Problem Statement and Background.....</b>            | <b>1</b>    |
| <b>1.2 Research Scope and Objectives .....</b>              | <b>7</b>    |
| <b>1.3 Outline of Chapters.....</b>                         | <b>10</b>   |
| <b>CHAPTER 2 LITERATURE REVIEW AND MARKET SURVEY ..</b>     | <b>13</b>   |
| <b>2.1 Introduction .....</b>                               | <b>13</b>   |
| <b>2.2 Review of Methods For Current Sensing.....</b>       | <b>14</b>   |
| 2.2.1 Current Transformer .....                             | 14          |
| 2.2.2 Rogowski Coil.....                                    | 16          |
| 2.2.1 Magneto-Optical Current Transformer.....              | 17          |
| 2.2.2 Hall-effect Sensor .....                              | 18          |
| 2.2.3 Magneto Resistive Sensors.....                        | 20          |
| 2.2.4 Drawbacks of Existing Current Sensing Techniques..... | 20          |
| 2.2.5 Current Sensor by Promethean Devices LLC .....        | 22          |
| 2.2.6 Newer Current Sensing Techniques .....                | 24          |
| <b>2.3 Review of Methods for Voltage Sensing .....</b>      | <b>25</b>   |
| <b>2.4 Review of Wireless Utility Sensors.....</b>          | <b>28</b>   |
| <b>2.5 Energy Harvesting for Wireless Sensors.....</b>      | <b>34</b>   |
| 2.5.1 Mechanical Energy Harvesting .....                    | 35          |
| 2.5.2 Thermal Energy Harvesting.....                        | 36          |
| 2.5.3 Solar Energy Harvesting.....                          | 37          |
| 2.5.4 Electromagnetic (EM) Wave Energy Harvesting.....      | 38          |

|   |   |           |
|---|---|-----------|
| 2.5.5   | Magnetic Field Energy Harvesting .....                                    | 39        |
| 2.5.6   | Electric Field Energy Harvesting .....                                    | 40        |
| <b>2.6</b>  | <b>Power Circuits for Energy Harvesting Applications .....</b>            | <b>41</b> |
| 2.6.1   | DC/DC Boost Converters.....   | 42        |
| 2.6.2   | AC/DC Boost Converter .....   | 45        |
| <b>2.7</b>  | <b>Conclusions .....</b>  | <b>48</b> |
| <br>  |   |           |
| <b>CHAPTER 3 ELECTRIC AND MAGNETIC FIELD ENERGY</b>     |   |           |
| <b>HARVESTING .....</b>                                 |   |           |
| <b>3.1</b>  | <b>Introduction .....</b>   | <b>49</b> |
| <b>3.2</b>  | <b>Electric Field Energy Harvesting .....</b>                             | <b>49</b> |
| <b>3.3</b>  | <b>Magnetic Field Energy Harvesting Using Piezoelectric Material.....</b> | <b>56</b> |
| <b>3.4</b>  | <b>Magnetic Field Energy Harvesting Using Electromagnetic Induction</b>   | <b>60</b> |
| <b>3.5</b>  | <b>Conclusions .....</b>  | <b>64</b> |
| <br>  |   |           |
| <b>CHAPTER 4 STICK-ON SENSOR DESIGN AND DEVELOPMENT</b> |   |           |
| <b>.....66</b>  |   |           |
| <b>4.1</b>  | <b>Introduction .....</b>   | <b>66</b> |
| <b>4.2</b>  | <b>A 0.2V-3.3V AC/DC Boost Converter.....</b>                             | <b>66</b> |
| 4.2.1   | Voltage Boost Analysis .....  | 69        |
| 4.2.2   | Simulation Study .....  | 70        |
| 4.2.2.1   | DCM Operation .....   | 70        |
| 4.2.2.2   | Combined CCM and DCM Operation .....                                      | 71        |
| <b>4.3</b>  | <b>Power Circuit Design .....</b>   | <b>74</b> |
| 4.3.1   | Black-Start Functionality .....   | 74        |
| 4.3.2   | Operation in an Outage.....   | 77        |
| 4.3.1   | Multi-source Energy Harvesting .....                                      | 78        |
| 4.3.1.1   | Solar Cell Model.....   | 79        |
| 4.3.1.2   | Integration of Solar Energy Harvesting.....                               | 80        |
| 4.3.2   | Wide Operating Range .....  | 82        |
| <b>4.4</b>  | <b>Sensing and Signal Conditioning Circuit Design .....</b>               | <b>83</b> |
| 4.4.1   | Current Sensor Design .....   | 83        |

|            |   |            |
|------------|---|------------|
| 4.4.2      | Temperature Sensor Design .....             | 86         |
| 4.4.3      | ZigBee® Radio and Microcontroller.....      | 86         |
| <b>4.5</b> | <b>Sensor Prototype Fabrication.....</b>    | <b>87</b>  |
| 4.5.1      | Experimental Testing and Validation.....    | 91         |
| 4.5.1.1    | Voltage Boost Operation.....                | 91         |
| 4.5.1.2    | Black-Start Demonstration .....             | 92         |
| 4.5.1.3    | Wide Range of Operation .....               | 92         |
| 4.5.1.4    | Current Sensing Operation.....              | 93         |
| 4.5.1.5    | Stick-on Sensor Operation.....              | 94         |
| 4.5.1.6    | Power Consumption.....                      | 94         |
| 4.5.1.7    | Minimum Reporting Time .....                | 95         |
| 4.5.1.8    | Operation in an Outage .....                | 96         |
| 4.5.1.9    | Operation with Solar Energy Harvesting..... | 96         |
| <b>4.6</b> | <b>Network Integration.....</b>             | <b>99</b>  |
| <b>4.7</b> | <b>Conclusions .....</b>                    | <b>104</b> |

**CHAPTER 5 MULTI-CORE TRIANGULATION METHOD FOR CURRENT SENSING ..... 105**

|            |   |            |
|------------|---|------------|
| <b>5.1</b> | <b>Introduction .....</b>                                   | <b>105</b> |
| <b>5.2</b> | <b>Problem Statement .....</b>                              | <b>107</b> |
| <b>5.3</b> | <b>Mathematical Model of the Current Sensor .....</b>       | <b>109</b> |
| 5.3.1      | Error Model in a Single Sensor Case .....                   | 112        |
| <b>5.4</b> | <b>Dual-Core Triangulation Method .....</b>                 | <b>113</b> |
| 5.4.1      | Preliminary Proof-of-Concept Experiment.....                | 115        |
| <b>5.5</b> | <b>Multi-core Triangulation Method.....</b>                 | <b>116</b> |
| 5.5.1      | Use of Three Core-Coil Assemblies.....                      | 116        |
| 5.5.2      | Use of Six Core-coil Assemblies .....                       | 117        |
| 5.5.2.1    | MCTM Case 1: $\psi = 0, \phi = 0$ .....                     | 119        |
| 5.5.2.2    | MCTM Case 2: $\psi = \pi, \phi = 0$ .....                   | 120        |
| 5.5.2.3    | MCTM Case 3: $\psi = \pi/2, \phi = 0$ .....                 | 120        |
| 5.5.2.4    | MCTM Case 4: $\psi \in [0, 2\pi], \phi = 0$ .....           | 121        |
| 5.5.2.5    | MCTM Case 5: $\psi \in [0, 2\pi], \phi \in [0, 2\pi]$ ..... | 123        |

|   |  |            |
|---|--|------------|
| 5.5.3   | Simulation Studies using MCTM.....   | 126        |
| 5.5.4   | Advantages and Limitations of MCTM.....  | 127        |
| <b>5.6</b>  | <b>Conclusions .....</b>   | <b>128</b> |
| <br>  |  |            |
| <b>CHAPTER 6 SMART DUAL-CORE TRIANGULATION METHOD</b> |  |            |
| <b>FOR CURRENT SENSING .....</b>                      |  |            |
| <b>129</b>  |  |            |
| <b>6.1</b>  | <b>Introduction .....</b>  | <b>129</b> |
| <b>6.2</b>  | <b>Using Historical Data AND Variability.....</b>  | <b>130</b> |
| <b>6.3</b>  | <b>‘Smart’ Dual-Core Triangulation Method .....</b>  | <b>130</b> |
| 6.3.1   | Solution Methodology .....   | 131        |
| 6.3.1.1   | Smart DCTM Case I: $\psi = 0, \phi = 0$ .....  | 133        |
| 6.3.1.2   | Smart DCTM Case II: $\psi \in [0, 2\pi], \phi = 0$ .....   | 135        |
| 6.3.1.3   | Smart DCTM Case III: $\psi \in [0, 2\pi], \phi \in [0, 2\pi]$ .....  | 137        |
| 6.3.1.4   | S-set versus O-set.....  | 140        |
| 6.3.2   | Confidence Index .....   | 143        |
| 6.3.2.1   | Absolute Change in $\min(F_r), \max(F_r)$ or $\min(F_r I_1^* > I_B)$ .....   | 143        |
| 6.3.2.2   | Number of Measurement Samples Since $\min(F_r), \max(F_r)$ or $\min(F_r I_1^* > I_B)$<br>Last Changed.....                     | 143        |
| 6.3.2.3   | Difference between $\max(F_r)$ and $\min(F_r)$ , or $\min(F_r I_1^* > I_B)$ and $\min(F_r)$ ,<br>whichever is applicable ..... | 144        |
| 6.3.2.4   | Confidence Index Formulation.....  | 144        |
| <b>6.4</b>  | <b>Practical Issues Addressed .....</b>  | <b>145</b> |
| 6.4.1   | 3-D Versus 2-D Analysis.....   | 145        |
| 6.4.2   | Multiple Far-off Utility Assets.....   | 147        |
| 6.4.3   | Designing the Sensor.....  | 150        |
| <b>6.5</b>  | <b>Simulation Study.....</b>   | <b>152</b> |
| 6.5.1   | Case Study I: General Scenario .....   | 152        |
| 6.5.2   | Case Study II: Different RMS Current Profiles .....  | 155        |
| 6.5.3   | Case Study III: Correlated Currents.....   | 156        |
| 6.5.4   | Case Study IV: Three-Phase Conductors.....   | 158        |
| <b>6.6</b>  | <b>Prototype Development and Experimental Testing.....</b>   | <b>160</b> |
| 6.6.1   | Prototype development.....   | 160        |
| 6.6.2   | Experimental Setup .....   | 162        |

|                  |   |            |
|------------------|---|------------|
| 6.6.2.1          | Experiment I .....  | 162        |
| 6.6.2.2          | Experiment II.....  | 164        |
| <b>6.7</b>       | <b>Conclusions .....</b>  | <b>166</b> |
| <br>             |   |            |
| <b>CHAPTER 7</b> | <b>SMART AND LOW-COST VOLTAGE SENSING ....</b>                    | <b>168</b> |
| <b>7.1</b>       | <b>Introduction .....</b>   | <b>168</b> |
| <b>7.2</b>       | <b>Challenges with Voltage Sensing .....</b>                      | <b>169</b> |
| <b>7.3</b>       | <b>A mathematical Model of the Voltage Sensor .....</b>           | <b>174</b> |
| <b>7.4</b>       | <b>Algorithm Development .....</b>                                | <b>177</b> |
| 7.4.1            | Information on Typical Profiles of Voltage and Distance.....      | 177        |
| 7.4.1.1          | Voltage Profile .....   | 177        |
| 7.4.1.2          | Distance Profile.....   | 178        |
| 7.4.2            | Single Phase Application .....                                    | 178        |
| 7.4.3            | Three Phase Application .....                                     | 181        |
| <b>7.5</b>       | <b>Simulation Studies.....</b>                                    | <b>185</b> |
| 7.5.1            | Case Study I: Single Phase Conductor – MATLAB® Simulations .....  | 185        |
| 7.5.2            | Case Study II: Three Phase Conductors – MATLAB® Simulations.....  | 189        |
| 7.5.3            | Case Study III: Validation of Concept through ANSYS® Maxwell..... | 193        |
| <b>7.6</b>       | <b>PROTOTYPE DEVELOPMENT and Experimental Testing.....</b>        | <b>195</b> |
| 7.6.1            | Prototype Development.....  | 195        |
| 7.6.2            | Experimental Testing .....  | 197        |
| 7.6.2.1          | High Voltage Test Setup.....                                      | 197        |
| 7.6.2.2          | Test Methodology .....  | 198        |
| 7.6.2.3          | Results and Discussion.....                                       | 199        |
| 7.6.3            | Electric-field Energy Harvesting using the Prototype.....         | 201        |
| <b>7.7</b>       | <b>Conclusions .....</b>  | <b>202</b> |
| <br>             |   |            |
| <b>CHAPTER 8</b> | <b>DESIGNING A ROBUST SENSOR.....</b>                             | <b>204</b> |
| <b>8.1</b>       | <b>Introduction .....</b>   | <b>204</b> |
| <b>8.2</b>       | <b>Optimal Energy Harvester Design.....</b>                       | <b>204</b> |
| 8.2.1            | Shape .....   | 205        |
| 8.2.2            | Dimensions.....   | 205        |
| 8.2.3            | Optimal Winding Design .....                                      | 209        |

|                  |   |            |
|------------------|---|------------|
| 8.2.3.1          | Resistance computation .....                          | 210        |
| 8.2.3.2          | Inductance Computation.....                           | 210        |
| 8.2.3.3          | Maximum Power Transfer .....                          | 212        |
| <b>8.3</b>       | <b>Fault Analysis .....</b>                           | <b>215</b> |
| <b>8.4</b>       | <b>Simulation Studies.....</b>                        | <b>216</b> |
| <b>8.5</b>       | <b>Experimental Results .....</b>                     | <b>218</b> |
| <b>8.6</b>       | <b>Protection Circuit Design.....</b>                 | <b>221</b> |
| 8.6.1            | Protection of the Flux Concentrator .....             | 222        |
| 8.6.2            | TVS Diodes for Winding Sections .....                 | 222        |
| 8.6.3            | MOV Design .....                                      | 223        |
| 8.6.4            | Secondary Transformer TVS diode design.....           | 223        |
| 8.6.5            | Zener Design .....                                    | 224        |
| 8.6.6            | Design Example for Protecting the Optimal Core.....   | 224        |
| <b>8.7</b>       | <b>ZigBee® Communication Link Performance .....</b>   | <b>226</b> |
| 8.7.1            | Distance Tests .....                                  | 226        |
| 8.7.2            | High Voltage Interference Tests .....                 | 228        |
| <b>8.8</b>       | <b>EMI/Corona Suppression and package design.....</b> | <b>230</b> |
| <b>8.9</b>       | <b>Conclusions .....</b>                              | <b>233</b> |
| <br>             |   |            |
| <b>CHAPTER 9</b> | <b>CONCLUSIONS, CONTRIBUTIONS AND FUTURE</b>          |            |
| <b>RESEARCH</b>  | <b>.....</b>  | <b>234</b> |
| <b>9.1</b>       | <b>Conclusions .....</b>                              | <b>234</b> |
| <b>9.2</b>       | <b>Summary of Contributions .....</b>                 | <b>237</b> |
| <b>9.3</b>       | <b>Recommended Future Research .....</b>              | <b>238</b> |
| 9.3.1            | Voltage Sensing .....                                 | 238        |
| 9.3.1.1          | Relaxing the assumptions.....                         | 238        |
| 9.3.1.2          | Field Testing.....                                    | 239        |
| 9.3.1.3          | Estimation of Distance to Ground .....                | 239        |
| 9.3.2            | Current Sensing .....                                 | 239        |
| 9.3.3            | Design and Testing.....                               | 240        |
| 9.3.3.1          | Testing the Protection Circuit .....                  | 240        |
| 9.3.3.2          | Designing a Robust Enclosure.....                     | 240        |
| 9.3.3.3          | Field Demonstration of a Sensor Network .....         | 240        |

|  |     |
|--|-----|
| APPENDIX A PZB-MAGNET TECHNICAL SPECIFICATIONS ...           | 241 |
| APPENDIX B BILL OF MATERIALS OF THE STICK-ON SENSOR<br>..... | 242 |
| APPENDIX C ERROR PLOTS FOR MCTM ALGORITHM.....               | 243 |
| APPENDIX D $F_R$ PLOTS FOR SMART DCTM ALGORITHM.....         | 245 |
| APPENDIX E VOLTAGE SENSOR MODEL DERIVATION.....              | 247 |
| APPENDIX F WINDING RESISTANCE MODEL DERIVATION ..            | 252 |
| BIBLIOGRAPHY .....   | 254 |
| VITA.....  | 263 |



## LIST OF TABLES

|  |     |
|--|-----|
| Table 2.1: Market Research of Wireless Current Sensor Units .....  | 29  |
| Table 2.2: Typical Power Densities from Different Energy Harvesting Sources .....  | 41  |
| Table 2.3: Typical Open Circuit Voltage for Various Energy Harvesting Sources .....  | 41  |
| Table 2.4: Modes of Operation of Direct AC/DC Boost Converter of Figure 2.20.....  | 47  |
| Table 3.1: Range of Values of Parameters $w$ , $d$ , $D$ , $\epsilon_r$ and $V_{ac}$ which were Simulated using ANSYS® Maxwell.....                | 52  |
| Table 3.2: Dimensions of the Lab Test Setup for Validating E-field Energy-harvesting ....  | 54  |
| Table 3.3: Piezoelectric-based Magnetic Field Energy Harvesting Test Results.....  | 60  |
| Table 3.4: Magnetic Field Energy Harvesting using Different Core Configuration. Note: CRGO is Cold Rolled Grain Oriented Steel .....               | 62  |
| Table 3.5: Qualitative Comparison between the Tested Core-Coil Assemblies.....   | 62  |
| Table 4.1: Summary of Operation of the Proposed AC/DC Boost Converter .....  | 68  |
| Table 4.2: Circuit Parameters Chosen for Simulation .....  | 70  |
| Table 4.3: Component List for the Modified Astable Multivibrator Figure 4.6.....   | 76  |
| Table 4.4: Component List for the Ultracapacitor Charging Circuit.....   | 78  |
| Table 4.5: Empirical Values of Fill Factors for Solar Cells.....   | 80  |
| Table 4.6: Characterization Results of the Solar Cell at 25 °C.....  | 82  |
| Table 4.7: Component List for Current Sensing Signal Conditioning in Figure 4.13(b) .....  | 85  |
| Table 4.8: Component List for Current Sensing Signal Conditioning in Figure 4.13(c) .....  | 85  |
| Table 4.9: Power Circuit Parameters.....   | 90  |
| Table 4.10: Converter Operation at Different Duty Cycle, Primary Current = 60 A, Load resistance= 50 k $\Omega$ , Switching frequency= 2 kHz ..... | 91  |
| Table 4.11: Power Consumption for Individual Components .....  | 95  |
| Table 4.12: Maximum Reporting Frequency of the Stick-on Sensor.....  | 95  |
| Table 5.1: Experimental Results Show High Errors in the Presence of Far Fields.....  | 107 |
| Table 5.2: Preliminary Results of the Dual Core Approach .....   | 115 |

|   |     |
|---|-----|
| Table 5.3: Parameters for the Simulation Study .....                                | 126 |
| Table 6.1: Statistics of the Currents used for Simulation Case Study-I .....        | 153 |
| Table 6.2: Statistics of Different Profiles used for Simulation Case Study-II ..... | 155 |
| Table 7.1: Test Cases for Single Conductor Above the Earth .....                    | 186 |
| Table 7.2: Test Cases for Three Conductors Above the Earth.....                     | 189 |
| Table 7.3: Voltage Sensing Simulation Cases .....                                   | 193 |
| Table 7.4: Voltage Profile Statistics used for Experimental Validation of MAVS..... | 199 |
| Table 7.5: Error Statistics for Sensed Results in HV1 and HV2 Tests .....           | 201 |
| Table 8.1: Design Space for Parametric Search .....                                 | 206 |
| Table 8.2: Constraints on Dimensions of the Flux Concentrator.....                  | 209 |
| Table 8.3: Design Space for Parametric Search .....                                 | 217 |
| Table 8.4: Measurement Equipment Used for the Impulse Test.....                     | 219 |
| Table 8.5: Experimental Results of Impulse Testing on Flux Concentrators.....       | 219 |
| Table 8.6: Pre-Post Impulse Test Analysis.....                                      | 221 |
| Table 8.7: Correlation of Variables with ZigBee® RSSI .....                         | 230 |

## LIST OF FIGURES

|  |    |
|--|----|
| Figure 1.1: Gaps/Opportunities for smart sensors in the volume-cost space .....  | 5  |
| Figure 1.2: Total cost of implementing a sensor network containing one million sensor nodes.....   | 7  |
| Figure 1.3: Network architecture and integration to SCADA .....  | 8  |
| Figure 2.1: a) Operating principle of a CT, b) oil immersed CT for high voltage applications (72-800 kV applications) [12], and c) bushing CT by ABB [13]. .....                                     | 15 |
| Figure 2.2: (a) ABB rogowski coil technology (4-1600A) [13], (b) flexible rogowski coil from Rocoil [15] .....   | 17 |
| Figure 2.3: (a) Operating principle of an MOCT, (b) ABB MOCT (measures upto 4000 A) [18].....  | 18 |
| Figure 2.4: a) Operating principle of Hall-effect sensors, b) Commercial Hall-effect sensors by LEM (measures up to 3000 A (LEM LF) and 15 kA (LEM LT)) [21] .....                                   | 20 |
| Figure 2.5: (a) A new concept of current measurement in three phase transmission lines using two search coils, (b) geometry of the current measurement scheme.....                                   | 22 |
| Figure 2.6: a) Conventional capacitive divider voltage sensing operating principle, b) PTs offered by ABB [10] and Trench [13].....  | 25 |
| Figure 2.7: Voltage sensor floating at the same potential as the conductor .....   | 26 |
| Figure 2.8: Voltage sensor using circular array of capacitor plates surrounding the conductor .....  | 27 |
| Figure 2.9: (a) Basic principle of operation of a piezoelectric energy harvester, (b) basic principle of operation of a microgenerator .....   | 36 |
| Figure 2.10: (a) Piezoelectric harvester by AdaptivEnergy [55], (b) microgenerator by Perpetuum [57], and (c) electrostatic energy harvesting shoe by Scientific Research Institute (SRI) [59] ..... | 36 |
| Figure 2.11: (a) Harvests 30 $\mu$ W at $\Delta T=5$ $^{\circ}$ C by Thermolife energy corporation [68], (b) Harvests 470 mW/cm <sup>3</sup> at $\Delta T=100$ $^{\circ}$ C by Tellurex [71]. .....  | 37 |
| Figure 2.12: (a) Solar charger by ICP Solar harvests 2 mW/cm <sup>3</sup> [77], (b) solar charger by Solio harvests 3.7 mW/cm <sup>3</sup> [78]. .....   | 38 |

|  |    |
|--|----|
| Figure 2.13: a) Operating principle of electromagnetic energy harvesting, b) electro-magnetic energy harvester by Powercast [80].                                      | 39 |
| Figure 2.14: Electric field energy harvesting experimental setup [83]  | 40 |
| Figure 2.15: (a) Conventional DC/DC boost converter, (b) Synchronous DC/DC boost converter   | 42 |
| Figure 2.16: Cockroft-Walton charge pump topologies, (a) Even multiplier, (b) Odd multipliers  | 43 |
| Figure 2.17: Dickson charge pump topology  | 44 |
| Figure 2.18: Hybrid charge pump-inductive step up converter architecture   | 45 |
| Figure 2.19: Conventionally used AC/DC boost converter for energy harvesting applications  | 45 |
| Figure 2.20: Direct AC/DC boost converters for energy harvesting applications  | 46 |
| Figure 2.21: Recently proposed AC/DC boost converters for low-voltage energy harvesting applications   | 47 |
| Figure 3.1: Parallel plate system for electric field harvesting  | 50 |
| Figure 3.2: Equivalent circuit of the electric field energy harvesting system  | 50 |
| Figure 3.3: ANSYS® Maxwell 2D simulation of the two plate energy harvesting system   | 52 |
| Figure 3.4: Sensitivity analysis of power harvested from electric field with respect to change in dielectric constant, distance between plates, plate size and voltage | 53 |
| Figure 3.5: (a) Schematic of E-field energy harvesting test setup, (b) Actual lab test setup used to validate the concept of E-field energy harvesting                 | 54 |
| Figure 3.6: Circuit schematic of the electric field energy harvesting system   | 55 |
| Figure 3.7: Plots showing power and power density of the electric field energy harvesting system at different loading levels and asset potential                       | 55 |
| Figure 3.8: Operating principle of piezoelectric based magnetic field energy harvesting  | 57 |
| Figure 3.9: (a), (b) and (c) show change in resonant frequency of PZB-magnet system with a change in configuration   | 58 |
| Figure 3.10: (a) Voltage at PZB terminals at different primary currents, (b) Power harvested at different load levels when primary current is 600                      | 58 |

|   |    |
|---|----|
| Figure 3.11: (a) Circuit diagram of the PZB-magnet test setup, (b) Experimental setup of the PZB-magnet system. ....  | 59 |
| Figure 3.12: Graph showing the typical operation cycle of a sensor node powered with a piezoelectric energy scavenging source.....  | 59 |
| Figure 3.13: Circuit schematic of the EM-Induction test system.....   | 61 |
| Figure 3.14: Maximum harvestable power from different core-coil configurations for different primary currents.....  | 63 |
| Figure 3.15: Zoomed in view of the x-shaped flux concentrator (XFC).....  | 63 |
| Figure 3.16: Graphs show linearity of the XFC with primary current over a wide range ..   | 64 |
| Figure 4.1: Proposed 0.2 V to 3.3 V AC/DC boost converter with a wide operating range. ....   | 67 |
| Figure 4.2: Modes of operation of the AC/DC boost boost converter .....   | 68 |
| Figure 4.3: Waveforms of transformer voltage, current and diode currents in pure CCM and pure DCM mode .....  | 69 |
| Figure 4.4: (a) Comparison of simulation results versus analytical results for output voltage in DCM Results at $D = 50\%$ , (b) Voltage at the output is nearly 40 V. The converter operates in DCM.....   | 71 |
| Figure 4.5: (a) Comparison of output voltage obtained using simulation results in combined CCM and DCM versus analytical results in pure DCM, (b) Results at $D = 20\%$ . Voltage at the output is nearly 4 V. The converter operates mostly in DCM as the duty cycle is low, (c) Comparison of output voltage obtained using $r_L = 1 \text{ m}\Omega$ , and $r_L = 200 \text{ m}\Omega$ , (d) Results at $D = 70\%$ . The voltage at the output is nearly 11 V. The converter operates mostly in CCM as the duty cycle is high..... | 73 |
| Figure 4.6: Modified astable multivibrator used for self-start.....   | 75 |
| Figure 4.7: Ultracapacitor charging circuit .....   | 78 |
| Figure 4.8: Equivalent circuit model of a solar cell.....   | 79 |
| Figure 4.9: Trajectory of operation for trickle charging an ultracapacitor using a solar cell. ....   | 81 |
| Figure 4.10: (a) Mini-solar cell having an OCV of 4V and SCC of 2.5 mA was used as the solar harvester, (b) Maximum harvestable power from the solar cell under different insolation characterized in the lab .....   | 81 |

|  |    |
|--|----|
| Figure 4.11: Ultracapacitor charging circuit .....   | 82 |
| Figure 4.12: Proposed overall power circuit diagram.....   | 83 |
| Figure 4.13: (a) SCC measurement, (b) and (c) Two different difference amplifier implementations.....  | 84 |
| Figure 4.14: Buffer amplifier used for temperature sensing .....   | 86 |
| Figure 4.15: TI's CC2530 SOC solution for ZigBee®.....   | 87 |
| Figure 4.16: Eagle schematic for (a) power circuit, and (b) signal conditioning circuit.....   | 88 |
| Figure 4.17: (a) and (b) show layouts for the Stick-on sensor circuit board, c) actual circuit boards kept side by side for comparison of size. ....   | 89 |
| Figure 4.18: (a) Bottom View of the PCB (through-hole version) with the micro- controller and transceiver attached to it, (b) Surface mount version .....  | 89 |
| Figure 4.19: a) Laboratory prototype of the Stick-on sensor kept close to a conductor, b) A functional Stick-on sensor mounted on a conductor with wire ties sends current and temperature signals to a remote coordinator. The coordinator is connected to a laptop and records the received data. ....               | 90 |
| Figure 4.20: Functional schematic of the test setup .....  | 91 |
| Figure 4.21: Screenshot showing VF - Flux concentrator voltage (0.2 V/Div.), VT - Transformer secondary voltage (2 V/Div.), IF - Flux concentrator current (10 mA/Div.), IT - Transformer secondary current (2 mA/Div.), ID1 and ID2 - Diode currents (1 mA/Div.). The converter is operated with 50% duty cycle. .... | 92 |
| Figure 4.22: Black-start functionality: Vo - output voltage (1V/Div.), VF - Flux concentrator voltage (0.2 V/Div.), Time base - (2.5 Sec/Div. ) .....  | 92 |
| Figure 4.23: Circuit operating at 60A and 1000A primary current, Vo - Output Voltage (2 V/Div.), SW1 - Mosfet Switch 1 Voltage (5 V/Div.) .....  | 93 |
| Figure 4.24: Different waveforms generated during current sensing .....  | 93 |
| Figure 4.25: Screenshot of the GUI that shows the sensed current and temperature results .....   | 94 |
| Figure 4.26: Screenshot of current consumption during active and sleep mode.....   | 95 |
| Figure 4.27: Linear approximation for the solar cell V-I characteristic .....  | 97 |
| Figure 4.28: Ultracapacitor recharge time in an outage using a solar cell .....  | 99 |

|  |     |
|--|-----|
| Figure 4.29: Conceptual smart substation with smart Stick-on sensors .....   | 100 |
| Figure 4.30: Operation regime of a smart wireless sensor .....   | 101 |
| Figure 4.31: Stack diagram of ZigBee <sup>®</sup> gateway device [110].....  | 103 |
| Figure 5.1: Open circuit test at different orientations and distances of the flux concentrator with respect to the conductor .....   | 105 |
| Figure 5.2: Single sensor approach- Two conductor case.....  | 106 |
| Figure 5.3: A general case having n current carrying conductors in the vicinity of the conductor of interest $C_1$ .....   | 108 |
| Figure 5.4: SCC vs. primary current recorded at different distances of the core from the conductor .....   | 109 |
| Figure 5.5: SCC vs. distance of the core from the conductor recorded at different values of primary current .....  | 110 |
| Figure 5.6: A cylindrical core coil geometry .....   | 111 |
| Figure 5.7: 3-D plot of the modeled SCC as a function of primary current and distance. ....  | 111 |
| Figure 5.8: Special case of Figure 5.3 with $n = 2$ and $\psi = 180^\circ$ .....   | 112 |
| Figure 5.9: Same system as in Figure 5.8 but with two sensor cores.....  | 113 |
| Figure 5.10: Errors in current measurement using the single core and two core methods. Note that $I_1$ is constant at 100 A.....   | 114 |
| Figure 5.11: Preliminary experiment validating the two core approach with specification Specifications: $D = 267$ mm, $d = 27.5$ mm, $x = 20$ mm, Core thickness = 10 mm, Wire = 30 AWG, 100 turns.....        | 115 |
| Figure 5.12: Same system as in Figure 5.8 but with three sensor cores.....   | 116 |
| Figure 5.13: Same system as in Figure 5.8 but with three sensor cores.....   | 118 |
| Figure 5.14: Same system as in Figure 5.8 but with three sensor cores.....   | 118 |
| Figure 5.15: Same system as in Figure 5.8 but with three sensor cores.....   | 127 |
| Figure 6.1: A general system geometry showing the presence of far-fields produced by far off conductor carrying current $I_2$ that couples with near fields produced by conductor carrying current $I_1$ ..... | 132 |

|   |     |
|---|-----|
| Figure 6.2: $F_r$ plotted against the primary current. The different curves are at different values of $I_2$ .  | 134 |
| Figure 6.3: $F_r$ plotted against primary current for (a) $\psi = 45^\circ$ and (b) $170^\circ$   | 136 |
| Figure 6.4: Nature of $F_r$ curves under two different scenarios (a) $\phi$ and $\psi$ in S-set, (b) $\phi$ and $\psi$ in the O-set   | 138 |
| Figure 6.5: S-set and O-set pictorially represented   | 139 |
| Figure 6.6: Variation of $F_r$ with changes in $I_1$ , $I_2$ , $\psi$ and $\phi$  | 139 |
| Figure 6.7: Flowchart for the smart DCTM algorithm  | 142 |
| Figure 6.8: Magnetic fields in 3-D space  | 146 |
| Figure 6.9: Use of superposition principle to lump the far-field conductors   | 148 |
| Figure 6.10: Maximum bound on $x$ given maximum permissible error $e_{\max}$ with variation in $D_{\min}$ and $d$   | 151 |
| Figure 6.11: Profile of near-field and far-field producing currents $I_1$ and $I_2$ respectively, used for the simulation case study I  | 152 |
| Figure 6.12: Simulation results for different sets of $\phi$ and $\psi$ , when $D = 300$ , $x = 20$ , $d = 25$ .  | 154 |
| Figure 6.13: Simulation results for profile A, profile B, profile C and profile D, when $D = 300$ mm, $x = 20$ mm, $d = 25$ mm.   | 156 |
| Figure 6.14: (a) Variability in current magnitudes of currents $I_1$ and $I_2$ , (b), (c) and (d) show simulation results for two conductors carrying same magnitude of current shifted by $180^\circ$ , $120^\circ$ and $240^\circ$ in phase, when $D = 300$ mm, $x = 20$ mm, $d = 25$ mm. | 158 |
| Figure 6.15: (a) and (b) show variability between magnitudes of $I_a - I_b$ and $I_a - I_c$ respectively, (c) simulation results in the case of a three-phase conductor system, when $D = 300$ mm, $x = 20$ mm, $d = 25$ mm.  | 160 |
| Figure 6.16: (a) Sensor core-coil assemble, (b) Stick-on sensor prototype containing the two sensor cores, (c) TI CC2530 microcontroller/ZigBee <sup>®</sup> transceiver used, (d) Zoomed in view of the sensor cores, (e) Signal conditioning circuit for sensor core signals              | 161 |
| Figure 6.17: Circuit schematic of the setup for testing the smart DCTM algorithm  | 162 |



|  |     |
|--|-----|
| Figure 6.18: (a) Actual test setup for experiment I showing the air-cored inductor kept very close to the sensor cores to create maximum disturbance, (b) Coordinator connected to laptop .....  | 163 |
| Figure 6.19: (a) Far-field profile, (b) actual current and sensed current profile, and (c) percentage error profile for experiment I. ....   | 164 |
| Figure 6.20: (a) Actual test setup for experiment II.....  | 165 |
| Figure 6.21: (a) Far-field profile, (b) actual current and sensed current profile, and (c) percentage error profile for experiment II. Here each data is separated by 5 sec duration. The algorithm itself does not require any specified time duration between measurements for proper functioning..... | 166 |
| Figure 7.1: A simple two plate system of voltage sensing of a single overhead conductor  | 170 |
| Figure 7.2: Voltage sensing using a floating two plate capacitor on a three phase overhead conductor system.....   | 171 |
| Figure 7.3: Electrical equivalent circuit of the system shown in Figure 7.2.....   | 172 |
| Figure 7.4: Single Conductor above the Earth.....  | 174 |
| Figure 7.5: Variation of current density around a concentric circle with the conductor having radius 20 mm for a 115 kV line 30 m above the earth.....   | 176 |
| Figure 7.6: Comparison of the variation of voltage and height of an overhead conductor   | 179 |
| Figure 7.7: Flowchart for implementing the MAVS algorithm on a microcontroller .....   | 181 |
| Figure 7.8: Case 1: Voltage is normally distributed with 115 kV mean and 10 kV std dev, Distance linearly drops from 30 m to 20m, algorithm window size is 100 .....   | 186 |
| Figure 7.9: Case 2: Voltage is normally distributed with 115 kV mean and 10 kV std dev, distance linearly drops from 30 m to 10m, algorithm window size is 25.....   | 187 |
| Figure 7.10: Case 3: Voltage has sinusoidal variation about a mean of 115 kV mean and 10 kV peak, distance linearly drops from 30 m to 10m, algorithm window size is 20 .....  | 187 |
| Figure 7.11: Case 4: Voltage has sinusoidal variation about a mean of 115 kV mean and 10 kV peak, distance also has a sinusoidal variation about a mean of 20 m and 10 m peak, algorithm window size is 20 .....   | 188 |
| Figure 7.12: Case 5: Voltage is normally distributed with 115 kV mean and 10 kV std dev, distance also has a sinusoidal variation about a mean of 20 m and 10 m peak, algorithm window size is 50 .....  | 188 |

|   |     |
|---|-----|
| Figure 7.13: Typical 345 kV Line Geometry.....  | 189 |
| Figure 7.14: Case 6: Voltage is normally distributed with 345 kV mean and 34 kV std dev, distance remains a constant at 34 m, algorithm window size is 100.....   | 190 |
| Figure 7.15: Case 7: Voltage is normally distributed with 345 kV mean and 34 kV std dev, distance linearly drops from 34 m to 14 m, algorithm window size is 40.....  | 191 |
| Figure 7.16: Case 8: Voltage has sinusoidal variation about a mean of 345 kV mean and 34 kV peak, distance linearly drops from 30 m to 10m, algorithm window size is 40 .....                                   | 191 |
| Figure 7.17: Case 9: Voltage has sinusoidal variation about a mean of 345 kV mean and 34 kV peak, distance also has a sinusoidal variation about a mean of 24 m and 10 m peak, algorithm window size is 40..... | 192 |
| Figure 7.18: Case 10: Voltage is normally distributed with 345 kV mean and 34 kV std dev, distance has a sinusoidal variation about a mean of 24 m and 10 m peak, algorithm window size is 100.....             | 192 |
| Figure 7.19: Case 11 Simulation results for a single conductor above the earth, w=20....  | 194 |
| Figure 7.20: Case 12 Simulation results for a single conductor above the earth, w=100..   | 194 |
| Figure 7.21: Case 13 Simulation results for three phase conductors above the earth, w=20 .....  | 195 |
| Figure 7.22: Case 14 Simulation results for three phase conductors above the earth. w=70 .....  | 195 |
| Figure 7.23: Final voltage sensor prototype schematic .....   | 196 |
| Figure 7.24. Voltage sensor prototype tested at NEETRAC .....   | 196 |
| Figure 7.25: Signal conditioning circuit for the final voltage sensor prototype.....  | 197 |
| Figure 7.26: Actual test setup at NEETRAC for validating the MAVS algorithm .....   | 198 |
| Figure 7.27: HV Test-I results .....  | 199 |
| Figure 7.28: HV Test-II results.....  | 200 |
| Figure 7.29: Power harvested from developed prototype at different output load levels and asset voltages .....  | 202 |
| Figure 8.1: (a) XEH, (b) power harvested by XEH as a function of distance from and current in the conductor. ....   | 205 |

|   |     |
|---|-----|
| Figure 8.2: H-shaped geometry for the flux concentrator (left), Sample ANSYS® Maxwell simulation for finding the optimal geometry (right) .....   | 206 |
| Figure 8.3: Parametric search plots for designing an optimal energy harvester. There are a total of 6 ( ${}^4C_2$ ) cases. PD = power density, P = Power. ....  | 207 |
| Figure 8.4: Plot showing convergence of solution .....  | 209 |
| Figure 8.5: Winding Geometry .....  | 210 |
| Figure 8.6: Equivalent Circuit of flux-concentrator and transformer.....  | 211 |
| Figure 8.7: Transformer Core and Winding Geometries (all dimensions are in mm) .....  | 212 |
| Figure 8.8: (a) Locus of maximum power for all configurations at I=100A, (b), (c) and (d) radius of various windings as a function of turns (e) Voltage at the flux concentrator winding as a function of $N_f$ and $N_1$ ..... | 213 |
| Figure 8.9: Flow Chart for Optimal Designs.....   | 215 |
| Figure 8.10: Parametric Simulation results depicting conductor current in green, inter-winding voltage in blue, total winding voltage in red, and winding SCC in blue. Note that the SCC is in amps.....                        | 217 |
| Figure 8.11: Different cores tested at NEETRAC .....  | 218 |
| Figure 8.12: Circuit diagram of high impulse test facility in NEETRAC .....   | 218 |
| Figure 8.13: Experimental setup for impulse testing on the flux concentrators.....  | 219 |
| Figure 8.14: Plots showing experimental results of impulse testing on the flux concentrators. The impulse currents are in green and the voltage induced on the flux concentrator is red. ....                                   | 220 |
| Figure 8.15: Proposed protection circuit for the optimal energy harvester.....  | 225 |
| Figure 8.16: Core laminations (Left to right: S1 - Sensor core design 1, S2 - sensor core design 1, TX - transformer, FC1 - flux concentrator design 1, FC2 - flux concentrator design 2) .....                                 | 226 |
| Figure 8.17: Optimal flux concentrator and sensor cores with the required protection (Left to right: S1, S2, TX, FC1, FC2).....   | 226 |
| Figure 8.18: ZigBee® PER Variation with Distance.....   | 227 |
| Figure 8.19: ZigBee® RSSI Variation with Distance .....   | 227 |
| Figure 8.20: NEETRAC High Voltage Test Setup .....  | 228 |

Figure 8.21: Development of Corona at 80 kV ..... 229

Figure 8.22: Relationship of Variables with ZigBee® RSSI ..... 230

Figure 8.23: Conceptual diagram of sensor, including shielding scheme ..... 231

Figure 8.24: 3-D conceptualization of Stick-on sensor showing dual-cage design..... 232

## SUMMARY

It is well known and accepted that the US power grid is aging and the investments made in this space have been low over the last few decades. Given that the growth in electricity demand is projected to be approximately 3% per year, the power system is expected to witness excessive electrical and thermal stresses in the foreseeable future, if proactive measures are not undertaken. This situation is further exacerbated with the introduction of renewable energy technologies, such as wind and solar. These renewable sources of energy are intermittent and mostly located away from the load centers. Therefore, increasing penetration of such technologies necessitates additional transmission and distribution builds. Without additional investments on the grid assets, the stresses imposed on the grid are expected to further amplify. In such an environment, maintaining high reliability of the grid becomes challenging due to limited visibility of the grid parameters and low situational awareness.

Moreover, as the assets become old they require increased maintenance. Given that currently a periodic maintenance regime is followed, the cost of ownership of the asset increases. A theoretical solution to this problem could be replacement of all the assets on the grid. However, revamping a \$300 billion system by replacement of older assets with newer ones is unrealistic, if not impossible. The gambit of solutions that promise to alleviate some of the aforementioned problems for utilities include condition monitoring of assets, increase in asset utilization, incipient fault detection, intelligent (and largely autonomous) asset management techniques, and expert systems that interact with a smart monitoring infrastructure and help utilities in decision making. All these solutions require low-cost smart sensing technologies as the most fundamental element.

However, the utility grid as a whole lacks intelligent sensing technologies as the cost of present day sensors is high. Furthermore, wireless sensing units available in the market

are large and bulky, with some requiring batteries for operation and therefore demanding periodic maintenance.

This dissertation presents the concept of a small, low-cost, self-powered smart wireless sensor that can be used for monitoring current, temperature and voltage on a variety of utility assets. Wireless sensor network architecture for integrating these sensors to information systems, such as SCADA, are proposed. The role of the proposed sensor is to provide real-time information and min-max history of asset parameters, and to detect faults and absence of power on assets. Novel energy harvesting approaches are proposed that enable the sensor to operate without batteries and to have an expected life of 20-30 years.

The sensor measures current flowing in an asset using an open ferromagnetic core, unlike a CT which uses a closed core, which makes the proposed sensor small in size, and low-cost. Further, it allows the sensor to operate in conjunction with different assets having irregular geometries, such as bus-bars, cables, overhead conductors, transformers, and shunt capacitors, and function even when kept in the vicinity of an asset. The proposed self-powered current and temperature *Stick-on sensor* has been designed, fabricated and operated using a novel power circuit developed in this research.

As the *Stick-on sensor* uses an open ferromagnetic core-coil assembly for current sensing, it is prone to errors from other current carrying assets that produce far-fields, which interact with the sensor. Further, a change in the position of the sensor relative to the asset causes a change in its characteristics. Therefore, the sensor needs expensive calibration at the time of installation. This research develops novel current sensing algorithms that help the sensor to autonomously calibrate and makes the sensor immune from far-fields and crosstalk. The current sensing algorithm has been implemented and tested in the lab at up to 1000 A current.

Further, a novel self-calibrating low-cost voltage sensing technique is also developed. The major purpose of voltage sensing is detection of sags, swells and power loss on the asset; therefore, the constraint on error in measurement is relaxed. The technique has

been tested through several simulation studies. Further, a voltage sensor prototype has been developed and tested on a high voltage bus at up to 35 kV.

Finally, this research also presents a study of sensor operation under faults, such as lightning strikes, and large short circuit currents. These studies are conducted using simulations and actual experiments. Based on the results of the experiments, a robust protection circuit for the sensor is proposed. Issues related to the corona and external electrical noise on the communication network are also discussed and experimentally tested. Further, a novel design of package for the sensor that prevents the circuitry from external electrical noise but prevents attenuation of power signals for the energy harvester is also proposed.

# CHAPTER 1

## INTRODUCTION

### 1.1 PROBLEM STATEMENT AND BACKGROUND

Electricity demand in the United States has been on the rise since the last few decades; growing at the rate of 3% per year with an increase in peak load of 1.8% per year [1]. Further, the peak demand is expected to grow by 19% over the next decade; however, the committed capacity is projected to grow by only 6% [2]. In addition, transmission and distribution system investments to support the demand and modernize the grid have been stagnant for a long time and only very recently have started gaining momentum. To exacerbate the problem, many assets on the utility grid are nearing their end of life. For instance, more than half of the transformers in the US are above 40 years of age [3].

Furthermore, introduction of new policies and initiatives, such as the SunShot initiative, which is a collaborative national effort to make solar energy cost competitive with other forms of energy by the end of the decade; the RPS mandates, a regulation that requires states to voluntarily participate in producing a percentage of their energy from renewable energy resources over a given period; and in general, an increase in governmental spending on the renewable energy technologies promise to boost the penetration of wind, solar and other renewable forms of energy on the grid. Such *green energy initiatives* seem to be attractive from the standpoint of improving energy security and reducing the dependence of US on foreign oil. However, as most of the renewable energy sources are either intermittent or remotely located from the load centers, without additional transmission and distribution builds, the stresses (electrical, thermal and mechanical) on the system are expected to amplify.

Other trends and policies, such as government subsidies on electric vehicles (EV) and introduction of EVs by several auto-manufacturers, for example Ford Focus EV, Nissan Leaf, and Chevrolet Volt, show an increasing penetration of EVs in the society.



Research studies have shown that without effective monitoring and smart charging schemes, high localized penetration of EVs can reduce the life of a 40 year distribution transformer to 3 years; thereby, severely impacting the already decrepit condition of some grid assets [4]. Therefore, with an ever evolving grid, energy policy and political climate, one of the major challenges seen by utilities today is maintaining high reliability of the assets on the grid.

A theoretical solution to these problems could be to replace all the existing assets with new ones. According to the U.S. Department of Energy, the total asset value of US infrastructure stands at around \$800 billion with close to 40% of the investments in transmission and distribution networks [5]. Revamping a \$320 billion system by replacement of older assets with newer ones is unrealistic, if not impossible. Therefore, solutions are needed that can:

- Defer and reduce capital investments without impacting the asset life
  - Instead of replacing all assets, if a layer of intelligent monitoring infrastructure is added, possibly, the expenditure on grid modernization can be reduced.
- Help perform condition monitoring rather than following a scheduled maintenance regime
  - Presently, all assets have pre-defined periodic maintenance regimes. As assets get old, they require frequent maintenance which increases their cost of ownership. Condition-based monitoring can lower these costs by servicing only the assets that require maintenance. Given that 45-65% of senior utility engineers are at or close to retirement age, a condition-based maintenance solution that requires minimal human intrusion is probably the only option.
- Help prioritize asset replacement based on economic and condition assessment

- An intelligent monitoring infrastructure can help prioritize asset replacement by analyzing the historical condition of the asset, comparing it with the present state and help make intelligent decisions.
- Increase the utilization of the assets by intelligent monitoring
  - Even though many grid assets are nearing their end of life, some assets are not as old and can be pushed to higher capacities. Further, without enough visibility of the grid parameters it is difficult to discriminate between assets that are being pushed to their physical limits from those that are lightly loaded. Therefore, the utilization of the entire grid is reduced.
- Reduce downtime during outages by helping expeditious forensic and diagnostic analysis to identify the root causes of a failure. Moreover, help pinpoint the failed asset to accelerate its replacement and reduce truck rolls.

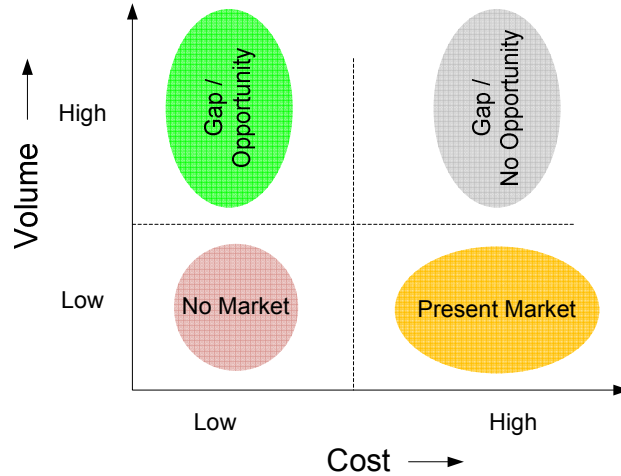
Using a *bottom-up approach* for finding the driving forces that enable these solutions, it is evident that at the bottom of the pyramid lie smart sensing technologies integrated with a variety of assets to give low-cost and meaningful measurement information. Information from these sensors can be utilized by asset managers, operators and system planners for taking proactive decisions and enabling the solutions for improving reliability, and utility of the assets.

However, the utility grid as a whole lacks intelligent sensing technologies. 60-80% of the generation and transmission assets are well monitored, however, only 20% of this information is used [6]. On the other hand, sub-transmission, distribution and substation assets are seldom monitored. The fundamental reason behind this disparity is the cost of sensors relative to the infrastructure of interest. Transmission and generation assets are considered critical, as a single point of failure of these assets may affect a large portion of the system. Moreover, these single point investments are much larger as compared to the distribution systems. For example, a 100 MVA transformer costs around \$5 M, while a 35

kVA distribution transformer costs around \$1000. Therefore, investment on sensing technologies for transmission and generation assets is usually justified. Nevertheless, even in transmission assets, such as transmission lines, given the high cost of the available sensors, it is not possible to monitor every span of the line. Hence, many opportunities in implementing smart sensing technologies in generation and transmission assets still exist [7]. On the other hand, if substations and distribution systems are considered, the cost of the present-day sensors relative to assets becomes comparatively large. Further, a distributed solution is required to cover all of the assets, and therefore, the cost multiplies.

In addition, there are other challenges associated with integrating the sensors through wired or wireless communication channels: strict conformance with utility security protocols, interoperability with different systems such as SCADA, HMI and substation LAN, and fulfillment of the highest standards of reliability [8]. Therefore, given the high-cost of present sensing technologies, the business case for monitoring a majority of utility assets becomes weak.

*Gaps analysis* in the market shows two gaps in the volume-cost space of the sensors, shown in Figure 1.1. The present market lies in the area of high-cost and low-volume trading. In this space, there exists a gap that the industry strives to move towards, which is represented by high-volume, high-cost and high-functionality sensors. However, given the past trends, moving the market towards high-cost, high-volume sensors has very low probability of occurrence, as profits and return on investment (ROI) drive businesses, and adopting expensive sensors in high volume may not be a wise business solution for utilities. However, there exists another gap represented by high-volume and low-cost sensors, which seems to have promise. Provided that low-cost sensors do not exist in the market today, presumably the major challenge is development of low-cost smart sensors.



**Figure 1.1: Gaps/Opportunities for smart sensors in the volume-cost space**

On the positive side, advancement in the low-power electronics industry has given rise to ultra-low power processors that can be easily interfaced with radio communication platforms. The system-on-chip (SoC) solutions of today can pack a relatively fast microcontroller, peripherals, radio and memory on a single chip. Therefore, these SoC solutions can help build intelligent sensors that perform not just routine measurements but also have the on-board capability to process and route data.

Moreover, developments in communication technologies in the last decade have given rise to wireless meshed systems, multi-hop and self-healing networks, and various low-power protocols having high security standards. In the past, wireless communication was thought to be unreliable and ineffective over long distances. However, different network topologies comprising effective wireless signal routing algorithms have improved range and reduced power consumption, for example, protocols like ZigBee<sup>®</sup> Pro and Ultra Link Processing (ULP<sup>™</sup>) from Onramp Wireless [9]. These improvements can be leveraged to form a highly reliable communication network. Thus, when the smart sensors are used in conjunction with the wireless sensor network (WSN) communication architecture, the entire network becomes an attractive solution for monitoring utility assets. The interest in the area of smart sensing and communications integrated with the grid assets is such that companies like Cisco and Motorola have also entered the *Smart Grid* arena. Moreover, it

has attracted venture funding and several start-ups in this space. For instance, in the last decade, more than ten startups have come up in the *smart grid* sensing and wireless communications arena.

Even with these developments, wireless sensing units available in the market are large and bulky, with some requiring batteries for operation and therefore demanding periodic maintenance [10]. Above all, most of the solutions currently available in the market are quite expensive. If these sensors were used to monitor all assets in a smart substation, with conventional sensors costing around \$1000 - \$5000, a total investment of close to a million dollars will be required for installing the sensing units for a single substation with a total of 300 sensors. This expenditure does not include the cost of calibration, installation, O&M and the total cost of integrating the communication network.

If a larger system is considered where a million end nodes are deployed, with conventional 900 MHz meshed protocols, expenditure on the order of \$40M for network integration and \$30M for deployment would be required [11]. These costs can be reduced by an order of magnitude by using newer network architectures (For instance, ULP<sup>TM</sup> proposed by On Ramp Wireless claims to reduce these costs to \$2M). Nevertheless, reduction in the network integration and deployment costs cannot be used to offset the capital costs of the sensor as a million present-day sensors would cost around \$1 billion (factoring in economies of scale). Therefore, the approach should be to reduce the per unit sensor cost by orders of magnitude. For instance, a reduction in per unit sensor cost to \$100 would lead to a total capital expenditure of \$100 M on sensors. If these proposed low-cost sensors are used in a network architecture that uses the conventional 900 MHz protocol, the total expenditure on the sensor network would be around \$200 M. With newer communication solutions, this cost could further scale down to slightly over a \$100 M, as shown in Figure 1.2.

Essentially, a new low-cost smart sensor needs to be developed that can be connected in a meshed network and work in conjunction with multiple utility assets to

provide intelligent information on the grid parameters such as voltage, current and temperature of assets.

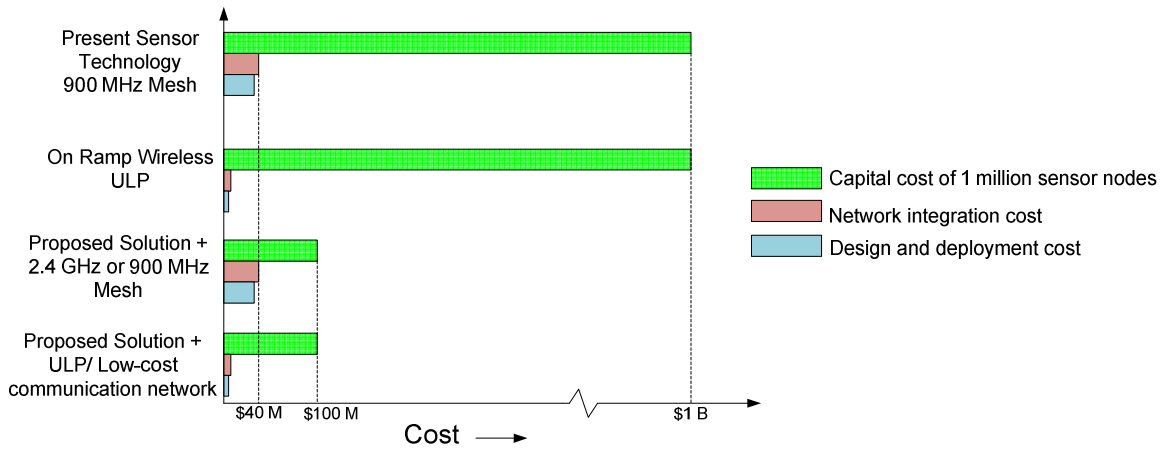


Figure 1.2: Total cost of implementing a sensor network containing one million sensor nodes

## 1.2 RESEARCH SCOPE AND OBJECTIVES

This research focuses on the development of small, low-cost, self-powered smart wireless sensors that use a low-power wireless sensor network (WSN) based communication architecture. The role of these sensors is:

- To provide real-time information of asset parameters such as current, voltage and temperature
- To store min-max history of asset parameters
- To detect faults / events on the asset
- To detect absence of power on the asset

The sensor needs to be designed to provide all these functionalities at a considerably low price point and with no maintenance requirements. Unlike conventional sensors that need to clamp around a utility asset for sensing current, the proposed sensor can *stick-on* to a utility asset; therefore, it is not limited by the geometry of the asset. The Stick-on sensor can be used in conjunction with a variety of utility assets, such as bus-bars, cables, overhead conductors, transformers, and shunt capacitors. The proposed conceptual network architecture of the sensor is shown in Figure 1.3.

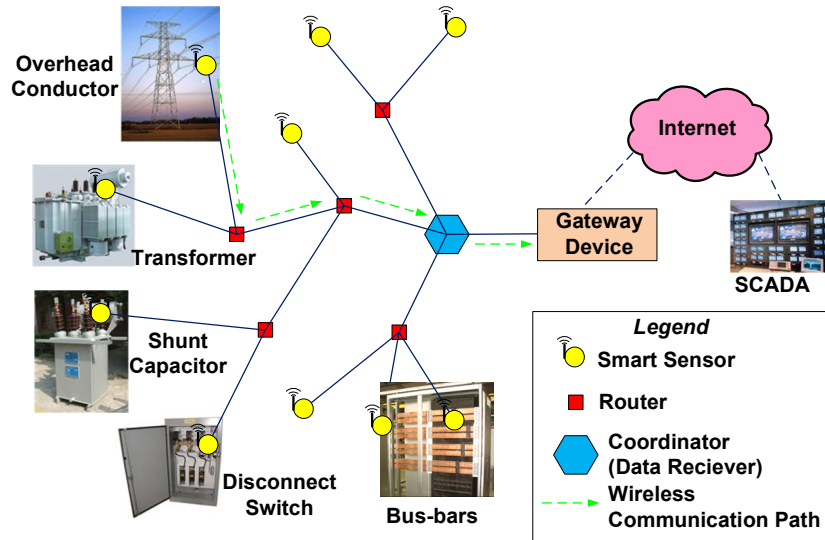


Figure 1.3: Network architecture and integration to SCADA

The primary objectives of this research can be divided into three parts:

1. Developing a power supply: The first major focus of this research is laid on self-powering the sensor. It is required:
  - a. To develop an energy harvesting method that can extract energy from the magnetic field, electric field or solar energy present in the vicinity of an energized current carrying asset.
  - b. To optimally design the energy harvester using mathematical modeling and simulation techniques so that it provides maximum power under all operating conditions.
  - c. To design a power converter circuit that can provide well regulated DC supply for the sensor electronics over a wide operating range.
  - d. To demonstrate operation of the proposed Stick-on sensor using the developed power supply.
2. Adding intelligence: The second major focus of this research is adding smartness to the sensor. Two different asset parameters namely current and voltage are considered.

- a. Low-cost current sensor: The current sensing is performed using an open ferromagnetic core, hence, the sensor doesn't require clamping around an asset. However, the sensor becomes prone to errors as other current carrying assets produce far-fields that interact with the sensor. Further, a change in the position of the sensor relative to the asset causes a change in its characteristics. Therefore, the sensor needs calibration at the time of installation. Field calibration is expensive, requires manpower and increases the effective cost of the sensor. Therefore for the current sensor, it is required to develop a smart method and algorithm by virtue of which the sensor becomes immune to the effects of far-fields in the presence of multiple current carrying assets and simultaneously performs self-calibration over time. Thereby, eliminating the need for calibration and making the sensor immune from far-fields and crosstalk.
  - b. Low-cost voltage sensor: It is required to develop a new low-cost voltage sensing technique that is self-calibrating and can provide status of power on a particular asset.
3. Making the design robust: As the sensor is being developed for utility networks, a robust design of the sensor is necessary to ensure that it keeps operating under all conditions including faults. It is required:
    - a. To design protection circuit that can help the sensor withstand high fault currents and lightning strikes.
    - b. To test wireless communication under corona and high voltage noise.
    - c. To develop a design for the enclosure that houses the sensor and which protects the sensor from external electrical noise and variable weather conditions.

The concept presented in this research resonates well with US Department of Energy's (DOE) policy framework for the smart grid. According to DOE, reducing the cost



of integrating such sensor information into utility operations forms a major part of the Smart Grid initiative [8]. It is of interest in this research to reduce the overall cost of the sensor including its integration into the power system by an order of magnitude as compared to conventional solutions so that these sensors can be deployed massively on the grid. A grid-wide monitoring solution comprising numerous smart sensors will lead to increased information on the condition of different assets. This additional information can then be used by asset managers and operators to take informed decisions regarding utilization, maintenance or replacement of their assets; reducing costs; enhancing situational awareness; and improving system reliability.

### **1.3 OUTLINE OF CHAPTERS**

Chapter 1: This chapter gave a high level overview of the present state of the sensing technology in the utility domain. A justification was provided for the need to develop a low-cost smart sensor that can be use for large scale monitoring of utility assets to increase situational awareness and visibility of the grid parameters. The problem statement was followed by the scope and objective of this research.

Chapter 2: An extensive review of the conventional current, and voltage sensing techniques, their fundamental theory of operation, and their advantages and disadvantages, is presented. Further, a market survey of the wireless current, temperature and voltage sensors is provided, and their limitations are identified. In addition, a literature review of techniques to self-power utility sensors to make them perennial devices is also given.

Chapter 3: A comparison is shown between different techniques that can be used to harvest energy present near utility assets. The two sources of energy, electric field and magnetic field that are present in abundance near utility assets are considered for the scoping study. Analytical and experimental results are presented, and the application space for each technique is identified.

Chapter 4: A novel power management circuit is proposed that suits utility requirements of high reliability, low maintenance, and low-cost. Further, simulation and experimental results are presented to validate the proposed concept. The design of a stick-on current and temperature wireless sensor is detailed. The developed circuit is used to power the stick-on current and temperature wireless sensor and all the attractive features of the sensor are showcased. Sensor network architecture using the Stick-on sensor is proposed using ZigBee® for an example substation application.

Chapter 5: Drawbacks associated with using a single core-coil assembly based current sensing are identified. A novel technique called the multi-core triangulation method (MCTM) for current sensing is proposed, rigorously developed and tested through simulations. The application space for the MCTM method is identified. Certain limitation that restrict this approach to niche applications are identified.

Chapter 6: A modification of the MCTM approach called the smart dual-core triangulation method (smart DCTM) is proposed. This approach uses two-cores for estimation of current in a general scenario containing multiple current carrying assets. Through rigorous mathematical derivations and simulation studies it is shown that this method is immune from far-fields and is self-calibrating. The smart DCTM approach for current sensing is implemented in the Stick-on sensor and operation is successfully demonstrated.

Chapter 7: The concept of a floating voltage sensor is modeled mathematically. The challenges in low-cost voltage sensing of a utility asset are identified. Based on certain realistic assumptions, novel self-calibrating voltage sensing technique called the moving average voltage sensing (MAVS) is proposed. The voltage sensing technique is implemented on a stick-on voltage sensor. The developed voltage sensor is tested on a high voltage bus and successful experimental results are provided.

Chapter 8: A process to optimally design the energy harvester and power management circuit is presented. Other practical issues, such as operation of the sensor under faulted conditions, such as high current impulses and lightning strikes, are analyzed

through simulations and experiments. Novel protection architecture to prevent the Stick-on sensor from permanent damage is proposed. The on wireless communication performance of ZigBee® in high voltage and corona based noisy environments is tested. A novel package that prevents the sensor from external electrical noise is proposed.

Chapter 9: A summary of the key results presented in this research is presented. Subsequently, a list of the major contributions made in this research is given. Finally, many interesting research projects that can be undertaken as a follow-up to this research are identified.

## CHAPTER 2

### LITERATURE REVIEW AND MARKET SURVEY

#### 2.1 INTRODUCTION

In the United States the demand for electric power has been rapidly increasing for the last few decades. Absence of commensurate growth in investments on the electricity grid have led to rise in congestion, equipment damage, system disturbances and the power grid being pushed to its technical limits. In addition, the present electricity grid is old, has started showing signs of aging and is in some sense *dumb*. Increasing dependence of society on electric power is compelling utilities to take measures that ensure high reliability of their power system apparatus.

A grid wide monitoring solution comprising numerous smart sensors would lead to increased information on the condition of different assets. This additional information can then be used by asset managers and operators to take informed decisions regarding utilization, maintenance or replacement of their assets, reducing costs, enhancing situational awareness and system reliability.

The information of utility asset parameters, such as current, voltage and temperature, is essential for intelligent decision making, health monitoring and maintenance of assets to improve the reliability of the entire power grid. Absence of this information from critical utility assets can be catastrophic and even lead to massive blackouts. In the utility arena, a variety of assets, such as conductors, cables, bus-bars, transformers, disconnect-switches, and shunt-capacitors, require monitoring. Presently, monitoring of AC current is performed using current transformer (CT), rogowski coil, and magneto-optic current transformer (MOCT). On the other hand, AC voltage sensing is performed using potential transformers. A review of all these techniques is presented in this chapter. The review presents the fundamental theory of operation, advantages and

disadvantages of all the presently used techniques for current and voltage sensing. Some of the conventionally used commercial products have also been highlighted in the review.

Further, this chapter also presents a comprehensive market survey of the wireless current, voltage and temperature sensors. The major limitations of presently available sensors are highlighted. In addition, a literature review of the methods to solve some of the problems with the state-of-the-art sensors is presented.

In a nutshell, this chapter presents an extensive review of conventional utility sensors, new wireless utility sensors, and the different techniques to self-power the sensor.

## 2.2 REVIEW OF METHODS FOR CURRENT SENSING

### 2.2.1 Current Transformer

Current transformers use the principle of Faraday's law of induction for current measurement which states that a time varying magnetic flux linking with a coil induces a voltage across the coil terminals. This can be mathematically represented as

$$V = -n \frac{d\Phi}{dt} \quad (1)$$

$$V = -\mu_o\mu_r nA \frac{dH}{dt} \quad (2)$$

where V is the voltage induced in the coil terminals, n is the number of turns in the coil,  $\mu_o$  is the permeability of free space,  $\mu_r$  is the relative permeability of the core material (for air cored coils  $\mu_r$  is one), A is the area of the coil, and H is the magnetic field intensity linking with the coil. The operating principles of a CT is shown in Figure 2.1(a).

Current transformers usually have very few turns on the primary side (one turn in the case of a conductor) and many turns on the secondary. The secondary is usually short circuited or connected to a small load. The core in these transformers is usually ring-shaped such that a conductor can pass through it. This approach has a limit on the maximum current measurement as the core saturates at high current values. Although, the

saturation of core depends on the core material, typically CTs can be used to measure currents up to 10 kA.

CTs are either used for revenue grade current monitoring or protection systems. Both the applications have different design metrics. On the one hand, protection systems require measurement of high currents; therefore, they are designed to not saturate at higher currents. While on the other, the revenue grade current metering requires high accuracy of measurement but may not require a wide measurement range. The revenue grade current meters are designed for high accuracy current sensing (up to 0.5% accurate) while protection system CTs may not be as accurate (up to 5%). There are a slew of CTs that exist in the commercial domain, and are used by utilities for current monitoring, as shown in Figure 2.1(b) and (c) [12], [13]. However, this approach has the following disadvantages:

- CTs are bulky due to the large ferromagnetic core
- They require clamping around the asset; therefore, they are limited in application
- They need different designs for different applications
- They are very expensive

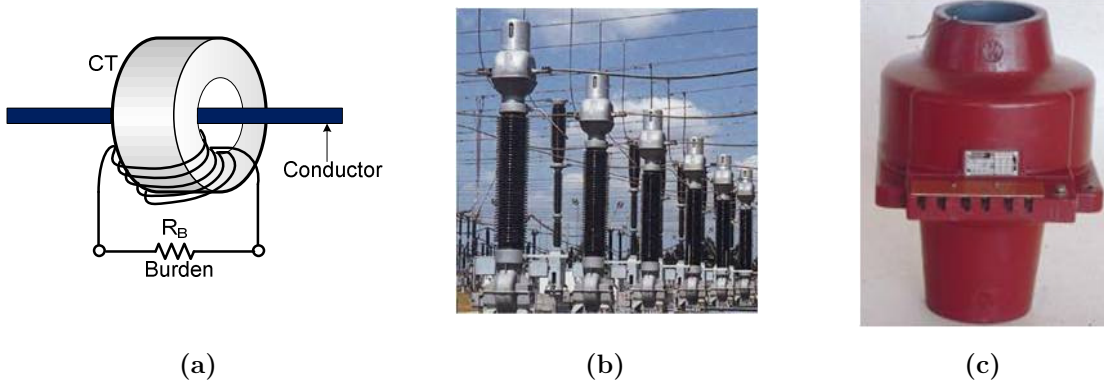


Figure 2.1: a) Operating principle of a CT, b) oil immersed CT for high voltage applications (72-800 kV applications) [12], and c) bushing CT by ABB [13].

### 2.2.2 Rogowski Coil

Rogowski coil is a helical air-core coil wound on a rectangular or circular strip. As it has an air core it is usually flexible and can be used in different applications. It wraps around the current carrying conductor, and its output signal is given by

$$V = -\mu_o \frac{n}{l} A \frac{dI}{dt} \quad (3)$$

where  $I$  is the current flowing through the conductor, and  $l$  is the mean path of magnetic field lines.

As compared to a CT, a rogowski coil does not have any ferromagnetic core; thus, it has excellent linearity and can be used for measurement of very large currents. Moreover, it has a relatively small inductance and provides higher bandwidth. Furthermore, it does not have the danger of high voltage induction at secondary terminals when the secondary is open-circuited, as the induced voltages are normally quite low due to lower coupling. Although, easier to construct, the design of rogowski coil is critical in ensuring a high performance and accuracy of current measurement. Since voltage induced is directly proportional to the derivative of current, the expression needs to be integrated to extract current information. For this reason, rogowski coils use integrators either analog or digital for sensing the current values. Use of analog integrators introduces offsets and reduces sensitivity of measurement. While, on the other hand, digital integrators require a DSP platform which increases cost of the sensor. Rogowski coils are widely used in applications that require very large currents, such as plasma current measurement in space, or to measure transient current pulses in the nanoseconds range [14]. As the rogowski coils are flexible, they may be used on utility assets which do not necessarily have a circular cross section [15]. Examples of rogowski coils are shown in Figure 2.2.



**Figure 2.2:** (a) ABB rogowski coil technology (4-1600A) [13], (b) flexible rogowski coil from Rocoil [15]

### 2.2.1 Magneto-Optical Current Transformer

The magneto-optical sensors use the Faraday’s effect which states:

When linearly polarized light passes through a medium comprising magnetic field in the direction of light propagation, the plane of polarization of light rotates. The angle of rotation  $F$  is proportional to the magnetic field  $H$  and to the length of magneto-optical material  $d$ , and is given by

$$F = VdH \tag{4}$$

where  $V$  is the Verdet constant. The operating principle is shown in Figure 2.3.

A change in direction of the magnetic field intensity changes the sign of rotation of polarization. Therefore, if the light goes back and forth through the same material the angle of polarization becomes twice. Equation (4) is valid for diamagnets and paramagnets but does not apply to magnetically ordered materials, such as Ferromagnets. In the case of ferromagnets there is a functional relationship between Faraday rotation and magnetization (not magnetic field intensity). The sign of  $F$  depends on the sign of magnetization [16]-[17].

The instruments used for current measurement which are based on this magneto-optical theory are called Magneto-optical current transformers (MOCT). MOCT can be either based on diamagnets or transparent ferromagnets. For diamagnets the equation that can be applied to measure current is given by



$$F = V \oint H dl = NVI \quad (5)$$

where I is the current being measured.

MOCTs find some applications in the utility industry. As it uses light beam propagating in air or through fiber optic cables, the insulation requirements are relatively simpler when compared to CTs in high voltage systems. Moreover, MOCTs have an improved bandwidth, a dynamic measurement range, and have shielding from electromagnetic interference. The same MOCT can be used to measure currents over a range of 5 A to 4000 A with high accuracy. An example of commercially available MOCT is shown in Figure 2.3 [18]. However, this technology is quite expensive and rather complex.

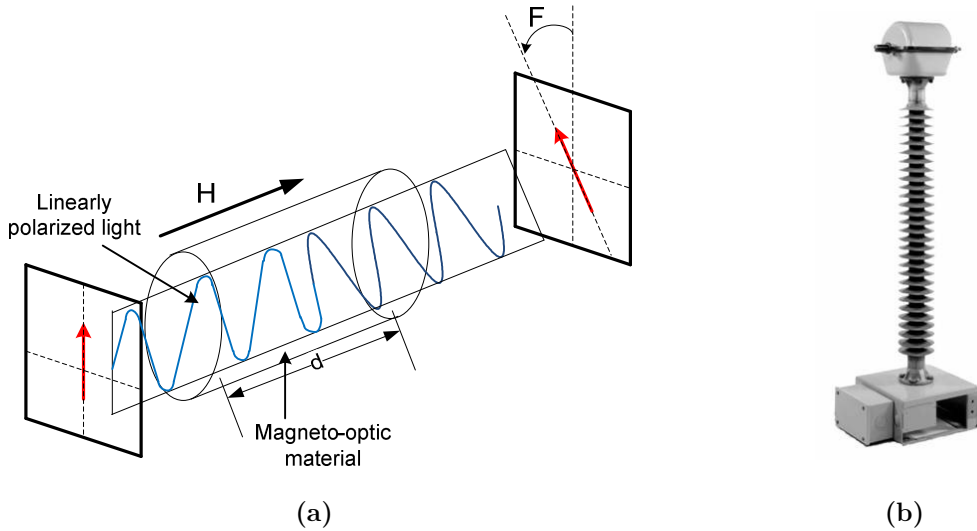


Figure 2.3: (a) Operating principle of an MOCT, (b) ABB MOCT (measures upto 4000 A) [18]

### 2.2.2 Hall-effect Sensor

Hall-effect sensors named after its inventor E. H. Hall are based on the principle of charge separation caused by Lorentz forces on charges travelling with velocity  $v$  in a traverse magnetic flux density  $B$ . The force experienced by the charges is represented as

$$F = qE + q(v \times B) \quad (6)$$

In an N-type extrinsic semiconductor material strip, if the Electric field  $E_e$  is applied along the length of the material the electrons move along the strip with a drift velocity. The magnetic-field forces the electrons to shift to the edges and give rise to space charges. These space charges then produce an electric field  $E_H$  which acts on the electrons. In the steady state, the force due to magnetic field and electric field balance, and the following relationship is obtained

$$E_H \simeq \mu_n (E_e \times B) \quad (7)$$

where  $E_H$  is called the Hall electric field. Equation (7) can also be represented in terms of current density as

$$E_H = R_H (J \times B) \quad (8)$$

where  $R_H = r_H / qn$ ,  $r_H$  is the Hall scattering factor. Voltage induced across the two edges of the semiconductor strip is then given by

$$V_H = R_H \frac{IB}{t} \quad (9)$$

where  $t$  is the thickness of the strip. The operating principle of Hall-effect sensors is shown in Figure 2.4(a).

Equation (9) shows that voltage  $V_H$  is linearly related to  $B$  across the strip. Hall-effect sensors can be placed in the air gap of a magnetic core which concentrates the flux linking with a current carrying asset. The biggest drawback of Hall-effect sensor is the offset voltage even when the magnetic field is zero. A typical offset drift of a 50 A sensor is 600  $\mu$ A [19]. Another problem with these sensors is that even if the Hall element is sandwiched between a ferromagnetic core, the Hall sensors tends to interact with the magnetic field leakage from close currents. Some solutions to improving sensitivity, accuracy and bandwidth of these sensors exist in literature and are also available in the commercial domain [20].

Furthermore, these sensors need a DC supply for sensing current, as the fundamental principle requires an electric field to be applied across the hall element. Hall-effect sensors are widely used in power electronics converters and motor drive applications

where high sensitivities and bandwidths are required along with the capability to measure AC and DC currents. Examples of commercially available Hall-effect sensors are shown in Figure 2.4(b). However, Hall-effect sensors do not find widespread applications in utility domain.

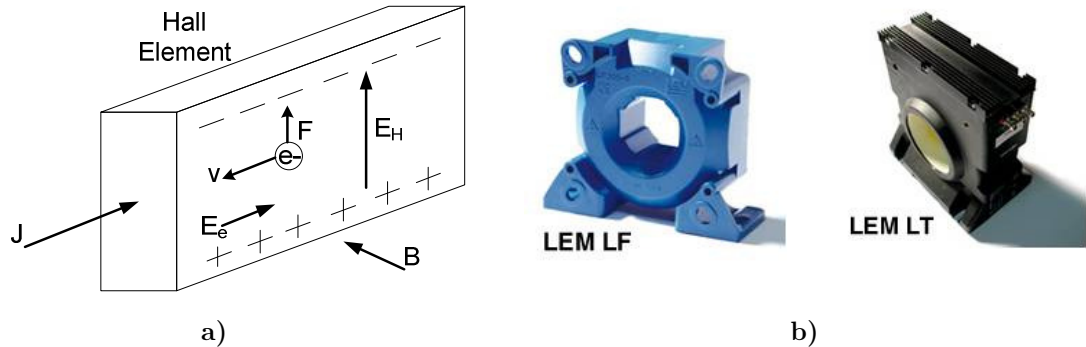


Figure 2.4: a) Operating principle of Hall-effect sensors, b) Commercial Hall-effect sensors by LEM (measures up to 3000 A (LEM LF) and 15 kA (LEM LT)) [21]

### 2.2.3 Magneto Resistive Sensors

Anisotropic magnetoresistance (AMR), giant magnetoresistance (GMR) and colossal magnetoresistance (CMR) sensors work on the principle of change in resistance of current carrying magnetic material when a magnetic field is applied. The resistance increases with an increase in parallel magnetic field to the current flow while reduces with increase in traverse magnetic field.

AMRs are arranged in bridge configuration for effective current measurement. Typical application is galvanically isolated current sensing in PWM regulated brushless motor. These sensors are manufactured by F.W. Bell and Sensitech with ranges from 5 to 50 A [19].

On the other hand, GMR sensors have a very high sensitivity, and can be directly formed on integrated circuits. GMR has been used for current sensing in motors [22], [23].

### 2.2.4 Drawbacks of Existing Current Sensing Techniques

Apart from the standard current sensing solutions listed above there are other current sensing technologies, such as Superconductive Quantum Interference Devices

(SQUID), etc. These techniques have found uses in measurement of magnetic fields in other applications like space research. However, they are not used in utility, motor drive, power electronics or power system applications due to high costs and difficulty of practical implementation.

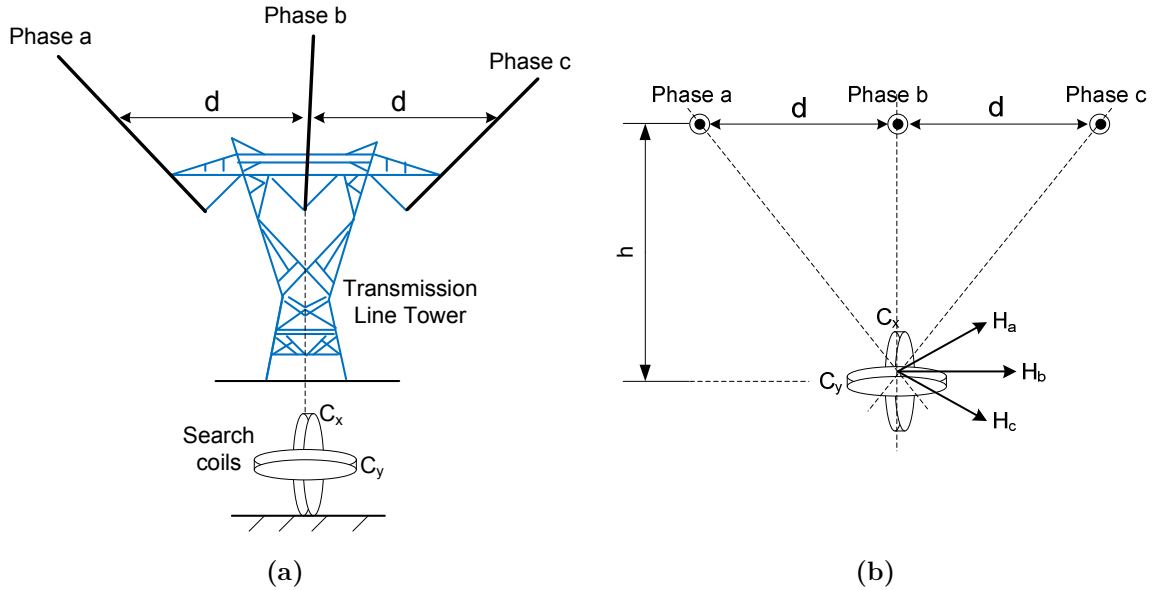
The current monitoring techniques reviewed above have major disadvantages which are listed below:

- All techniques are expensive and aim at measuring current in specific utility assets
- Some of the more prevalent techniques, such as CTs, are quite large and bulky
- CTs require redesigning for different applications. An accurate and highly sensitive CT cannot measure large currents; while, a CT which measures large currents is not very accurate
- Except for rogowski coil, there is no other technique which has the flexibility of being used on a variety of assets. Most of the techniques, especially the most widely used CTs, are limited by the geometry of the asset
- Even rogowski coils have strict design constraints as they have higher errors
- Techniques, such as hall-effect sensors and magneto resistive sensors are usually not used in utility applications which require monitoring high currents. Moreover, they have the problem of offsets and other design challenges
- MOCTs are rather complex and quite expensive.
- Some techniques, such as SQUIDS are quite complex and have not found interest in the utility arena due to complexity and cost of installation

Furthermore, if at all used, these techniques are installed on only a few critical utility assets as most of these methods are quite expensive. Moreover, presently these techniques use power line communication or some form of wired network for data transmission. Wired communication adds to the complexity of the already obscure problem and increases overall cost and maintenance, if it were to be deployed on a grid wide scale. It was highlighted earlier that information on utility assets is essential to improve reliability. However, the present state of technology suggests that it is close to impossible to deploy existing monitoring solutions on a grid wide scale comprising a variety of utility assets.

### 2.2.5 Current Sensor by Promethean Devices LLC

Recently, an interesting approach to sensing current in overhead three-phase conductors was developed by Promethean Devices LLC. It is worth including this approach in the literature review as the approach is quite unconventional and uses an intelligent technique of sensing current. The current sensor developed by Promethean Devices LLC is called the RT-TLM (included in Table 2.1). This technique can be used for computation of current in a three phase conductor system having a geometry shown in Figure 2.5 [24].



**Figure 2.5:** (a) A new concept of current measurement in three phase transmission lines using two search coils, (b) geometry of the current measurement scheme

Figure 2.5(b) shows a pair of search coil  $C_x$  and  $C_y$  kept right below the middle conductor (phase b). Using this figure, the magnetic fields produced by phases a, b and c, that links with the two coils are given by

$$H_{ax} = \frac{I_a}{2\pi} \left( \frac{h}{h^2 + d^2} \right) \quad (10)$$

$$H_{bx} = \frac{I_b}{2\pi} \left( \frac{1}{h} \right) \quad (11)$$

$$H_{cx} = \frac{I_c}{2\pi} \left( \frac{h}{h^2 + d^2} \right) \quad (12)$$

$$H_{ay} = \frac{I_a}{2\pi} \left( \frac{d}{h^2 + d^2} \right) \quad (13)$$

$$H_{by} = 0 \quad (14)$$

$$H_{cy} = \frac{I_b}{2\pi} \left( \frac{-d}{h^2 + d^2} \right) \quad (15)$$

The total magnetic field linking with  $C_x$  is given by

$$H_x = H_{ax} \angle 0 + H_{bx} \angle 120 + H_{cx} \angle 240 \quad (16)$$

Replacing  $H_{ax}$ ,  $H_{bx}$  and  $H_{cx}$  from (10) - (12) the magnitude of  $H_x$  is given by

$$|H_x| = \frac{I}{2\pi} \left( \frac{1}{h} - \frac{h}{h^2 + d^2} \right) \quad (17)$$

$$|H_y| = \frac{I}{2\pi} \frac{\sqrt{3}d}{h^2 + d^2} \quad (18)$$

Dividing (17) and (18) gives

$$h = \frac{d}{\sqrt{3}} \frac{H_y}{H_x} \quad (19)$$

Equation (19) can be used to compute the value of  $h$  given that  $d$  is known. Further, the voltage induced on the coil is directly proportional to the magnetic fields linking with the coil. Using the values of voltage induced the height of the conductor from the ground can be determined. Finally, from (18) the RMS value of  $I$  can be found as

$$I = 2\pi |H_y| \frac{h^2 + d^2}{\sqrt{3}d} \quad (20)$$

Equation (20) above gives a closed form solution for current. However, this current is for a particular geometry and is not applicable for a different geometry. Moreover, its calculation requires the knowledge of  $d$  (distance between the two conductors). Also, it was assumed in the above calculations that  $h$  and  $d$  is fairly constant and is the same for all conductors, which may not be the case. If the geometry of the three phase conductors is

changed, the positioning of the sensors has to be changed to compute a meaningful solution.

Therefore, the above approach alone cannot give enough information to compute the value of the conductor currents. The patent makes use of three different pairs of coils giving information on the current flowing in the overhead conductors. Moreover, the concept makes use of an iterative approach for computation of current phases and magnitudes. In the most general sense the voltage induced on the coils can be represented as

$$V(t) = -nA \frac{dB}{dt} \quad (21)$$

$$B_x(t; x_o, y_o) = -\frac{\mu_o}{2\pi} \sum_{i=1}^3 \left[ I_i(t) \left( \frac{y_o - y_i}{r_{1i}^2} \right) \right] \quad (22)$$

$$B_y(t; x_o, y_o) = \frac{\mu_o}{2\pi} \sum_{i=1}^3 \left[ I_i(t) \left( \frac{x_o - x_i}{r_{1i}^2} \right) \right] \quad (23)$$

$$r_{1i} = \sqrt{(x_o - x_i)^2 + (y_o - y_i)^2} \quad (24)$$

The technique used by Promethean devices gives some additional insight on potential techniques of designing intelligent sensing algorithms. However, this technique can only be used with overhead conductors. In fact, in the presence of far fields due to other distant assets, the technique would fail. Furthermore, it requires computationally intensive algorithm for determining the current values; therefore, the sensor requires more power for operation.

### 2.2.6 Newer Current Sensing Techniques

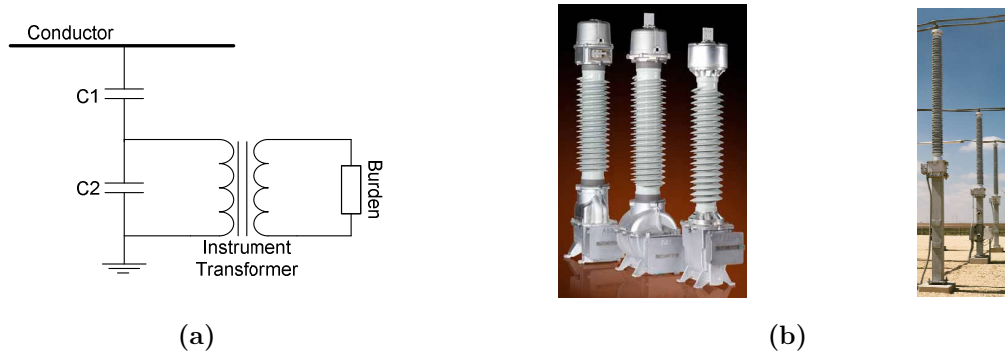
Another interesting technique uses a circular array of magnetic sensors around a DC busbar [25]-[26]. This technique requires solving four variables in a set of non-linear equations, which can be implemented on a DSP. However, due to the computational intensive nature of the algorithm, it cannot be implemented on a low-power sensor. The paper deals with a method to reduce cross-talk from far-fields; however, the issue of

calibration is not discussed as the paper assumes a circular geometry and approximates the Ampere’s circuital law. Therefore, the sensor itself needs to wrap around the busbar, which makes the sensor unwieldy. Finally, the algorithm has been shown to operate with DC currents only.

### 2.3 REVIEW OF METHODS FOR VOLTAGE SENSING

Voltage is another important parameter for utilities and if low-cost voltage sensing functionality is added to the smart sensor, it would be a highly beneficial feature having great value.

In the past, voltage measurement of high voltage assets up to 765 kV has been accomplished with the use of potential transformers (PT) and capacitively coupled voltage transformers (CCVT). A CCVT comprises a capacitor divider circuit, and the voltage induced on both the capacitors is proportional to the asset voltage, as shown in Figure 2.6. Thus, the asset voltage can be determined by measuring the voltage across one of the capacitors. However, as this technique requires two physically connected capacitors across a high voltage asset and ground, it has stringent insulation requirements. This requirement increases the design challenges, size and cost of these sensors. In the present form, it is not feasible to use this technology for voltage sensing in low-cost sensors.

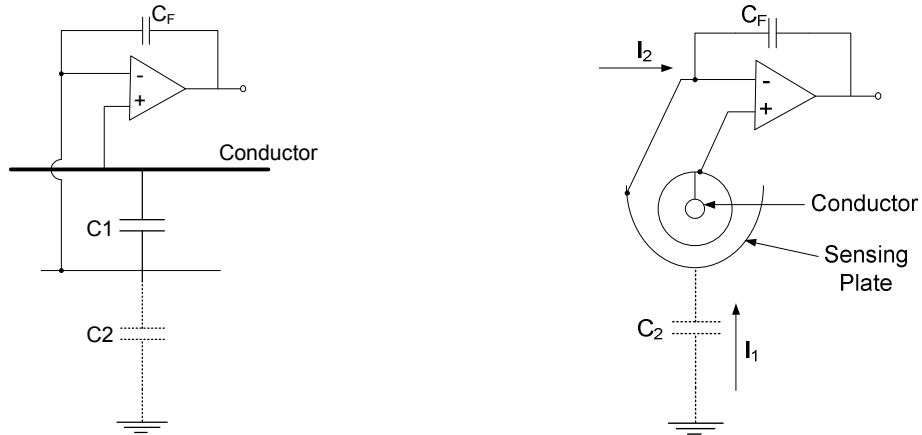


**Figure 2.6: a) Conventional capacitive divider voltage sensing operating principle, b) PTs offered by ABB [10] and Trench [13]**

To reduce the insulation requirements of the voltage sensor, the sensor can be floated at the same potential as the asset, as shown in Figure 2.7. In this case, the air



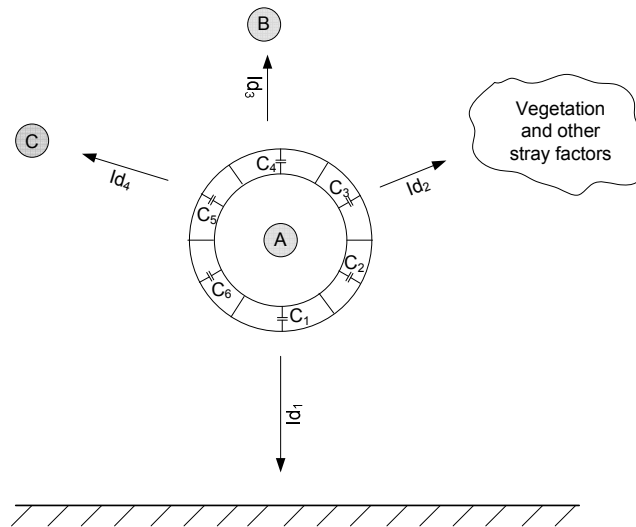
between the sensing plate  $S_1$  and ground acts as a dielectric medium between capacitance to ground. The capacitor  $C_1$  is then used to measure the voltage of the conductor. A low impedance integrating amplifier between the sensing plate and the conductor can be added which brings the sensing plate to the asset potential and effectively eliminates  $C_1$  from the circuit. The displacement current in capacitor  $C_2$  flows through  $C_F$  of the op-amp and results in a voltage output across the op-amp which is directly proportional to the asset voltage. A major drawback that ensues with this approach pertains to deposition of water drops or snow on the sensing plate, changing the displacement current flowing through the op-amp. To minimize the errors due to this effect, the width and length of the sensing plate has to be very large as compared to the gap between the two sensing plates; this solution has been implemented in [27]-[28]. However, this approach is not immune to the effect of tree branches in the vicinity of the asset or the presence of multiple assets in the vicinity. Moreover, the physical geometry requirements to reduce spurious external effects are demanding and tend to increase the overall size of the sensor.



**Figure 2.7: Voltage sensor floating at the same potential as the conductor**

Recently, to tackle the effects of vegetation, distance to ground, nearby assets, a novel method of using a circular array of capacitor plates was introduced [29], as shown in Figure 2.8. The main idea of this method is the use of multiple capacitors (six capacitor plates) for eliminating the effects due to external conditions in voltage measurements. The

displacement current flowing through each of the capacitor plates has information embedded in it related to external conditions, such as geometry of nearby conductors and vegetation. An algorithm analogous to rotating reference frames in electrical machines has been devised for extracting the information of the nearby asset geometry from the six displacement currents. The approach presented in this research has been validated in simulations. However, it has not been demonstrated experimentally. This approach suffers from a major drawback in that it requires six capacitor plates distributed in space encircling the conductor which increases the size of the sensor. Moreover, this approach can only be used with conductors and does not have the flexibility of being used in conjunction with other assets. Furthermore, the algorithm is fairly involved and requires increased computation power to solve for the voltage, phase angle, and conductor clearance. The increased computation demands more power for operating the sensor, and is a cause for concern in a self-powered low-cost sensing application. In addition, the algorithm is based on the premise that the conductor is a part of a three phase system and cannot operate in a single phase electrical system.



**Figure 2.8: Voltage sensor using circular array of capacitor plates surrounding the conductor**

All in all, different techniques exist in the market and in research for sensing voltage in high voltage utility assets. However, none of the techniques provide a flexible low-cost solution for voltage sensing.

## **2.4 REVIEW OF WIRELESS UTILITY SENSORS**

The transformation of the power grid from a less informed or a *dumb* system to a smart and more intelligent system is imperative. Cognizant of the present scenario, there have been some improvements in the sensing technology for utility assets. Research in the area of asset monitoring has led to the development of some solutions in the commercial domain, which use wireless communication for data transmission. Wireless communication has some conspicuous advantages as compared to wired networks as it doesn't require additional space, it is less expensive to deploy, additional wireless equipment can automatically connect into an existing wireless network, it is mobile, portable, and less susceptible to ground potential [30]. Some of the newer technologies which utilize wireless communication and are available in the market and in research are presented in Table 2.1.

**Table 2.1: Market Research of Wireless Current Sensor Units**




| Product<br>(Company)                           | Description   | Picture   |
|--|---|---|
| <p><b>Power Line Sensor (Protura) [31]</b></p> | <ul style="list-style-type: none"> <li>Measures conductor temperature, ambient temperature and distance to ground.</li> <li>Sends the information using General packet radio service (GPRS)</li> <li>Powered by a current transformer which scavenges power from the magnetic field around the transmission line. Further, an auxiliary supply of 12V is also available onboard. The harvesting circuit powers the sensor when the current in the line is more than 55 A. Below this current the auxiliary supply powers the device.</li> <li>The auxiliary supply comprises a rechargeable battery system. Charging of the battery begins when the current in the line is above 90 A and the total charge time is 6 hours.</li> <li>The power line sensor measures 37 cm in diameter, 120 cm long and weighs 34 Kg.</li> </ul> |                              |
|  |   |  <p>CT that pulls energy</p> |
| <p><b>Power Donut (USi) [32]</b></p>           | <ul style="list-style-type: none"> <li>Measures current, voltage, and conductor temperatures. The data is saved on-board and transmitted on demand using Global system for mobile communication (GSM) wireless cell phone technology.</li> <li>Powered by magnetic flux coupling from the conductor and operates at voltages up to 500 kV. It is powered from a minimum start up current of 50 amperes and functions on battery for 12 hours when line current is less than 50 amps. Charging begins when the line current is above 120 amperes and has a total charge time of 6 hours.</li> <li>Dimensions: 32 cm in diameter, 14 cm in thickness and weighs 10 kg.</li> </ul>   |                             |

Table 2.1 continued


| Product<br>(Company)  | Description  | Picture   |   |
|---|--|---|---|
| <p><b>GridSync</b><br/>(ABB) [33]</p>   | <ul style="list-style-type: none"> <li>Measures current and voltage.</li> <li>Designed to be used with a wide range of communication applications.</li> <li>Requires an external power supply.</li> <li>Dimensions: t measures 56cm x 38 cm x 17.8 cm and weighs 41 Kg.</li> </ul>   |    |   |
| <p><b>VaultSense<br/>Wireless<br/>Current<br/>Sensor</b><br/>(Eaton) [34]</p>       | <ul style="list-style-type: none"> <li>This wireless current sensor clamps around secondary cables in underground vaults and reports current measurements every thirty seconds.</li> <li>Powered inductively through current that runs through the power cable on to which the sensor clamps.</li> <li>Current measurement range: 40A – 1000A.</li> <li>Voltage rating range: 600V (AC).</li> <li>Unit dimensions: 57 mm x 98 mm.</li> <li>Temperature operation range: -40°C to +70°C.</li> <li>ZigBee® wireless communication (IEEE 802.15.4, 915 MHz or 2.4GHz).</li> </ul> |   |   |
| <p><b>WSO<br/>Wireless<br/>Sensor for<br/>Overhead<br/>Lines (SEL)</b><br/>[35]</p> | <ul style="list-style-type: none"> <li>Monitors load current, temperature, fault threshold, and outage history.</li> <li>Reports to SCADA via radio communications network.</li> <li>Fault-Sensing Range: 50 to 1200 A.</li> <li>System Voltage Range (L-L): 4.16 to 34.5 kV.</li> <li>Powered by batteries.</li> <li>Approximate Weight: 570 g.</li> </ul>  |  |  |

Table 2.1 continued






| Product<br>(Company)   | Description  | Picture   |   |
|--|--|---|---|
| <p><b>LightHouse<br/>MV Sensor<br/>(Tollgrade)</b><br/>[36]</p>  | <ul style="list-style-type: none"> <li>Measures current, before, during, and after significant events.</li> <li>Inductively powered and has the ability to store energy which maintains communications in the event of an outage.</li> <li>Operating voltage: 4 – 35 kV.</li> <li>Conductor diameter range: 4.1 mm – 26 mm.</li> <li>Case Dimensions (HxWxD): 152 mm x 305 mm x 127 mm.</li> <li>Antenna Cover Height: 210 mm.</li> <li>Weight: 2.5 kg.</li> <li>Operating Temperature: -40 C to 50 C.</li> <li>Energy Storage: Maintenance free ultracapacitors.</li> <li>Operating current range Operating : 12 to 600 A.</li> </ul> |    |  |
| <p><b>Real-Time<br/>Transmission<br/>Line Monitor<br/>RT-TLM<br/>(Promethean<br/>Devices LLC)</b><br/>[37]</p> | <ul style="list-style-type: none"> <li>Measures 3-Phase currents, conductor clearance, and maximum conductor temperature. Uses wireless, encrypted data communication and secure data storage.</li> <li>Uses solar-battery power supply.</li> </ul>  |    |  |
| <p><b>Power Line<br/>Sensor using<br/>Backscatter<br/>(EPRI, SwRI,<br/>TVA)</b> [38]</p>                       | <ul style="list-style-type: none"> <li>Measures the present temperature, the present line current, the peak temperature and the line current measured at the time of the peak temperature.</li> <li>Uses the radio backscatter technology.</li> <li>Powered through line current for currents greater than 80 A. However, it requires backup batteries.</li> </ul>   |  |   |

Table 2.1 continued








| Product<br>(Company)  | Description   | Picture   |   |
|---|---|---|---|
| <p>UNC<br/>Charlotte,<br/>TVA and<br/>EPRI [39]</p>                                 | <ul style="list-style-type: none"> <li>Transformers: Transformer surface temperatures are continuously monitored in order to detect anomalous conditions.</li> <li>Circuit breakers: Oil-filled circuit breaker surface temperatures are continuously monitored, and relative tank temperature differences are used to indicate fault conditions.</li> <li>Transformer bushings: A bushing monitoring node that captures representative data for measuring phase differences and transmits over the wireless network has been developed.</li> <li>Ambient temperature sensing.</li> <li>Uses MICAz motes that are battery operated except for a few sensor nodes which are equipped with solar energy harvesting.</li> <li>Reporting frequency of once every 15 minutes.</li> </ul> |    |  |
| <p>Line IQ<br/>previously<br/>called Line<br/>Tracker (Grid<br/>Sense)<br/>[40]</p> | <ul style="list-style-type: none"> <li>Measures load profile, line status, voltage, fault waveforms, ambient and conductor temperature, time stamped event recording.</li> <li>Multiple wireless communication options</li> <li>Line voltage &lt; 138 kV<sub>p-p</sub></li> <li>Can clamp onto conductors upto 32 mm</li> <li>Solar powered with battery back up</li> <li>Housing material: UV stabilized Polycarbonate and/or aluminum diecast</li> <li>Weight = 2.2 kg</li> <li>Dimensions: 35 x 13 x 13 cm</li> </ul>  |   |   |
| <p>Line Sentry,<br/>Load Sentry<br/>and PQ<br/>Sentry (Grid<br/>Sentry, LLC)</p>    | <ul style="list-style-type: none"> <li>Power from magnetic field around conductor and uses super capacitors for backup.</li> <li>Line and load sentry measures current, line temperature.</li> <li>PQ sentry line current and temperature, and estimates voltage from fields</li> <li>PQ sentry computes power factor, harmonics (upto 32<sup>nd</sup>), and power</li> </ul>   |  |   |

Table 2.1 continued

| Product<br>(Company)   | Description   | Picture   |
|--|---|---|
| [41]   | <ul style="list-style-type: none"> <li>• Wireless data transfer through DNP 3.0 and iDEN cellular</li> <li>• Weighs less than 4 pounds</li> <li>• Current range = 10 – 1000 A</li> <li>• Temp. range = -55 C to 125 C</li> <li>• Voltage range = 1 kV to 36 kV</li> <li>• Clamps on to cable sizes up to 1.14 inches</li> <li>• Dimension: 30.5 cm x 13.9 cm</li> <li>• Weight = 1.45 kg</li> </ul> |    |
| <b>Outage<br/>Advisor<br/>(Cooper<br/>Power<br/>Systems)</b><br>[42] | <ul style="list-style-type: none"> <li>• Measures current up to 1000A (saturates above this)</li> <li>• Contains Lithium batteries having a life of 10-12 years accompanying inductive power</li> <li>• Dimensions: 14.5 cm x 9.3 cm</li> <li>• Similar product suite is VAR-Advisor which reports blown fuses on fixed/distributed capacitor bank</li> </ul>                                       |    |
| <b>AMP Master<br/>Monitor 2<br/>(Sentient<br/>Energy)</b><br>[43]    | <ul style="list-style-type: none"> <li>• Measures current, temperature and waveform capture</li> <li>• Battery backup</li> <li>• No information on size, weight, technical specification available</li> </ul>   |  |



Wireless communication enabled sensors presented in Table 2.1 are based on the conventional methods of current and voltage monitoring presented in Section 2.2. Therefore, they face the same challenges that are faced by the fundamental approaches. Most of them are bulky, large and expensive. In fact, most of the commercially available wireless current sensors are developed to monitor only conductors or cables. They cannot be used in other applications, such as monitoring transformers, bus-bars or a slew of other utility assets.

All in all, it is clear that there is a strong need for the development of low-cost utility asset monitoring wireless sensors which can be massively deployed on the grid.

## **2.5 ENERGY HARVESTING FOR WIRELESS SENSORS**

A feature observed in the review from Table 2.1 is that most of the wireless communication enabled sensors utilize power hungry communication protocols. These protocols require high power for transmission and reception of signals, and also need relatively higher powers during quiescent conditions. Some of these sensors require batteries for operation; while, some other utilize magnetic field present around the asset for harvesting power, but still use batteries for backup power. Consider a typical scenario where the active mode power requirement of the sensor is 25 mA and the sleep mode requirement is 100  $\mu$ A [44]. The sensor stays in the active mode for 1 sec and operates after every 10 min. If the sensor is sourced with a 3.7 V, 600 mAh battery, it can be shown that the battery will not last for more than 180 days (nearly half a year). The batteries would require replacement after every few months and will discourage utilities from implementing sensing technologies on their assets. Therefore, relying solely, or even, partly on batteries for powering these sensors is not a feasible solution for implementing sensors on multiple assets in a substation and in general on the utility grid.

The simple analysis performed above shows that the sensing technology can be made feasible for monitoring the power grid assets only if the sensors were to derive power autonomously from the environment. A slew of energy sources are available near the

utility assets. All the sources provide different power densities and are associated with different challenges. It is essential to understand the challenges associated with each technique and investigate the optimal source for powering utility sensors.

This section presents a review of the different energy harvesting technologies that exist in the literature. In the review, an effort has been made to highlight the power density of all these techniques along with their benefits and limitations applied to utility assets.

### 2.5.1 Mechanical Energy Harvesting

Mechanical vibrations can be converted to electrical energy using a number of techniques. In the literature, these have been broadly divided into three groups:

- Piezoelectric Technique - uses the piezoelectric property of a material to generate electric potential under mechanical stress. This method is shown in Figure 2.9.
- Inductive spring mass system (also called a microgenerator) - uses Faraday's law of electromagnetic induction by placing a magnet attached to a spring inside a coil. Vibration of the magnet causes an induced voltage in the coil. This method is shown in Figure 2.9.
- Electrostatic method - relies on changing the capacitance of a vibration dependent variable capacitor.

In general, the governing equation for energy from mechanical vibration is given by

$$E = \frac{1}{2} Kx^2 \quad (25)$$

where E is the energy stored harvested, x is the displacement of the harvester, F is the external force applied, and K is the stiffness-constant.

Designing a generalized energy harvesting system that operates for an arbitrary vibrating source becomes challenging as the efficiency with which the energy is harvested depends on the resonant frequency of vibration, which may not be the same for the different sources. Some techniques developed to tackle these issues are found in the literature [45] - [51]. Many energy harvesters based on these fundamental principles have also found market applications, as shown in Figure 2.10 [52] - [58].

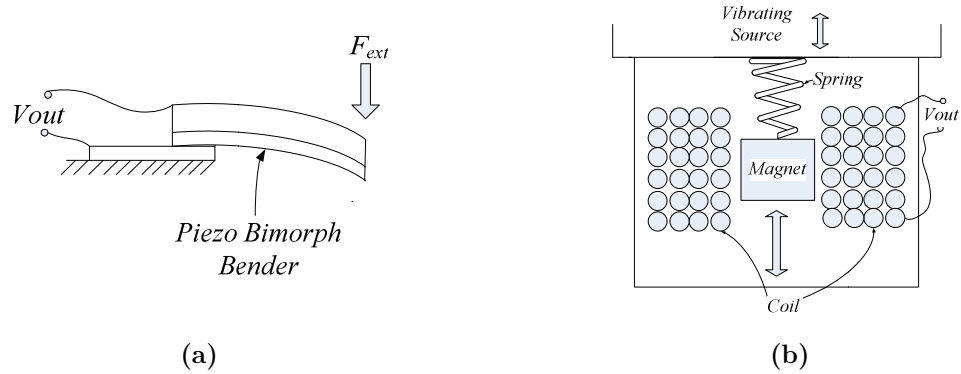


Figure 2.9: (a) Basic principle of operation of a piezoelectric energy harvester, (b) basic principle of operation of a microgenerator

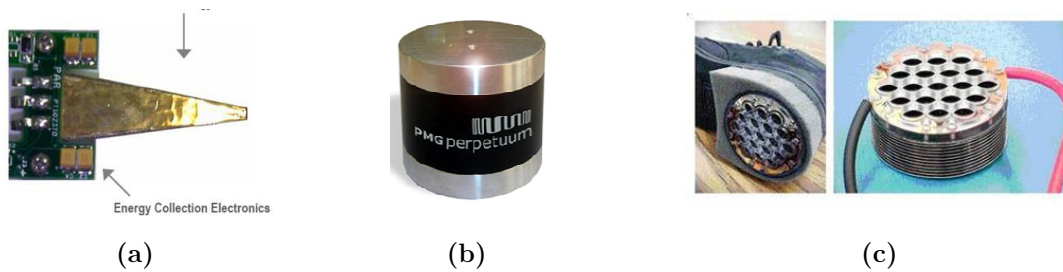


Figure 2.10: (a) Piezoelectric harvester by AdaptivEnergy [55], (b) microgenerator by Perpetuum [57], and (c) electrostatic energy harvesting shoe by Scientific Research Institute (SRI) [59]

### 2.5.2 Thermal Energy Harvesting

Systems, environments, or objects at different temperatures offer the opportunity for harvesting energy through heat transfer. The devices used to scavenge the energy due to temperature difference are called thermo-generators and this concept is called thermal energy harvesting. A thermo-generator is based on the Seebeck effect, which states that two dissimilar metals joined at two junctions maintained at different temperatures produce an electrical voltage across the junction. The resultant voltage is proportional to the difference in temperature between the hot and the cold junction.

Carnot cycle imposes a fundamental limit to the maximum efficiency at which energy can be harvested from a temperature gradient. Carnot efficiencies are limited for

small  $\Delta T$ . For example, going from body temperature ( $37^\circ\text{C}$ ) to a cool room ( $20^\circ\text{C}$ ) yields only 5.5% efficiency [59].

In order to increase the effective power output from a thermo-generator, good design practices have to be undertaken. Most of these design practices pertain to improving the quality of the thermoelectric material, or selecting an optimal shape and geometry. These design practices are discussed in literature [60] - [67]. The principle of thermal energy harvesting has also found niche applications in the commercial domain, as shown in Figure 2.11 [68] - [71].



**Figure 2.11:** (a) Harvests  $30\ \mu\text{W}$  at  $\Delta T=5\ ^\circ\text{C}$  by Thermolife energy corporation [68], (b) Harvests  $470\ \text{mW}/\text{cm}^3$  at  $\Delta T=100\ ^\circ\text{C}$  by Tellurex [71].

### 2.5.3 Solar Energy Harvesting

Solar energy harvesting has been prevalent for a long time and is a mature technology. Solar energy can be harnessed with the help of a photovoltaic (PV) system that converts sunlight into electricity. Solar panels are characterized by two parameters, the open circuit voltage ( $V_{oc}$ ) and the short circuit current ( $I_{sc}$ ). A solar panel behaves as a voltage limited current source. As the amount of incident solar radiation decreases (increases), the value of  $I_{sc}$  also decreases (increases). However,  $V_{oc}$  remains almost constant. Due to its current source-like behavior, it is difficult to power the load system directly from the solar panel. Hence, an energy storage element, such as a rechargeable battery or an ultracapacitor, is used to store the energy harvested by the panel and provide a stable voltage to the system [72].

A perennial supply of sunlight is necessary for harvesting solar energy which may not be feasible all the time. Moreover, solar cells suffer from the major disadvantage of

very low efficiency of energy conversion (8-16%). Nevertheless, PV modules are quite popular and myriad products are available in research and in the market, as shown in Figure 2.12 [73] - [78].



Figure 2.12: (a) Solar charger by ICP Solar harvests  $2 \text{ mW/cm}^3$  [77], (b) solar charger by Solio harvests  $3.7 \text{ mW/cm}^3$  [78].

#### 2.5.4 Electromagnetic (EM) Wave Energy Harvesting

With the proliferation of wireless technologies, such as Wireless fidelity (WiFi), Bluetooth, radio frequency (RF), etc., EM waves have become potential candidates for energy scavenging. The concept of EM wave based energy harvesting is shown in Figure 2.13. The power density of electromagnetic waves is equal to

$$W = \frac{E^2}{Z_o} \quad (26)$$

where  $Z_0$  is the radiation resistance of free space ( $377 \Omega$ ) and  $E$  is the local electric field strength in volts/meter. Thus, an electric field of  $1 \text{ V/m}$  yields  $0.26 \mu\text{W/cm}^2$ . However, electric fields on this order are rare except when close to a powerful transmitter; therefore, harvesting energy from EM waves has been a difficult problem until now [59].

A solution to this problem can be the deliberate transmission of RF energy solely for the purpose of powering devices. This practice is commonplace in Radio frequency identification system (RFID) which derives energy inductively, capacitively or radiatively from the tag reader.

There are two different principles on which RFID tags are powered, active and passive [79]. Active RFID tags are powered by batteries. Passive RFIDs derive power

autonomously using the RF signals from the base station. The passive concept is used in the P2100 and P1100 power harvester receiver modules manufactured by Power Cast [80].

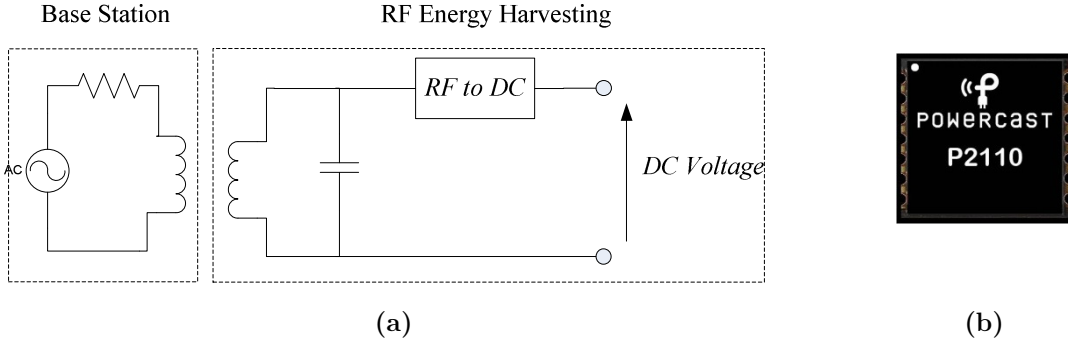


Figure 2.13: a) Operating principle of electromagnetic energy harvesting, b) electromagnetic energy harvester by Powercast [80].

### 2.5.5 Magnetic Field Energy Harvesting

The magnetic field near utility assets produced by the AC current flowing through these assets can be used to power sensors installed in the vicinity. The principle of Faraday's law of electromagnetic induction can be used to convert the magnetic field energy to electric energy. If an air-cored coil is considered to envelop a utility asset carrying  $i$  amperes of RMS current such that  $i$  is given by,

$$i = I \cos(\omega t) \quad (27)$$

The voltage induced across the coil terminals is given by,

$$v = \frac{\mu_0 A n}{l} I \sin(\omega t) \quad (28)$$

The power harvested by the air-core coil when a load  $R_L$  is applied across the terminals of the winding is given by,

$$P = \frac{\mu_o^2 A^2 n^2 I^2}{2R_L l^2} \quad (29)$$

where  $I$  is the amplitude of the current,  $l$  is mean length of magnetic field lines,  $\mu_o$  is the permeability of free space,  $A$  is the area of cross section of the coil, and  $n$  are the number of turns.

### 2.5.6 Electric Field Energy Harvesting

According to Maxwell's equation, a time varying electric field produces a displacement current given by

$$I_d = \epsilon \frac{d\phi_E}{dt} \quad (30)$$

where  $I_d$  is the displacement current,  $\epsilon$  is the electric permittivity, and  $\phi_E$  is the electric flux.

This displacement current can be used to charge a pair of capacitor plates to store the electric field energy in the capacitor. The stored energy is given by

$$E = \frac{1}{2} CV^2 \quad (31)$$

where  $E$  is the energy stored in the capacitor,  $C$  is the capacitance of the plates, and  $V$  is the voltage across the plates. The concept of electric field energy harvesting was proposed in this research and theoretical results have been presented in later sections. Recently, an experimental validation of this concept was implemented [81]. The idea presented in the paper is similar to the one proposed in this research and is contemporary with this research. The paper suggests that a maximum energy on the order of  $148 \mu\text{J}/\text{m}^3$  can be harvested in a 400 kV substation comprising maximum electric field strength of 5.8 kV/m, nearly 10 m above the ground plane [82]. There is minimal research in the area of electric field energy harvesting and presently no products that utilize this technique exist in the market. Analysis and feasibility of implementing this technique has been presented in Section 3.2.

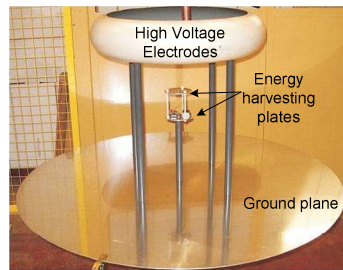


Figure 2.14: Electric field energy harvesting experimental setup [83]

A summary of the power density and performance of all the discussed energy harvesting techniques is presented in Table 2.2.

**Table 2.2: Typical Power Densities from Different Energy Harvesting Sources**

| Source                | Power Density / Performance   |
|-----------------------|---|
| Vibration             | Piezoelectric generator: 375 $\mu\text{W}/\text{cm}^3$ at 120 Hz [84]<br>Microgenerator: 800 $\mu\text{W}/\text{cm}^3$ at 110 Hz and 200 $\mu\text{m}$ amplitude [85]<br>Electrostatic: 800 mW at 3 mm compression and 2 steps per sec [59] |
| Thermal               | 470 $\text{mW}/\text{cm}^3$ at $\Delta T=100$ °C [69]   |
| Solar                 | 1 $\text{mW}/\text{cm}^2$ in sunlight and 1 $\mu\text{W}/\text{cm}^2$ in bright indoor light [86]   |
| Electromagnetic waves | 200 mW @ 902-928 MHz with 0-20 RF dBm input power [80]  |
| Magnetic field        | CT : 1-3 W/g at 200A primary current [29]   |
| Electric field        | 8.8 $\text{mW}/\text{m}^3$ in a 400 kV substation [83]  |

## 2.6 POWER CIRCUITS FOR ENERGY HARVESTING APPLICATIONS

Most of the energy harvesting technologies that were identified in Section 2.5 produce low open circuit voltages. Some examples of open circuit voltages generated by the various energy harvesting technologies are given in Table 2.3.

**Table 2.3: Typical Open Circuit Voltage for Various Energy Harvesting Sources**

| Energy Harvesting Source | Typical open circuit voltage | Operating conditions/comments  |
|--------------------------|------------------------------|--|
| Thermopile               | 330 mV DC [87]               | Produced 38 $\mu\text{W}/\text{mm}^2$ power  |
| Single solar cell        | 500 - 700 mV DC [88]         | Si solar cells   |
| Microgenerator           | 400 mV RMS [89]              | 108 Hz vibrations  |
| Rogowski coil            | 19 mV RMS (based on (29))    | number of turns is 1000, area of cross section of coil is $\text{cm}^2$ (radius of coil is 1 cm), mean length of magnetic field lines is 4 cm (diameter of conductor is 3 cm), and RMS current in the conductor is 50 A at 60 Hz |

Table 2.3 shows that the voltages obtained by the energy harvesters are not enough for operating sensor electronics which usually have operating range of 2 – 3.3 V DC. Therefore, depending on the application it becomes essential to have either a DC/DC or AC/DC/DC boost converter that can boost the voltage to the levels required by the sensor electronics. This section presents a review of the power electronics techniques that



have been used in the past for obtaining pertinent voltage boost functionality in different energy harvesting applications.

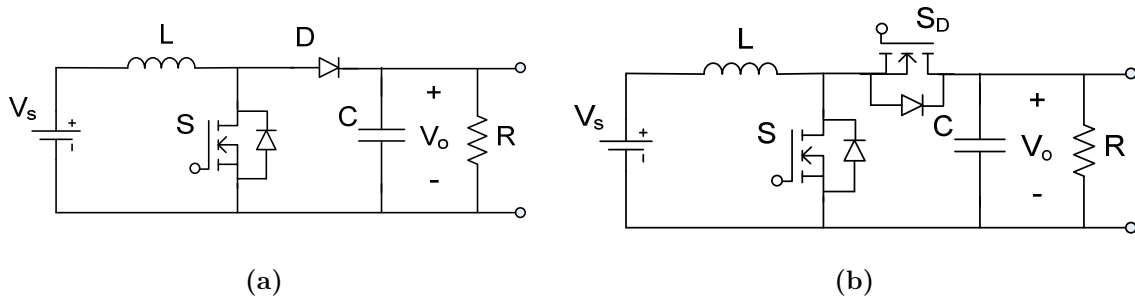
### 2.6.1 DC/DC Boost Converters

In case of an energy harvesting source that provides DC voltage (thermopiles, solar cell, etc.), a DC/DC boost converter is required. This functionality can be either provided with a conventional charge pump or an inductive boost converter. Charge pumps can also be used for AC/DC boost conversion.

A conventional inductive boost converter is shown in Figure 2.15(a). The voltage output of an ideal inductive boost converter is given by

$$V_o = \frac{V_s}{1-D} \quad (32)$$

where  $V_s$  is the supply voltage and  $D$  is the duty cycle.

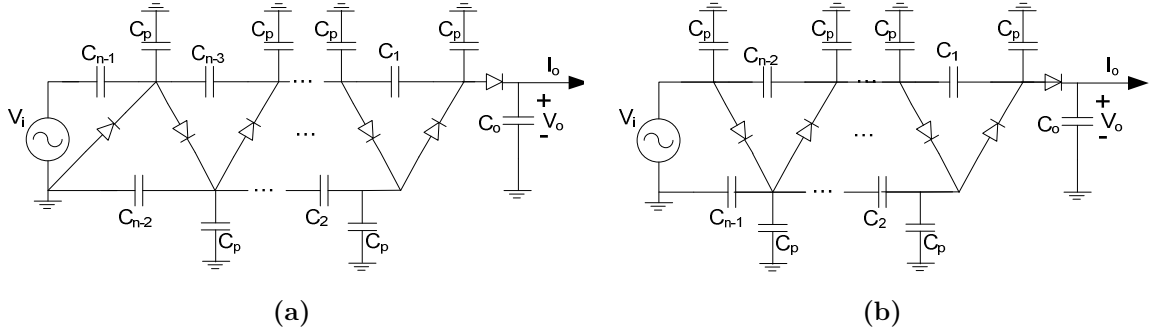


**Figure 2.15:** (a) Conventional DC/DC boost converter, (b) Synchronous DC/DC boost converter

However, with the introduction of parasitic elements the boost functionality of these converters becomes limited. Moreover, at lower input voltages these converters have a very low efficiency due to forward drops of diodes. Synchronous boost converters have been proposed in the past for low voltage applications, shown in Figure 2.15(b) [90]. However, to reach higher voltage levels they require close to ideal devices, low forward drop diodes, ideal gating signals and start-up circuits.

Another approach of boosting voltages is through the use of charge pumps. Historically, the Cockroft Walton charge pumps have been widely used for achieving high

DC voltage from an AC input, shown in Figure 2.16. The output voltage of a conventional Cockroft Walton charge pump is given by (33) and (34) [91].



**Figure 2.16: Cockroft-Walton charge pump topologies, (a) Even multiplier, (b) Odd multiplies**

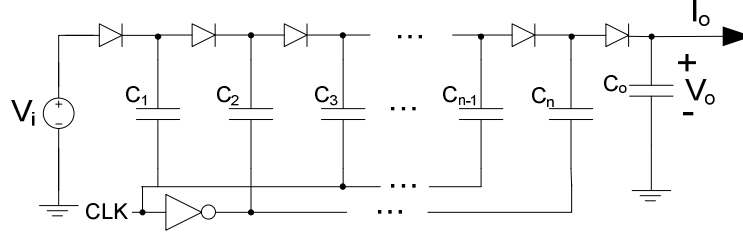
$$V_{o(n=even)} = nV_i - \frac{n}{6} \left( \frac{n^2}{2} + 1 \right) \frac{I_o}{Cf} \quad (33)$$

$$V_{o(n=odd)} = nV_i - \frac{n}{12} (n^2 + 1) \frac{I_o}{Cf} \quad (34)$$

In (33) and (34),  $V_i$  is the peak of AC voltage oscillating with frequency  $f$ ,  $I_o$  is the load current, and the number of capacitors is  $n-1$ . The above circuit equations assume that  $C_p$  (parasitic capacitance) is negligible as compared to the main charge pumping capacitors. It can be observed from (33) and (34) that a higher voltage multiplication can be obtained by increasing the number of capacitors in the charge pump. Further, the voltage multiplication is not exactly  $n$  times the input voltage as the second term reduces the effective output term. Therefore, with an increase in load current, or frequency of oscillation of the source, effectively reduce the voltage multiplication. Moreover, the above analysis also does not include the forward drops of diodes which also reduce the effective output voltage.

In addition, in the Cockroft Walton charge pump, effective multiplication of voltage occurs only when the coupling capacitors are very large as compared to the parasitic capacitances  $C_p$ . If this constraint is not satisfied, the voltage boost is limited to twice the input voltage irrespective of the number of stages of the charge pump [92].

A newer charge pump topology has been proposed in the past called the Dickson charge pump and is shown in Figure 2.17 [92].



**Figure 2.17: Dickson charge pump topology**

The output voltage of this charge pump topology is given by

$$V_o = (N + 1)(V_{in} - V_T) - \frac{nI_o}{Cf} \quad (35)$$

where  $V_T$  is the threshold voltages of MOS transistors. If this technology is used in integrated circuits the diodes are realized using MOS transistors. However, due to the body effect the threshold voltage ( $V_T$ ) of the MOS transistors increase with an increase in the number of stages. Increase in  $V_T$  leads to decrease in  $V_o$ ; consequently, a decrease in voltage step of each stage causes a reduction in the overall efficiency of the converter. Numerous topologies for effective charge pumps have been proposed in the past [93] - [98]. However, the charge pump approach by itself does not seem to be the optimal solution to low voltage energy harvesting applications as multiple stages lead to increase in complexity, low efficiency, and increase in the total diode drop. All these challenges pose major limitations when implementing the technique of charge pumps in energy harvesting applications where the amount of energy is limited and needs to be used judiciously.

A recent research presented in [99] developed a hybrid configuration of a boost converter that uses an inductive boost converter followed by a two stage charge pump. The authors claim that the converter can boost voltages from 0.2V to 1.2 V for a thermopile application. A block diagram of this approach is given in Figure 2.18. The boosted voltage is still not sufficiently high for operating electronics upto 3.3V DC. Some

other research efforts have tried to analyze and implement charge pumps in other energy harvesting applications also [100] - [101].

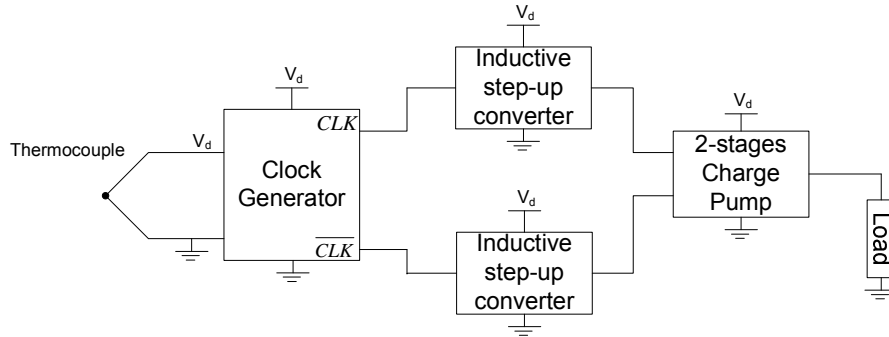


Figure 2.18: Hybrid charge pump-inductive step up converter architecture

### 2.6.2 AC/DC Boost Converter

As highlighted earlier that some energy harvesting sources produce AC voltages. Conventionally, simple AC/DC bridge rectifiers followed by a DC/DC boost converter have been used to realize boost functionality for AC/DC boost conversion, shown in Figure 2.19.

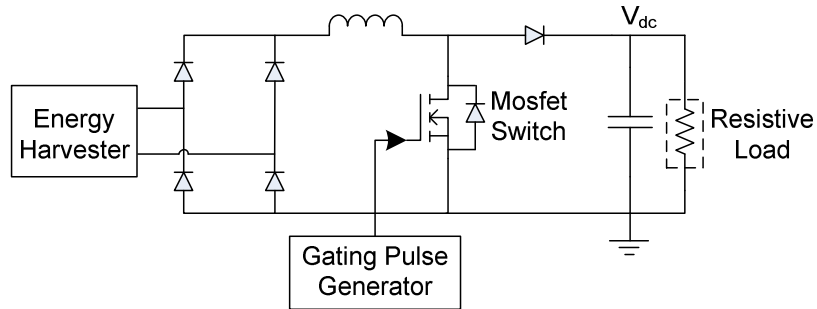


Figure 2.19: Conventionally used AC/DC boost converter for energy harvesting applications

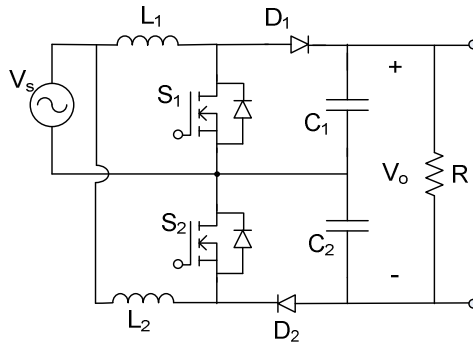
However, this circuit is not an effective solution for energy harvesting application due to the following reasons –

- 1) In most energy harvesting applications, the open circuit voltages induced at the energy harvester terminals are on the order of mVs which is even lower than the forward threshold voltage of diodes (0.3 – 0.7 V) in the diode bridge rectifier. This poses a big challenge for functioning of the converter under lower voltages.

- 2) The circuit requires two energy conversion stages, AC to DC and DC to DC. This leads to reduction in overall efficiency of the converter.
- 3) The semiconductor device count of this circuit is also relatively large. As lowering the cost is one of the major drivers for designing utility sensors, this solution is clearly not optimal. Its cost can be reduced further by reducing the component count.

The main idea is to reduce the number of energy conversion stages so that the efficiency of the circuit can be improved without compromising the voltage boost functionality.

Consider a simple boost converter shown in Figure 2.15(a). This converter operates only for positive input voltages. If the number of power conversion stages is to be reduced, the circuit shown in Figure 2.15(a) will be required to operate even at negative input voltages. One simple solution to this problem is appending another boost converter in parallel with the existing boost converter as shown in Figure 2.20. The parallel boost converter provides boost functionality during the negative cycle of the source voltage  $V_s$ . The operation of this converter is briefly discussed in Table 2.4. This converter allows direct AC/DC boost conversion and reduction of the number of energy conversion stages to only one. However, it requires two separate inductors for operation. Moreover, it has an increased component count. Furthermore, the switches need to have isolated gate drive circuits for practical implementation. The gate drive problem can be solved by selecting S1 to be an n-channel MOSFET and S2 as a p-channel MOSFET as opposed to two n-channel MOSFETs. This converter was proposed in [102].



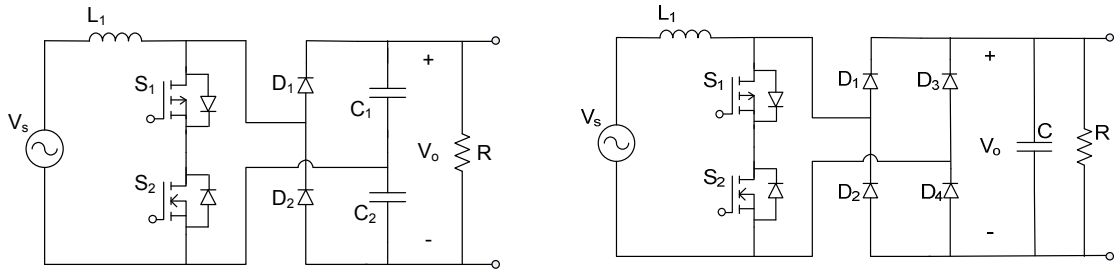
**Figure 2.20: Direct AC/DC boost converters for energy harvesting applications**

**Table 2.4: Modes of Operation of Direct AC/DC Boost Converter of Figure 2.20**

| Mode                     | Switch Status  | Operation                                       |
|--------------------------|----------------|---|
| Mode 1: $0 < t < \pi$    | S1 ON, S2 OFF  | Charging of L1                                  |
|                          | S1 OFF, S2 OFF | Energy stored in L1 is transferred to the load. |
| Mode 2: $\pi < t < 2\pi$ | S1 OFF, S2 ON  | Charging of L2                                  |
|                          | S1 OFF, S2 OFF | Energy stored in L2 is transferred to the load. |

Table 2.4 shows that the converter requires the knowledge of voltage polarity of the supply for proper operation (as switches S1 and S2 are pulsed alternately in positive and negative half cycles respectively). Hence, the converter requires a relatively complex control. A complex control strategy results in the use of additional active circuit components and increases power consumption. As the circuit is required to operate at low power levels, it becomes difficult to justify the use of this converter in practical applications.

Recently, based on the idea introduced in [102], direct AC/DC boost converters for micro-generators have been proposed [89], [103], [104], shown in Figure 2.21. These converters are contemporary to the research presented in this proposal. However, they face some additional problems. Almost all proposed topologies require batteries, multiple diodes and capacitor combination for start-up; therefore, they cannot be used for utility applications.



**Figure 2.21: Recently proposed AC/DC boost converters for low-voltage energy harvesting applications**

## 2.7 CONCLUSIONS

In conclusion, the state-of-the-art sensing technology focuses at single point (single asset) solutions. The conventional techniques, such as CT, MOCT, PT, CCVT, and EOVT, for current and voltage sensing are bulky, large, have strict insulation requirements and are expensive. In addition, these conventional methods utilize expensive wired communication techniques for data transmission which limits their massive deployment on the grid.

A few sensing solutions that use some form of wireless communication are also large, bulky and expensive. The high costs limit their widespread deployment on the utility grid. Furthermore, most of these technologies are customized solutions for a particular asset and cannot be used on different kinds of asset. They have high installation and field calibration costs, and require regular maintenance as they are not completely self-powered. They need batteries for operation which limits their effective life.

As discussed in Section 2.5 novel energy harvesting techniques can be potentially used to make these sensors maintenance free. However, due to circuit level constraints identified in this section it has been difficult to develop low-cost maintenance free and flexible sensing solutions for monitoring current, voltage and temperature in utility assets.

## CHAPTER 3

# ELECTRIC AND MAGNETIC FIELD ENERGY

## HARVESTING

### 3.1 INTRODUCTION

It was identified in Chapter 2 that if a typical sensor node were to derive its power from a battery, the battery would be depleted in less than a year. If these sensors were to be deployed on hundreds of thousands of assets on the grid, it would become close to impossible for the utilities to replace the batteries in all these sensors after every few months. A thorough literature review of all the state-of-the-art energy harvesting technologies for self-powering sensors in various applications, for instance, smart homes, substation sensing, habitat monitoring etc. was presented in Section 2.5. However, it was found that barring a few contemporary solutions, none of the technologies were focused at utility asset monitoring. As most of the sensors presented in the literature review require batteries for either powering, start-up or backup, it was considered worthwhile to develop and test energy harvesting solutions for powering sensors for utility assets.

Usually, near a substation environment or any utility asset, high magnitudes of electric and magnetic fields are present. Any approach that scavenges the energy from these fields and transforms it into useful electrical energy can be used to power the sensor nodes.

This chapter presents a comparison between different techniques that can be used to harvest energy present near utility assets. Analytical and experimental results are presented, and the application space for each technique is identified.

### 3.2 ELECTRIC FIELD ENERGY HARVESTING

The electric field emanating from an energized utility asset, such as a high voltage overhead cable, can be used to harvest power. The time varying electric field produces a



displacement current which can be used to charge the plates of a capacitor if kept close to the energized asset. To analyze such a system, consider two plates kept close to a current carrying high voltage conductor such that the plate nearer to the conductor is shorted to it. The plates are square in shape with width  $w$ , and the two are  $d$  distance apart. The conductor is  $D$  distance above the earth. This configuration is shown in Figure 3.1, and its equivalent circuit is depicted in Figure 3.2.

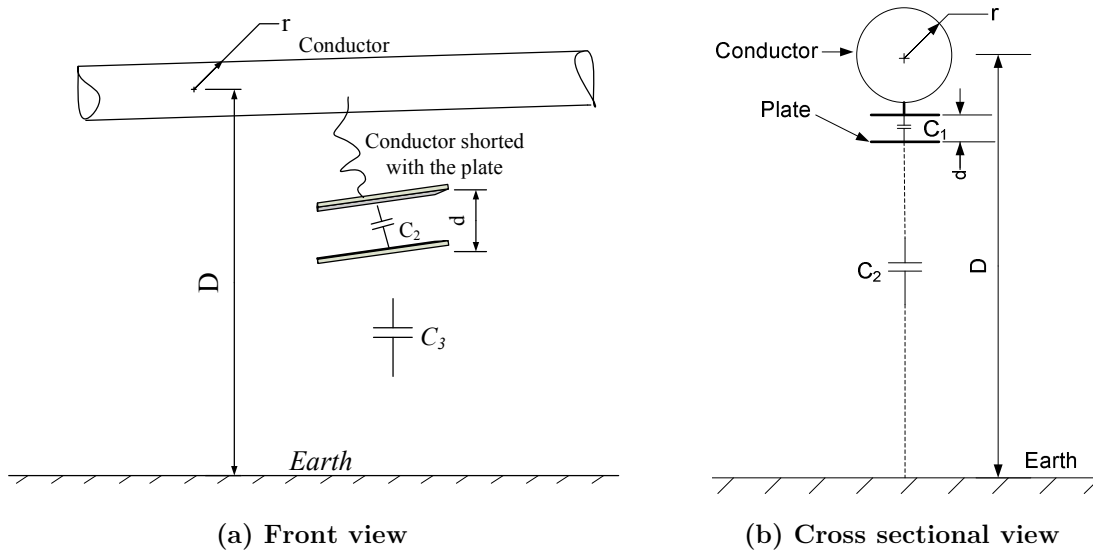


Figure 3.1: Parallel plate system for electric field harvesting

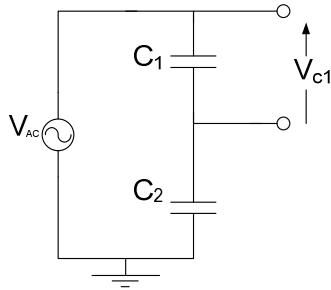


Figure 3.2: Equivalent circuit of the electric field energy harvesting system

The two plates essentially form a parallel plate capacitor which has a capacitance given by (36). The computed value of capacitance  $C_1$  is valid if the distance between the two plates is small as compared to the size of the plates, and the distance of the plates from the earth is large. In a realistic scenario, due to the presence of fringing at the edges

of the plates, the value of actual capacitance is bound to deviate from the theoretical value.

The value of capacitance  $C_2$  can be found by using the method of images and considering only the capacitance of the conductor over ground. The expression for  $C_2$  is given in (37). Computation of accurate capacitances, when fringing effects are taken into account, requires the use of numerical method and finite element analysis (FEA). It was found that the capacitances found using these classical expressions differ by a large amount from the simulated values using FEA software (ANSYS® Maxwell). Hence, it was decided to make use of the FEA simulations to compute the value of capacitances. With the knowledge of these capacitances, the peak power can be found using (38) and (39). A sample ANSYS® Maxwell FEA simulation for the considered system is shown in Figure 3.3.

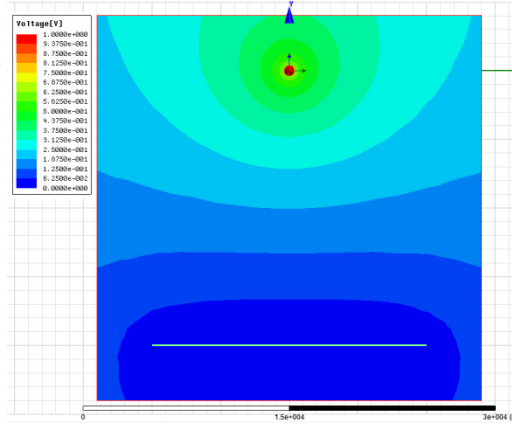
$$C_1 = \frac{w^2 \epsilon_o \epsilon_r}{d} \quad (36)$$

$$C_2 = \frac{2\pi w \epsilon_o}{\ln\left(\frac{2D}{r}\right)} \quad (37)$$

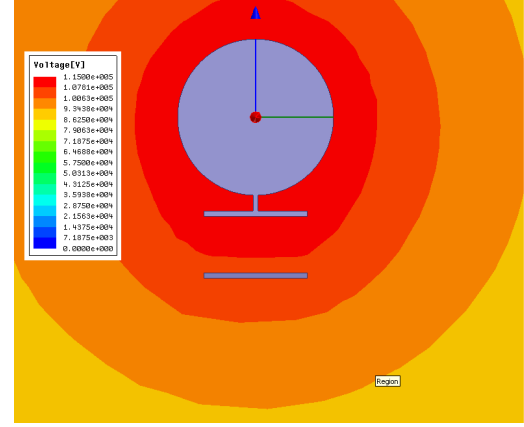
$$V_{C_1} = \frac{C_2}{C_1 + C_2} V_{ac} \quad (38)$$

$$P_{peak} = \omega C_1 V_{C_1}^2 \quad (39)$$

In (36), (37) (38) and (39),  $V_{ac}$  is the RMS line voltage,  $V_{C_1}$  is the RMS voltage across capacitance  $C_1$ ,  $\epsilon_r$  is the dielectric constant,  $w$  is the width of the plate and  $\omega$  is frequency of supply in radians per second.



Zoomed out view



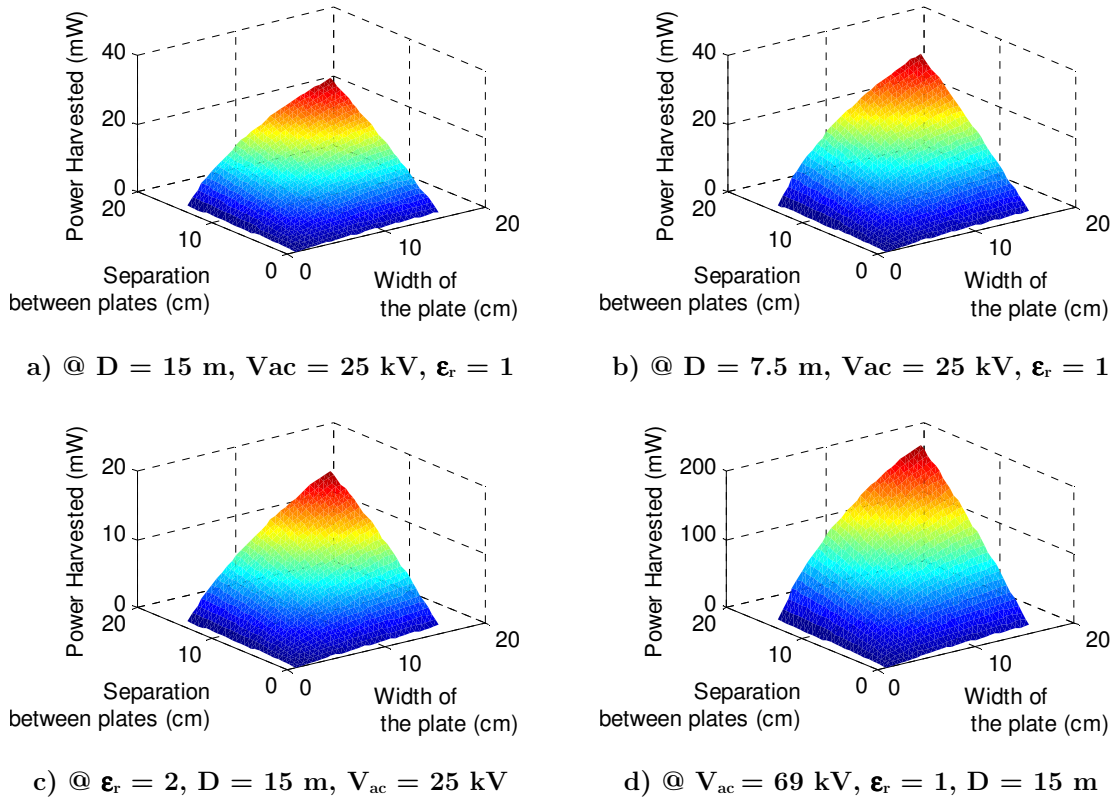
Zoomed in view

**Figure 3.3: ANSYS® Maxwell 2D simulation of the two plate energy harvesting system**

The range of values of  $d$ ,  $w$ ,  $D$ ,  $\epsilon_r$  and  $V_{ac}$  over which the peak harvested power was computed are given in Table 3.1. To test the feasibility of the concept, a total of 1800 distinct simulations were run and power for every parameter combination was computed. The effect of variation of  $d$ ,  $w$ ,  $D$ ,  $\epsilon_r$  and  $V_{ac}$  on the power harvested is shown in Figure 3.4.

**Table 3.1: Range of Values of Parameters  $w$ ,  $d$ ,  $D$ ,  $\epsilon_r$  and  $V_{ac}$  which were Simulated using ANSYS® Maxwell**

| Parameter    | Minimum value | Step size | Maximum value |
|--------------|---------------|-----------|---------------|
| $w$          | 1 cm          | 0.5 cm    | 15.5 cm       |
| $d$          | 1 mm          | 0.5 cm    | 14.6 cm       |
| $D$          | 7.5 m         | 7.5 m     | 15 m          |
| $\epsilon_r$ | 1             | 1         | 2             |
| $V_{ac}$     | 25 kV         | 44 kV     | 69 kV         |



**Figure 3.4: Sensitivity analysis of power harvested from electric field with respect to change in dielectric constant, distance between plates, plate size and voltage**

The following trends can be observed from Figure 3.4:

1. The harvested power increases non-linearly with an increase in width of the plate  $w$  and distance between the plates  $d$ .
2. A decrease in the distance between the conductor and the earth  $D$  increases the power harvested by the plates marginally.
3. The harvested power increases dramatically with an increase in voltage as it follows a squared relationship.

The plots show that at higher voltages, power on the order of hundreds of mWs can be harvested from the two-plate system. However, it should be noted that the power density of the system is very low. As a matter of fact, the power density reduces dramatically with an increase in size of the plates. Consider, for instance, the width of the plates and the distance between the plates to be 15 cm each, then at 25 kV around 27 mW of peak power can be harvested. However, the power density is only  $7.4 \mu\text{W}/\text{cm}^3$ . If the

voltage is increased to 69 kV, the power density becomes close to  $59 \mu\text{W}/\text{cm}^3$ , which is still quite low.

To validate the concept of E-field energy harvesting, two different experiments were conducted. The first experiment was conducted at low voltages, up to 145 V in the lab, while the second experiment was conducted at voltages up to 35 kV in a high voltage test facility at NEETRAC. The results of the first experiment are given here as a baseline case. However, the results of the second experiment are detailed in Chapter 7 as it finds more relevance with the voltage sensor, which will be evident at the end of this section.

For the first experiment, a setup was built in the lab. The schematic of the setup is shown in Figure 3.5(a). The actual setup is shown in Figure 3.5(b). The setup comprises three plates; the top plate mimics a utility asset and is connected to a variac, the middle plate is the energy harvesting plate which gets charged by the displacement current, the bottom plate is kept at the ground potential. The sizes of the plates and the distance between them are given in Table 3.2.

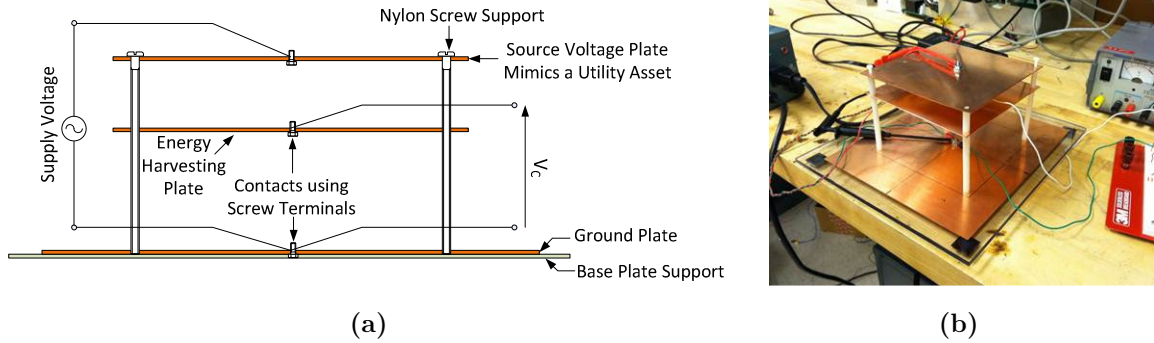


Figure 3.5: (a) Schematic of E-field energy harvesting test setup, (b) Actual lab test setup used to validate the concept of E-field energy harvesting

Table 3.2: Dimensions of the Lab Test Setup for Validating E-field Energy-harvesting

| Top Plate Dimensions (lxbxt) (mm) | Middle Plate Dimensions (lxbxt) (mm) | Bottom Plate Dimensions (lxbxt) (mm) | Top-to-Middle Plate Distance (mm) | Middle-to-Bottom Plate Distance (lxbxh) (mm) |
|-----------------------------------|--------------------------------------|--------------------------------------|-----------------------------------|--|
| 152 x 152 x 1                     | 152 x 152 x 1                        | 215 x 254 x 1                        | 24                                | 100  |

The energy was harvested by rectifying the AC voltage induced on the middle plate with respect to the ground plane to form a DC voltage across a DC capacitor. To compute the power harvested, the DC capacitor was discharged using different known load resistances ( $R_{Li}$ ) and the voltage across the load resistor was measured. The power harvested was computed using  $V^2/R_{Li}$ . The circuit schematic of the electric field energy harvesting setup is shown in Figure 3.6. The harvested power and power density under different conditions are shown in Figure 3.7.

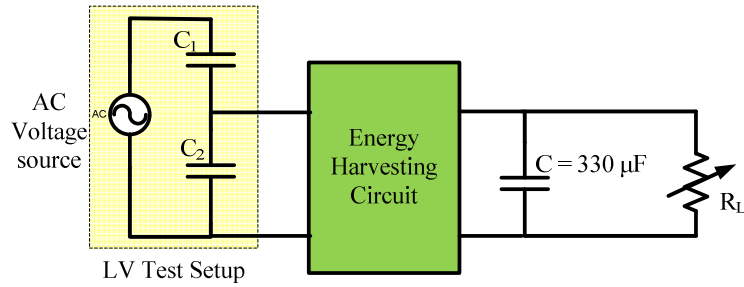


Figure 3.6: Circuit schematic of the electric field energy harvesting system

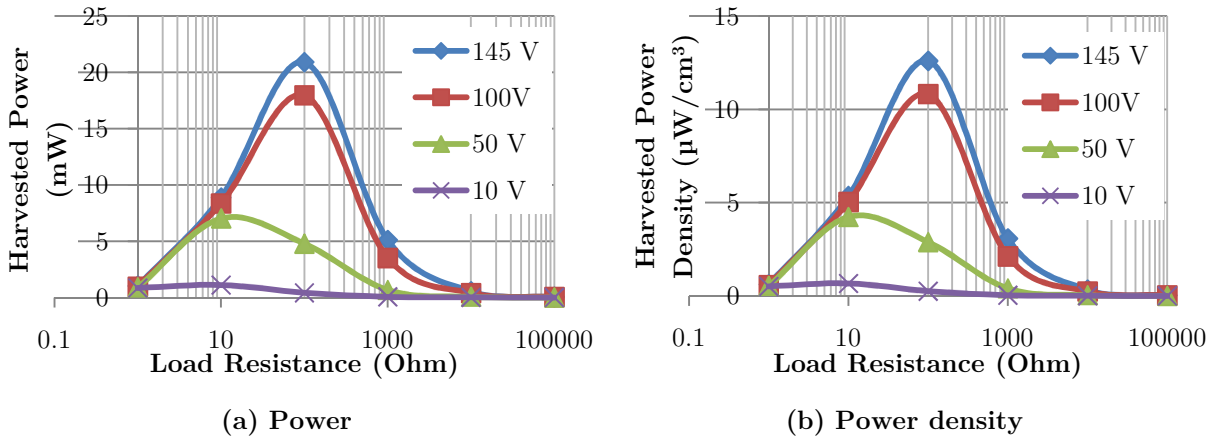


Figure 3.7: Plots showing power and power density of the electric field energy harvesting system at different loading levels and asset potential.

The experimental results validate the concept of electric field energy harvesting using a simple parallel plate capacitor. The maximum power that was harvested using the developed system was close to 20 mW, which may be sufficient for certain low duty cycle sensing applications. However, the power density was found to be quite low, around 12.5

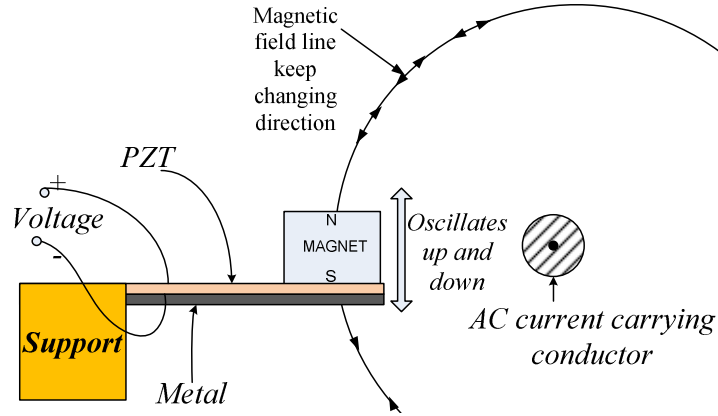
$\mu\text{W}/\text{cm}^3$ . A note of caution is that the harvested power found from these experiments may not be representative of a true system as the relative distances in a practical scenario may be quite different, which would impact the harvested power. Nevertheless, the experimental results show promise in the concept.

Considering the simulation and experimental results, it seems that this technique is quite challenging to be made practical for many applications. It might still have niche applications for very high voltage conductors, where even with a smaller sized system relatively more power can be harvested. For instance, at 345 kV voltage levels, 3 cm plate width and 1 cm distance between the plates, 200 mW of power can be harvested. Provided that voltage sensing is of interest in many utility assets, electric field energy harvesting can be a viable option for powering medium and high voltage sensors.

### **3.3 MAGNETIC FIELD ENERGY HARVESTING USING PIEZOELECTRIC MATERIAL**

Another approach that was investigated involves harvesting the magnetic field present near utility assets. Two different methods were used to harvest the magnetic field energy, the first method used a piezoelectric and magnet system, and the second method used an open ferromagnetic core-coil arrangement.

To test the first method, a system was designed where a magnet was attached to the edge of a piezoelectric bimorph bender (PZB) and kept in the varying magnetic field of an AC current. A PZB consists of a passive metal substrate glued to a piezo-ceramic strip. Under the influence of the time varying magnetic field of the AC current the magnet vibrates. The time varying oscillation of the PZB produces a proportional AC voltage. This concept is shown in Figure 3.8. The frequency of mechanical vibration of the magnet is the same as the alternating magnetic field frequency. Therefore, the voltage produced at the terminals of the piezoelectric material is also at 60 Hz. In essence, the magnetic field energy is converted to electrical energy through the vibrational kinetic energy of the piezoelectric bender.



**Figure 3.8: Operating principle of piezoelectric based magnetic field energy harvesting**

To ensure maximum energy transfer, the PZB should to be kept at an angle of 45 degrees to the magnetic field lines of the conductor and very close to it [105]. Furthermore, as the PZB is sharply tuned at the resonant frequency, an experiment was conducted to investigate the resonant frequency of the PZB-magnet system. Different combinations of PZBs and NdFeB (Neodymium Iron Boron) magnets were tested with a variable frequency source, and a frequency response plot was computed. These plots are shown in Figure 3.9. The technical specifications of the PZB strips and NdFeB magnets are given in Appendix A.

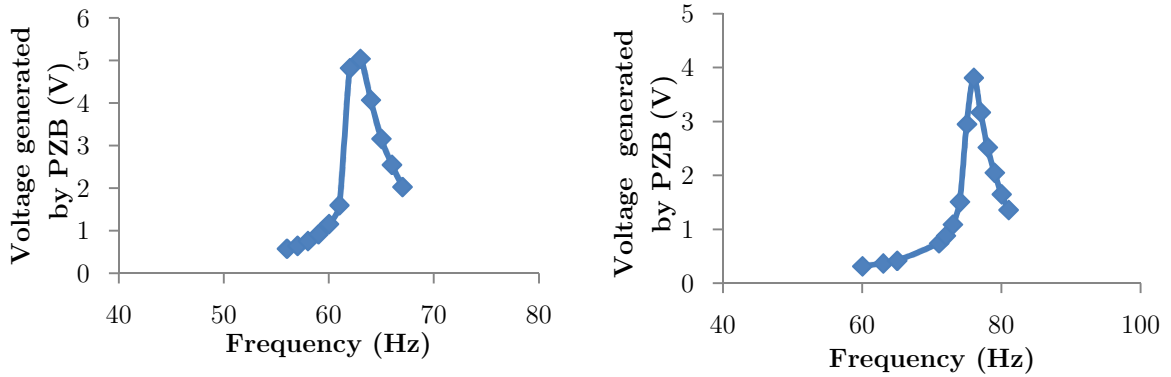
It can be observed that the rate of reduction of voltage is greater than 35% per Hz, when moving away from the resonant frequency, in all the cases. Moreover, all the systems have different resonant frequencies. The system that gave resonance frequency closest to 60 Hz was chosen to perform energy harvesting studies.

Next, a set of experiments were performed to estimate the amount of energy that can be obtained from the PZB-magnet system. The first experiment was aimed at finding the voltage levels obtained at different primary currents. The result of this experiment is shown in Figure 3.10. As expected, with an increase in primary current the voltage developed at the PZB terminals also increases.

Another experiment was performed to estimate the power transfer capability of the PZB-magnet system. The result of this experiment is shown in Figure 3.10. It can be

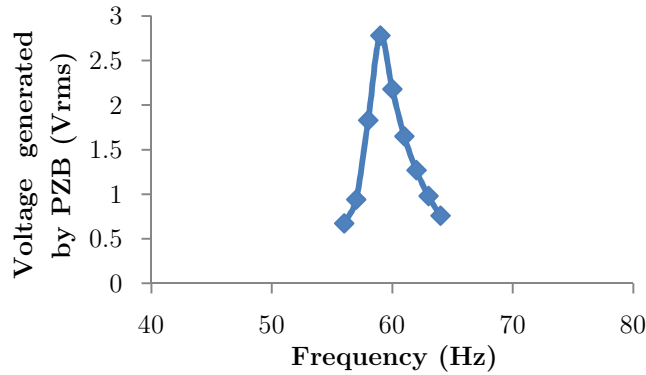


observed that, at a load resistance of 50 k $\Omega$ , maximum energy is transferred. This shows that the source impedance of the PZB is very high (close to 50 k $\Omega$ ).



(a) Configuration 1 has resonant frequency close to 64 Hz

(b) Configuration 2 has resonant frequency close to 78 Hz



(c) Configuration 3 has resonant frequency close to 60 Hz

Figure 3.9: (a), (b) and (c) show change in resonant frequency of PZB-magnet system with a change in configuration

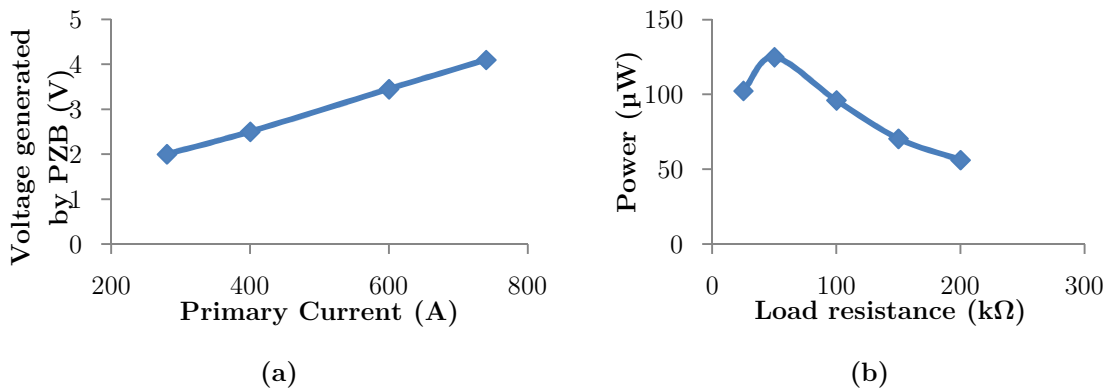


Figure 3.10: (a) Voltage at PZB terminals at different primary currents, (b) Power harvested at different load levels when primary current is 600

Finally, the PZB-magnet system was used to drive a load that emulated a sensor node operation. The equivalent circuit of the setup used for this experiment is shown in Figure 3.11(a). The actual setup is shown in Figure 3.11(b). The PZB-magnet system converted the magnetic field energy to DC power using an energy harvesting circuit and stored it in a 6.6 mF capacitor. A typical sensor node operation was emulated using a single pole double throw switch (SPDT). When the capacitor voltage reached 5V, the SPDT was switched to a low impedance load and the capacitor discharged. In this way the active mode of the sensor was emulated. On the other hand, when the capacitor voltage went below 3V the SPDT was switched to a high impedance load, this way the sleep mode of the sensor was emulated. The charging and discharging of the capacitor under the described operation regime is shown in Figure 3.12. The results of the experiment are shown in Table 3.3.

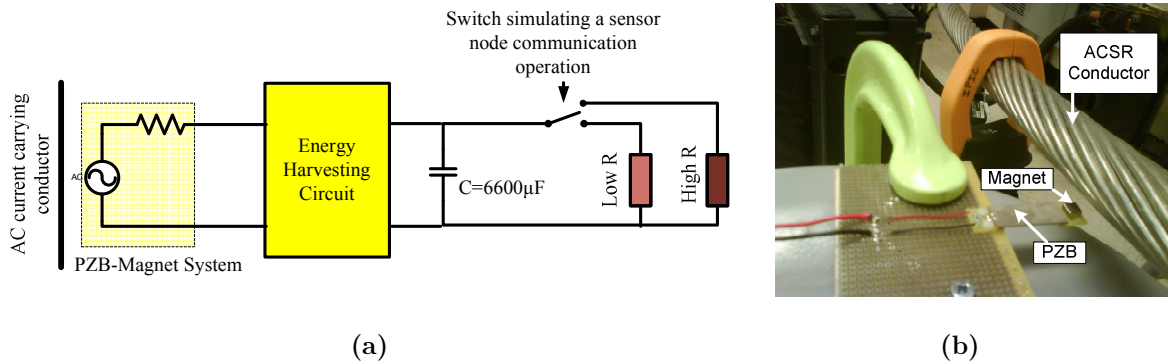


Figure 3.11: (a) Circuit diagram of the PZB-magnet test setup, (b) Experimental setup of the PZB-magnet system.

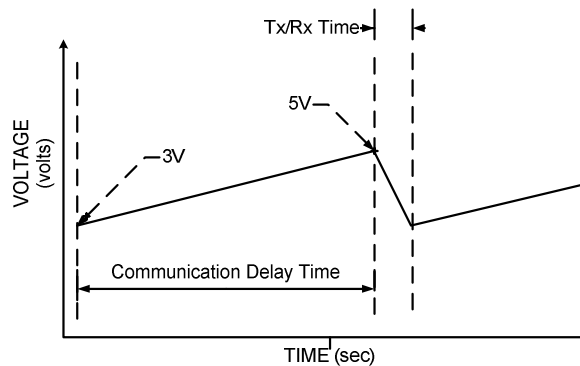


Figure 3.12: Graph showing the typical operation cycle of a sensor node powered with a piezoelectric energy scavenging source.

**Table 3.3: Piezoelectric-based Magnetic Field Energy Harvesting Test Results**

| Primary Current (Amps) | Load (ohm) | Tx/Rx Time (sec) | Communication Delay Time (min) | Duty Cycle (%) | Average Power ( W) |
|------------------------|------------|------------------|--------------------------------|----------------|--------------------|
| 600                    | 560        | 2                | 13.42                          | 0.248          | 65.4               |
|                        | 1000       | 4                |                                | 0.494          | 65.2               |
|                        | 1500       | 6                |                                | 0.741          | 60.7               |
| 800                    | 560        | 2                | 10.36                          | 0.32           | 84.4               |
| 1000                   | 560        | 2                | 8.12                           | 0.41           | 108.24             |

The capacitor is discharged from 5V to 3V every time it is loaded (which corresponds to the case when the sensor is transmitting/receiving data), which results in the harvested energy given by

$$E = \frac{1}{2}C(V_1^2 - V_2^2) = 52.8 \text{ mJ}$$

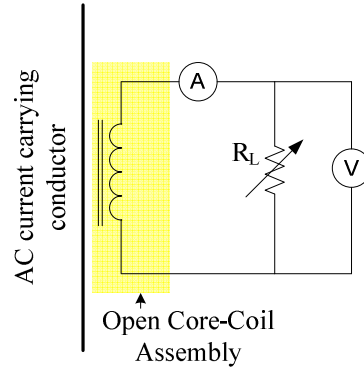
Considering the time taken for this discharge to be 2 sec (see Table 3.3), the effective power delivered is 26.4 mW. Therefore, although the average power of the entire charge discharge cycle is very low, the effective power is sufficient for a sensor node operation.

This experiment demonstrates that even though a piezoelectric bimorph bender has the disadvantage of very high source impedance resulting in a low-power output, it might prove to be feasible for an application that requires a very low duty cycle. However, this approach would require mechanical protection under primary side faulted conditions as the PZB displacement is directly proportional to the magnitude of the current. Complex mechanical design and a fairly low power density restrict the use of this approach to only a select applications.

### **3.4 MAGNETIC FIELD ENERGY HARVESTING USING ELECTROMAGNETIC INDUCTION**

The second method to harvest magnetic field energy is through the use of the Faraday’s law of electromagnetic induction. In this experiment, different configurations of coils wound around a core were placed near (or wrapped around) a current carrying

conductor. The current in the conductor was varied over a range of 100 A – 1000 A. The open circuit and short circuit tests were conducted on all the core-coil assemblies to find the maximum power harvested in all possible operating conditions cases. The schematic used for performing the experiments is given in Figure 3.13. Equation (40) was used for computing the maximum power harvested. The results of the experiment are summarized in Table 3.4. Further, Table 3.5 gives a qualitative comparison between the different core-coil assemblies that were tested. Maximum power plots generated from all the configurations are shown in Figure 3.14.




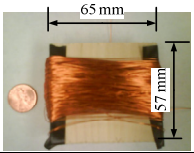
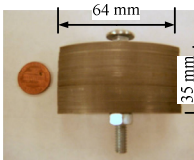
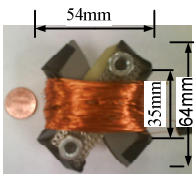
**Figure 3.13: Circuit schematic of the EM-Induction test system**

$$P_{\max} = \frac{V_{oc} I_{sc}}{4} \quad (40)$$

where  $V_{oc} = V$  as  $R$  tends to infinity,

$I_{sc} = A$  as  $R$  tends to zero

**Table 3.4: Magnetic Field Energy Harvesting using Different Core Configuration.**  
**Note: CRGO is Cold Rolled Grain Oriented Steel**

| Type of Coil  | No. of turns | O.C. Voltage at 200A primary current (V) | OC Voltage at 1000A Primary Current (V) | Max. Harvestable Power at 1000A (mW) | Picture/Test Set up  |
|---|--------------|--|---|--------------------------------------|--|
| Rogowski Coil   | 18           | 0.03                                     | 0.16                                    | 8                                    |   |
| 28AWG wire wound on a Wooden Core                                     | 200          | 0.24                                     | 1.21                                    | 29.8                                 |   |
| 28AWG wire wound on a hollow semi cylindrical CRGO Silicon Steel Core | 250          | 0.37                                     | 1.77                                    | 210.2                                |   |
| 28AWG wire wound on a Flux Concentrator                               | 300          | 0.50                                     | 2.64                                    | 257                                  |  |

**Table 3.5: Qualitative Comparison between the Tested Core-Coil Assemblies**

| Type of Core-Coil Assembly | Absolute Harvested Power | Power Density | Voltage Induced   | Sensor Linearity |
|----------------------------|--------------------------|---------------|-------------------|------------------|
| Rogowski                   | Very low                 | Very low      | Very low          | Extremely high   |
| Wooden                     | Low                      | Low           | Low               | Extremely high   |
| Semi-cylindrical           | High                     | High          | Sufficiently high | High             |
| Flux Concentrator          | Very high                | Very High     | High              | High             |

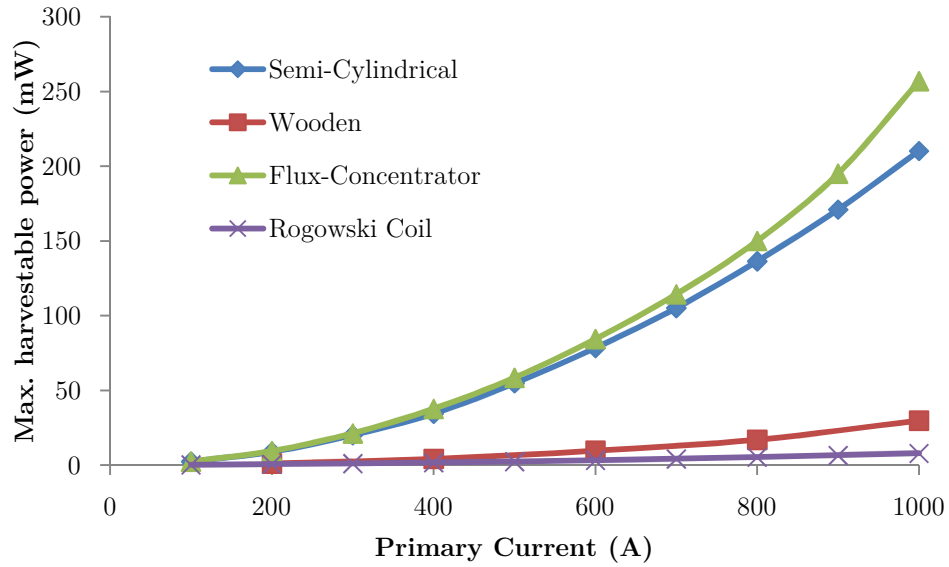


Figure 3.14: Maximum harvestable power from different core-coil configurations for different primary currents.

As can be seen in Table 3.4, both the rogowski coil and wooden core-coil have very low energy densities and low voltages induced. The experimental results show that the flux concentrator (XFC), an x-shaped core, has the ability to concentrate the nearby flux in the most efficient manner. A zoomed in view of XFC is shown in Figure 3.15.

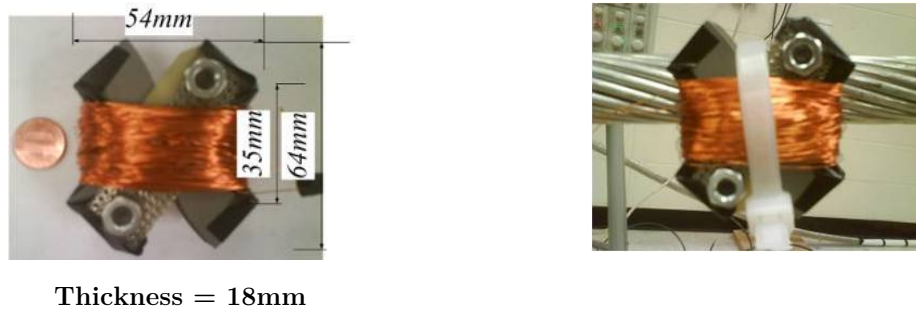


Figure 3.15: Zoomed in view of the x-shaped flux concentrator (XFC)

The open circuit voltage (OCV) and short circuit current (SCC) of the XFC is a linear function of the primary RMS current. As the XFC does not form a closed loop around the asset, it does not saturate easily and has a highly linear characteristic. Linearity up to 1000 A has been tested in the laboratory and is shown in Figure 3.16. Therefore, the XFC can also be used as a current sensor (the fundamental principle being

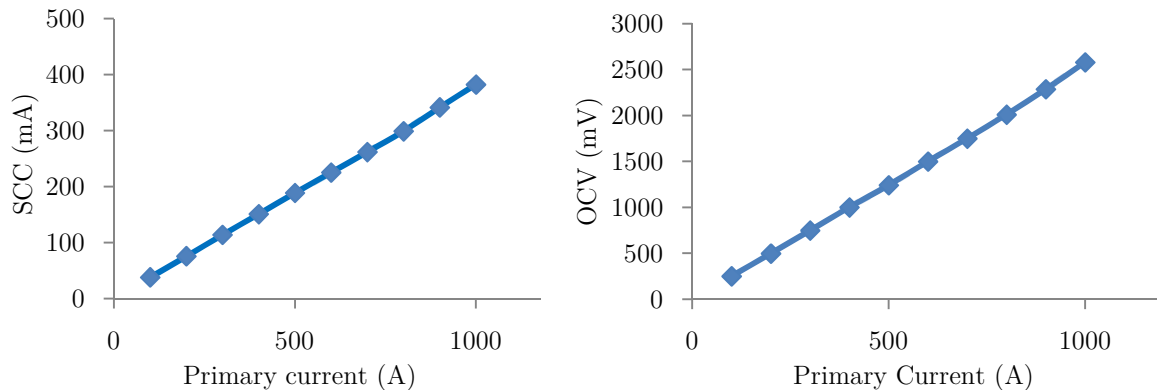
very similar to a CT). If curve fitting techniques are used to find the equation of a line which fits the SCC and OCV versus primary current curves, the linear equations given by

$$I_{sc} = 0.3776I_p \text{ with } R^2 = 0.9996 \quad (41)$$

$$V_{oc} = 2.5304I_p \text{ with } R^2 = 0.9992 \quad (42)$$

are obtained. Both these equations have a high goodness of fit ( $R^2$  very close to 1) which shows high linearity over the range shown in the plot. As the core is open, it is expected to have a high linearity over a fairly wide range.

Furthermore, as the XFC does not require clamping around the asset unlike a CT; it can be either kept in the vicinity of or stuck on the asset for monitoring the current. As the XFC can function by simply sticking on the asset, it provides a novel method of measuring current. Therefore, the open core-coil assembly based current sensor-cum-energy harvester is termed as the *Stick-on sensor* in this research.



**Figure 3.16: Graphs show linearity of the XFC with primary current over a wide range**

### 3.5 CONCLUSIONS

In summary, several techniques were explored for electric and magnetic field energy harvesting. A technique that exploits the electric field available near a current carrying conductor was analytically investigated. This technique shows that sufficient amount of

energy can be harvested from the electric field to power a sensor node. However, the size of such a device would be quite large. Therefore, it finds use in a niche group of high voltage applications. Experimental results show promise in the proposed electric-field energy harvesting technique.

Different techniques of energy harvesting using the magnetic field around a current carrying conductor were tested. The PZB-magnet system was used to scavenge energy by converting the magnetic field energy into mechanical energy and then to electrical energy. It was shown that in a typical sensor node operation, a maximum energy of 26.4 mW can be provided using this technique. It was identified that due to the high source impedance of the PZB it was not possible to supply continuous power to the load. Therefore, this technique is suitable in cases where a relatively low-duty cycle of operation is acceptable.

Finally, different configurations of cores with wire wound around them were tested based on the principle of electromagnetic induction. An x-shaped core referred to as the flux concentrator (XFC) was found to provide a maximum power of 257 mW. The XFC is small in size and does not require clamping around the utility asset. Moreover, it has the maximum energy density among all the considered energy harvesting techniques. In addition, the voltage induced at the XFC terminals is directly proportional to the current in the asset. Therefore, the XFC can be used for the dual purpose of energy harvesting and current sensing.



## CHAPTER 4

### STICK-ON SENSOR DESIGN AND DEVELOPMENT

#### 4.1 INTRODUCTION

The x-shaped flux concentrator (XFC) proves to be an attractive approach for harvesting magnetic field energy present near utility assets. However, enough energy may not warrant reliable operation of the sensor at all times. The electronic circuits on the sensor board require regulated DC voltage supply (typically 2 – 3.3V) for operation. However, the XFC provides an open circuit voltage (OCV) of 125 mV at 50 A of conductor current; this OCV is not even sufficient to overcome the forward threshold of semiconductor switches and diodes. A transformer can be used to step – up the voltage. However, as the current in the assets vary over a wide range the voltage stress on the transformer may become very high at higher currents. This limits the step-up function of the transformer. The main role of the transformer can be to provide enough voltage-boost to surpass the forward threshold of the semi-conductor devices. After the first stage, the voltage can be boosted further by using a power electronics converter. Some power electronic converter designs were presented in Section 2.6, but all of them suffer from major limitations and are not suited for utility applications that require long life and battery-free operation.

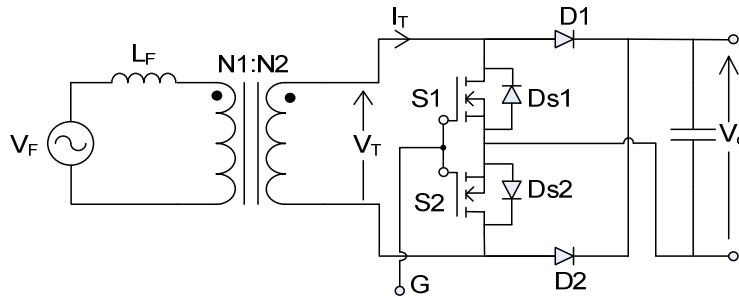
In this chapter, a novel power management circuit that suits utility requirements of high reliability, low maintenance, and low-cost is proposed. Further, simulation and experimental results are presented with detailed design of the proposed concept of a universal Stick-on sensor.

#### 4.2 A 0.2V-3.3V AC/DC BOOST CONVERTER

This research proposes a novel technique of realizing boost functionality in energy harvesting applications. The proposed converter is shown in Figure 4.1. This circuit uses a

bi-directional switch connected in a common source configuration. The switches can be pulsed together and do not require a floating gate circuit as the ground of the circuit is common with the source of the MOSFETs. Hence, this converter has a relatively simple gate drive circuit. Moreover, the circuit requires only one inductor as an energy transfer element. As the transformer is already a part of the energy harvester system, the circuit uses the leakage inductance of the energy harvester and transformer as the energy transfer element and does not require an external inductor. This helps in making the circuit compact. The operation of the converter is briefly presented in Table 4.1 and depicted in Figure 4.2.

The proposed converter can be operated in either the continuous conduction mode (CCM) or the discontinuous conduction mode (DCM). The conceptual waveforms that are realized in both these modes are given in Figure 4.3. These figures show the voltage across the secondary of the transformer ( $V_T$ ), current in the secondary of the transformer ( $i_T$ ), current in the two diodes ( $i_{D1}$ ,  $i_{D2}$ ), and devices conducting in each interval. It should be noted that since the source is AC, for certain operating conditions, the converter can operate in a combined CCM and DCM mode as well.



**Figure 4.1: Proposed 0.2 V to 3.3 V AC/DC boost converter with a wide operating range.**

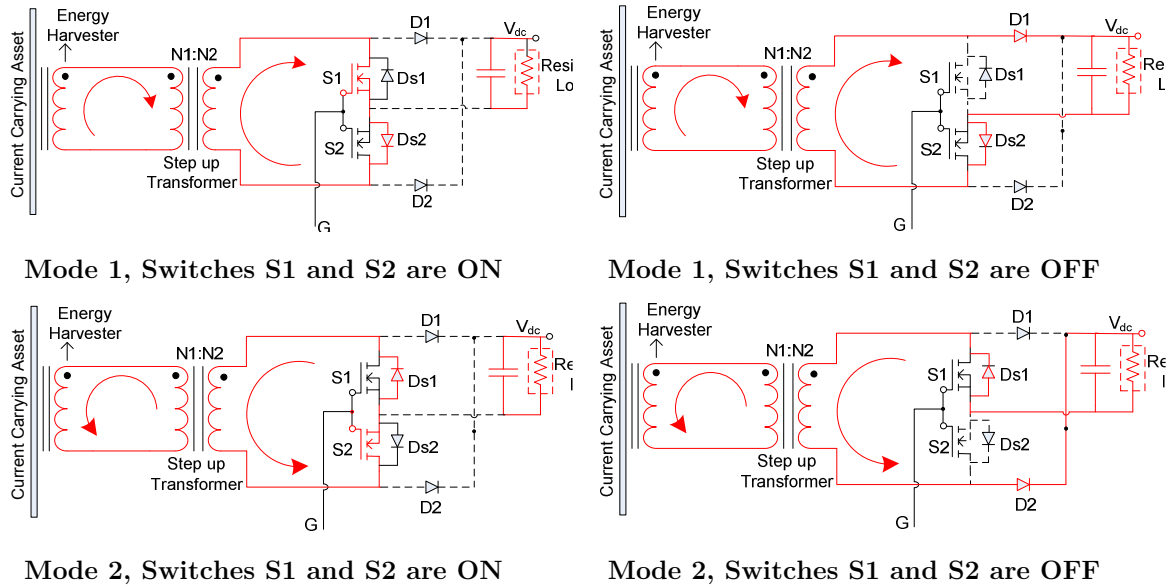


Figure 4.2: Modes of operation of the AC/DC boost boost converter

Table 4.1: Summary of Operation of the Proposed AC/DC Boost Converter

| Mode                               | Switch Status                            | Primary Side  | Secondary Side   |
|------------------------------------|--|---|--|
| Mode 1:<br>$0 < \omega t < \pi$    | $S = 1$<br>(SW1 and SW2<br>both are ON)  | Current goes into the<br>dot of the<br>transformer    | Current comes out of the dot and<br>flows through $S_1$ and $D_{s2}$ . This leads<br>to short circuit of the transformer<br>secondary and hence charging of the<br>transformer leakage inductance. |
|                                    | $S = 0$<br>(SW1 and SW2<br>both are OFF) | Same as above   | Current comes out of the dot and<br>flows through $D_1$ , output load and<br>$D_{s2}$ . This leads to transfer of energy<br>stored in the leakage inductance to<br>the load.                       |
| Mode 2:<br>$\pi < \omega t < 2\pi$ | $S = 1$<br>(SW1 and SW2<br>both are ON)  | Current comes out of<br>the dot of the<br>transformer | Current goes into the dot and flows<br>through $S_2$ and $D_{s1}$ . This leads to<br>short circuit of the transformer<br>secondary and hence charging of the<br>transformer leakage inductance.    |
|                                    | $S = 0$<br>(SW1 and SW2<br>both are OFF) | Same as above   | Current goes into the dot and flows<br>through $D_2$ , output load and the $D_{s1}$ .<br>This leads to transfer of energy<br>stored in the leakage inductance to<br>the load.                      |

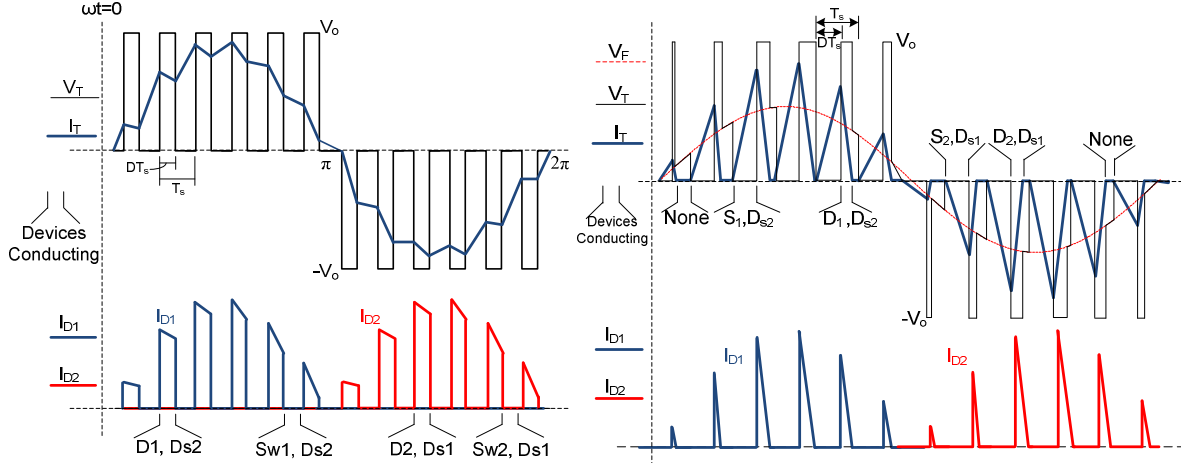


Figure 4.3: Waveforms of transformer voltage, current and diode currents in pure CCM and pure DCM mode

#### 4.2.1 Voltage Boost Analysis

Let the input voltage,  $V_f$  be assumed to be sinusoidally varying as

$$V_f = V_m \sin(\omega t) \quad (43)$$

Two different modes of operation need to be considered for computing the output voltage of the converter. In CCM, the current through the inductor is time varying at the frequency of supply with ripple at the switching frequency. However, it should be observed that the converter will not be able to operate in pure CCM at all times as at lower inductor currents the converter is bound to enter DCM. Therefore, it is difficult to compute a closed-form expression for the output voltage. Nonetheless, an approximate CCM output voltage can be derived using a large signal (RMS) approximation of the circuit given by

$$V_o^{CCM} = \frac{nV_m}{\sqrt{2}} \left( \frac{1-D}{R_L/R + (1-D)^2} \right) \quad (44)$$

While, in the case of pure DCM, the inductor current goes to zero after every switching period; therefore, volt-second balance can be applied in one switching period. Again using a large signal model the output voltage in DCM is given by

$$V_o^{DCM} = \frac{nV_m}{2\sqrt{2}} \left( 1 + \sqrt{1 + \frac{2D^2R}{f_sLn^2}} \right) \quad (45)$$

where  $n$  is the transformer turns ratio,  $R_L$  is the equivalent series resistance of the inductor,  $D$  is the duty cycle,  $R$  is the load resistance,  $L$  is the inductance,  $f_s$  is the switching frequency, and  $V_o$  is the output voltage.

Equations (44) and (45) can be written as

$$V_o = HV_m \quad (46)$$

where  $H$  is the boost operation function in CCM or DCM. Depending on the mode of operation  $H$  is a function of parameters  $R$ ,  $R_L$ ,  $n$ ,  $L$ ,  $f_s$  and on the duty cycle  $D$ .

Detailed simulations studies were performed to test the voltage boost functionality of the converter and test the results with the computed analytical models.

## 4.2.2 Simulation Study

Simulation of the proposed converter was performed in Synopsys Saber<sup>TM</sup> to validate the concept. The results of the simulations are shown below.

### 4.2.2.1 DCM Operation

In the simulation, circuit parameters were chosen to mimic a realistic scenario. The chosen circuit parameters are shown in Table 4.2.

**Table 4.2: Circuit Parameters Chosen for Simulation**

| Parameter  | Value         | Description                          |
|------------|---------------|--------------------------------------|
| $V_F$      | 0.2 Vpeak     | Flux concentrator voltage            |
| $f_s$      | 2 kHz         | Switching frequency                  |
| $L_F$      | 10 $\mu$ H    | Flux concentrator leakage inductance |
| $N_1:N_2$  | 1:20          | Transformer step up ratio            |
| $C$        | 10 $\mu$ F    | Filter capacitance                   |
| $R$        | 10 k $\Omega$ | Load resistance                      |
| $R_{dsON}$ | 60 m $\Omega$ | On state resistance of MOSFETs       |
| $V_{dON}$  | 0.3 V         | Diode On state voltage               |

The conformance of computed analytical voltage boost expression (45) with the simulation results is shown in Figure 4.4(a). A relatively small inductor ensures pure DCM operation of the converter. An example time domain plot of input voltage, output voltage, transformer secondary voltage and diode current is shown in Figure 4.4(b).

The simulation results show that the converter is able to boost voltages as low as 0.2 V to output voltages much greater than 3V. Moreover, with an increase in duty cycle, the output voltage also increases. Figure 4.4 shows that large output voltages can be achieved at the cost of higher current in switches, as the inductance is relatively small. In a practical application, the harvested power is limited. Therefore, as the load current increases, the input voltage reduces to keep power limited to its maximum value, which consequently, reduces the output voltage.

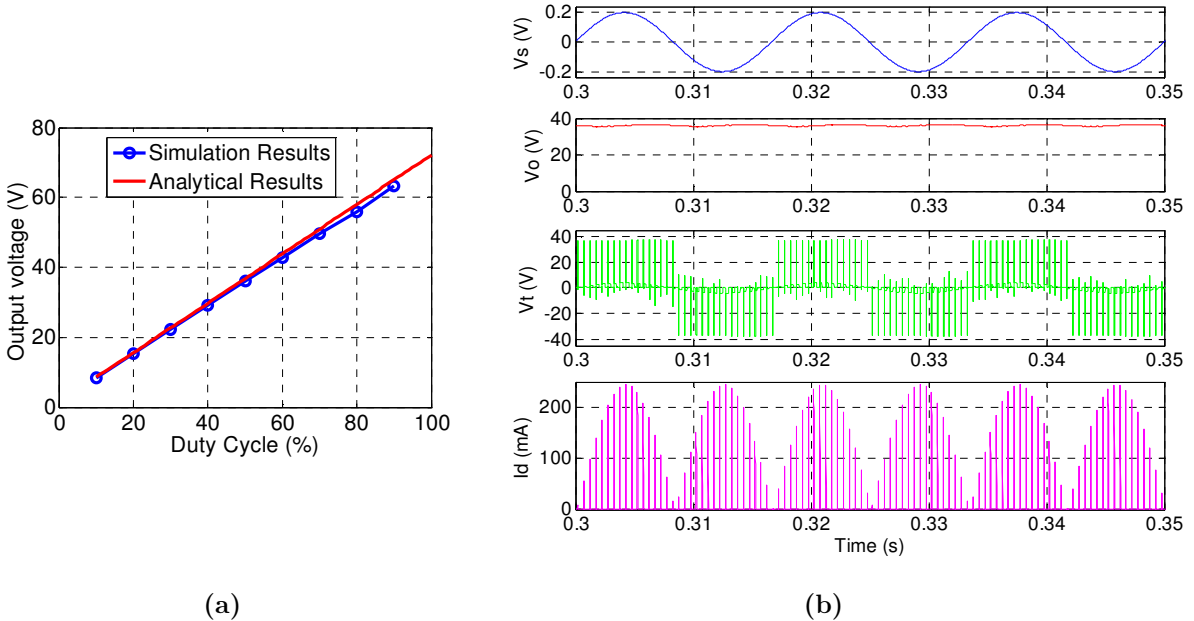


Figure 4.4: (a) Comparison of simulation results versus analytical results for output voltage in DCM Results at  $D = 50\%$ , (b) Voltage at the output is nearly 40 V. The converter operates in DCM.

#### 4.2.2.2 Combined CCM and DCM Operation

To simulate a case with combined CCM and DCM operation, the value of flux concentrator leakage inductance was increased to 0.5 mH with all the other circuit

parameters remaining the same as in Table 4.2. A plot of output voltage obtained from simulation results versus analytical results is shown in Figure 4.5(a). The validation of the combined CCM and DCM operation of the converter at different duty cycles is shown in Figure 4.5(c) and (d).

The output voltage of the converter decreases at higher duty ratios due to the small equivalent series resistance (ESR) of  $1 \text{ m}\Omega$  included with the inductor. In practical applications, the transformer and XFC will have a larger ESR which can dramatically change the output voltage characteristics. Output voltages obtained at two different values of ESRs ( $1 \text{ m}\Omega$  and  $200 \text{ m}\Omega$ ) are compared in Figure 4.5. It can be seen that the converter has characteristics very similar to a DC/DC converter and the output voltage dramatically reduces with an increase in ESR.

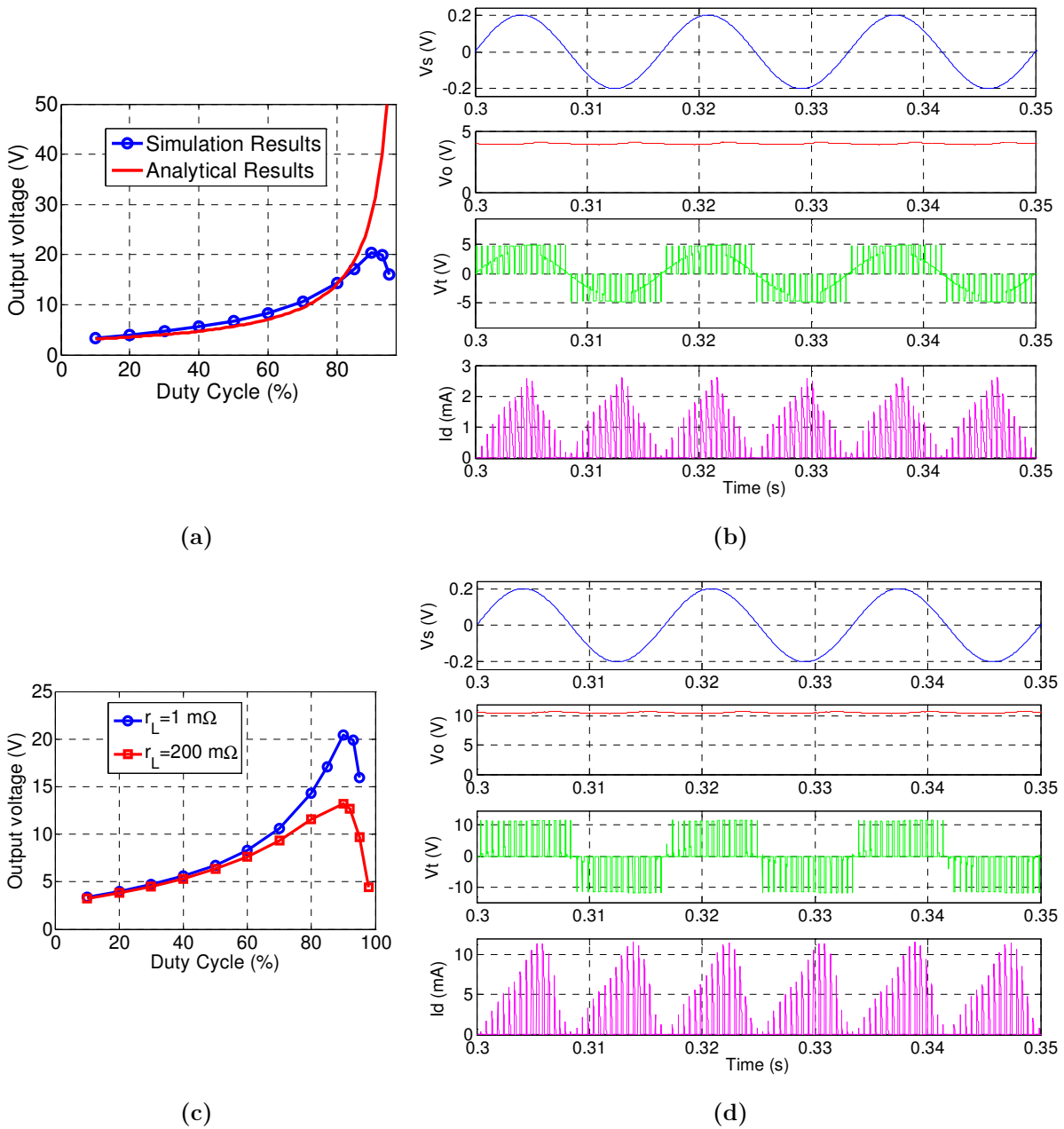


Figure 4.5: (a) Comparison of output voltage obtained using simulation results in combined CCM and DCM versus analytical results in pure DCM, (b) Results at  $D = 20\%$ . Voltage at the output is nearly 4 V. The converter operates mostly in DCM as the duty cycle is low, (c) Comparison of output voltage obtained using  $r_L = 1 \text{ m}\Omega$ , and  $r_L = 200 \text{ m}\Omega$ , (d) Results at  $D = 70\%$ . The voltage at the output is nearly 11 V. The converter operates mostly in CCM as the duty cycle is high.



### 4.3 POWER CIRCUIT DESIGN

The successful voltage boost operation obtained from the simulation of the proposed converter topology motivated the development of an experimental prototype of the proposed converter. The prototype was constructed to validate the operation of the proposed converter in practice. Certain important practical issues such as, black-start, operation in an outage, multi-source energy harvesting, wide operation range, were also addressed. Moreover, solutions to these issues were incorporated in the proposed power circuit to form a robust power management system that is devoid of any batteries and that requires no maintenance.

Finally, a self-powered wireless *Stick-on sensor* for monitoring asset current, surface temperature and ambient temperature was fabricated and was powered with the help of the developed power management system. The details of fabricating the self-powered wireless sensor are given in the sections to follow. Furthermore, various tests to validate effective operation of the power circuit and the sensor were also conducted, and are discussed in the following sections.

#### 4.3.1 Black-Start Functionality

One of the major functionalities required by utilities for smart sensors is to have the sensors start automatically after an outage condition. Consider a situation when the utility asset carries no current; therefore, it has no magnetic field around it. In this situation, the voltage built up on the DC capacitor will be discharged in some time after the power outage and the DC supply would reduce to zero. Note that a similar situation will be observed when the sensor is installed for the first time on a utility asset. Even if after some time the utility asset is re-energized, as there is no DC supply on the power circuit to begin with, no gating pulses would be generated. In the absence of gating pulses, the voltage boost functionality will not be realized and the sensor would not operate. Therefore, generation of gating pulses for the MOSFET switches is a major challenge for self-starting the power circuit.

A simple solution is proposed to solve this problem by using a push-pull circuit that builds the output voltage and gating pulses using a positive feedback. As shown in Figure 4.6, an astable multivibrator having a wide operating range and that can start pulsating at relatively low voltage ( $< 1V$ ) can be used to realize this functionality. The astable multivibrator along with the transformer essentially creates a boot strapping system that builds up the output voltage with even a small amount of input voltage. In this manner, when the sensor is powered for the first time or after an outage, the power circuit is able to boot-strap a potential slightly above the gate-source threshold of the MOSFETs. Once the MOSFETs start switching, a boost in the output voltage is observed.

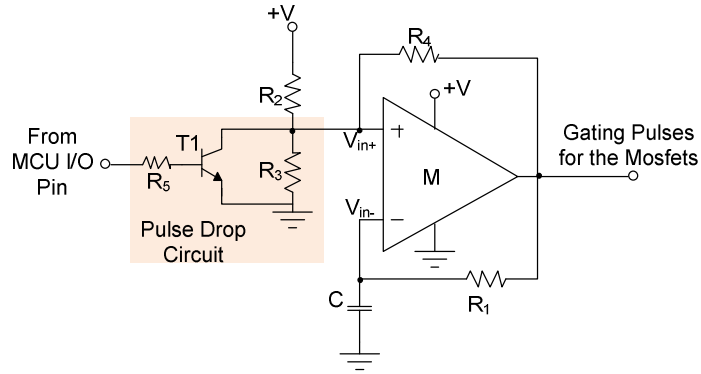


Figure 4.6: Modified astable multivibrator used for self-start

The astable multivibrator can be designed using the following equations:

$$V_{iHL} = V_{OH} \left( \frac{R_{23}}{R_{23} + R_4} \right) + V_{23} \left( \frac{R_4}{R_{23} + R_4} \right) \quad (47)$$

$$V_{iLH} = V_{OL} \left( \frac{R_{23}}{R_{23} + R_4} \right) + V_{23} \left( \frac{R_4}{R_{23} + R_4} \right) \quad (48)$$

where  $R_{23}$  is the thevenin equivalent of  $R_2$  and  $R_3$  given by,

$$R_{23} = \frac{R_2 R_3}{R_2 + R_3} \quad (49)$$

$V_{23}$  is the thevenin equivalent source given by

$$V_{23} = +V \left( \frac{R_3}{R_2 + R_3} \right) \quad (50)$$

$V_{OH}$  is the voltage when the output is in the high state

$V_{OL}$  is the voltage when the output is in the low state

$V_{iHL}$  is the  $V_{in}$  required to transition from  $V_{OH}$  to  $V_{OL}$  at the output

$V_{iLH}$  is the  $V_{in}$  required to transition from  $V_{OL}$  to  $V_{OH}$  at the output.

The time taken by the capacitor to charge from  $V_{iLH}$  to  $V_{iHL}$  at  $V_{in}$  is given by

$$t_{charge} = \tau \ln \left( \frac{V_{iHL} - V_{OH}}{V_{iLH} - V_{OH}} \right) \quad (51)$$

where  $\tau = R_1 C$

Also, the time taken by the capacitor to discharge from  $V_{iHL}$  to  $V_{iLH}$  at  $V_{in}$  is given by

$$t_{discharge} = \tau \ln \left( \frac{V_{iLH} - V_{OL}}{V_{iHL} - V_{OL}} \right) \quad (52)$$

Duty cycle is given by

$$D = \frac{t_{charge}}{t_{discharge} + t_{charge}} \quad (53)$$

Using the above equations the values for  $R_1$ ,  $R_2$ ,  $R_3$ ,  $R_4$ , and  $C_1$  were selected such that the frequency of oscillations of the multivibrator output was 2 kHz at a 50% duty cycle. The values of all the components are shown in Table 4.3.

**Table 4.3: Component List for the Modified Astable Multivibrator Figure 4.6**

| Component Name | Value          | Part Number / Company |
|----------------|----------------|-----------------------|
| M              | Comparator     | MCP 6541 / Microchip  |
| R2,R3          | 1 M $\Omega$   | N.A.                  |
| R1, R4         | 510 k $\Omega$ | N.A.                  |
| C              | 470 pF         | N.A.                  |
| T1             | NPN Transistor | ZTX1047A / Zetex      |
| R5             | 100 k $\Omega$ | N.A.                  |

### 4.3.2 Operation in an Outage

One of the major applications of these low-cost sensors is to inform the control center, a data collector, or utility operators, about loss of power on a particular asset. This could help utilities to promptly identify the point of failure, estimate the root causes of failure using the recent history of the sensed parameters, and take expeditious actions such as asset replacement or maintenance to resume normal operation of the asset.

One way to operate the sensor in the absence of any magnetic field is through the use of an on-board energy storage element. Given that in an outage, utilities need the sensor to operate at-least once to inform about the outage, the energy storage requirement is dramatically reduced. Energy on the order of 100 mJ may be sufficient for this purpose and can be served by an ultra-capacitor. The advantage of using an ultra-capacitor over a battery is that the charge-discharge cycles of an ultracapacitor are several thousand times greater than a battery. Large number of charge-discharge helps in achieving long life (up to 20 years) for the sensor. The proposed power management uses a 1 F ultracapacitor as the backup source.

The challenge with using an ultracapacitor is that it cannot be connected directly across the DC bus of the power circuit. To understand the reason, take an example of an outage. Suppose, the ultracapacitor discharges completely during the outage. When power resumes, the ultracapacitor appears as a low impedance load and restricts the circuit to develop the required voltage at the output till the ultracapacitor is charged. Charging of the ultracapacitor may take hours depending on the magnetic field energy available. During this time, the sensor would not get sufficient voltage; therefore, it would not operate.

The problem at hand can be solved by providing a constant current charging to the ultracapacitor as shown in Figure 4.7. The charging is governed by

$$C_u \frac{dV_c}{dt} = \left( \frac{V_{D1} + V_{D2} - V_{BE}}{R_E} \right) \quad (54)$$

where  $V_{D1}$  and  $V_{D2}$  are diode forward drops,  $V_{BE}$  is the base to emitter voltage of the pnp transistor, and  $V_c$  is the ultra-capacitor voltage. Overcharging is avoided by clamping the ultracapacitor to the bus voltage through diode  $D_3$  when enough energy is available in the field. The components used to build the ultra-capacitor charging circuit are given in Table 4.4.

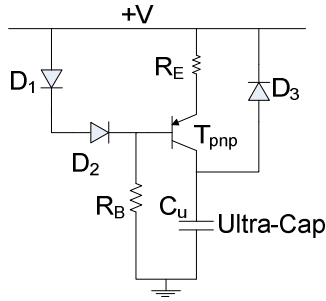


Figure 4.7: Ultracapacitor charging circuit

Table 4.4: Component List for the Ultracapacitor Charging Circuit

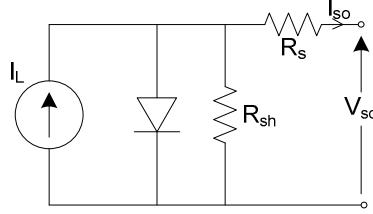
| Component Name | Value                          | Part Number / Company    |
|----------------|--------------------------------|--------------------------|
| D1, D2         | General Purpose Diode          | 1N4148 / Vishay          |
| D3, D4         | Schottky Diode                 | 1N5818 / Vishay          |
| T              | General Purpose PNP Transistor | 2N3906                   |
| RE             | 15 k $\Omega$                  | N.A.                     |
| RB             | 1 M $\Omega$                   | N.A.                     |
| Cu             | 1 F                            | PB-5R0V105-R / PowerStor |

### 4.3.1 Multi-source Energy Harvesting

Most utility assets are present in open areas with abundance of sunlight. Hence, solar energy can act as another energy source for the sensor. However, solar energy has a diurnal variation and cannot be used as a primary source. It can, however, be used as a source of trickle charge for the ultracapacitor. In this way, the rating, size and cost of the solar cell can be kept very low, and minimal dependence on solar power can be realized. This is one way of including multiple sources of energy harvesting for powering the sensor. In this sub-section a method to design and integrate a solar cell to the existing energy harvesting circuit is elucidated.

#### 4.3.1.1 Solar Cell Model

A solar cell can be represented by a circuit model shown in Figure 4.8 [106]. The characteristic equation of the circuit is given in (55)



**Figure 4.8: Equivalent circuit model of a solar cell**

$$I_{so} = I_L - I_o \left( e^{\frac{q(V_{so} + I_{so}R_s)}{nKT}} - 1 \right) - \frac{V_{so} + I_{so}R_s}{R_{sh}} \quad (55)$$

where  $I_o$  is the saturation current of the cell and  $I_L$  is the current due to the presence of a light source,  $R_s$  and  $R_{sh}$  are the parasitic resistances. The above circuit can be used to compute the value of OCV ( $V_{oc}$ ) and SCC ( $I_{sc}$ ) of the solar cell. To compute  $I_{sc}$ ,  $R_s$  and  $R_{sh}$  can be replaced with zero and infinity respectively, and  $V$  with zero. This gives

$$I_{sc} = I_L \quad (56)$$

To compute  $V_{oc}$ ,  $I_{so}$  can be replaced with 0 which gives

$$V_{oc} = \frac{KT}{q} \ln \left( \frac{I_L}{I_o} + 1 \right) \quad (57)$$

For selecting an optimal solar cell for the sensor it is important to understand the concept of the fill factor FF. Fill factor is defined as

$$FF = \frac{V_{mp} I_{mp}}{V_{oc} I_{sc}} \quad (58)$$

where,  $V_{mp}$  and  $I_{mp}$  are the voltage and current at the maximum power point for the considered solar cell. In the past, empirical solutions for FF have been found for different conditions of normalized  $R_{sh}$ ,  $R_s$  and  $V_{oc}$  [107]. The expressions are given in Table 4.5. The normalization is given by,

$$v_{oc} = \frac{V_{oc}}{K T / q} \quad r_{sh} = \frac{R_{sh}}{V_{oc} / I_{sc}} \quad r_s = \frac{R_s}{V_{oc} / I_{sc}} \quad (59)$$

**Table 4.5: Empirical Values of Fill Factors for Solar Cells**

| Condition                                 | Empirical expression for the fill factor FF                                    |
|---|--|
| $R_{sh} = \infty, R_s = 0, v_{oc} > 10$   | $FF_o = \frac{v_{oc} - \ln(v_{oc} + 0.72)}{v_{oc} + 1}$                        |
| $R_{sh} = \infty, R_s < 0.4, v_{oc} > 10$ | $FF_s = FF_o (1 - 1.1r_s) + \frac{r_s^2}{5.4}$                                 |
| $R_s + 1 / R_{sh} < 0.4, v_{oc} > 10$     | $FF = FF_s \left( 1 - \frac{v_{oc} + 0.7}{v_{oc}} \frac{FF_s}{r_{sh}} \right)$ |

In the case of the Stick-on sensor, the solar cell may not necessarily operate at the maximum power point at all times, yet it is important to select a solar cell which has a high fill factor. A high fill factor corresponds to high efficiency represented by

$$\eta = \frac{V_{oc} I_{sc} FF}{P_{in}} \quad (60)$$

where  $P_{in}$  is the solar power incident on the cell. Using the empirical expression for FF, the fill factor of the solar cell can be determined. A simple rule of thumb that can be followed while selecting a solar cell for the sensor is to select a cell with a higher  $V_{oc}$ .

#### 4.3.1.2 *Integration of Solar Energy Harvesting*

For the Stick-on sensor a solar cell having an OCV of 4 V and SCC of 2.5 mA, shown in Figure 4.10(a), was used. This solar cell is composed of 8 cells in parallel each having an OCV of 0.5 V. The current density of the considered solar cell is equal to 34.6 mA/cm<sup>2</sup>. The maximum harvestable power of the solar cell was characterized in the laboratory for different operating conditions. One of the plots is shown in Figure 4.10(b).

The ultracapacitor can be connected directly to the solar cell through a Schottky diode ( $D_4$ ), as shown in Figure 4.11. Assuming the ultracapacitor is initially uncharged, it behaves as a short circuit. Finally, when the capacitor is charged up to the solar cell's

OCV diode  $D_4$  opens. The trajectory of operation obtained on the V-I curve during charging of the ultracapacitor is shown in Figure 4.9.

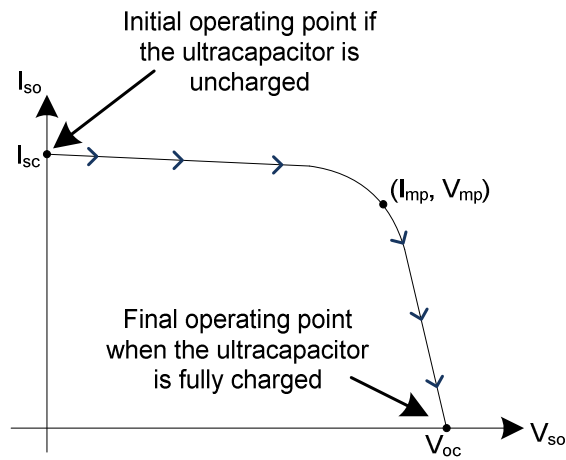


Figure 4.9: Trajectory of operation for trickle charging an ultracapacitor using a solar cell.

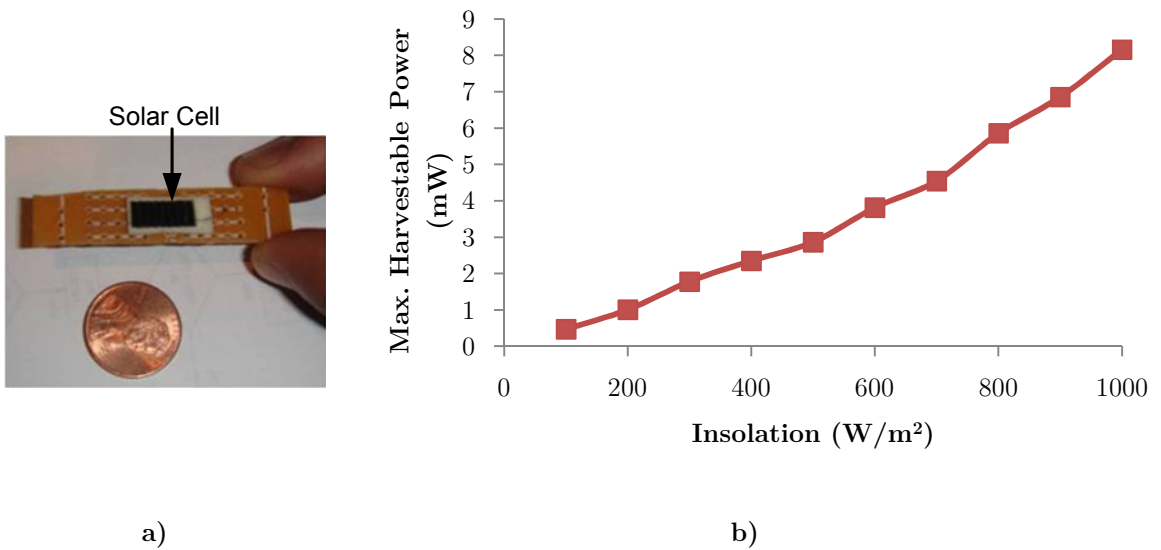


Figure 4.10: (a) Mini-solar cell having an OCV of 4V and SCC of 2.5 mA was used as the solar harvester, (b) Maximum harvestable power from the solar cell under different insolation characterized in the lab



Table 4.6: Characterization Results of the Solar Cell at 25 °C

| Insolation (W/m <sup>2</sup> ) | I <sub>sc</sub> (mA) | V <sub>oc</sub> (V) | FF <sub>o</sub> | Power at MPP (mW) | Efficiency at MPP % |
|--------------------------------|----------------------|---------------------|-----------------|-------------------|---------------------|
| 200                            | 0.34                 | 3.7                 | 0.79            | 1                 | 8.6                 |
| 400                            | 0.74                 | 3.97                | 0.8             | 2.35              | 10.2                |
| 600                            | 1.18                 | 4.04                | 0.8             | 3.8               | 11                  |
| 800                            | 1.8                  | 4.07                | 0.81            | 5.93              | 12.8                |
| 1000                           | 2.5                  | 4.08                | 0.81            | 8.26              | 14.3                |

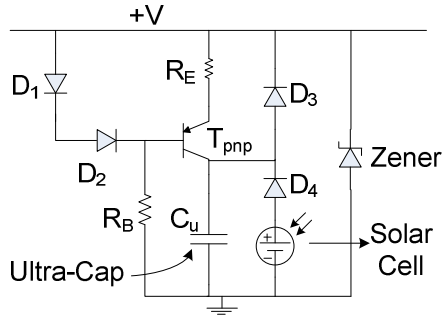


Figure 4.11: Ultracapacitor charging circuit

### 4.3.2 Wide Operating Range

Another major requirement for these utility sensors is high reliability of operation. As the sensor can be used on assets that carry current in the range of 100 to 2000 A, it has to be ensured that apart from providing uninterrupted power, the power management system should also be able to protect the sensor from large voltage stresses that might develop at higher currents. This problem can be solved by using a zener diode at the output of the power circuit such that it clamps the voltage to be within the safe operating area (SOA) of the MOSFET switches and diodes. Further, a low dropout voltage regulator (LDO) is used to ensure that over the wide operating range a constant supply is provided to the sensor.

The detailed diagram of the novel power circuit utilizing the proposed converter is shown in Figure 4.12.

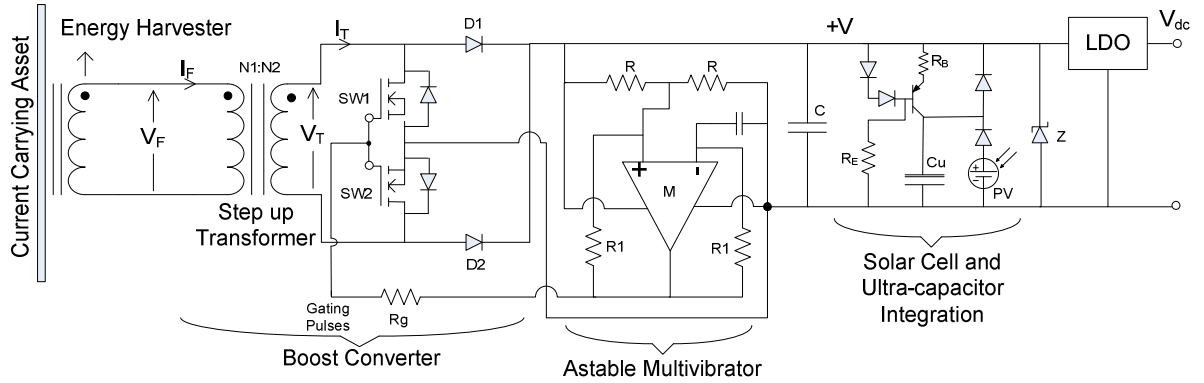


Figure 4.12: Proposed overall power circuit diagram

#### 4.4 SENSING AND SIGNAL CONDITIONING CIRCUIT DESIGN

The aim of this research is to develop a self-powered wireless *Stick-on sensor* for monitoring asset current, surface temperature and ambient temperature. The details on designing the current and temperature sensor along with the necessary signal conditioning circuitry are presented in this section.

##### 4.4.1 Current Sensor Design

It was shown in Section 3.4 that the OCV and SCC of the XFC are linearly proportional to the conductor current. When using the OCV to measure higher currents, the voltage stress on the diode and MOSFET switches may increase and surpass their ratings. For this reason, it was deemed preferable to use the SCC for current measurement. The use of SCC for current measurement avoids unnecessary stress on the switching devices and diodes during measurement. The XFC plays a dual role of energy harvesting (during normal operation) and current sensing (during measurement), ensuring a compact design.

The circuit used to measure the SCC is shown in. Whenever a current measurement is required, the microcontroller (MCU) generates a pulse that switches on the NPN transistor  $T_{sc}$ , which shorts the DC bus through resistance  $R_{sc}$ . The voltage developed across  $R_{sc}$  ( $V_{eh1}-V_{eh2}$ ) is sent to a difference amplifier. The difference amplifier designs that were tested are given in Figure 4.13(b) and (c).

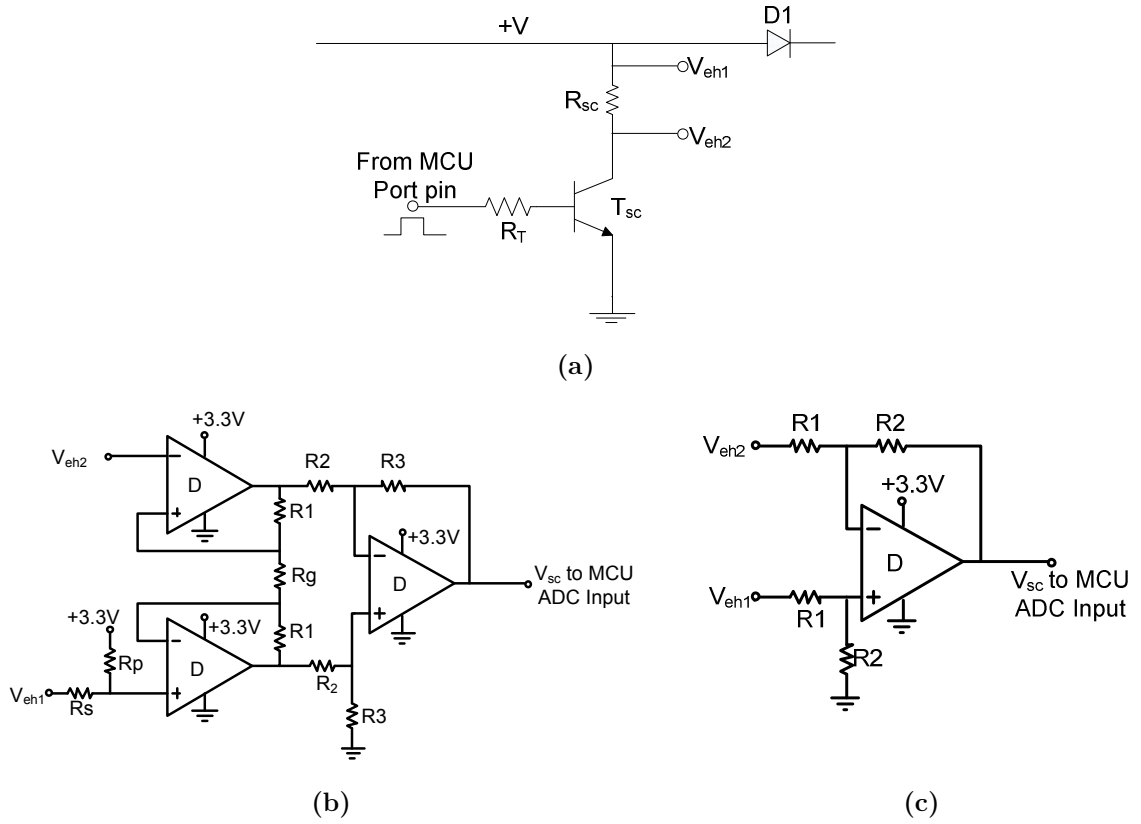


Figure 4.13: (a) SCC measurement, (b) and (c) Two different difference amplifier implementations

The equations that were used to design the difference amplifier shown in Figure 4.13(b) and (c) are given by

$$V_o = \left[ (V_{s1} - V_{s2}) \left( \frac{R_p}{R_s + R_p} \right) + 3.3 \left( \frac{R_s}{R_s + R_p} \right) \right] \left[ 1 + \frac{2R_1}{R_G} \right] \left( \frac{R_3}{R_2} \right) \quad (61)$$

$$V_o = (V_{eh1} - V_{eh2}) \left( \frac{R_2}{R_1} \right) \quad (62)$$

The values selected for implementing the difference amplifiers in Figure 4.13(b) and (c) are shown in Table 4.7 and Table 4.8 respectively.

**Table 4.7: Component List for Current Sensing Signal Conditioning in Figure 4.13(b)**

| Component Name       | Value            | Part Number / Company |
|----------------------|------------------|-----------------------|
| $R_s$                | 510 k $\Omega$   | N.A.                  |
| $R_p$                | 10 M $\Omega$    | N.A.                  |
| $R_g, R_1, R_2, R_3$ | 1 M $\Omega$     | N.A.                  |
| A                    | Low Power Op-Amp | TC1029 / Microchip    |

**Table 4.8: Component List for Current Sensing Signal Conditioning in Figure 4.13(c)**

| Component Name | Value            | Part Number / Company |
|----------------|------------------|-----------------------|
| $R_1$          | 510 k $\Omega$   | N.A.                  |
| $R_2$          | 1 M $\Omega$     | N.A.                  |
| A              | Low Power Op-Amp | TC1029 / Microchip    |

The output of the difference amplifier is connected to the ADC channel of the MCU. Subsequently, the value of current is computed in the MCU using

$$I_{pri} = C_K \frac{\int_{T_1}^{T_2} I_{sc}(t) dt}{T_2 - T_1} \quad (63)$$

where

$$I_{sc}(t) = \frac{V_{eh1}(t) - V_{eh2}(t)}{R_{sc}}$$

Plugging the value of  $I_{sc}(t)$  in (63)

$$I_{pri} = C_K^1 \frac{\int_{T_1}^{T_2} (V_{eh1}(t) - V_{eh2}(t)) dt}{T_2 - T_1} \quad (64)$$

where  $T_1$  is the time at start of the measurement,  $T_2$  is the time at end of the measurement and  $C_K^1$  is the constant of proportionality.

During current measurement, diode D1 blocks the capacitor at the DC bus from being discharged. In essence, diode D1 decouples the sensor from the power converter. During this short duration, the sensor remains powered up using the charge on the DC capacitor. It should be noted that the gating pulses for the MOSFET switches generated

by the multivibrator need to be dropped to measure the correct SCC value. If the gating pulses are not dropped, the converter will keep operating and a pulsed current will be measured, which may not be indicative of the true current in the asset.

When the measurements are complete, the MCU I/O signal goes low, consequently, the transistor switches off, gating pulses to the MOSFET switches are restored, and the normal operation resumes.

#### 4.4.2 Temperature Sensor Design

The prototype developed in this research is also equipped with temperature sensing. Temperature measurement can be performed by using either, RTDs, thermistors, thermocouples or temperature transducer ICs. Every technique has its own pros and cons. For the fabricated sensor, the transducer IC is a good candidate as it has a linear relationship to the temperature, and provides a stable voltage source output which requires only a buffer amplifier circuit to follow, as shown in Figure 4.14. The sensed signal can be directly measured using a microcontroller, eliminating the need for any additional circuits, and reducing the power further. The goal was to measure the asset and ambient temperature. Temperature sensing was implemented only to demonstrate a proof-of-concept design and is not a focus of this research.

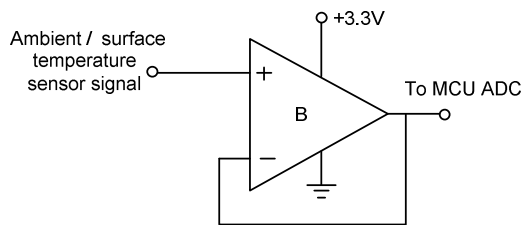


Figure 4.14: Buffer amplifier used for temperature sensing

#### 4.4.3 ZigBee® Radio and Microcontroller

The Stick-on sensor uses TI's CC2530 SOC solution for ZigBee®, shown in Figure 4.15, which contains a high performance and low-power 8051 microcontroller core, 256 kB flash, 8 kB RAM, 12 bit ADC with 8 channels and a ZigBee® transceiver. It uses an Antenova Titanis swivel antenna designed for 2.4 GHz communication.



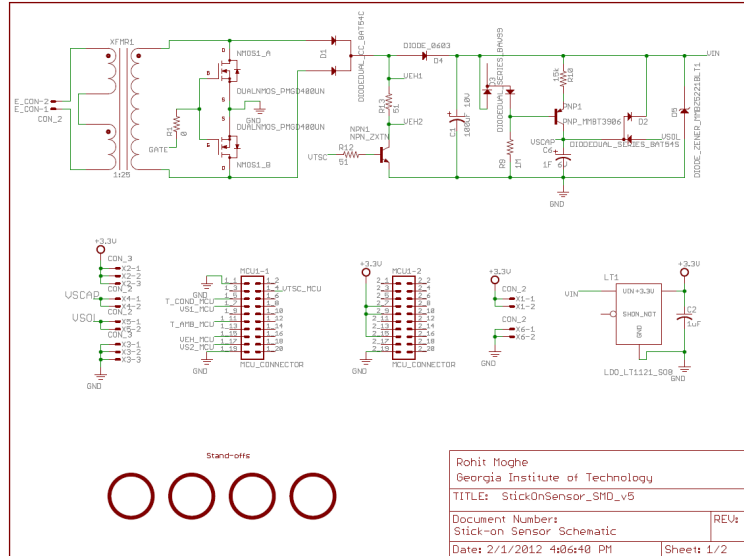
Figure 4.15: TI's CC2530 SOC solution for ZigBee®

#### 4.5 SENSOR PROTOTYPE FABRICATION

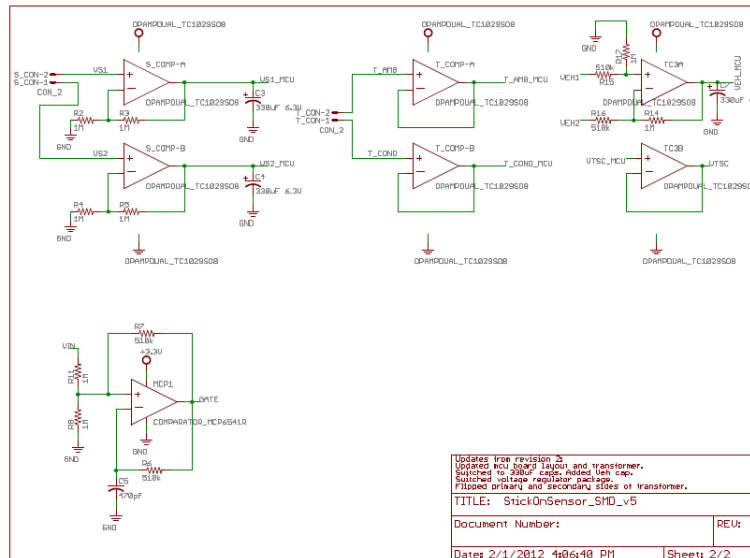
Two different versions of a self-powered wireless *Stick-on sensor* were fabricated in the lab. The sensor was designed to measure asset current, asset temperature and ambient temperature. The asset used for testing the sensor was an ACSR conductor that had the capability to carry up to 1500 A current. The power and signal conditioning circuit schematic were routed using Eagle™. The schematic of the power circuit is shown in Figure 4.16. The circuit schematic for both the versions is the same. However, one circuit was implemented using mostly through-hole components while, the other was implemented using surface mount components to reduce the size. The layouts of the two versions and the fabricated circuits are shown in Figure 4.17.

As parasitic resistances increase losses in the system, the circuits were designed with the objective of minimization of trace lengths between any two components. Further, to minimize size of the sensor, headers were provided on the main circuit board to mount the CC2530 module. The final circuit boards connected to the CC2530 modules are shown in Figure 4.18.

The list of components used for building the power circuit along with their values is shown in Table 4.9. Note that the parameters of the flux concentrator and the transformer were computed using standard open-circuit and short-circuit tests.



(a)



(b)

Figure 4.16: Eagle schematic for (a) power circuit, and (b) signal conditioning circuit.

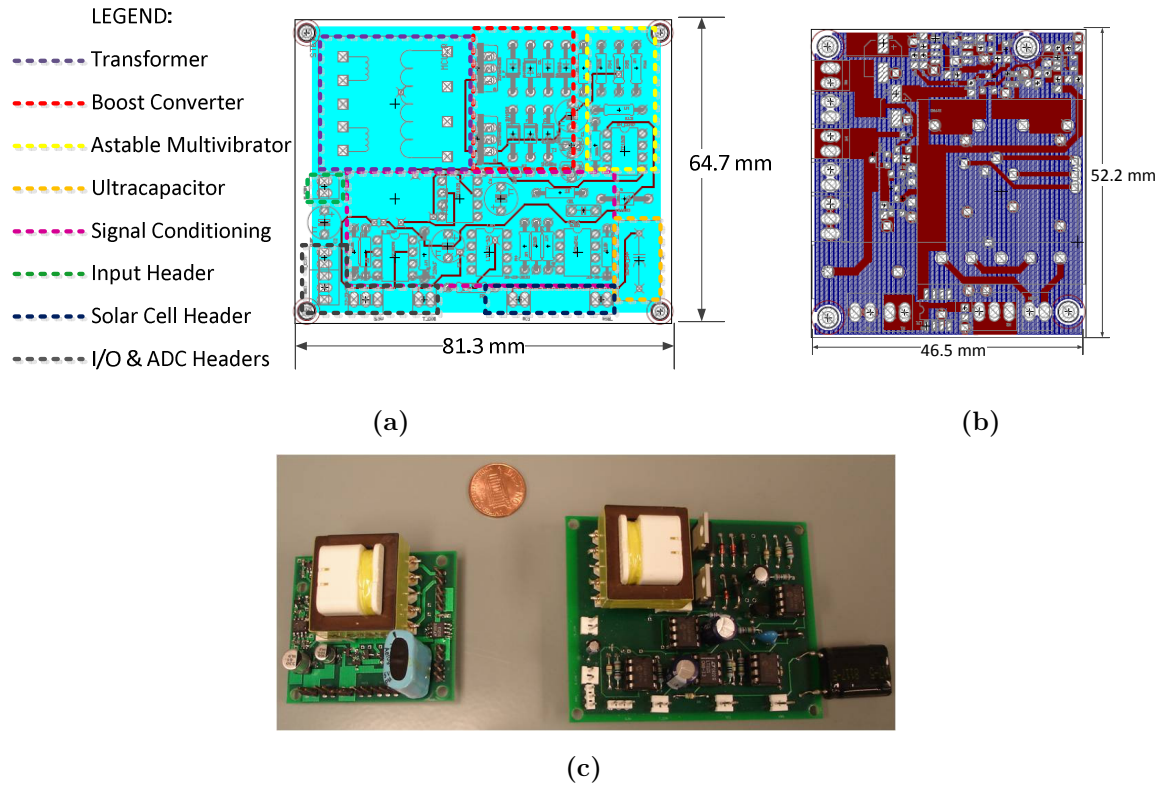


Figure 4.17: (a) and (b) show layouts for the Stick-on sensor circuit board, c) actual circuit boards kept side by side for comparison of size.



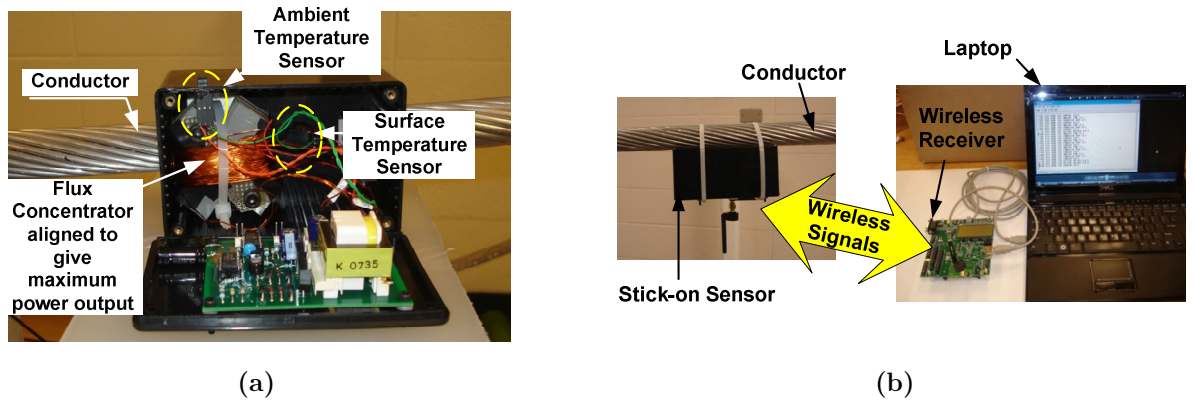
Figure 4.18: (a) Bottom View of the PCB (through-hole version) with the micro-controller and transceiver attached to it, (b) Surface mount version



**Table 4.9: Power Circuit Parameters**

| Component         | Value / Rating   |
|-------------------|--|
| Flux Concentrator | Type = XFC   |
|                   | $N_F = 300$  |
|                   | $LF = 7.62 \text{ mH}$   |
|                   | $R_F = 5.93 \Omega$  |
| Transformer       | $L_1 = 0.285 \text{ mH}$   |
|                   | $L_2' = 0.285 \text{ mH}$  |
|                   | $R_1 = 1.3 \Omega$   |
|                   | $R_2' = 1.3 \Omega$  |
| Schottky Diodes   | $V_{RRM} = 30V$  |
|                   | Forward Drop = 0.55V (@1A)                                       |
| N-channel Mosfet  | $V_{(BR)DS} = 35V$   |
|                   | $I_D = 13A$  |
|                   | $V_{GSth} = 1V$  |
|                   | $R_{DSon} = 60m\Omega$ (@ $V_{GS} = 10V, I_D = 3.7A$ )           |
|                   | Forward drop of body diode = 0.95V (@ $V_{GS} = 0, I_D = 3.7A$ ) |
| Capacitor         | 100 $\mu F$  |

The developed circuit board was integrated to the XFC, and two temperature sensors. The final prototype of the Stick-on sensor and the test setup for demonstrating operation of the sensor is shown in Figure 4.19. The test setup comprised the sensor stuck on to the conductor and a remote coordinator (data collector) connected to a laptop through a serial-to-USB connector.



**Figure 4.19:** a) Laboratory prototype of the Stick-on sensor kept close to a conductor, b) A functional Stick-on sensor mounted on a conductor with wire ties sends current and temperature signals to a remote coordinator. The coordinator is connected to a laptop and records the received data.

The functional block diagram of the developed Stick-on sensor is shown in Figure 4.20.

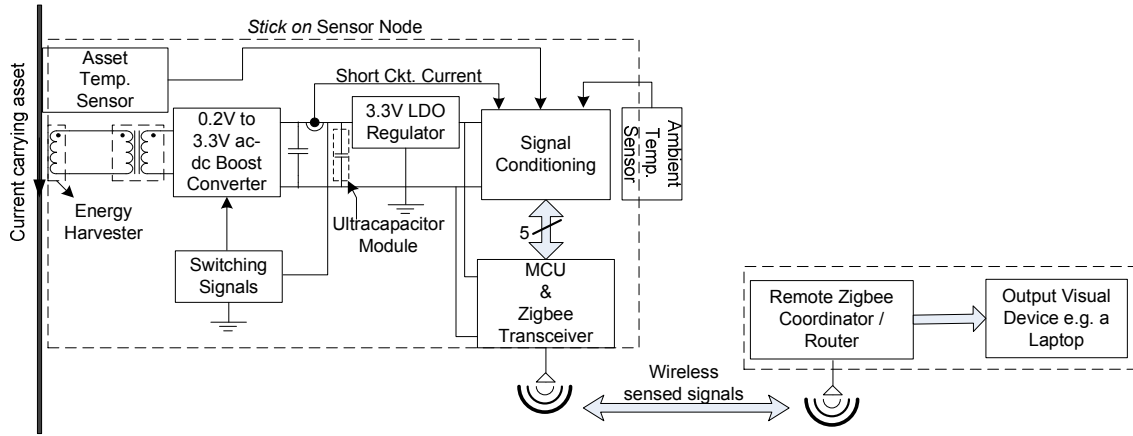


Figure 4.20: Functional schematic of the test setup

## 4.5.1 Experimental Testing and Validation

### 4.5.1.1 Voltage Boost Operation

The boost functionality of the sensor at different duty cycle and 60 A of conductor current was tested. The results of the experiment are shown in Table 4.10. It can be observed that the voltage is boosted to sufficiently high values even at a low conductor current. The efficiency of the converter was calculated to be 75% at 200 A conductor current. The current and voltage waveforms at different points in the circuit are shown in Figure 4.21.

Table 4.10: Converter Operation at Different Duty Cycle, Primary Current = 60 A, Load resistance= 50 kΩ, Switching frequency= 2 kHz

| AC Voltage (RMS Volts) | Duty Cycle (%) | DC Voltage (Volts) |
|------------------------|----------------|--------------------|
| 0.2                    | 0              | 2.25               |
| 0.2                    | 10             | 2.5                |
| 0.2                    | 30             | 3                  |
| 0.2                    | 50             | 3.5                |
| 0.2                    | 70             | 4.4                |

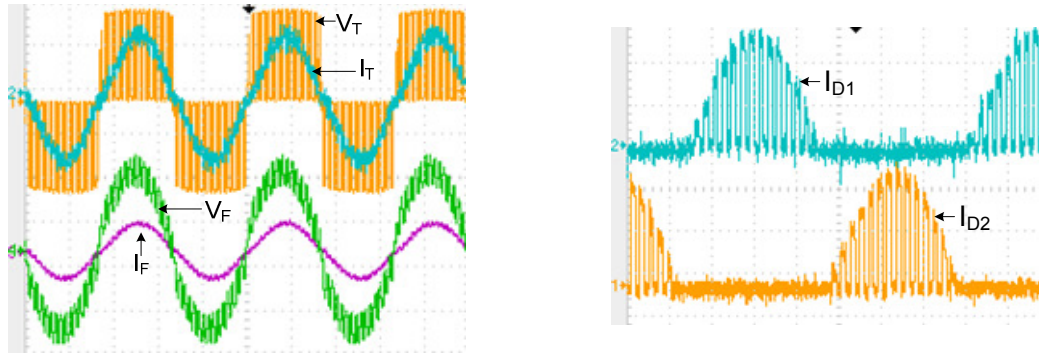


Figure 4.21: Screenshot showing VF - Flux concentrator voltage (0.2 V/Div.), VT – Transformer secondary voltage (2 V/Div.), IF - Flux concentrator current (10 mA/Div.), IT – Transformer secondary current (2 mA/Div.), ID1 and ID2 – Diode currents (1 mA/Div.). The converter is operated with 50% duty cycle.

#### 4.5.1.2 *Black-Start Demonstration*

As the current in the conductor was ramped up from 15 A to 60 A, the DC voltage is built up from  $0.4 V_{dc}$  to  $3.3 V_{dc}$ . In this manner, the overall power circuit was able to autonomously power up the sensor at primary currents as low as 60 A, as shown in Figure 4.22.

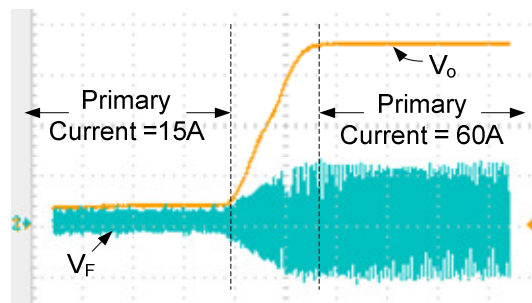


Figure 4.22: Black-start functionality: Vo – output voltage (1V/Div.), VF – Flux concentrator voltage (0.2 V/Div.), Time base – (2.5 Sec/Div. )

#### 4.5.1.3 *Wide Range of Operation*

The sensor has been tested for current measurement from 60 A to a 1000 A and the power circuit works reliably over the entire range. Figure 4.23 shows experimental results depicting flawless operation of the power circuit at 60 A, and 1000 A of conductor current.

It can be observed that in both the cases, the power circuit maintains a stable 3.3 V DC supply for the sensor.

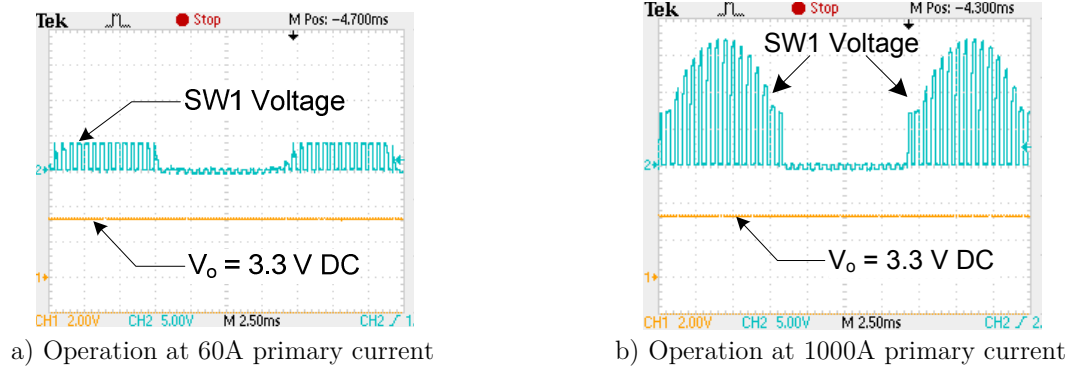


Figure 4.23: Circuit operating at 60A and 1000A primary current,  $V_o$  – Output Voltage (2 V/Div.), SW1 – Mosfet Switch 1 Voltage (5 V/Div.)

#### 4.5.1.4 Current Sensing Operation

Apart from harvesting magnetic field energy, the XFC was also used for current sensing as described in Section 3.4. A screenshot when the sensor starts the measurement of current is shown in Figure 4.24. It can be observed that as the astable multivibrator pulses are dropped, a rectified sine wave is obtained at the output of the converter which is sampled by the ADC of the MCU and current measurement is performed. When the measurement period is over, the pulses are restored.

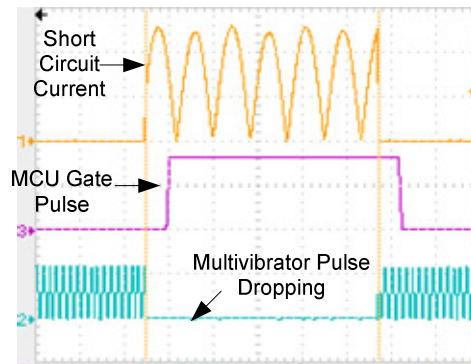


Figure 4.24: Different waveforms generated during current sensing

#### 4.5.1.5 Stick-on Sensor Operation

The remote data collector was responsible for establishing the ZigBee® network. Subsequently, the sensor joined the network. The sensor stayed in the sleep mode for most of the time, woke-up at certain intervals, sensed current, and temperature and sent the packets to the data collector. The data collector displayed the sensed results on a graphical user interface (GUI) developed in this research. The GUI displayed the time stamped current, and temperature data along with the min-max history. A sample GUI plot of sensed current and temperature is shown in Figure 4.25.

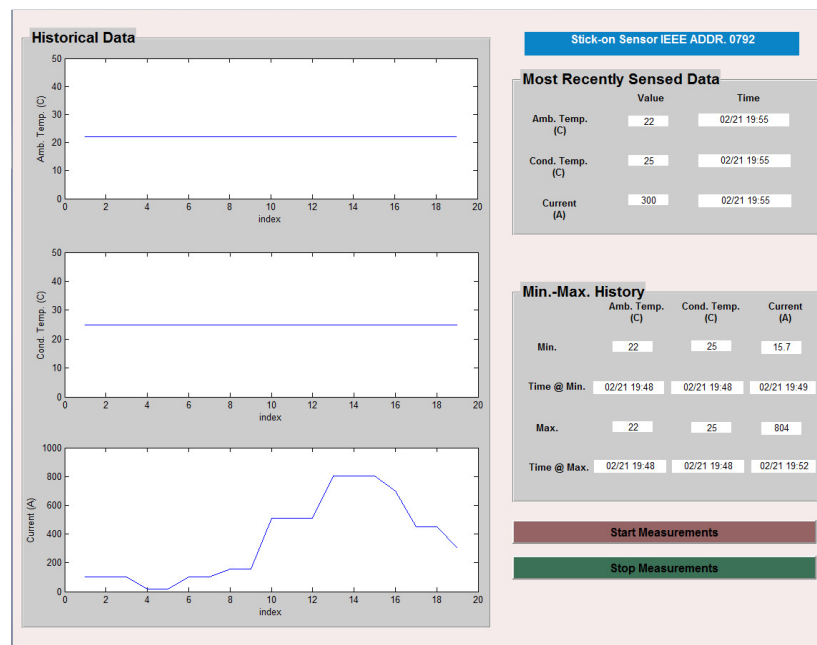


Figure 4.25: Screenshot of the GUI that shows the sensed current and temperature results

#### 4.5.1.6 Power Consumption

As discussed previously, for this application energy is limited and judicious use of the available energy is essential. The signal conditioning circuit was designed to ensure very low-power consumption. The microcontroller and transceiver were programmed using the appropriate power saving practices and utilizing low-power modes. Oscilloscope screenshots of the total power consumed by the Stick-on sensor during transmission of

data and during sleep mode is shown in Figure 4.26. A summary of power consumption of every component is shown in Table 4.11.

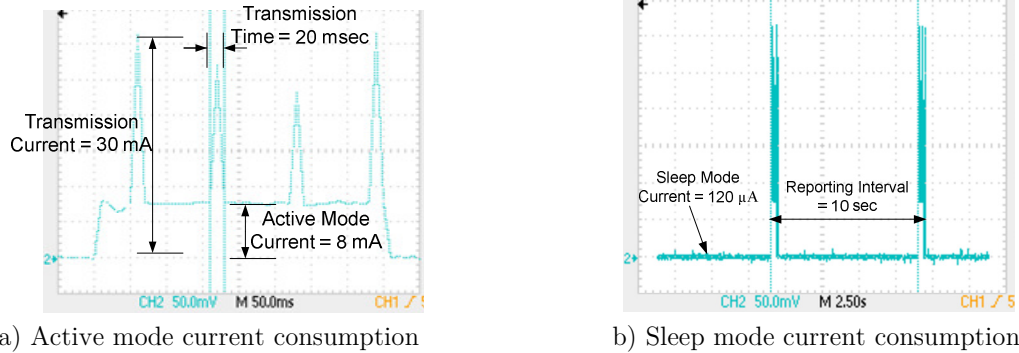


Figure 4.26: Screenshot of current consumption during active and sleep mode

Table 4.11: Power Consumption for Individual Components

| Device / Circuit                                    | Mode      | Current Consumption | Power Consumption |
|---|-----------|---------------------|-------------------|
| MCU and ZigBee® Transceiver                         | Active    | 8 mA                | 26.4 mW           |
|   | Transmit  | 30 mA (max)         | 99 mW             |
|   | Sleep     | < 10 µA             | 33 µW             |
| Signal conditioning circuit for current measurement | Quiescent | 50 µA               | 165 µW            |
| Temperature sensors                                 | Quiescent | 60 µA               | 198 µW            |

#### 4.5.1.7 Minimum Reporting Time

Another test was performed to investigate the maximum reporting frequency and the minimum current level at which the sensor can remain self powered. The results are shown in Table 4.12. It can be seen from the table that at 100 Amps, the sensor node can be operated with a frequency as high as once every minute. This monitoring frequency is sufficiently high for most utility assets.

Table 4.12: Maximum Reporting Frequency of the Stick-on Sensor

| Conductor Current (A) | Time (sec)         |
|-----------------------|--------------------|
| 100                   | 61 ( nearly 1 min) |
| 200                   | 8.4                |
| 300                   | 4.3                |
| 400                   | 2.9                |

#### 4.5.1.8 Operation in an Outage

During a power outage, the ultracapacitor enables the Stick – on sensor to operate for some additional time. If a duty cycle of 10 minutes is assumed. Then, the energy required by the sensor in quiescent mode and active mode is given by,

$$\text{Quiescent mode} = 120 \mu\text{A} \times 3.3 \text{ V} \times 600 \text{ sec} \approx 240 \text{ mJ}$$

$$\text{Active mode} = 40 \text{ mW} \times 400 \text{ msec} = 16 \text{ mJ}$$

CC2530 (MCU and transceiver) has the ability to operate over a wide voltage range 2 V – 3.3 V. Energy that can be stored in the ultracapacitor within the given voltage range is given by

$$E = 0.5C(V_i^2 - V_f^2) = 0.5 \times (3.3^2 - 2^2) = 3.445J$$

Total number of reports that can be sent with an ultracapacitor charged to 3.3 V in the event of a power outage,

$$3.445J/256mJ \approx 13 \text{ cycles}$$

Therefore, even in the event of a power outage the Stick-on sensor has the capability to provide at least 13 more reports, enough to inform the coordinator about the power outage status of the asset. However, if power does not resume, the sensor will stop functioning after 13 data transmissions. In such a situation, the presence of a solar cell can help the sensor operate even in an outage.

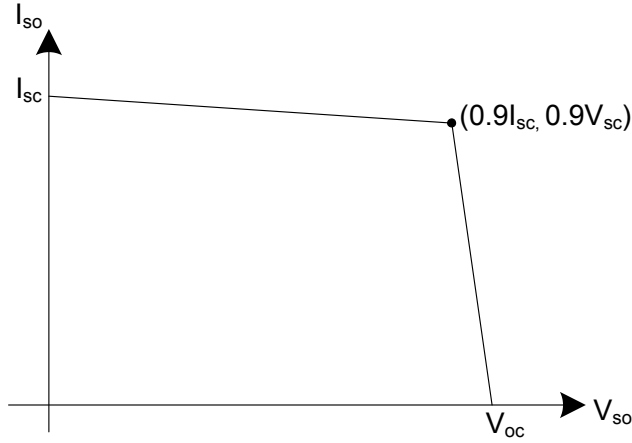
#### 4.5.1.9 Operation with Solar Energy Harvesting

The goal is to compute the time taken to fully charge the capacitor after an outage (or in normal operation) when a solar cell is used by the sensor. This requires solving the capacitor differential equation given by (65) This equation contains the current provided by the solar cell given by (55). However, a closed form solution of  $I_{s0}$  cannot be found which makes it very difficult to find a closed form solution of (65). Therefore, for computing the time it is fairly accurate to assume the characteristic curve of the solar cell to be as shown in Figure 4.27. To keep the fill factor constant at 0.81 (see Table 4.6) the

characteristic curve can be approximated with two linear curves such that the maximum power point is obtained at 90% of  $I_{sc}$  and 90% of  $V_{oc}$ .

$$C \frac{dV_c}{dt} = \begin{cases} I_{so}(V_c) - I_L, & \text{Active mode} \\ I_{so}(V_c) - I_Q, & \text{Sleep mode} \end{cases} \quad (65)$$

$I_{so}(V_c)$  represents the linearized characteristic of the solar cell,  $I_L$  and  $I_Q$  are the load and quiescent current demanded by the power circuit.



**Figure 4.27: Linear approximation for the solar cell V-I characteristic**

Using Figure 4.27, in an outage condition, the charging equation can be replaced by

$$I_{so}(V_C) = \begin{cases} -\frac{1}{9} \frac{I_{sc}}{V_{oc}} V_{so} + I_{sc} , & 0 < V_{so} < 0.9V_{oc} \\ -9 \frac{I_{sc}}{V_{oc}} V_{so} + 9I_{sc} , & 0.9V_{oc} < V_{so} < V_{oc} \end{cases} \quad (66)$$

Further,  $V_{so}$  can be written as,

$$V_{so} = \frac{V_c + V_{D4}}{N}$$

where  $N$  is the number of cells connected in parallel which in this case is eight.

Consider that the ultracapacitor is completely charged ( $V_c$  is 3.3V) when an outage occurs. During the active mode, based on the discharge equation (66), the voltage of the ultracapacitor will reduce. After the active mode, the sensor goes into sleep mode and



charging of the ultracapacitor begins. The time taken to charge the ultracapacitor back to 3.3 V will determine the time when another packet of data can be sent by the sensor. This would also be the minimum operating time between any two sensor operations. This minimum charge time can be computed and is given by  $T_c$  in

$$T_c = \frac{C}{M} \ln \left( \frac{(K_2 - K_1)/M + (K_1/M + 3.3)e^{-0.4M/C}}{K_2/M - 3.3} \right) \quad (67)$$

where

$$K_1 = I_{sc} (1 - V_{DA}/(9NV_{oc})) - I_L,$$

$$K_2 = K_1 + I_L - I_Q,$$

$$M = I_{sc}/(9NV_{oc}).$$

Another scenario that should also be considered is the time taken to start the sensor from a zero charge state (black-start). In this particular case, the ultracapacitor is required to be charged from 0 V to 2 V (2 V is sufficient for powering all the analog circuitry and microcontroller). Figure 4.28 shows a plot of the minimum charge time of the ultracapacitor and the black-start time.

It can be seen from Figure 4.28 that even at a low insolation level, 100 W/m<sup>2</sup> in the case of a cloudy day, the minimum charge time is close to 100 sec (~2 min). In other words, in the presence of a solar cell, in an outage, the sensor can be operated every 2 min, sufficient for most utility assets.

Further, the time taken to start the sensor from a completely discharged state ranges from 14 min in high insolation levels (at 1000 W/m<sup>2</sup>) to 45 min in average insolation levels (at 500 W/m<sup>2</sup>), again suitable for most applications. Furthermore, in normal operation, the rate of operation of the sensor is increased even further due to the presence of an additional current from the source side. This analysis clearly shows that with the addition of an inexpensive solar cell which trickle charges the ultracapacitor, a utility sensor becomes even more attractive.

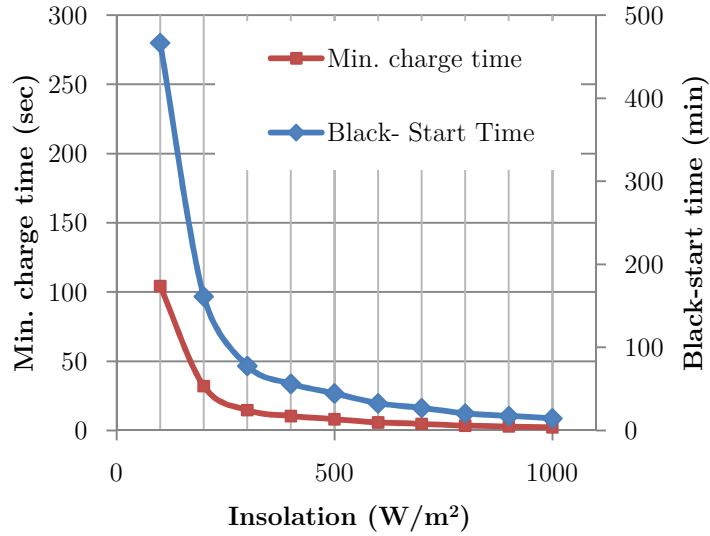


Figure 4.28: Ultracapacitor recharge time in an outage using a solar cell

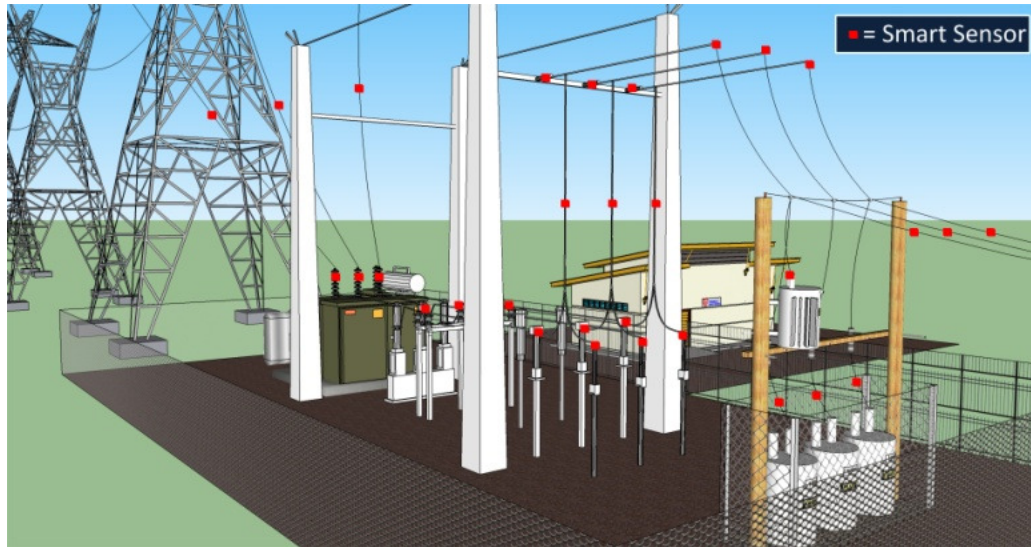
#### 4.6 NETWORK INTEGRATION

The cost of the Stick-on sensor based on single quantity prices was estimated to be around \$ 50, much lower than presently available utility asset monitoring sensors. The bill of materials of the developed sensor is given in Appendix B. The additional advantage of these sensors is that they can be used in large numbers in the form a meshed networked system.

Consider a smart substation comprising bus-bars, disconnect switches, cables, shunt-capacitors and transformers. Moreover, consider that there are distribution lines and transmission lines going out/coming into the substation. Further, suppose that to monitor all the assets, 150 Stick-on sensors are required in the substation, as shown in Figure 4.29.

The status of all these assets can be directly given to operators or the control room through these intelligent sensors that are flexible enough to be either stuck on or placed in the vicinity of the asset and begin autonomous monitoring. Each sensor module operates as a communication node, and exchanges information through formation of smaller networks between adjacent working sensor nodes. This type of an ad-hoc network also helps in reducing the power budget of the individual sensors as the distance of data

transmission is considerably reduced as compared to a direct collector link communication network.



**Figure 4.29: Conceptual smart substation with smart Stick-on sensors**

In this scenario, suppose ZigBee<sup>®</sup> communication protocol is used by the network. ZigBee<sup>®</sup> is a reliable, low-power and low-cost, open standard for Wireless personal area networks (WPAN) developed by the ZigBee<sup>®</sup> alliance. It has found applications in home energy management, automated metering, habitat monitoring, etc. It is built on top of IEEE 802.15.4 media access (MAC) and physical (PHY) layers, and utilizes 2.4 GHz (250 kbps), 915 MHz (40 kbps) and 868 MHz (20 kbps) radio bands [108]. One of the most advantageous features of ZigBee<sup>®</sup> is its self-configuring, multi-hop, and self-healing network nature. To enable these features, the network consists of three different types of networking devices, namely, coordinator node, router, and end device. In this scenario, the Stick-on sensors act as the end devices.

The end devices can be pre-programmed to transmit data at regular intervals. Under normal operation, the sensor remains in the sleep mode for most of the time. During the active mode, the sensor wakes up, performs default assessment routines, sensing operations, sensed information processing, and transmission of the processed information to

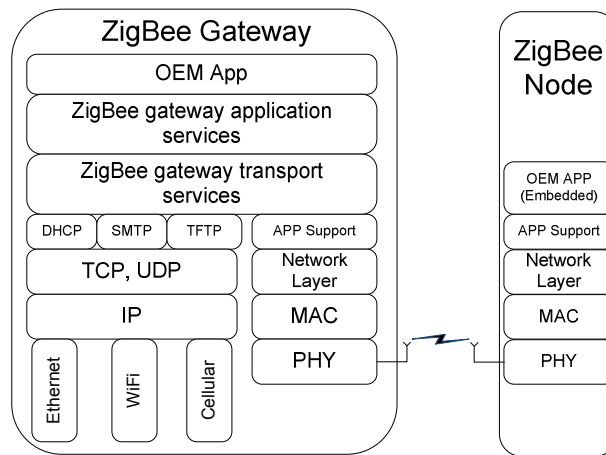


gives a total of 15 routers to support the sensor network operation. The router can communicate directly to the coordinator or direct the signal via other routers to the coordinator depending on which option provides the shortest path.

Finally, a master node serves as the ZigBee® coordinator (data-collector). The coordinator receives data from all the end devices through an indirect or a direct link. The ZigBee® coordinator can be connected directly to Supervisory control and data acquisition (SCADA) system or to Internet protocol (IP) devices through a ZigBee® gateway device (ZGD) or a ZigBee® bridge (or expansion) device (ZED). On the one hand, the gateway acts as a mediator between the ZigBee® network and the IP device through an abstraction interface. On the other hand, a ZED extends a ZigBee® network over the IP network. Although, there are certain fundamental differences between the two approaches, they have their own pros and cons [110]. The stack diagram of ZigBee® gateway as outlined by the ZigBee® alliance is given in Figure 4.31. A link between the ZigBee® network with the IP devices through a gateway (or a bridge) allows interoperability of the wireless sensor network with other standards. Furthermore, it allows direct binding with the SCADA system which has tremendous value for utility. ZGD are already available in the commercial domain and are used to interface to existing utility SCADA systems [111]. In this scenario, the coordinator has a direct link with the gateway. This way, all the intelligent information collected by the coordinator is directly sent to the SCADA system over the internet. If it is not essential to connect the coordinator to SCADA, the collected information may be kept local to the substation.

Finally, one of the major requirements identified by DOE as a part of the Smart Grid initiative is having interoperability between different devices (and protocols) and ensuring cyber security of the disparate networks [8], [112]. As the future smart grid will have different types of sensors, intelligent electronic devices and communication protocols, it will become necessary to develop standards which allow for the sensors under different local networks to communicate with each other. Presently, different parts of the utility network are associated with different communication requirements and hence have

different types of communication links. For instance, a DNP 3.0 is commonly used for integration of IEDs within the substation, cellular communication protocols like CDMA, GSM, GPRS, etc., are used for transmission lines sensors, etc. Moreover, for substation automation, the common standard followed is based on the IEC 61850. However, as the complexity of the system increases, a strong need for a single standard is felt, which shall in streamlining the integration of sensor information from disparate sources into utility operations and asset management database.



**Figure 4.31: Stack diagram of ZigBee<sup>®</sup> gateway device [110]**

As wireless communication becomes ubiquitous in the utility domain, maintaining the security of the grid information will become crucial. Therefore, impacts of cyber attacks in the form of intrusion into the data systems, malwares, hacking, etc., need to be investigated. Further, standards and guidelines have to be developed for managing and mitigating these risks.

With security and reliability in mind, it is worth emphasizing that the ZigBee<sup>®</sup> protocol has the advantage of being self-organizing and self-healing in nature. If a particular router or an end device (or devices) fails, the signal is re-routed through another efficient path which minimizes latency time, and further improves reliability of the overall

network. In addition, increased research on security and encryption techniques for ZigBee® can make it a preferred solution for meshed utility asset monitoring.

The initiatives pertaining to interoperability and cyber security will ensure that the future networks are highly resistant to attacks, have a resilient nature, are self healing and maintain the highest levels of reliability of the system. Therefore, a wireless sensor network solution that uses the low-cost Stick-on sensors developed in this research has high value for utilities.

#### **4.7 CONCLUSIONS**

To summarize, in this chapter, a novel power circuit was developed to boost the voltages developed at the energy harvester terminals from as low as 0.2 V to stable 3.3 V. The power circuit starts up autonomously and operates completely on the magnetic field harvested. It contains ultra-capacitors to operate for some time during an outage. Further, a solar cell was included as a secondary energy source in the power management circuit. The developed power circuit was fabricated and integrated with a stick-on current and temperature wireless sensor. The detail design of signal conditioning circuits for current and temperature sensing was also presented. The entire module was tested on an ACSR conductor in the lab at currents up to 1000 A. The sensor was able to autonomously start up at currents as low as 60 A, and transmit sensed signals over ZigBee®. The signals were received by a coordinator that was connected to a laptop to display the sensed results.

Finally, the chapter was concluded with an approach to integrate the Stick-on sensors into a wireless network to monitor assets in a substation. All the necessary machinery required for achieving such a network were discussed and presented.

## CHAPTER 5

# MULTI-CORE TRIANGULATION METHOD FOR CURRENT SENSING

### 5.1 INTRODUCTION

In Chapter 3, it was shown that the OCV and the SCC of the flux concentrator are linearly proportional to the RMS value of conductor current. Further, in Section 4.5 successful current sensing results using the Stick-on sensor were presented. As the XFC does not form a closed loop around the conductor, a change in orientation and distance of the XFC can cause a change in slope of the linear characteristic. This is shown in Figure 5.1. The relationship between the OCV and conductor current is still linear and the line passes through the origin. Thus, with the knowledge of only one point, the entire line can be extrapolated. This provides a very simple method of calibrating the current sensor when used in practice.

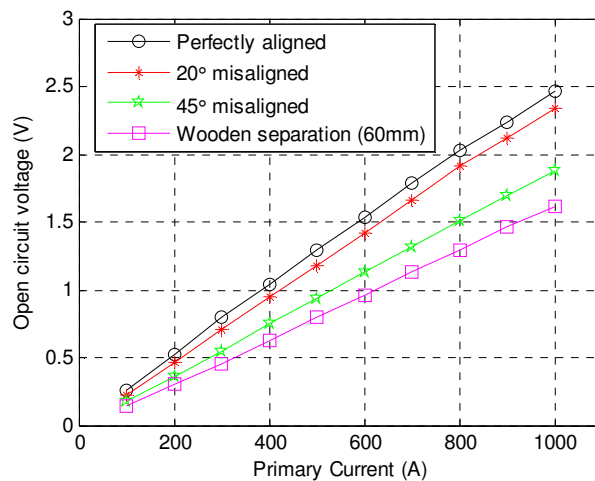


Figure 5.1: Open circuit test at different orientations and distances of the flux concentrator with respect to the conductor



Even though the sensor can be easily calibrated at the time of installation, field calibrations are expensive and increase the effective cost of the utility sensor.

Further, if it was assumed that calibration was unavoidable, the sensor would provide close to accurate measurement in the presence of a single conductor. However, consider the case when there are multiple current carrying conductors located close to the sensor. This is typically seen in a low voltage secondary network, in underground cables, cables in a conduit, three phase overhead conductors, etc. Since the structure of the XFC is open, it would be affected by the magnetic fields of the other current carrying conductors in the vicinity leading to errors in measurement. This would not affect a conventionally used closed core structure (clamp-around current sensor) that inhibits coupling of any far-off magnetic fields.

To emphasize the issue of multiple current carrying assets in the vicinity, consider a simple scenario comprising two conductors  $C_1$  and  $C_2$  lying close to each other and carrying currents  $I_1$  and  $I_2$ , respectively, as shown in Figure 5.2. In addition, consider that the sensor,  $S_1$ , is installed on  $C_1$  and is calibrated such that when  $I_2$  is zero, the sensor measures accurate values of  $I_1$  flowing through  $C_1$ . Experimental studies were performed to find the error induced in the sensor when  $I_2$  is non-zero. The results are shown in Table 5.1. It can be observed that when  $I_2$  is 900 A and  $I_1$  is zero, the sensor, instead of showing zero, measures the value of  $I_1$  as 270 A (at  $D = 100$  mm). This is due to the stray magnetic fields from  $I_2$  picked up by the sensor.

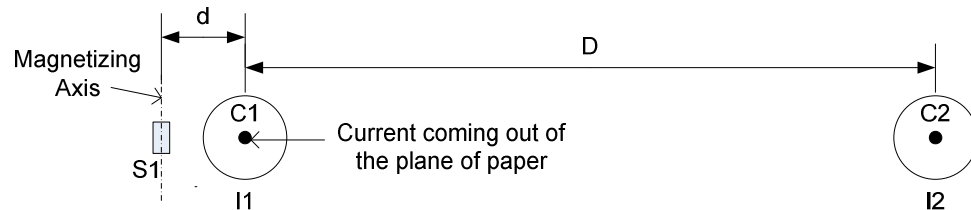


Figure 5.2: Single sensor approach- Two conductor case

**Table 5.1: Experimental Results Show High Errors in the Presence of Far Fields**

| I1 (A) | I2 (A) | Measured Current I <sub>m</sub> (A) |               |
|--------|--------|-------------------------------------|---------------|
|        |        | at D = 100 mm                       | at D = 200 mm |
| 0      | 100    | 30                                  | 15            |
| 0      | 500    | 150                                 | 75            |
| 0      | 900    | 270                                 | 135           |

Therefore, although the approach of using the XFC as an energy harvester and current sensor proposed in this research is attractive because of its small size, low-cost and low-maintenance requirements; in a real world scenario, it suffers from two fundamental issues- the need for calibration and influence from far-fields.

## 5.2 PROBLEM STATEMENT

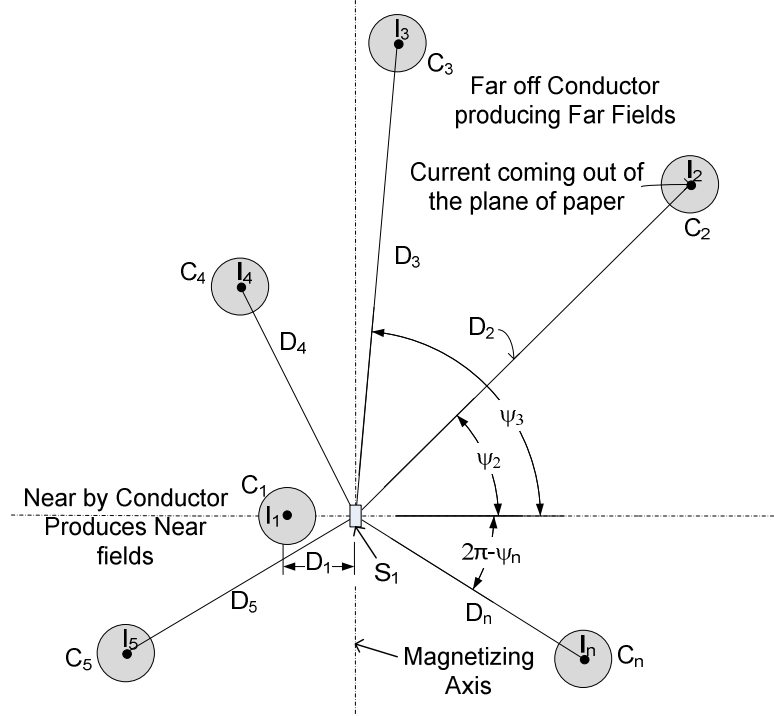
In the most general case, the problem can be thought to have a configuration shown in Figure 5.3. Where, C<sub>1</sub> is the conductor of interest which is at an unknown distance d from the sensor S<sub>1</sub>. The sensor S<sub>1</sub> is essentially an open core-coil assembly. The other n assets are located at distances D<sub>1</sub> through D<sub>n</sub> from the conductor C<sub>1</sub>. The fields induced by the other assets on the sensor S<sub>1</sub> are essentially the far-fields which are to be rejected and tend to induce errors in measurements. While, the fields induced on S<sub>1</sub> due to C<sub>1</sub> is the near field, which is of interest. In general, either the V<sub>oc</sub> or I<sub>sc</sub> is used as a proxy for measurement of current. Without loss of generality suppose, I<sub>sc</sub> is used in this case. The expression for I<sub>sc</sub>, using the superposition theorem, can be expected to contain contributions from all the assets present in the 3-D space, also shown in (68)

$$I_{sc} = I_{sc1}(D_1, \psi_1) + I_{sc2}(D_2, \psi_2) + \dots + I_{scn}(D_n, \psi_n) \quad (68)$$

It is quite clear that in this general scenario it is impossible to decouple the effects due to all the other fields and compute the value of the current flowing in C<sub>1</sub> using a single sensor. The problem can now be broken down into two distinct problems:

- Rejection of contributions from far-fields, i.e. eliminating all terms except for I<sub>sc1</sub>(D<sub>1</sub>, ψ<sub>1</sub>) in (68)

- Estimating the value of  $D_1$  autonomously by the sensor; in other words, self-calibration.



**Figure 5.3:** A general case having  $n$  current carrying conductors in the vicinity of the conductor of interest  $C_1$

These issues have not been widely researched as the proposed concept of measuring current with an open core XFC is new and has not been applied to any application in the past. Nonetheless, there has been some interesting research in the area of current sensing using magnetic search coils. Specifically, the technique developed by Promethean Devices LLC is a unique technique which uses two axis magnetic field measurements to sense the current which was highlighted in Section 2.2.5. However, this technique has the disadvantages in that it can only be used with three-phase overhead conductors. In fact, in the presence of far-fields due to other distant assets, the technique would fail. Furthermore, it requires computationally intensive algorithm for determining the current values; therefore, requires more power for operation. Moreover, the system is quite bulky, expensive and has high cost of implementation.

Some other techniques that exist in research literature that attempt to address some, if not all, of the issues identified are given in Section 2.2.6. However, even these techniques do not completely address the issue that is being dealt with in this research.

### 5.3 MATHEMATICAL MODEL OF THE CURRENT SENSOR

A rational approach to solving the problem at hand is to form a mathematical model of the system. The system in an abstract sense can be represented in the following manner,

$$\vec{I}_{sc} = f(\vec{I}, \vec{D}, \vec{\psi}, \vec{\phi}) \quad \forall \vec{I}, \vec{D}, \vec{\psi}, \vec{\phi} \in \mathbb{R}^{n \times 1}, \vec{I}_{sc} \in \mathbb{R}^{m \times 1} \quad (69)$$

where  $\vec{I}_{sc}$  is the output of the sensor and  $(\vec{I}, \vec{D}, \vec{\psi}, \vec{\phi})$  is the effect due to multiple magnetic fields of all the conductors, while  $f(\cdot)$  is an operation on  $(\vec{I}, \vec{D}, \vec{\psi}, \vec{\phi})$  that gives  $\vec{I}_{sc}$ . To obtain such a model an experiment was performed where the OCV and SCC were recorded as the XFC was moved away from the conductor at a fixed value of primary conductor current. This experiment was repeated at different primary current values. The plots from this experiment are shown in Figure 5.4 and Figure 5.5.

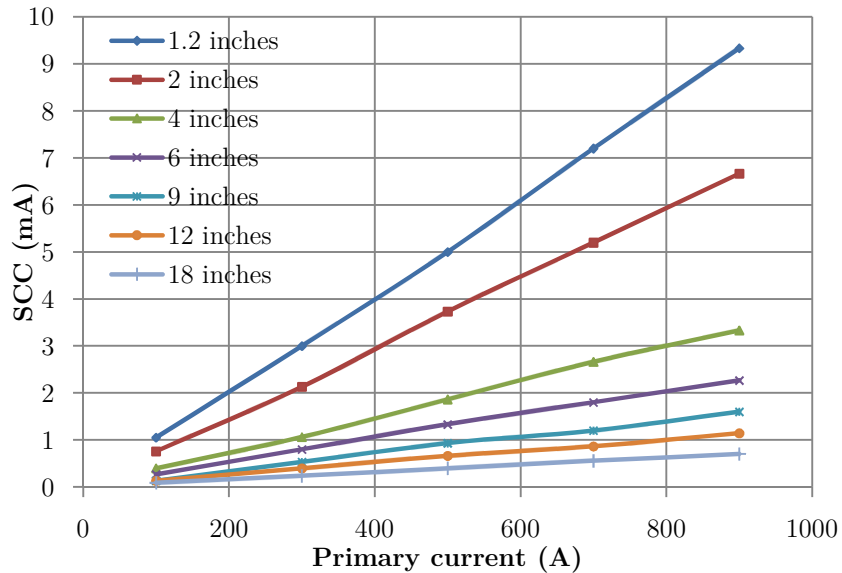
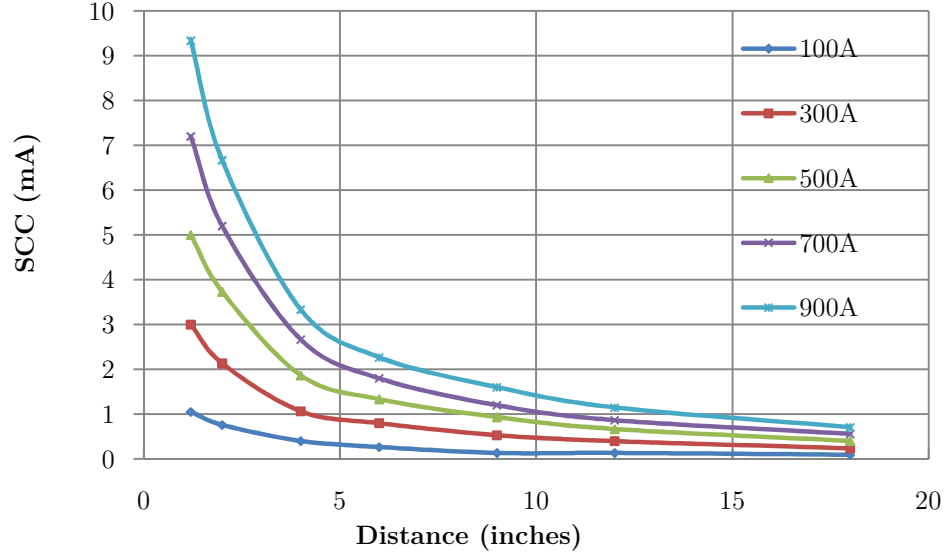


Figure 5.4: SCC vs. primary current recorded at different distances of the core from the conductor



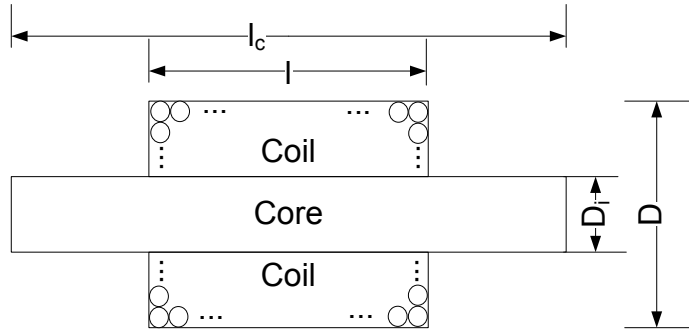
**Figure 5.5: SCC vs. distance of the core from the conductor recorded at different values of primary current**

It can be observed in Figure 5.4 and Figure 5.5 that the SCC of the current sensor is directly proportional to the current flowing in the nearby conductor and inversely proportional to the distance from it. Using nonlinear curve fitting techniques, functions for the SCC were found. In general the equations for the SCC can be modeled as shown in (70).

$$V_{oc} = \frac{\beta I_{pri}}{d^\gamma} \quad I_{sc} = \frac{\alpha I_{pri}}{d^\gamma} \quad \beta = Z\alpha \quad (70)$$

where  $Z$  is  $V_{oc}/I_{sc}$  and is fixed,  $\alpha$  is dependent on the core properties, structure, and frequency of primary current, and  $\gamma$  is a constant for all geometries and close to 1. In the case of a core with cylindrical cross section as shown in Figure 5.6, the value of  $\alpha$  is given by [14]

$$\alpha \cong 0.9 \times 10^{-5} \cdot f \cdot \frac{l^3}{D^2} \cdot D_i \cdot \frac{1}{\ln\left(\frac{2l}{D_i}\right) - 1} \quad (71)$$



**Figure 5.6: A cylindrical core coil geometry**

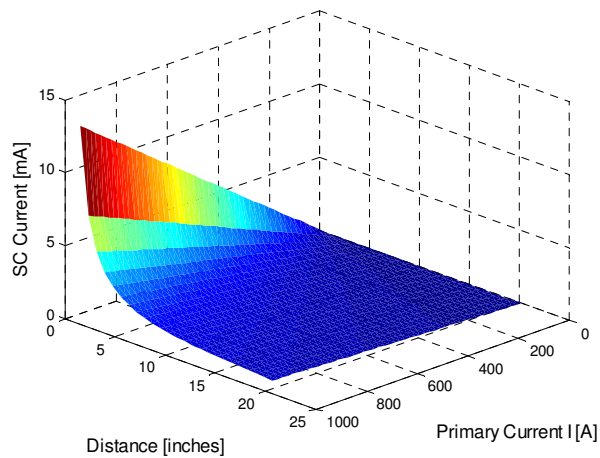
However, in the case of other complex core geometries, a closed form solution for  $\alpha$  is not possible to find. It is required to be computed from experimental results or through FEA simulations.

Incorporating the knowledge of  $\alpha$  and  $\gamma$  in (71) gives a relatively simple equation for the SCC measured by the sensor which is given as

$$I_{SC} = \frac{\alpha I_{pri}}{d} \quad (72)$$

In principle, either SCC or OCV can be used for determining the current in the nearby asset. Without any loss of generality, SCC shall be used in the analysis to follow.

Figure 5.7 shows a 3-D plot with SCC as a function of primary current and distance of the core from the conductor obtained from the model obtained in (72).



**Figure 5.7: 3-D plot of the modeled SCC as a function of primary current and distance**

### 5.3.1 Error Model in a Single Sensor Case

Using the model developed in the previous sub-section, (68) can be re-written as

$$\tilde{I}_{sc} = \frac{\alpha I_1 e^{j\phi_1}}{D_1} \cos \psi_1 + \frac{\alpha I_2 e^{j\phi_2}}{D_2} \cos \psi_2 + \dots + \frac{\alpha I_n e^{j\phi_n}}{D_n} \cos \psi_n \quad (73)$$

to incorporate the far-field contributions into the measurement results.

To get an intuition of the percentage error introduced in measurements, consider a specific scenario obtained from the geometry shown in Figure 5.8 where

$$\begin{aligned} n &= 2, \quad m = 1, \\ \vec{D} &= (D_1, D_2) \equiv (d, D + d), \\ \vec{\psi} &= (\psi_1, \psi_2) \equiv \vec{0}, \\ \vec{\phi} &= (\phi_1, \phi_2) \equiv \vec{0}. \end{aligned}$$

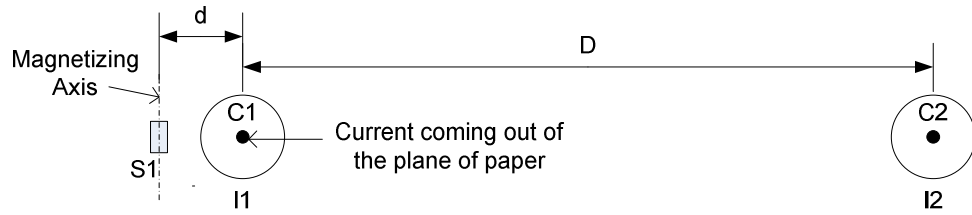


Figure 5.8: Special case of Figure 5.3 with  $n = 2$  and  $\psi = 180^\circ$

$I_{sc}$  measured by the sensor  $S_1$  is given by

$$I_s = \frac{\alpha I_1}{d} + \frac{\alpha I_2}{D + d} \quad (74)$$

If  $I_{sc}$  was used to measure the primary current  $I_1$ , then the measured current would be given by

$$\tilde{I}_1 = I_1 + I_2 \left( \frac{d}{D + d} \right) \quad (75)$$

where  $\tilde{I}_1$  is the estimated current.

Equation (75) shows that there is an inherent error in the primary current measurement given by

$$e_{\text{SingleCore}} = \begin{cases} 0 & I_2 = 0 \\ I_2 \left( \frac{d}{D+d} \right) & \text{Otherwise} \end{cases} \quad (76)$$

The above result shows that  $I_{sc}$ , which is representative of the magnetic field around the asset, would give erroneous primary current measurement because of the presence of the far magnetic field.

An observation that is made in the analysis performed above is that there is lack of system information. Only one sensor is available for decoupling the interaction between far and near magnetic fields and thus the task is not achievable. Therefore, the dimension (value of  $m$ ) of the output needs to be increased to extract more information from the system.

#### 5.4 DUAL-CORE TRIANGULATION METHOD

If two sensors were considered to be spaced at a known distance  $x$  from each other, due to the presence of two cores some additional information can be extracted to reduce the error in measurement. Note that  $d$  and  $x$  are much smaller than  $D$ . Consider the geometry shown in Figure 5.9, where  $S_2$  is the second sensor core at a distance  $x$  from  $S_1$ . The parameters of the governing equations are given by

$$\begin{aligned} n &= 2, \quad m = 2, \\ \vec{D}_1 &= (D_{11}, D_{12}) \equiv (d, D+d), \\ \vec{D}_2 &= (D_{21}, D_{22}) \equiv (d+x, D+d+x), \\ \vec{\psi} &= (\psi_{11}, \psi_{21}, \psi_{21}, \psi_{22}) \equiv \vec{0}, \\ \vec{\phi} &= (\phi_1, \phi_2) \equiv \vec{0}. \end{aligned}$$

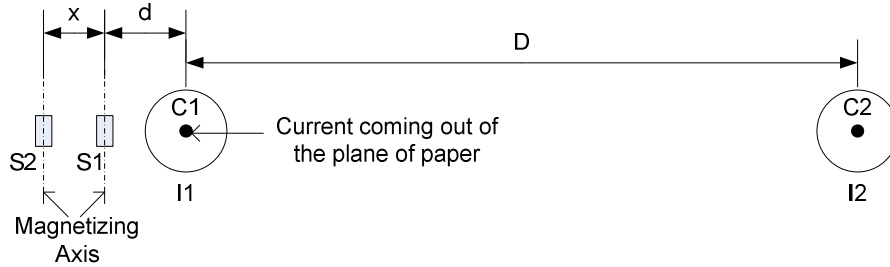


Figure 5.9: Same system as in Figure 5.8 but with two sensor cores



The SCC induced in the two sensor cores,  $I_{s1}$  and  $I_{s2}$ , is given by

$$I_{s1} = \frac{\alpha I_1}{d} + \frac{\alpha I_2}{D+d} \quad (77)$$

$$I_{s2} = \frac{\alpha I_1}{d+x} + \frac{\alpha I_2}{D+x+d} \quad (78)$$

Subtracting (78) from (77), and using the assumption that  $D$  is very large as compared to  $x$  and  $d$ ,  $I_1$  is obtained as

$$I_1 = \frac{(I_{s1} - I_{s2})d(d+x)}{\alpha x} \quad (79)$$

Due to the assumption in the calculation of  $I_1$ , there is still an error in measurement given by

$$e = \begin{cases} 0 & , I_2 = 0 \\ I_2 \left( \frac{d(x+d)}{(D-d)(D-(x+d))} \right) & , \text{Otherwise} \end{cases} \quad (80)$$

A plot showing the measurement errors using the two approaches for different values of  $I_2$  and  $D$  is shown in Figure 5.10. It can be seen that the error when two cores are used is always less than the error when only a single core is used. Moreover, as the distance between  $C_1$  and  $C_2$  increases, the error decreases. This decrease is faster in the case of two cores due to the presence of a quadratic ( $D^2$ ) term in the denominator.

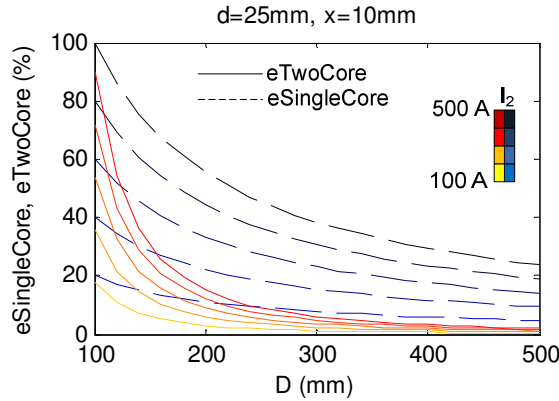


Figure 5.10: Errors in current measurement using the single core and two core methods. Note that  $I_1$  is constant at 100 A.

### 5.4.1 Preliminary Proof-of-Concept Experiment

A preliminary experiment was performed to test the concept of using two sensor cores for measuring current in a utility asset. The test configuration is shown in Figure 5.11 and the experimental results are shown in Table 5.2. Two cases were tested.  $I_2$  is zero in the first case when there are no far fields.  $I_2$  is non-zero and  $I_1$  is zero in the second case to represent the extreme case when there is no current in the conductor being monitored and high current in the conductor in the vicinity.

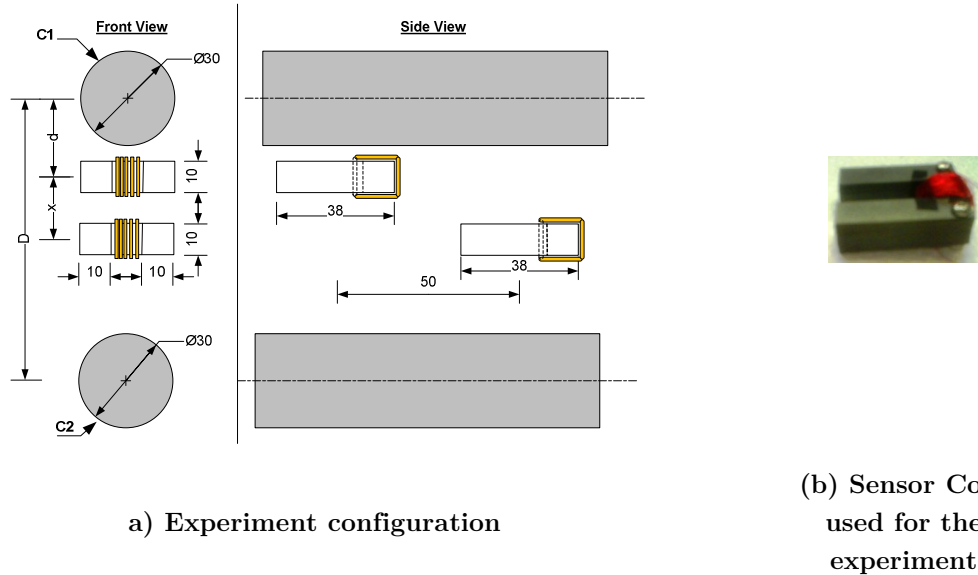


Figure 5.11: Preliminary experiment validating the two core approach with specification Specifications:  $D = 267$  mm,  $d = 27.5$  mm,  $x = 20$  mm, Core thickness = 10 mm, Wire = 30 AWG, 100 turns

Table 5.2: Preliminary Results of the Dual Core Approach

| $I_1$<br>(A) | $I_2$ (A) | $I_{sc1}$<br>(mA) | $I_{sc2}$<br>(mA) | Single<br>Core<br>(A) | Error<br>(Single<br>Core)<br>(%) | Two<br>Core<br>(A) | Error (Two<br>Core) (%) |
|--------------|-----------|-------------------|-------------------|-----------------------|----------------------------------|--------------------|-------------------------|
| 100          | 0         | 6.85              | 3.92              | 99                    | 1                                | 101                | 1                       |
| 500          | 0         | 34.3              | 19.6              | 496                   | 0.8                              | 505                | 1                       |
| 0            | 500       | 4.04              | 4.24              | 61                    | -                                | 7                  | -                       |
| 0            | 900       | 9.01              | 9.34              | 135                   | -                                | 11                 | -                       |

Table 5.2 shows that even in the presence of zero current in  $C_1$ , the single core approach showed 61 A and 135 A when the current in  $C_2$  was 500 A and 900 A respectively. However, the two core approach showed only 7A and 11A which is small and very close to the actual value. This experimental result validates the theoretical concept developed above.

## 5.5 MULTI-CORE TRIANGULATION METHOD

### 5.5.1 Use of Three Core-Coil Assemblies

Although, using two cores instead of one reduces the error in current measurement, it still does not eliminate the error. Extending the concept of dual-core triangulation method (DCTM) further to include one more sensor core can help in introducing an additional level of insight into the system. In fact, it is found that for the system parameters given by

$$\begin{aligned}
 n &= 2, \quad m = 3, \\
 \vec{D}_1 &= (D_{11}, D_{12}) \equiv (d, D + d), \\
 \vec{D}_2 &= (D_{21}, D_{22}) \equiv (d + x, D + d + x), \\
 \vec{D}_3 &= (D_{31}, D_{32}) \equiv (d + 2x, D + d + 2x), \\
 \vec{\psi} &= (\psi_{11}, \psi_{12}, \psi_{21}, \psi_{22}, \psi_{31}, \psi_{32}) \equiv \vec{0}, \\
 \vec{\phi} &= (\phi_1, \phi_2) \equiv \vec{0},
 \end{aligned}$$

the error can be reduced to zero. The system configuration is shown in Figure 5.12.

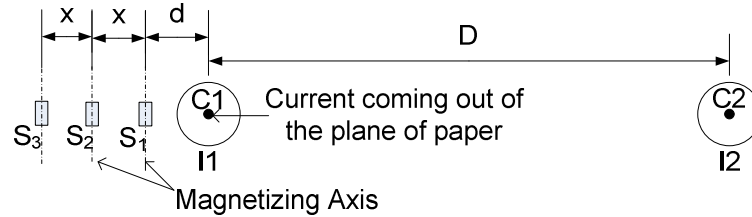


Figure 5.12: Same system as in Figure 5.8 but with three sensor cores

The closed form solution for the estimated current is given by

$$I_1 = \frac{d}{\alpha} \left( I_{s1} - \frac{A(D + (x + d))(x + d)}{Dx} \right) \quad (81)$$

where

$$D = \sqrt{2A}(d + x) + \sqrt{B}(d + 2x) \quad (82)$$

$$A = I_{s2} - \frac{d}{x + d} I_{s1}, \quad B = I_{s3} - \frac{d}{d + 2x} I_{s1} \quad (83)$$

The approach developed above of using three sensor cores is a novel and an elegant way of solving the problem of multiple adjacent conductors. However, this approach requires the knowledge of  $d$  for calculating  $I_1$ . This implies that, although, the above method is able to reject the effects of far-fields, a field calibration is still necessary for proper operation of such a sensor. Moreover, the system considered in the above analysis is highly symmetric comprising only two well aligned conductors, and the method works only when the two currents are in the same phase.

### 5.5.2 Use of Six Core-coil Assemblies

A logically extension to the concept of multi-core triangulation method (MCTM) to solve a general scenario requires increasing the dimensionality of the output, i.e. the value of  $m$ . As there are six unknowns,  $I_1$ ,  $I_2$ ,  $D$ ,  $d$ ,  $\psi$  and  $\phi$ , it is rational for  $m$  to be at least six. Consequently, at-least six cores are required in the system to be able to solve for a closed form solution of  $I_1$ .

Furthermore, the cores need to be positioned in a specific manner relative to the conductor of interest to extract complete information of the system using the sensed short circuit currents. The proposed arrangement of the cores is shown in Figure 5.13(a). The cores are arranged as couples in space, in such a fashion that the magnetic axis of one core is completely aligned with the near conductor, while, the magnetic axis of the other core is completely misaligned ( $90^\circ$  space apart). Further, the core-couples  $S_{iy}$  and  $S_{ix}$  are placed equidistant from the near conductor. All the three core-couples,  $S_{1x}$ ,  $S_{1y}$ ,  $S_{2x}$ ,  $S_{2y}$ ,  $S_{3x}$  and  $S_{3y}$

are arranged next to a conductor as shown in Figure 5.13(b). For simplicity of notation,  $S_{1x}$ ,  $S_{1y}$ ,  $S_{2x}$ ,  $S_{2y}$ ,  $S_{3x}$  and  $S_{3y}$  are denoted as  $S_1$ ,  $S_2$ ,  $S_3$ ,  $S_4$ ,  $S_5$  and  $S_6$ .

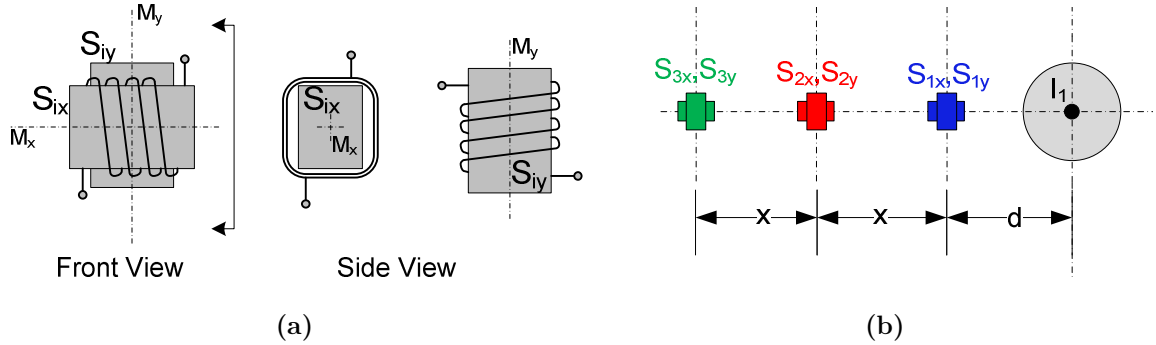


Figure 5.13: Same system as in Figure 5.8 but with three sensor cores

Suppose a far-field producing conductor  $C_2$  is present in the space at an angle  $\psi$  with respect to the near-field conductor  $C_1$ , as shown in Figure 5.14(a). The vector field interactions due to both  $C_1$  and  $C_2$  will induce short circuit current in all the six cores, as shown in Figure 5.14(b). Note that  $B_{Ni}$  and  $B_{Fi}$  represent near and far-fields respectively, interacting with the  $i^{\text{th}}$  core-coil assembly.

To analyze the general scenario, the analysis is broken down into several cases to attain insight into the solution of the governing equations. These cases are discussed in the sections to follow.

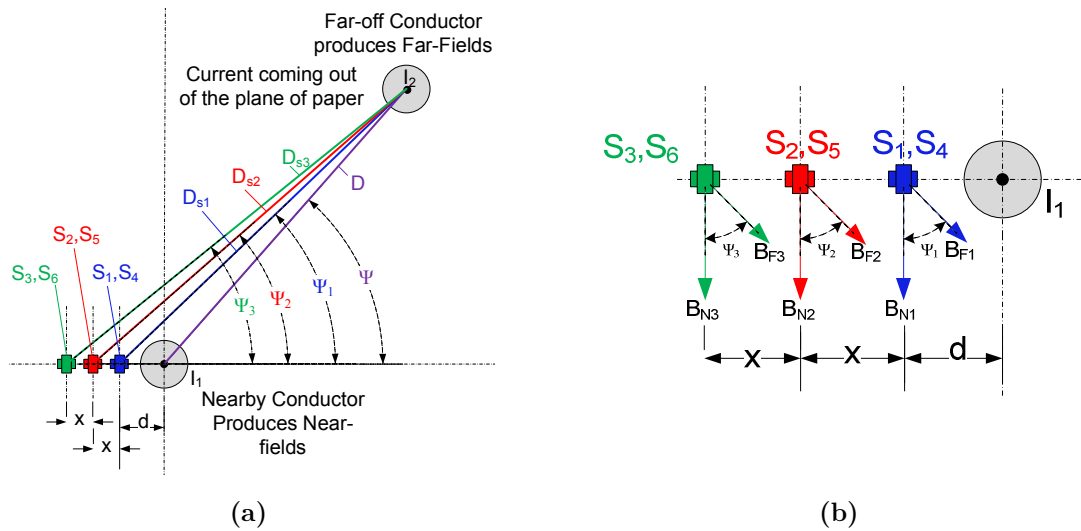


Figure 5.14: Same system as in Figure 5.8 but with three sensor cores

5.5.2.1 MCTM Case 1:  $\psi = 0, \phi = 0$

Consider a case where  $\psi$  and  $\phi$  are zero. This takes the discussion back to the spatially aligned conductors having no phase difference. The short circuit current induced in the six core-coil assemblies is given by

$$I_{s1} = \frac{\alpha I_1}{d} + \frac{\alpha I_2}{D+d} \quad (84)$$

$$I_{s2} = \frac{\alpha I_1}{d+x} + \frac{\alpha I_2}{D+d+x} \quad (85)$$

$$I_{s3} = \frac{\alpha I_1}{d+2x} + \frac{\alpha I_2}{D+d+2x} \quad (86)$$

$$I_{s4} = I_{s5} = I_{s6} = 0 \quad (87)$$

In a realistic scenario D can be a 50 - 100 times greater than d or x. Therefore, given that

$$D \gg d, x$$

, a difference between (84) and (85) gives

$$I_{s12} = I_{s1} - I_{s2} = \alpha I_1 \left( \frac{x}{d(d+x)} \right) \quad (88)$$

Similarly, a difference between (85) and (86) gives

$$I_{s23} = I_{s2} - I_{s3} = \alpha I_1 \left( \frac{x}{(d+x)(d+2x)} \right) \quad (89)$$

Dividing (88) by (89) and solving for d gives

$$d^* = \frac{2xI_{s23}}{I_{s12} - I_{s23}} \quad (90)$$

Plugging the estimate of d, i.e.  $d^*$  into (88) gives the value of  $I_1$  as

$$I_1^* = \frac{I_{s12}d^*(d^*+x)}{\alpha x} \quad (91)$$

$I_{s4}$ ,  $I_{s5}$  and  $I_{s6}$  do not give any information other than the fact that the far-off conductor is at  $\psi = 0$ . Therefore, the values of  $I_2$  and  $D$  are not possible to be found in this case.

### 5.5.2.2 MCTM Case 2: $\psi = \pi$ , $\phi = 0$

The short circuit currents induced in the six core-coil assemblies are given by

$$I_{s1} = \frac{\alpha I_1}{d} - \frac{\alpha I_2}{D-d} \quad (92)$$

$$I_{s2} = \frac{\alpha I_1}{d+x} - \frac{\alpha I_2}{D-d-x} \quad (93)$$

$$I_{s3} = \frac{\alpha I_1}{d+2x} - \frac{\alpha I_2}{D-d-2x} \quad (94)$$

$$I_{s4} = I_{s5} = I_{s6} = 0 \quad (95)$$

As in MCTM Case 1, it is possible to solve for  $d^*$  and  $I_1^*$ , however, the values of  $D$  and  $I_2$  cannot be found.

### 5.5.2.3 MCTM Case 3: $\psi = \pi/2$ , $\phi = 0$

The short circuit currents induced in the six core-coil assemblies are given by

$$I_{s1} = \frac{\alpha I_1}{d} + \frac{\alpha I_2 d}{D^2 + d^2} \quad (96)$$

$$I_{s2} = \frac{\alpha I_1}{d+x} + \frac{\alpha I_2 (d+x)}{D^2 + (d+x)^2} \quad (97)$$

$$I_{s3} = \frac{\alpha I_1}{d+2x} + \frac{\alpha I_2 (d+2x)}{D^2 + (d+2x)^2} \quad (98)$$

$$I_{s4} = \frac{\alpha I_2 D}{D^2 + d^2} \quad (99)$$

$$I_{s5} = \frac{\alpha I_2 D}{D^2 + (d+x)^2} \quad (100)$$

$$I_{s6} = \frac{\alpha I_2 D}{D^2 + (d + 2x)^2} \quad (101)$$

Dividing (100) by (99), and (101) by (99) gives (102) and (103) respectively:

$$\frac{I_{s5}}{I_{s4}} = k_1 = \frac{D^2 + d^2}{D^2 + (d + x)^2} \quad (102)$$

$$\frac{I_{s6}}{I_{s4}} = k_2 = \frac{D^2 + d^2}{D^2 + (d + 2x)^2} \quad (103)$$

Solving (102) and (103) for d gives

$$d^* = x \frac{(3k_1 k_2 + k_1 - 4k_2)}{(4k_2 - 2k_1 - 2k_1 k_2)} \quad (104)$$

Plugging the value of d\* in (102) the value of D is found as

$$D^* = \sqrt{\frac{d^{*2} - k_1 (d^* + x)^2}{k_1 - 1}} \quad (105)$$

Using d\* and D\*, the value of I<sub>2</sub> is found as

$$I_2^* = \frac{I_{s4} (D^{*2} + d^{*2})}{\alpha D^*} \quad (106)$$

Subsequently, the value of I<sub>1</sub> can be found from (96) as

$$I_1^* = \frac{d^*}{\alpha} \left[ I_{s1} - \frac{\alpha I_2^* d^*}{D^{*2} + d^{*2}} \right] \quad (107)$$

#### 5.5.2.4 MCTM Case 4: $\psi \in [0, 2\pi]$ , $\phi = 0$

The short circuit currents induced in the six core-coil assemblies are given by

$$I_{s1} = \frac{\alpha I_1}{d} + \frac{\alpha I_2 (D \cos \psi + d)}{D^2 + d^2 + 2dD \cos \psi} \quad (108)$$

$$I_{s2} = \frac{\alpha I_1}{d + x} + \frac{\alpha I_2 (D \cos \psi + d + x)}{D^2 + (d + x)^2 + 2(d + x)D \cos \psi} \quad (109)$$



$$I_{s3} = \frac{\alpha I_1}{d+2x} + \frac{\alpha I_2 (D \cos \psi + d + 2x)}{D^2 + (d+2x)^2 + 2(d+2x)D \cos \psi} \quad (110)$$

$$I_{s4} = \frac{\alpha I_2 D \sin \psi}{D^2 + d^2 + 2dD \cos \psi} \quad (111)$$

$$I_{s5} = \frac{\alpha I_2 D \sin \psi}{D^2 + (d+x)^2 + 2(d+x)D \cos \psi} \quad (112)$$

$$I_{s6} = \frac{\alpha I_2 D \sin \psi}{D^2 + (d+2x)^2 + 2(d+2x)D \cos \psi} \quad (113)$$

$I_1$  and  $d$  can be computed as in Cases 1 and 2 as

$$d^* = \frac{2xI_{s23}}{I_{s12} - I_{s23}} \quad (114)$$

$$I_1^* = \frac{I_{s12}d^*(d^* + x)}{\alpha x} \quad (115)$$

To compute the values of  $I_2$ ,  $D$  and  $\psi$ , the approach given in Case 3 can be followed.

Define constants,  $k_1$  and  $k_2$ , such that

$$k_1 = \frac{I_{s5}}{I_{s4}} = \frac{D^2 + d^2 + 2dD \cos \psi}{D^2 + (d+x)^2 + 2(d+x)dD \cos \psi} \quad (116)$$

$$k_2 = \frac{I_{s6}}{I_{s4}} = \frac{D^2 + d^2 + 2dD \cos \psi}{D^2 + (d+2x)^2 + 2(d+2x)D \cos \psi} \quad (117)$$

Equations (116) and (117) can be solved to compute the value of  $\cos(\psi)$  as

$$\cos \psi = \frac{(1 - k_1)D^2 + p_1}{D^2 [p_3 - p_5]} \quad (118)$$

where

$$p_1 = d^{*2} - k_1 (d^* + x)^2$$

$$p_3 = 2k_1 (d^* + x)$$

$$p_5 = 2d^*$$

Plugging the value of  $\cos(\psi)$  back into (116) and (117) gives the value of  $D^*$  as

$$D^* = \sqrt{\frac{p_1 \frac{(p_5 - p_4)}{(p_3 - p_5)} - p_2}{k_2 - 1 + \frac{(1 - k_1)(p_4 - p_5)}{(p_3 - p_5)}}} \quad (119)$$

where

$$p_2 = k_2 (d^* + 2x)^2 - d^{*2}$$

$$p_4 = 2(d^* + 2x)k_2$$

The estimated value of  $\psi^*$  is given by

$$\psi^* = \cos^{-1} \left( \frac{(1 - k_1)D^{*2} + p_1}{D^{*2}[p_3 - p_5]} \right) \quad (120)$$

Finally, the value of  $I_2^*$  is given by

$$I_2^* = I_{s4} \frac{(D^{*2} + d^{*2} + 2d^*D^* \cos \psi^*)}{\alpha D^* \sin \psi^*} \quad (121)$$

#### 5.5.2.5 MCTM Case 5: $\psi \in [0, 2\pi]$ , $\phi \in [0, 2\pi]$

As previously, the governing equations are given by

$$|\tilde{I}_{s1}| = \left| \frac{\alpha I_1}{d} + \frac{\alpha I_2 e^{j\phi} (D \cos \psi + d)}{D^2 + d^2 + 2dD \cos \psi} \right| \quad (122)$$

$$|\tilde{I}_{s2}| = \left| \frac{\alpha I_1}{d+x} + \frac{\alpha I_2 e^{j\phi} (D \cos \psi + d+x)}{D^2 + (d+x)^2 + 2(d+x)D \cos \psi} \right| \quad (123)$$

$$|\tilde{I}_{s3}| = \left| \frac{\alpha I_1}{d+2x} + \frac{\alpha I_2 e^{j\phi} (D \cos \psi + d+2x)}{D^2 + (d+2x)^2 + 2(d+2x)D \cos \psi} \right| \quad (124)$$

$$|\tilde{I}_{s4}| = \left| \frac{\alpha I_2 e^{j\phi} D \sin \psi}{D^2 + d^2 + 2dD \cos \psi} \right| \quad (125)$$

$$|\tilde{I}_{s5}| = \left| \frac{\alpha I_2 e^{j\phi} D \sin \psi}{D^2 + (d+x)^2 + 2(d+x)D \cos \psi} \right| \quad (126)$$

$$|\tilde{I}_{s6}| = \left| \frac{\alpha I_2 e^{j\phi} D \sin \psi}{D^2 + (d + 2x)^2 + 2(d + 2x)D \cos \psi} \right| \quad (127)$$

Note that the governing equations in this case represent the most general scenario. As the computing power on the sensor is limited and is directly proportional to the power requirements, it is not feasible to compute a phasor quantity using the sensor. Therefore, in a realistic scenario only absolute quantities are available to the sensor for computing the system information. Clearly, in this case, it is quite tedious to compute the estimated values for the system parameters without valid assumptions. Squaring (122) and using the assumption that  $D \gg d, x$ , the following equation is obtained:

$$|\tilde{I}_{s1}|^2 = \left( \frac{\alpha I_1}{d} \right)^2 + \frac{\left( \alpha I_2 \left( \cos \psi + \frac{d}{D} \right) \right)^2}{D^2} + \frac{2\alpha^2 I_1 I_2 \left( \cos \psi + \frac{d}{D} \right) \cos \phi}{dD} \quad (128)$$

If  $\psi$  is close to 0, (128) reduces to

$$|\tilde{I}_{s1}|^2 = \left( \frac{\alpha I_1}{d} \right)^2 + \frac{(\alpha I_2)^2}{D^2} + \frac{2\alpha^2 I_1 I_2 \cos \phi}{dD} \quad (129)$$

Similarly, the other equations reduce to a similar form given by

$$|\tilde{I}_{s2}|^2 = \left( \frac{\alpha I_1}{d} \right)^2 + \frac{(\alpha I_2)^2}{D^2} + \frac{2\alpha^2 I_1 I_2 \cos \phi}{(d + x)D} \quad (130)$$

$$|\tilde{I}_{s3}|^2 = \left( \frac{\alpha I_1}{d} \right)^2 + \frac{(\alpha I_2)^2}{D^2} + \frac{2\alpha^2 I_1 I_2 \cos \phi}{(d + 2x)D} \quad (131)$$

Even if  $\psi$  is close to  $\pi/2$ , with the assumption that  $d \ll D$ , the same equations as in (129), (130) and (131) are obtained. Subtracting (130) from (129), and (131) from (130) gives

$$|\tilde{I}_{s12}|^2 = |\tilde{I}_{s1}|^2 - |\tilde{I}_{s2}|^2 = (\alpha I_1)^2 \left( \frac{1}{d^2} - \frac{1}{(d + x)^2} \right) + \frac{2\alpha^2 x I_1 I_2 \cos \phi}{d(d + x)D} \quad (132)$$

$$|\tilde{I}_{s23}|^2 = |\tilde{I}_{s2}|^2 - |\tilde{I}_{s3}|^2 = (\alpha I_1)^2 \left( \frac{1}{(d+x)^2} - \frac{1}{(d+2x)^2} \right) + \frac{2\alpha^2 x I_1 I_2 \cos \phi}{(d+2x)(d+x)D} \quad (133)$$

The last term in (132) and (133) can be neglected relative to the first term under the assumption that either the currents are nearly the same, or  $I_1$  is relatively large as compared to  $I_2$ . Another interesting observation is, under the assumption that  $I_1/I_2 > 1$ , the constraint on  $\psi$  can be relaxed. Therefore, for all  $\psi$  between 0 to  $2\pi$ , the same equations are obtained as given in (132) and (133), if the last term was neglected. This makes the solution-set of Case 5, the most general solution-set, giving the final equation as

$$\frac{|\tilde{I}_{s12}|^2}{|\tilde{I}_{s23}|^2} = M = \left( \frac{x+2d}{3x+2d} \right) \frac{(d+2x)^2}{d^2} \quad (134)$$

$$2(M-1)d^3 + (3M-9)xd^2 - 12x^2d - 4x^3 = 0 \quad (135)$$

If  $M$  is nearly equal to 1, (135) reduces to a quadratic equation that has a solution given by

$$d^* = 2x \left| \frac{-1 \pm \sqrt{1 - \frac{1}{3}(3-M)}}{(3-M)} \right| \quad (136)$$

If  $M$  is not equal to 1, the third order polynomial (135) has to be solved for  $d$  using non-linear equation solving techniques.

Once  $d^*$  is found,  $I_1$  can be easily found using

$$I_1^* = \frac{|\tilde{I}_{s12}| d^* (d^* + x)}{\alpha \sqrt{x^2 + 2xd^*}} \quad (137)$$

The values for  $I_2$ ,  $D$ , and  $\psi$  can be found as in Case 4.

In Case 5, as the complexity of the governing equations is high, it is not possible to compute  $\phi$ . One method to compute the phase could be to perform phasor analysis of the sensed currents; however, it requires additional computational power, and therefore,

energy. As this research targets low-power application, for all practical purposes computation of phasors is avoided.

All in all, with MCTM, the current in the near conductor, current in the far-field conductor, position of the far-field conductor with respect to the near conductor, and distance of the sensor cores from near-field conductor can be found with a fairly high level of accuracy.

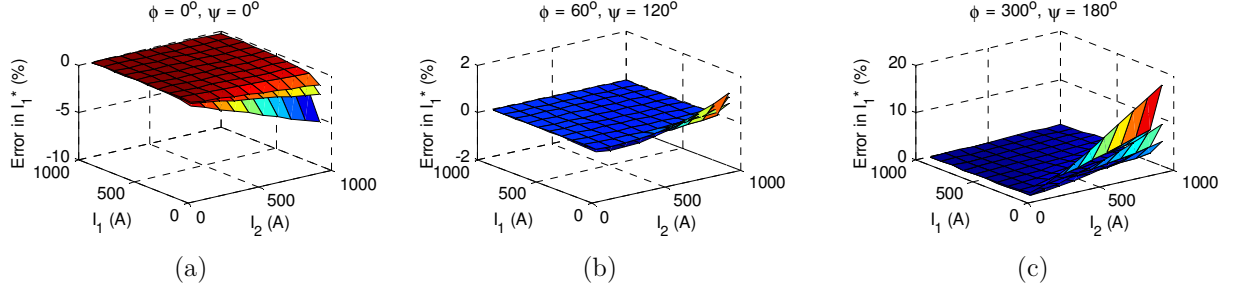
### 5.5.3 Simulation Studies using MCTM

Simulation studies were conducted using MATLAB<sup>®</sup> to test the validity of the developed current sensing method. As the focus of the triangulation method is computation of current by decoding the information on the geometry of the far-field and near-field assets, the simulation studies were conducted to test the errors in near-field current under various cases. The parameters chosen for the study with their step sizes are shown in Table 5.3.

**Table 5.3: Parameters for the Simulation Study**

| Parameter | Min Value | Max Value | Step Size |
|-----------|-----------|-----------|-----------|
| $I_1$     | 100 A     | 1000 A    | 100 A     |
| $I_2$     | 100 A     | 1000 A    | 100 A     |
| D         | 1 m       | 2 m       | 0.5 m     |
| $\psi$    | 0         | $2\pi$    | $\pi/3$   |
| $\phi$    | 0         | $2\pi$    | $\pi/3$   |
| d         | 3 cm      | 3 cm      | 0         |
| x         | 1 cm      | 1 cm      | 0         |

A total of 36 surface plots showing the error in computation of  $I_1$  for all the combinations of  $\psi$ ,  $\phi$ , D,  $I_1$ , and  $I_2$  can be found in Appendix C. Some of the interesting cases are presented in Figure 5.15. Note that every plot has three graphs, showing three different error surfaces for three different D. The absolute value of error surfaces increases with a decrease in D.



**Figure 5.15: Same system as in Figure 5.8 but with three sensor cores**

As expected, it is observed in Figure 5.15, that the errors for most cases are quite low, and in some cases even less than 0.5%. However, as it was highlighted in the discussion in Section 5.5.2.5 that the ratio  $I_1/I_2$  affects the errors in measurement, a ratio of less than 1 leads to relatively large errors. Therefore, for some cases the errors increase to as high as 20% when  $I_1/I_2$  is close to 0.01. Although, the error is high, as the absolute value of current is low, the large errors may not cause a huge concern. Furthermore, the large errors are seen in the cases with the lowest value of  $D$  (1 m). For higher  $D$  values, the errors reduce exponentially to zero.

#### 5.5.4 Advantages and Limitations of MCTM

Overall, the proposed technique of MCTM for current sensing is novel and proves to be promising. The two major issues, introduced in the beginning of this chapter, related to self-calibration and far-field rejection are solved with the use of MCTM. Moreover, the errors in measurement are found to be fairly low in most cases. However, certain limitations of the MCTM technique are highlighted below:

- It requires 6 core-coil assemblies; therefore, the method is relatively complex
- For  $I_1/I_2 \ll 1$ , and  $d/D > 10\%$ , the errors in measurement of  $I_1$  increase
- It requires a relatively higher computing power and therefore energy

Further, with the use of MCTM (apart from  $I_1$ )  $I_2$ ,  $D$ ,  $\psi$ , and  $d$  can also be computed. However, the information on  $I_2$ ,  $D$  and  $\psi$  although helps in improving the accuracy of measurement, it does not have any significance from a current sensing perspective. Therefore, if it was possible to reject the effects of far-fields, rather than

focusing on computing the exact values of these parameters, the method would bode more practical relevance.

## 5.6 CONCLUSIONS

This chapter addressed some of the major challenges of using a Stick-on open core-coil assembly for current sensing. Two distinct challenges were identified, namely, the ability of the sensor to self-calibrate and the ability to reduce crosstalk or reject the effects of far-fields. A novel method for current sensing called the multi-core triangulation method, which uses six core-coil assemblies specially arranged in space, was proposed, developed, and tested through extensive simulation studies. The MCTM method was able to solve both the problems pertaining to self-calibration and far-field rejection, and was able to estimate the value of current in the near conductor with a high degree of accuracy for most cases. However, it was observed that in certain cases, the method gave relatively higher errors. Furthermore, as the method uses six core-coil assemblies it tends to be slightly bulky and complex. Moreover, it requires relatively large computational power and therefore energy. Nevertheless, it is novel method of solving two very difficult problems of current sensing. Further, the complexity of MCTM can be reduced by decreasing the dimensionality of the problem, and considering that the only parameter of interest is  $I_1$ . Reduction of the MCTM to a more practical method is presented in the next chapter.

## CHAPTER 6

# SMART DUAL-CORE TRIANGULATION METHOD FOR CURRENT SENSING

### 6.1 INTRODUCTION

In the previous chapter, a novel multi-core triangulation method (MCTM) for current sensing was introduced that could solve the problems of self-calibration and far-field rejection. However, the complexity of the introduced method is relatively high. Further, it has the ability to compute the values of parameters such as  $I_2$ ,  $D$ , and  $\psi$ , apart from computing  $I_1$ . These parameters give a greater insight into the system configuration, and help in decoding the parameter of interest, i.e.  $I_1$ . However, their accurate computation does not hold a large significance from a practical view. Therefore, if the focus is shifted from accurate computation of the external parameters ( $I_2$ ,  $D$ , and  $\psi$ ), and laid only upon the computation of  $I_1$ , the dimensionality of the problem can be reduced without losing information. This way the computational effort can be greatly simplified and complexity of the method can be reduced. This chapter introduces a more practical method that reduces the dimensionality of the MCTM current sensor without losing information.

In this chapter, a framework for the new reduced MCTM technique is developed. The technique is extensively tested through simulations, and finally, a prototype smart current sensor incorporating the method and algorithm is built and tested in the laboratory on an ACSR conductor. This chapter also discusses some practical issues of implementing the smart current sensor in a realistic utility environment and presents all the design constraints.



## 6.2 USING HISTORICAL DATA AND VARIABILITY

In the most general scenario, it is evident that with less than six core-coil assemblies, the information collected is not sufficient to compute the parameter of interest,  $I_1$ . In such a case, the information gathered by the sensor cores inhibits the ability to reject the far-fields and simultaneously self-calibrate. However, it should be noted that the current sensor will be used in utility applications where it will be installed on the asset for extended periods of time, nearly 20 - 30 years. If the current measurement algorithm is designed in such a manner that the sensed parameters and measurement values are stored in an onboard memory, then, over time it may be possible to gather enough information to decouple the effects of far-fields from near fields. This idea will work only if the geometry of the nearby assets is fairly constant (or slow changing) with respect to the change in current in the asset. The assumption is true for utility applications.

Further, the current flowing in utility assets is not constant and varies over time. Therefore, although the geometry of nearby assets may be fairly constant over extended periods of time, the currents in all the assets are bound to vary relatively fast. This variability in current flowing in the assets can be leveraged to collect more data points and can be used to estimate and refine present measurements. Ultimately, eliminate the requirement for field calibration at the time of installation. It is expected that in this method, the sensor may require an initial period (depending on the application) right after the installation to gather information so that statistical estimation algorithms can be executed over time to converge to a solution. Using this concept, during the initial learning period it may be possible to provide a level of confidence to the measurements, which may be low to begin with, and as the gathered data increases over time the confidence level of the measurements will improve.

## 6.3 'SMART' DUAL-CORE TRIANGULATION METHOD

It was mathematically proved in Section 5.4, that the error in measurement due to far-fields is reduced dramatically with the use of two sensor cores. Further, it was also

proved that at-least two core-coil assemblies are required to reject far-fields. Far-field rejection is impossible with the help of only one core. This gives a lower bound to the dimensionality of the problem ( $m_{\min} = 2$ ).

### 6.3.1 Solution Methodology

Consider a general scenario with two core-coil assemblies, configured as shown in Figure 6.1. The near conductor strongly couples with the two sensor cores and produces a magnetic field along the magnetic field axis of the cores. On the other hand, the far conductor produces a magnetic field at an angle of say,  $\psi_1$  and  $\psi_2$  with respect to the two sensor cores. The short circuit currents induced in the two sensor cores will be given by

$$I_{s1} = \frac{\alpha \tilde{I}_1}{d} + \frac{\alpha \tilde{I}_2}{D_1} \cos \psi_1 \quad (138)$$

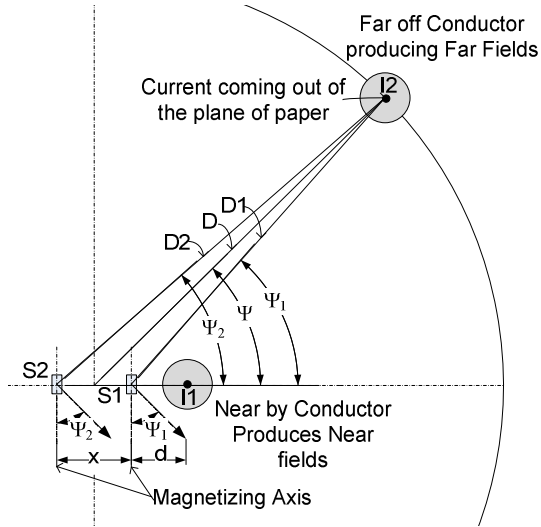
$$I_{s2} = \frac{\alpha \tilde{I}_1}{d+x} + \frac{\alpha \tilde{I}_2}{D_2} \cos \psi_2 \quad (139)$$

where

$$D_1 = \left[ D^2 + \frac{x^2}{4} - Dx \cos \psi \right]^{\frac{1}{2}} \quad D_2 = \left[ D^2 + \frac{x^2}{4} + Dx \cos \psi \right]^{\frac{1}{2}}$$

$$\cos \psi_1 = \frac{\left( D \cos \psi - \frac{x}{2} \right)}{D_1} \quad \cos \psi_2 = \frac{\left( D \cos \psi + \frac{x}{2} \right)}{D_2}$$

$$\tilde{I}_{1,2} = I_{1,2} e^{j\phi}$$



**Figure 6.1: A general system geometry showing the presence of far-fields produced by far off conductor carrying current  $I_2$  that couples with near fields produced by conductor carrying current  $I_1$**

$I_1$  and  $I_2$  are considered to have a phase angle difference of  $\phi$  between them. In (138) and (139)  $I_1$ ,  $I_2$ ,  $d$ ,  $D$ ,  $\phi$  and  $\psi$  are the unknowns, for a total of six. There are only two equations available to extract these unknowns. If another set of sensed information is available, assuming that the geometry and other external conditions ( $D$ ,  $d$ ,  $\phi$  and  $\psi$ ) do not change, it would be possible to have four equations.  $I_1$  and  $I_2$  could have changed from the previous sensed time. Hence, there are eight unknowns and four equations. If the sensed information is again gathered and saved, this would lead to ten unknowns and six equations. Over a period of time a lot of sensed information can be collected and in general, if there are  $n$  equations there would be  $n+4$  unknowns. With the knowledge of history of measurements, it is possible to gradually estimate the position of the two sensor cores with respect to the nearby and far-off conductor and concurrently find an improved estimate of the current flowing in the nearby utility conductor. This idea of using historical measurements for estimating the present values is at the heart of the smart current sensing algorithm.

Therefore, if it is assumed that the current values in the nearby and far-off utility conductors naturally change over the course of time, it would be possible to estimate the

parameter of interest, i.e. nearby conductor current. This assumption is valid in almost all utility scenarios where the utility conductor current is always associated with some variability over a period of time.

To formulate an algorithm that could help in solving for the parameter of interest, i.e.  $I_1$ , some indicators need to be defined. Over a period of time, the indicator serves to provide a confidence level to the current measurements. Suppose  $I_c$  and  $I_d$  are the common mode and differential mode SCCs from the two sensors respectively, such that

$$I_c = I_{s1} + I_{s2} \quad (140)$$

$$I_d = I_{s1} - I_{s2} \quad (141)$$

Also, a term called the Far Field Rejection Ratio ( $F_r$ ) is defined and is given by

$$F_r = \left| \frac{I_d}{I_c} \right| \quad (142)$$

### 6.3.1.1 Smart DCTM Case I: $\psi = 0, \phi = 0$

Suppose,  $\psi$  and  $\phi$  are 0. The configuration shown in Figure 6.1 is reduced to the one shown in Figure 5.8. However, here  $d$  is unknown. Plugging  $\psi$  and  $\phi$  as 0 in (138) and (139) and simplifying the expressions gives

$$I_d = \beta_1 I_1 + \beta_2 I_2 \quad (143)$$

$$I_c = \gamma_1 I_1 + \gamma_2 I_2 \quad (144)$$

where

$$\beta_1 = \frac{\alpha x}{d(d+x)} \quad \beta_2 = \frac{\alpha x}{D^2 - \frac{x^2}{4}} \quad \gamma_1 = \frac{\alpha(2d+x)}{d(d+x)} \quad \gamma_2 = \frac{2D\alpha}{D^2 - \frac{x^2}{4}}$$

Consider the two extreme conditions,

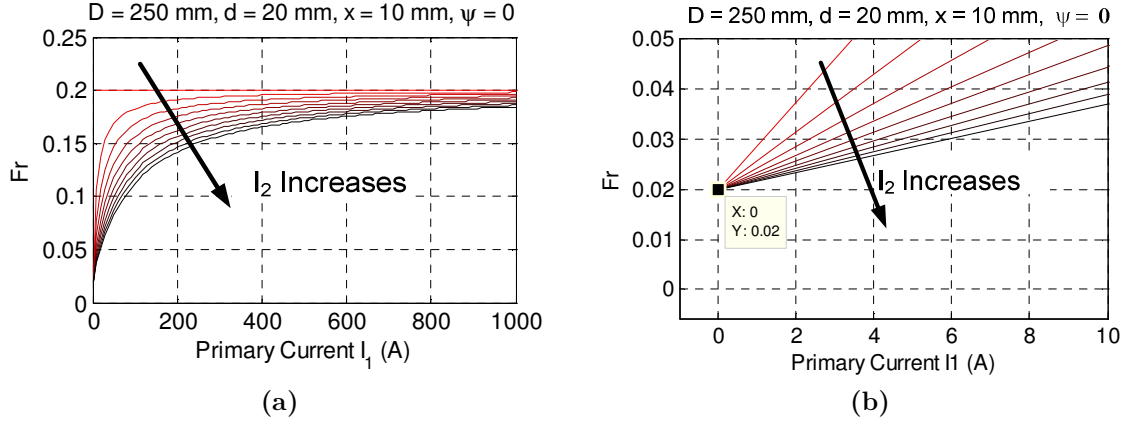
- When  $I_2 = 0$ ,

$$F_r = \frac{I_d}{I_c} = \frac{\beta_1}{\gamma_1} = \text{constant}$$

- When  $I_1 = 0$ ,

$$F_r = \frac{I_d}{I_c} = \frac{\beta_2}{\gamma_2} = \text{constant}$$

A plot is shown in Figure 6.2 to understand the variation of  $F_r$  with the change in currents in the two conductors.



**Figure 6.2:  $F_r$  plotted against the primary current. The different curves are at different values of  $I_2$ .**

It can be observed that when  $I_2 = 0$ ,  $F_r$  is a straight line that does not change with a change in  $I_1$ . This implies that in the presence of no far fields,  $F_r$  is a constant. Moreover, in the absence of near fields when  $I_1 = 0$ ,  $F_r$  is again a constant, although it has a different value. Another observation is that for non-zero values of  $I_1$  and  $I_2$ , curves increasing in a polynomially concave fashion are obtained. The minima for all such curves is the same and is given by  $F_r = \beta_2/\gamma_2$  when  $I_1 = 0$ . Furthermore, all such curves are asymptotes to the line given by  $F_r = \beta_1/\gamma_1$ ; hence, this value of  $F_r$  is a maxima for all such curves.

If the sensor keeps measuring the current over a period of time and keeps storing the maximum and minimum value of  $F_r$ , it would be possible to determine  $d$  and  $D$  as given by

$$\max(F_r) = \frac{\beta_1}{\gamma_1} = \frac{x}{2d+x} \Rightarrow d^* = \frac{x}{2} \left( \frac{1}{\max(F_r)} - 1 \right) \quad (145)$$

$$\min(F_r) = \frac{\beta_2}{\gamma_2} = \frac{x}{2D} \Rightarrow D^* = \frac{x}{2\min(F_r)} \quad (146)$$

Subsequently,  $I_1$  and  $I_2$  can be found by using (140) and (141), i.e. using the indicators  $I_d$  and  $I_c$ , in the following manner:

$$\begin{bmatrix} I_1^* \\ I_2^* \end{bmatrix} = \begin{bmatrix} \beta_1 & \beta_2 \\ \gamma_1 & \gamma_2 \end{bmatrix}^{-1} \begin{bmatrix} I_d \\ I_c \end{bmatrix} \quad (147)$$

Where,  $I_1^*$  and  $I_2^*$  are estimates of  $I_1$  and  $I_2$  respectively. The values of  $\beta_1$ ,  $\beta_2$ ,  $\gamma_1$  and  $\gamma_2$  would improve over a period of time due to an improvement in the estimates of  $d$  and  $D$ . Consequently, result in an improvement in the estimation of  $I_1$  as well.

### 6.3.1.2 Smart DCTM Case II: $\psi \in [0, 2\pi]$ , $\phi = 0$

Suppose that the spatial angle  $\psi$  of the far-field is non-zero. New values for  $\beta_1$ ,  $\beta_2$ ,  $\gamma_1$ , and  $\gamma_2$  are given as,

$$\beta_1 = \frac{\alpha x}{d(d+x)} \quad \gamma_1 = \frac{\alpha(2d+x)}{d(d+x)}$$

$$\beta_2 = \frac{\left[ D^2 x (2 \cos^2 \psi - 1) - \frac{x^3}{4} \right]}{\left[ \left( D^2 + \frac{x^2}{4} \right)^2 - (Dx \cos \psi)^2 \right]}, \quad \gamma_2 = \frac{\left[ 2D \cos \psi \left( D^2 - \frac{x^2}{4} \right) \right]}{\left[ \left( D^2 + \frac{x^2}{4} \right)^2 - (Dx \cos \psi)^2 \right]}$$

To get further insight, the variation in  $F_r$  is plotted against different values of currents in the two conductors for two different spatial angles. The results are shown in Figure 6.3.

It can be observed that the nature of  $F_r$  is the same as in the case of zero spatial angle whenever,

$$-90^\circ \leq \psi \leq 90^\circ$$

However, the nature of the  $F_r$  curves change completely from being polynomially increasing concave curves to curves that have a discontinuity whenever,

$$90^\circ \leq \psi \leq 270^\circ$$

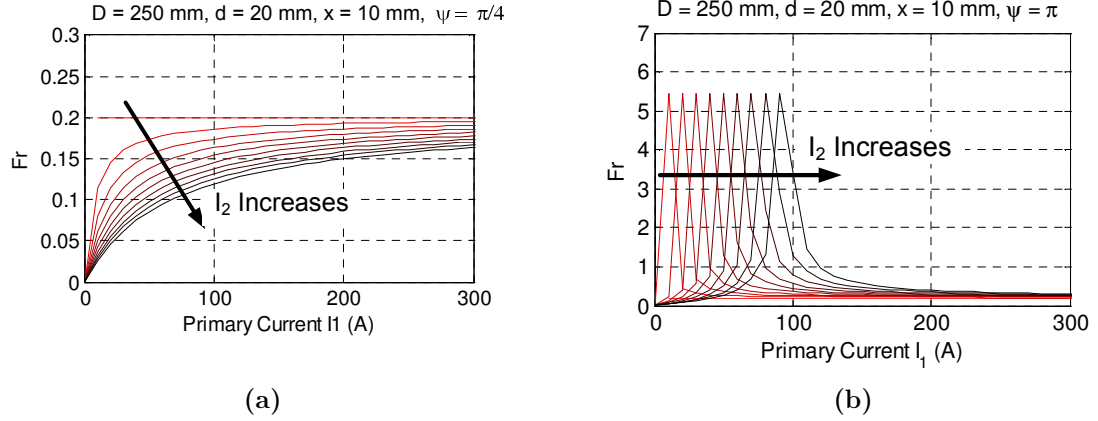


Figure 6.3:  $F_r$  plotted against primary current for (a)  $\psi = 45^\circ$  and (b)  $170^\circ$

The discontinuity can be explained through the definition of  $F_r$ , i.e. ratio of  $I_d$  and  $I_c$ . When  $I_c$  goes to zero,  $F_r$  tends to infinity. Mathematically,

$$I_c = 0 \Rightarrow \frac{\alpha(2d+x)}{d(d+x)} I_1 + \alpha \left[ \frac{2D \cos \psi \left( D^2 - \frac{x^2}{4} \right)}{\left( D^2 + \frac{x^2}{4} \right)^2 - (Dx \cos \psi)^2} \right] I_2 = 0.$$

When  $\psi$  is in the 1<sup>st</sup> and 4<sup>th</sup> quadrant, the value of cosine is positive, and therefore,  $I_c$  can never be zero. However, whenever  $\psi$  is in the 2<sup>nd</sup> or the 3<sup>rd</sup> quadrant, the value of cosine is negative, and hence,  $I_c$  can become zero for a particular combination of  $I_1$  and  $I_2$

$$F_r = \begin{cases} \infty & \forall (I_1, I_2) \mid I_c = 0 \\ \text{finite} & \text{otherwise} \end{cases}$$

If the extreme cases of  $I_1 = 0$  and  $I_2 = 0$  are considered as before, it is found that it is still possible to calculate  $d$  from the above equations. Consider again, the two extreme cases,

- When  $I_2 = 0$

$$\min(F_r) = \frac{\beta_1}{\gamma_1} = \frac{x}{2d+x} \Rightarrow d^* = \frac{x}{2} \left( \frac{1}{\max(F_r)} - 1 \right)$$

- When  $I_1 = 0$

$$\min(Fr) = \frac{\beta_2}{\gamma_2} = \frac{D^2 x (2 \cos^2 \psi - 1) - \frac{x^3}{4}}{2D \cos \psi \left( D^2 - \frac{x^2}{4} \right)}$$

$$D^* = \frac{D \cos \psi \left( D^2 - \frac{x^2}{4} \right)}{D^2 (2 \cos^2 \psi - 1) - \frac{x^3}{4}} = \frac{x}{2 \min(Fr)}$$

It is possible to calculate  $d$  from the above equations. However, it is not possible to decouple  $D$  and  $\psi$  from the highly non-linear underspecified equation. Nevertheless, it is possible to compute an effective  $D^*$ , which is a function of  $D$ ,  $\psi$  and  $x$ . As before, the values of  $d^*$  and  $D^*$  can be used to compute the values of  $I_1$ .

### 6.3.1.3 Smart DCTM Case III: $\psi \in [0, 2\pi]$ , $\phi \in [0, 2\pi]$

The phase angle between the two currents is now assumed to be non-zero to introduce a further level of complexity to the governing equations. Without any loss of generality, it can be assumed that  $I_1$  is the reference current, and the other conductor is phase  $\phi$  apart. Taking the phase angle into consideration leads to the following set of equations:

$$\tilde{I}_d = (\beta_1 I_1 + \beta_2 I_2 \cos \phi) + j(\beta_2 I_2 \sin \phi) \quad (148)$$

$$\tilde{I}_c = (\gamma_1 I_1 + \gamma_2 I_2 \cos \phi) + j(\gamma_2 I_2 \sin \phi) \quad (149)$$

As discussed before, the general nature of  $F_r$  under various conditions can help in determining the parameters of interest. The interaction between  $\phi$  and  $\psi$  causes different characteristic curves. In fact, it can be shown that there exist two such distinct sets of characteristic curves based on the position of  $\phi$  and  $\psi$  on the Cartesian plane. These two distinct sets of characteristic curves for  $F_r$  are obtained due to the effect of the product  $\cos(\psi)\cos(\phi)$  terms in  $I_d$  and  $I_c$ . If two sets  $S$  and  $O$  are defined, such that

$$\text{When, } \cos(\psi)\cos(\phi) > 0$$

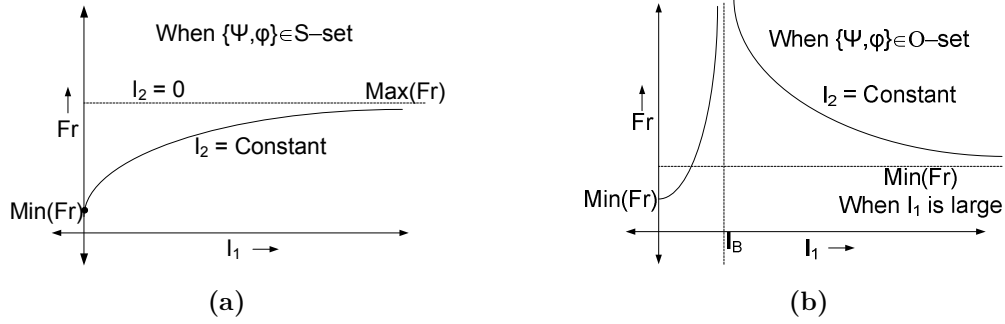


$$S \subseteq [\{\phi, \psi\} \in (-\pi/2, \pi/2)] \cup [\{\phi, \psi\} \in (\pi/2, 3\pi/2)]$$

When,  $\cos(\psi) \cos(\phi) < 0$

$$O \subseteq [\phi \in (-\pi/2, \pi/2), \psi \in (\pi/2, 3\pi/2)] \cup [\phi \in (\pi/2, 3\pi/2), \psi \in (-\pi/2, \pi/2)]$$

, when  $\psi$  and  $\phi$  are in the S-set, the  $F_r$  characteristic curve shown in Figure 6.4(a) is obtained. While, when  $\phi$  and  $\psi$  are in the O-set, the  $F_r$  characteristic curve shown in Figure 6.4(b) is obtained.



**Figure 6.4:** Nature of  $F_r$  curves under two different scenarios (a)  $\phi$  and  $\psi$  in S-set, (b)  $\phi$  and  $\psi$  in the O-set

The S and O sets are depicted in Figure 6.5, with one example geometry for each case.

The plots for  $F_r$  versus  $I_1$  and  $I_2$  for different spatial and phase angles were computed. A total of 36 plots showing the nature of the  $F_r$  curves are shown in Appendix D. Two distinct types of  $F_r$  plots, shown in Figure 6.6, are observed.

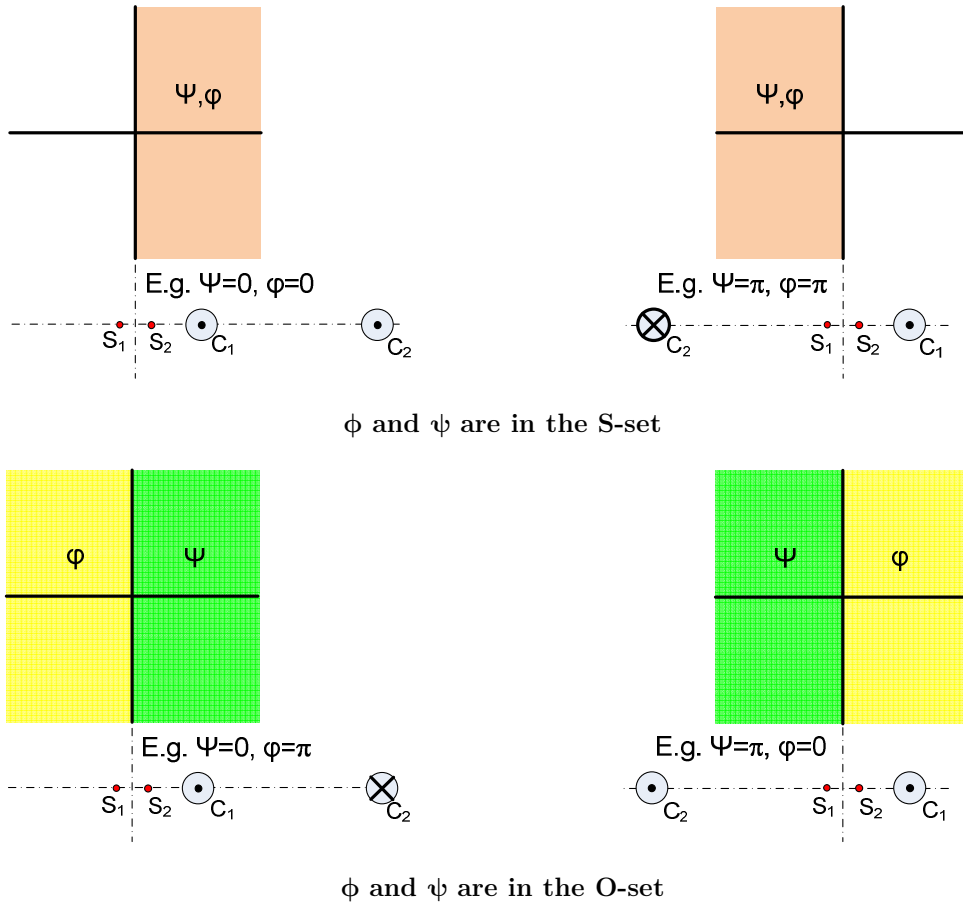


Figure 6.5: S-set and O-set pictorially represented

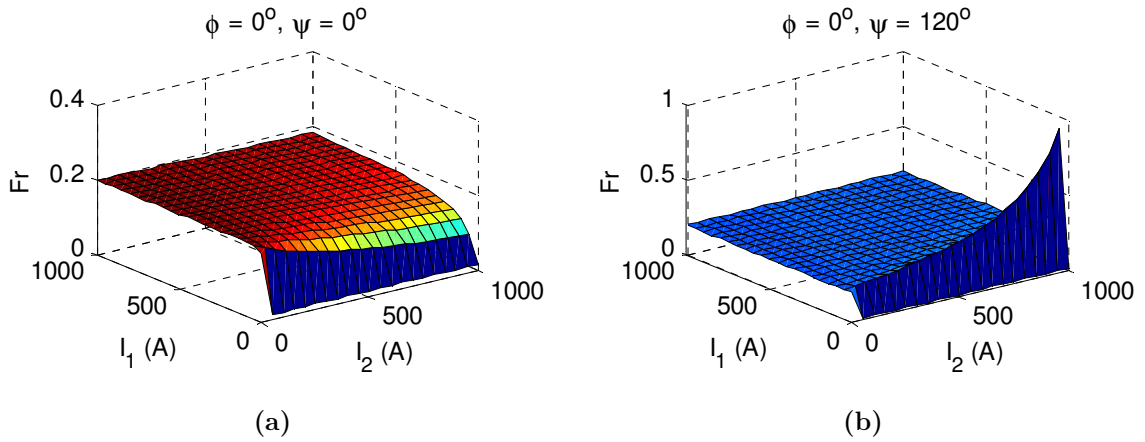


Figure 6.6: Variation of  $F_r$  with changes in  $I_1$ ,  $I_2$ ,  $\psi$  and  $\phi$

Using these characteristics the values of  $d$  and  $D$  can be estimated as follows:

If  $\psi$  and  $\phi$  are in the S-set.

- If  $I_2 = 0$

$$\max(Fr) = \frac{\beta_1}{\gamma_1} = \frac{x}{2d + x} \Rightarrow d = \frac{x}{2} \left( \frac{1}{\max(Fr)} - 1 \right)$$

- If  $I_1 = 0$

$$\min(Fr) = \frac{\beta_2(\psi, \phi, D)}{\gamma_2(\psi, \phi, D)}$$

$$D^*(\psi, \phi, D) = \frac{x}{2\min(F_r)}$$

If  $\psi$  and  $\phi$  are in the O-set.

- If  $I_2 = 0, I_1 = \text{Large}$  (say,  $I_1 > I_B$ )

$$d = \frac{x}{2} \left( \frac{1}{\min(Fr | I_1 > I_B)} - 1 \right)$$

- If  $I_1=0$

$$\min(Fr) = \frac{\beta_2(\psi, \phi, D)}{\gamma_2(\psi, \phi, D)}$$

$$D^*(\psi, \phi, D) = \frac{x}{2\min(F_r)}$$

The algorithm that is presented above can be used to estimate the value of  $I_1$ . However, in the most general case, the complexity of the problem demands the dimensionality of the output vector to be increased by at-least one. In other words, it is not possible to estimate the current in the primary conductor with a high level of confidence, if the information on the sets where  $\phi$  and  $\psi$  belong is not available.

#### 6.3.1.4 S-set versus O-set

As the sensor proposed in this research is powered through an energy harvester, the energy harvester can potentially act as another source of information. The energy harvester can be used momentarily for sensing current; therefore, provide sanity check on the sensed results obtained from the two sensor cores. This approach is quite attractive as it allows more information to be gathered without adding any new hardware.

The way sanity check works is as follows: The algorithm provides two different values of  $d$ , namely  $d_o$  and  $d_s$  based on the fact that  $\phi$  and  $\psi$  are in the S-set or in the O-set. The energy harvester is then used to compute the error in measurement of  $d^*$  using the S-set results and the O-set results. The set which gives lower error is used for future estimations. In this manner, the energy harvester is used once every few measurements to realign the sensor with the correct far-field position and phase.

Assume without any loss of generality that the energy harvester is in between the two sensor cores. The SCC produced by the energy harvester would be given by

$$I_{EH} = \frac{\alpha I_1}{d + \frac{x}{2}} + \frac{\alpha I_2}{D} \cos \psi \quad (150)$$

Mathematical simplifications using (138), (139) and (150) give

$$d_{sanity} = \frac{x(I_d - I_{deh})}{(2I_{deh} - I_d)} \quad (151)$$

where  $I_{deh} = I_{s1} - I_{EH}$ .

The value of  $d$ , i.e.  $d_{sanity}$ , obtained above is not accurate. However, it is used as a sanity check against which the estimated  $d$  from the two different calculations can be compared, and are given by

$$e_o = \frac{|d_{sanity} - d_o|}{d_{sanity}}, \quad e_s = \frac{|d_{sanity} - d_s|}{d_{sanity}}.$$

Further, if  $e_o < e_s$ ,  $\beta_{1O}$ ,  $\gamma_{1O}$ ,  $\beta_{2O}$ ,  $\gamma_{2O}$  are used, otherwise  $\beta_{1S}$ ,  $\gamma_{1S}$ ,  $\beta_{2S}$ ,  $\gamma_{2S}$  are used for computation of  $I_1$  using (17).

The analysis of  $F_r$  and its effects on estimating the current, performed in this section, was used to formulate a smart algorithm for current sensing. The flow chart of the algorithm is shown in Figure 6.7.

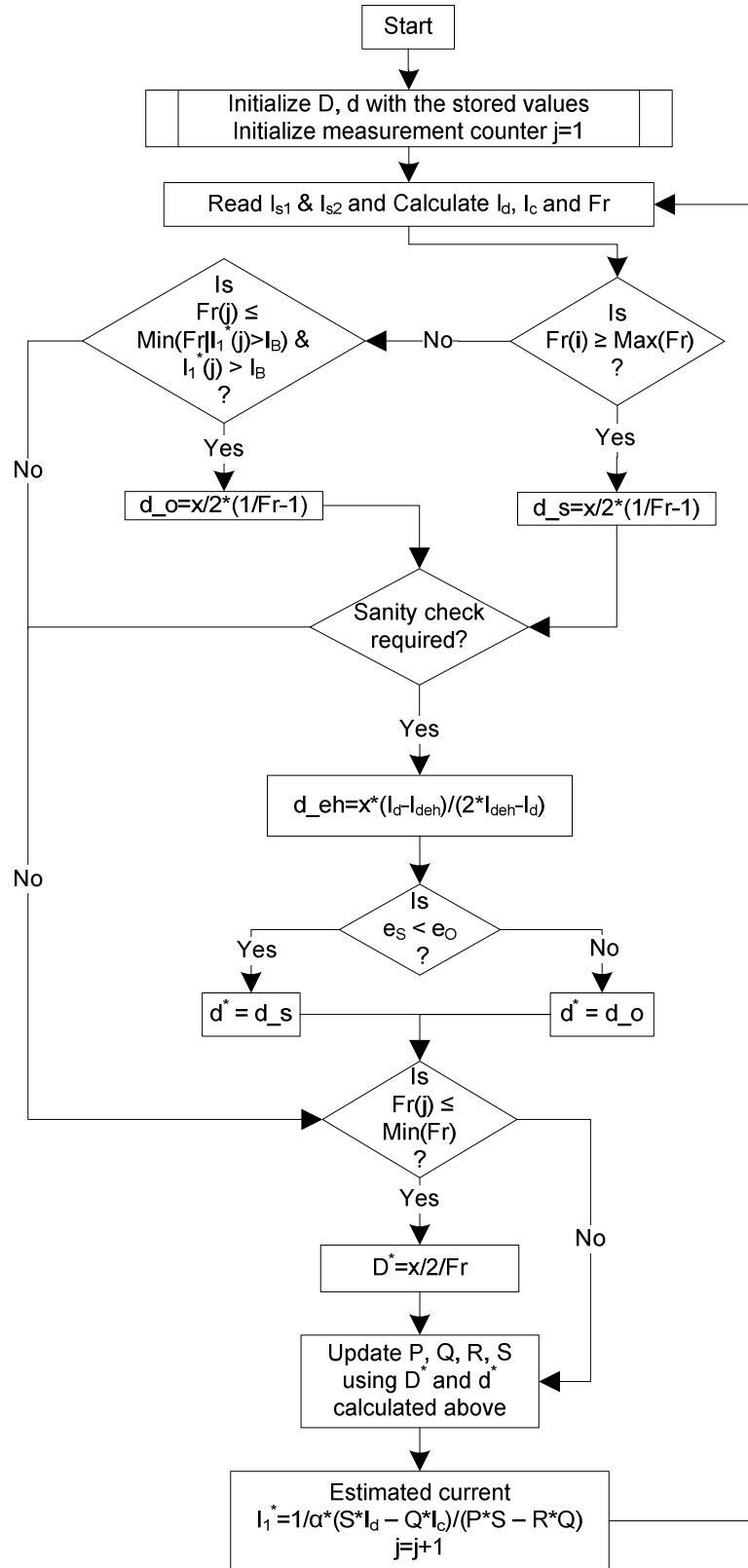


Figure 6.7: Flowchart for the smart DCTM algorithm

### 6.3.2 Confidence Index

The smart DCTM algorithm is based on the assumption of variability in asset currents for successful convergence of sensed results and minimization of error. As the variability in current has a random behavior, it may take some time before the sensed result converges. Therefore, quantifying the time it takes for solutions to converge is highly essential from a practical standpoint. However, the task of quantifying the time of convergence is not straightforward, as the sensor is essentially *blind*. In fact, for the sensor, the sensed results are the true values and the sensor doesn't have any baseline to compare its sensed results with. Nevertheless, in a realistic utility asset monitoring application, it is essential to predict, if not time of convergence, some confidence level associated with the measured results which can help operators in decision making.

As the smart DCTM algorithm requires storage of  $F_r$  in the sensor memory, the history of  $F_r$  and changes in it over time can be used to associate a confidence level to the presently sensed current. Three distinct parameters that can be used to determine the confidence of measurements are given in the sections below.

#### 6.3.2.1 Absolute Change in $\min(F_r)$ , $\max(F_r)$ or $\min(F_r|I_1^* > I_B)$

Any changes in  $\min(F_r)$ ,  $\max(F_r)$  or  $\min(F_r|I_1^* > I_B)$ , would imply that the algorithm is still learning the geometry of assets around it and trying to settle down to a stable value. As the changes in  $\min(F_r)$ ,  $\max(F_r)$  or  $\min(F_r|I_1^* > I_B)$  start decreasing, the confidence of measurement should increase.

#### 6.3.2.2 Number of Measurement Samples Since $\min(F_r)$ , $\max(F_r)$ or $\min(F_r|I_1^* > I_B)$ Last Changed

The confidence of measurement should increase with an increase in the number of measurement samples since the last change in  $\min(F_r)$ ,  $\max(F_r)$  or  $\min(F_r|I_1^* > I_B)$ . This condition is in accordance with the intuitive justification that if the change in  $\min(F_r)$ ,  $\max(F_r)$  or  $\min(F_r|I_1^* > I_B)$  has seized over time, the algorithm has converged to the true solution; greater this time interval, greater the confidence.

6.3.2.3 Difference between  $\max(F_r)$  and  $\min(F_r)$ , or  $\min(F_r|I_1^* > I_B)$  and  $\min(F_r)$ , whichever is applicable

The most distinct mathematical indicator that differentiates a non-convergent result from a converged solution is the difference between  $\max(F_r)$  and  $\min(F_r)$ , or  $\min(F_r|I_1^* > I_B)$  and  $\min(F_r)$ , whichever is applicable. The difference between the two should increase over time as the result approaches the true solution.

6.3.2.4 Confidence Index Formulation

The three distinct indicators of convergence can be combined together to form a single confidence index (CI), given by

$$CI = \left[ w_1 (1 - (\Delta F_d \oplus \Delta F_D)) + w_2 \left( 1 - e^{-\frac{N_{Fs}}{\max(N_{Fs})}} \right) + w_3 \frac{(F_d - F_D)}{F_d} \right] \times 100$$

Where

$w_1$ ,  $w_2$  and  $w_3$  are the weights,

$F_d = \max(F_r)_k$  or  $(\min(F_r|I_1^* > I_B))_k$  whichever is applicable

$F_D = \min(F_r)_k$

$\Delta F_d = (\max(F_r)_k - \max(F_r)_{k-1})$  or  $(\min(F_r|I_1^* > I_B)_k - \min(F_r|I_1^* > I_B)_{k-1})$  whichever is

applicable

$\Delta F_D = \min(F_r)_k - \min(F_r)_{k-1}$

$k =$  sample corresponding to the last change in  $\max$  or  $\min F_r$

$N_{Fs} =$  number of samples since  $k^{\text{th}}$  sample

Note that  $\Delta F_d$  and  $\Delta F_D$  cannot be non-zero at the same time as the updating of  $F_d$  and  $F_D$  are mutually exclusive events. Therefore, they have been ORed.

Further, the equation for confidence index given in this text is only one way of combining the three indicators to form a confidence index; there may be multiple ways of melding the indicators to form a robust confidence level.

## 6.4 PRACTICAL ISSUES ADDRESSED

The ‘smart’ DCTM method for current sensing promises to solve both the problems, identified in Chapter 5, of self-calibration and far-field rejection. Moreover, it achieves this functionality with only two sensor cores and one energy harvester. As the energy harvester is already present in the sensor, no additional hardware is needed. Further, the computational burden on the microcontroller is significantly reduced as compared to MCTM. In addition, the complexity of implementing the smart DCTM method is relatively low. Therefore, the smart DCTM algorithm provides an intelligent low-cost solution to current sensing.

However, till now, all results found are for a two dimensional system with infinitely long conductors. Note that the assumption of having fairly long conductors is valid in most utility applications as the size of sensor itself is quite small as compared to the length of the asset where the sensor is used. Nonetheless, the need for a 3-D analysis in addition to the 2-D analysis is discussed in this section.

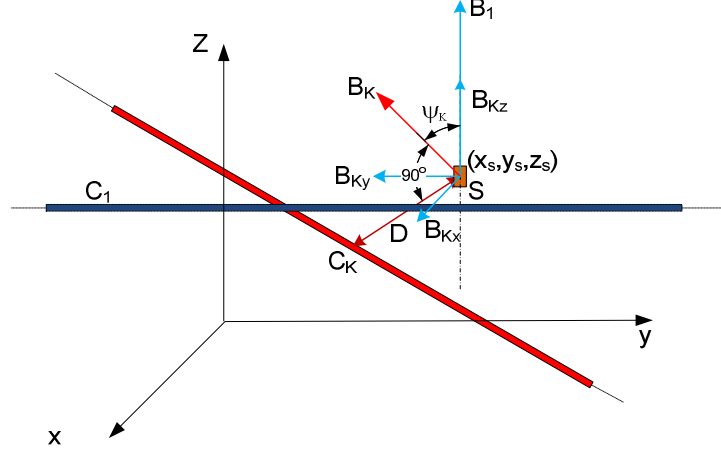
In addition, till now, the analysis considered only one far-field producing asset. In a realistic scenario, such as a secondary utility network, there may be many assets present in the vicinity. All the assets could carry current and produce crosstalk with the sensor. Therefore, generalization of the algorithm to a case with multiple assets present in the vicinity of the sensor is required. All these practical issues, with some additional issues related to errors in measurements and bounds on  $D$  and  $x$  have been discussed in this section.

### 6.4.1 3-D Versus 2-D Analysis

To justify the generality of the two dimensional analysis performed till now, consider a three dimensional system shown in Figure 6.8. In this system, the conductor of interest  $C_1$  is close to the sensor and oriented parallel to the  $zy$ -plane passing through  $(x_1, y_1, z_1)$ . Further, a  $k^{\text{th}}$  far-field producing conductor  $C_k$  is oriented randomly in space. Moreover, a sensor  $S$  is located at  $(x_s, y_s, z_s)$  which is at a distance  $d$  from  $C_1$ . Without loss of generality,



the magnetic axis of the sensor S is assumed to be in the z-direction. The area of the sensor coil is  $A_c$ .  $D$  is the perpendicular distance of the sensor at  $(x_s, y_s, z_s)$  to conductor  $C_K$ . For simplicity, only one sensor is considered, although the method can be repeated for a second sensor also to make it applicable to the DCTM algorithm.



**Figure 6.8: Magnetic fields in 3-D space**

The fields induced at the sensor produced by  $C_1$  and  $C_K$  are together given by

$$\vec{B}_s = \vec{B}_1 + \vec{B}_K \quad (152)$$

where

$$\vec{B}_1 = B_1 \vec{a}_z = \frac{\kappa I_1(t)}{d} \vec{a}_z,$$

$$\begin{aligned} \vec{B}_K &= B_{Kx} \vec{a}_x - B_{Ky} \vec{a}_y + B_{Kz} \vec{a}_z, \\ &= \frac{\kappa I_K(t)}{D} \sin(\psi_K) \cos(\delta_K) \vec{a}_x - \frac{\kappa I_K(t)}{D} \sin(\psi_K) \sin(\delta_K) \vec{a}_y + \frac{\kappa I_K(t)}{D} \cos(\psi_K) \vec{a}_z, \end{aligned}$$

$\psi_K$  = projection angles of  $B_K$  with respect to the z-axis,

$\delta_K$  = projection angle of  $B_K$  with respect to x-axis,

$\kappa$  = the constant of proportionality,

$\vec{a}_x, \vec{a}_y, \vec{a}_z$  = unit vectors in x, y and z directions.

The voltage induced in the coil at S is given by,

$$V(t) = N \frac{\partial}{\partial t} (\vec{B}_s(t) \cdot \vec{A}) \quad (153)$$

where  $\vec{A} = A_c \vec{a}_z$ .

Plugging the value for  $B_s$  into (153) gives

$$V(t) = NA_c \frac{\partial}{\partial t} \left( \frac{\kappa I_1(t)}{d} + \frac{\kappa I_K(t)}{D} \cos(\psi_K) \right) \quad (154)$$

The expression obtained in (154) clearly depicts that even in the most general scenario only those components of magnetic field affect the voltage induced on the coil which are in the direction of the magnetic axis. The functional form of the equation is the same as the one considered in Section 6.3 where the concept is first introduced and developed. A similar analysis can be repeated for any other conductor in space. Hence, all the analysis and results presented in this research are valid for 3-D cases and realistic scenarios where the conductors may be present anywhere in space.

#### 6.4.2 Multiple Far-off Utility Assets

The proposed method is not limited to only two conductors and can be easily extended and used for a more general case where there are many conductors distributed in space and carry different magnitudes of current at differing phase angles. In the presence of multiple conductors in space, the governing equations will be given by

$$I_{s1} = \frac{\alpha I_1}{d} + \sum_{k=2}^N \left( \frac{\alpha I_k e^{j\phi_{1k}}}{D_{1k}} \cos \psi'_{1k} \right) \quad (155)$$

$$I_{s2} = \frac{\alpha I_1}{x+d} + \sum_{k=2}^N \left( \frac{\alpha I_k e^{j\phi_{2k}}}{D_{2k}} \cos \psi'_{2k} \right) \quad (156)$$

For simplicity, consider the  $k^{\text{th}}$  conductor acting on the sensor cores. Further, for simplicity, consider only one core as the concept can be easily extended to the second core. The  $k^{\text{th}}$  conductor produces an H-field of magnitude  $H_k$  in the direction of a unit vector  $\mathbf{a}_k$  which interacts with the core-coil assembly, as given in Figure 6.9(a).

$$\vec{H}_k = \frac{\alpha I_k}{D_k} \vec{a}_k \quad (157)$$

Now suppose the  $k+1^{\text{th}}$  conductor was energized. The  $k+1^{\text{th}}$  conductor will also produce an H-field which has  $H_{k+1}$  magnitude and is in the direction of  $\vec{a}_{k+1}$  unit vector. The new field that interacts with the core-coil assembly is the vector sum of  $H_k$  and  $H_{k+1}$ , given by  $H_r$ , as shown in Figure 6.9(b) and mathematically represented as

$$\vec{H}_{k+1} = \frac{\alpha I_{k+1}}{D_{k+1}} \vec{a}_{k+1} \quad (158)$$

$$\vec{H}_r = \frac{\alpha I_k}{D_k} \vec{a}_k + \frac{\alpha I_{k+1}}{D_{k+1}} \vec{a}_{k+1} = \frac{\alpha I_r}{D_r} \vec{a}_r \quad (159)$$

Only that component of  $H_r$  will induce a voltage in the core-coil assembly which is in direction of the magnetizing axis. The resultant H-field can be thought of as being created by a resultant asset carrying current  $I_r$ , at a distance  $D_r$  and spatial angle  $\psi_r$ .

$$\vec{H}_r \cdot \vec{a}_x = \frac{\alpha I_k}{D_k} \vec{a}_k \cdot \vec{a}_x + \frac{\alpha I_{k+1}}{D_{k+1}} \vec{a}_{k+1} \cdot \vec{a}_x = \frac{\alpha I_r}{D_r} \vec{a}_r \cdot \vec{a}_x \quad (160)$$

$$\frac{\alpha I_k}{D_k} \cos \psi_k + \frac{\alpha I_{k+1}}{D_{k+1}} \cos(\psi_{k+1}) = \frac{\alpha I_r}{D_r} \cos(\psi_r) \quad (161)$$

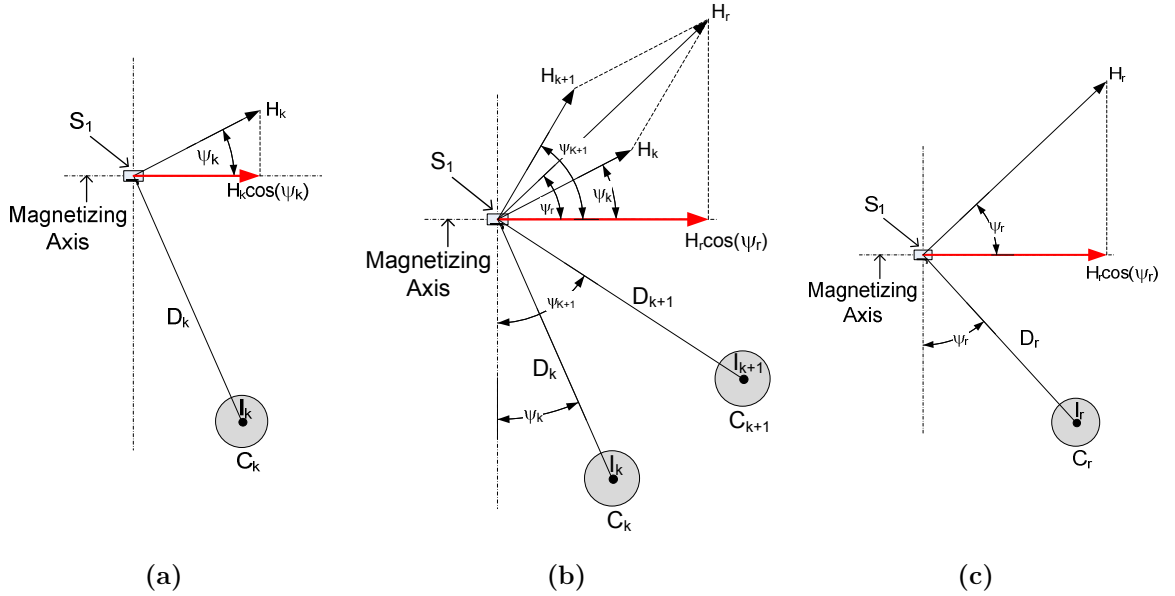


Figure 6.9: Use of superposition principle to lump the far-field conductors

This concept of superposition can be repeated for all the other assets to obtain the final resultant as shown in Figure 6.9(c) and mathematically represented as

$$\sum_{k=2}^N \left( \frac{\alpha I_k e^{j\phi_k}}{D_{1k}} \cos \psi_{1k} \right) = \frac{\alpha I_r e^{j\phi_r}}{D_{1r}} \cos(\psi_{1r}) \quad (162)$$

$$\sum_{k=2}^N \left( \frac{\alpha I_{2k} e^{j\phi_{2k}}}{D_{2k}} \cos \psi_{2k} \right) = \frac{\alpha I_r e^{j\phi_r}}{D_{2r}} \cos(\psi_{2r}) \quad (163)$$

Incorporating (162) and (163), in (155) and (156) gives

$$I_{s1} = \frac{\alpha I_1}{d} + \frac{\alpha I_r e^{j\phi_r}}{D_{1r}} \cos(\psi_{1r}) \quad (164)$$

$$I_{s2} = \frac{\alpha I_1}{x+d} + \frac{\alpha I_r e^{j\phi_r}}{D_{2r}} \cos(\psi_{2r}) \quad (165)$$

The functional form of equations (164) and (165) is the same as that of (138) and (139); therefore, the smart DCTM algorithm that was developed for a two conductor system will also work for a multiple conductor system.

The above discussion shows that a change in system conditions over time, due to change in current, distance, or spatial angle of any one asset, would impact the location and current carried by the resultant asset. Essentially, the resultant becomes a single asset that moves in space and whose current changes over time. It seems that this moving resultant asset would demand the sensor to converge to the true solution before the resultant asset changes geometry. Therefore, the sensor may need to use the energy harvester more frequently than a two-conductor case to realign itself with the geometry of the assets around it. The sampling rate of measurements may also need to increase to converge faster. It appears that the computational burden would increase on the sensor in a general scenario.

However, as it was highlighted earlier that the system geometry is fairly constant, and the only parameter that is expected to change relatively fast is the current in assets. Further, the absolute changes in current are small over time. These small changes in the asset currents provide the smart DCTM algorithm with the variability required to

converge to a solution with only minor changes in the position of the resultant asset. In a realistic scenario, the sensor would have enough time to converge to a solution before the position of the asset changes dramatically. Therefore, the computational power demand on the sensor would not increase in a practical application.

### 6.4.3 Designing the Sensor

This section provides basic equations to design the smart current sensor for a practical utility application. The discussion presented so far uses the terms *far-fields* and *near-fields* regularly. *Far* and *near* are relative terms. Quantifying the term *far* is essential for designing smart sensors for field applications. Further, the distance between the two sensor cores ( $x$ ) is also critical for the smart DCTM algorithm to operate with low errors.

The design of the smart sensor developed in this research can be performed by considering the worst case scenario. Worst case error occurs when  $\phi$  and  $\psi$  are zero, and  $D$  is at its minimum (given multiple far assets).

For a given application, it is possible to find a minimum distance ( $D_{\min}$ ) of the far-field such that for all  $D$  greater than  $D_{\min}$ , the sensor is able to reject the effect of the far-fields and give close to accurate results. In general, if the error in measurement that is acceptable is  $e_{\max}\%$  (given that the error is computed at  $I_1 = 100$  A) and the maximum far-field current is  $I_{2\max}$  at which this maximum error occurs, then the limiting condition on  $D$  can be found using

$$I_{2\max} \left( \frac{d(x+d)}{(D-d)(D-(x+d))} \right) < e_{\max} \quad (166)$$

Simplification of (166) gives

$$D^2 - (x+2d)D + d(x+d) \left( 1 - \frac{I_2^{\max}}{e_{\max}} \right) > 0 \quad (167)$$

For instance, if  $x = 10$  mm,  $d = 20$  mm,  $e = 3\%$  and the maximum far-field current at which the error occurs is 1000 A. Then, solving (167) gives the range for  $D$  as,

$$D > 472 \text{ mm}$$

Furthermore, this range can be improved by reducing  $x$ .

Alternately,  $x$  can be designed by fixing  $D$  to be its minimum expected value, rest of the parameters being the same. The value of  $x_{\max}$  is given by

$$x_{\max} = \frac{\frac{e_{\max}}{100} (D_{\min} - d)^2 - I_{2\max} d^2}{I_{2\max} d + (D_{\min} - d) \frac{e_{\max}}{100}} \quad (168)$$

Further, as  $x$  is a physical dimension, it cannot be arbitrarily small. It has a minimum value determined mainly by practical sizes for cores

$$x_{\min} < x < \frac{\frac{e_{\max}}{100} (D_{\min} - d)^2 - I_{2\max} d^2}{I_{2\max} d + (D_{\min} - d) \frac{e_{\max}}{100}}$$

For instance, if  $d = 20$  mm,  $e_{\max} = 3\%$ ,  $D_{\min} = 600$  mm, the maximum far-field current at which the error occurs is 1000 A and the minimum allowable  $x$  is 10 mm. Then, solving (168) gives the range for  $x$  as

$$10 \text{ mm} < x < 28 \text{ mm}$$

Note that decrease in  $d$  increases the upper bound for  $x$ . Figure 6.10 shows surface plot for maximum bound on  $x$  for a set of constraints on  $e_{\max}$ ,  $D_{\min}$  and  $d$ .

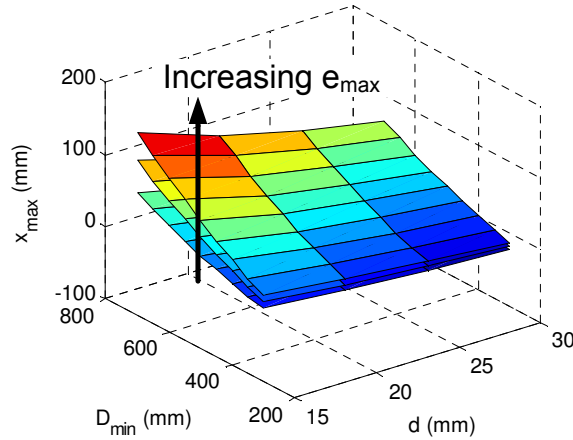


Figure 6.10: Maximum bound on  $x$  given maximum permissible error  $e_{\max}$  with variation in  $D_{\min}$  and  $d$

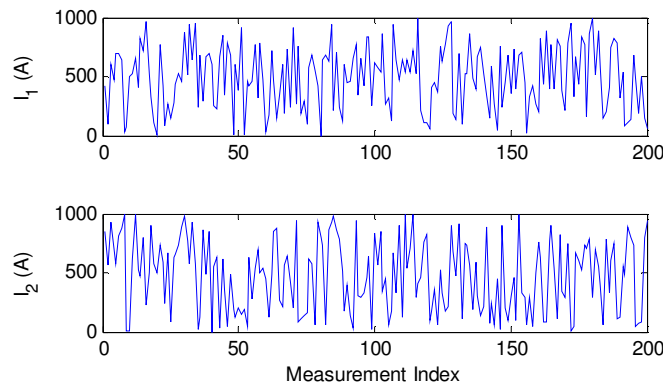
Based on requirements given by the utilities, these sensors are not required to compete with revenue grade current meters having errors less than 1%. Their main purpose is to indicate the level of current in a utility asset, and therefore, have some leeway on the percentage errors. The estimate on percentage errors for this sensor is on the order of 3 – 5%.

## 6.5 SIMULATION STUDY

Simulation studies were conducted to test the new current sensing technique using MATLAB® and validated using ANSYS® Maxwell. Different case studies were formed to test the algorithm under many different operating conditions. The different cases help in validating the performance and robustness of the algorithm and sensor under many realistic scenarios. All the case studies are analyzed in the following sub-sections.

### 6.5.1 Case Study I: General Scenario

To create a practical scenario, two current carrying utility conductors were considered. Both of them were programmed to carry RMS current that varied over time using a uniformly distributed random function. The plot for the RMS currents in the two conductors is shown in Figure 6.11. The randomness, seen in this figure, is present in the current even in the real world scenario. The statistic of the test currents are shown in Table 6.1.



**Figure 6.11: Profile of near-field and far-field producing currents  $I_1$  and  $I_2$  respectively, used for the simulation case study I.**

**Table 6.1: Statistics of the Currents used for Simulation Case Study-I**

| <b>Statistic</b>   | <b>I<sub>1</sub> (A)</b> | <b>I<sub>2</sub> (A)</b> |
|--------------------|--------------------------|--------------------------|
| Mean               | 494                      | 480                      |
| Standard Deviation | 303                      | 265                      |
| (Minimum, Maximum) | (0, 994)                 | (0, 999)                 |

The ability of the algorithm to sense currents was tested using the percentage error in the estimated current as compared to the actual current. Further, the confidence index given by the sensor was also plotted on the same graph to test the correlation between the confidence index and the actual error. Note that in a real world scenario, computation of error would not be possible; nevertheless, the confidence index associated with each measurement given by the sensor would help in determining the percentage error. Therefore, in the simulation results, the confidence index is expected to be negatively correlated to the error.

Thirty six different cases were simulated for all possible combinations of  $\psi$  and  $\phi$  over  $(0, 2\pi)$  with a step size of  $\pi/3$ . A few diverse cases are shown here in Figure 6.12. The cases correspond to different spatial geometry of the two conductors and different phase angles between the currents in the two conductors.

It can be observed that in all the cases, irrespective of the position of the far-off conductor with respect to the nearby conductor and phase angle between the two currents, the error goes down to near zero values after a few measurements. In all the cases, the error goes down from 100% to 30% in the first 10 samples, and progressively goes down to less than five percent in most cases by the 50<sup>th</sup> sample. Further, it is observed that the confidence index tracks the error very well on an average. During the initial few samples when the sensor is trying to learn the geometry, the confidence index is lower than 50 %; as the error goes down to less than 1 %, the confidence index also increases to 70 % ; and subsequently, increases further with an increase in data samples. At the 200<sup>th</sup> sample, the confidence index becomes nearly 85% for most cases, showing that the results have



converged and the sensor is giving good results. The confidence index goes to 100% exponentially with time.

The results obtained in this case study show that the smart DCTM algorithm is indeed able to perform self-calibration of the sensor and is able to reject the effect of far-fields without any prior information. Therefore, the smart DCTM algorithm provides a truly intelligent method for low-cost current sensing.

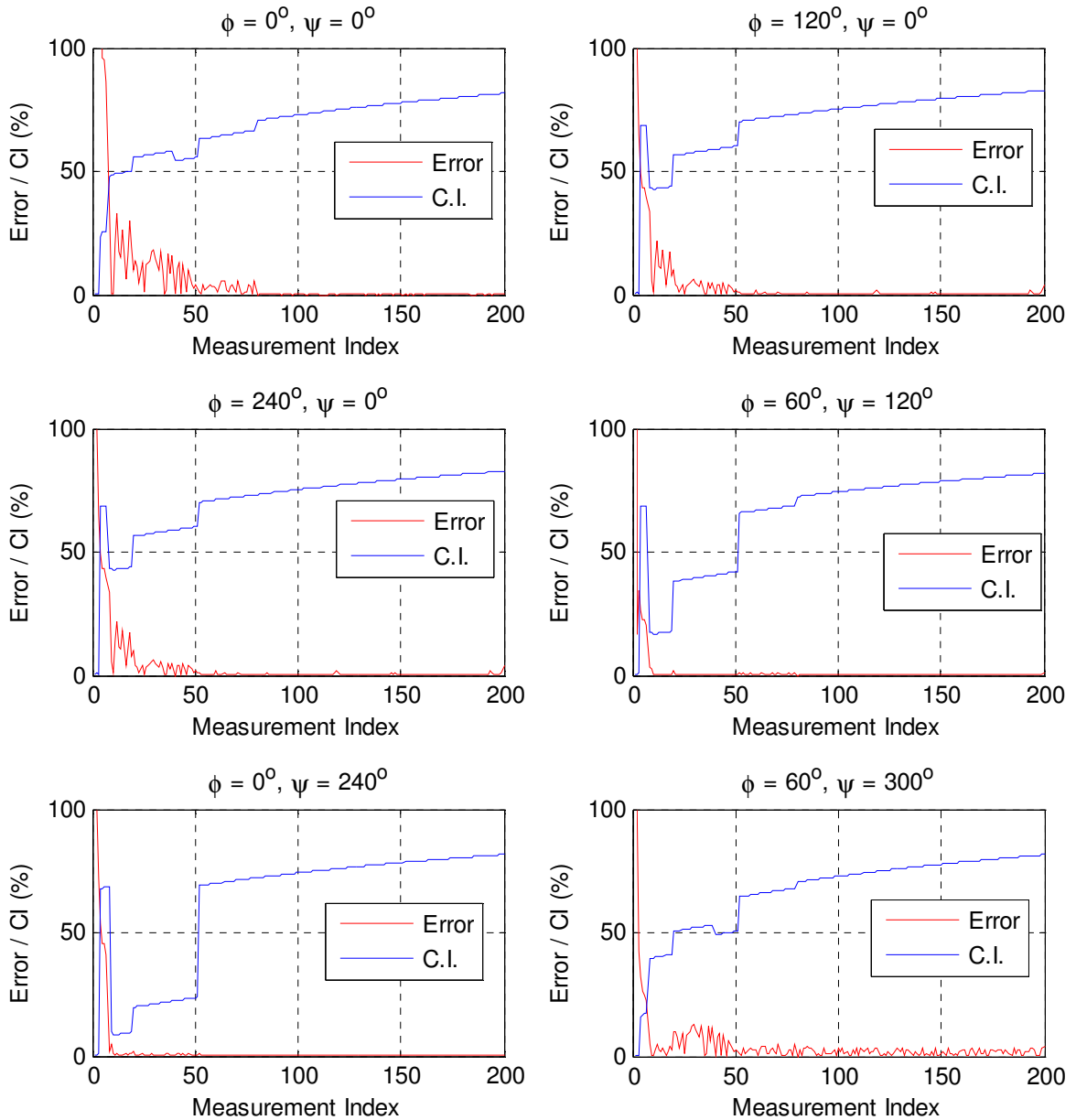


Figure 6.12: Simulation results for different sets of  $\phi$  and  $\psi$ , when  $D = 300$ ,  $x = 20$ ,  $d = 25$ .

### 6.5.2 Case Study II: Different RMS Current Profiles

In this case study, the smart DCTM algorithm was tested on four different RMS profiles for  $I_1$  and  $I_2$ . The RMS profiles were generated in a fashion similar to case study I. The statistics of all the RMS profiles are given in Table 6.2.

The results of the simulation study are shown in Figure 6.13. As before, it can be seen that the error goes down to near zero values in all the cases. Further, the confidence index increases with a decrease in error.

Successful results in this study show that even with different current profiles, assuming variability in the currents, it is possible for the smart DCTM current sensor to converge to the true solution.

**Table 6.2: Statistics of Different Profiles used for Simulation Case Study-II**

| Statistic          | Profile A    |              | Profile B    |              | Profile C    |              | Profile D    |              |
|--------------------|--------------|--------------|--------------|--------------|--------------|--------------|--------------|--------------|
|                    | $I_{1a}$ (A) | $I_{2a}$ (A) | $I_{1b}$ (A) | $I_{2b}$ (A) | $I_{1c}$ (A) | $I_{2c}$ (A) | $I_{1d}$ (A) | $I_{2d}$ (A) |
| Mean               | 507          | 464          | 498          | 530          | 480          | 508          | 552          | 502          |
| Standard Deviation | 279          | 298          | 286          | 295          | 289          | 290          | 290          | 288          |
| (Minimum, Maximum) | (0, 993)     | (4, 994)     | (3, 998)     | (1, 992)     | (0, 1000)    | (1, 995)     | (0, 992)     | (0, 989)     |

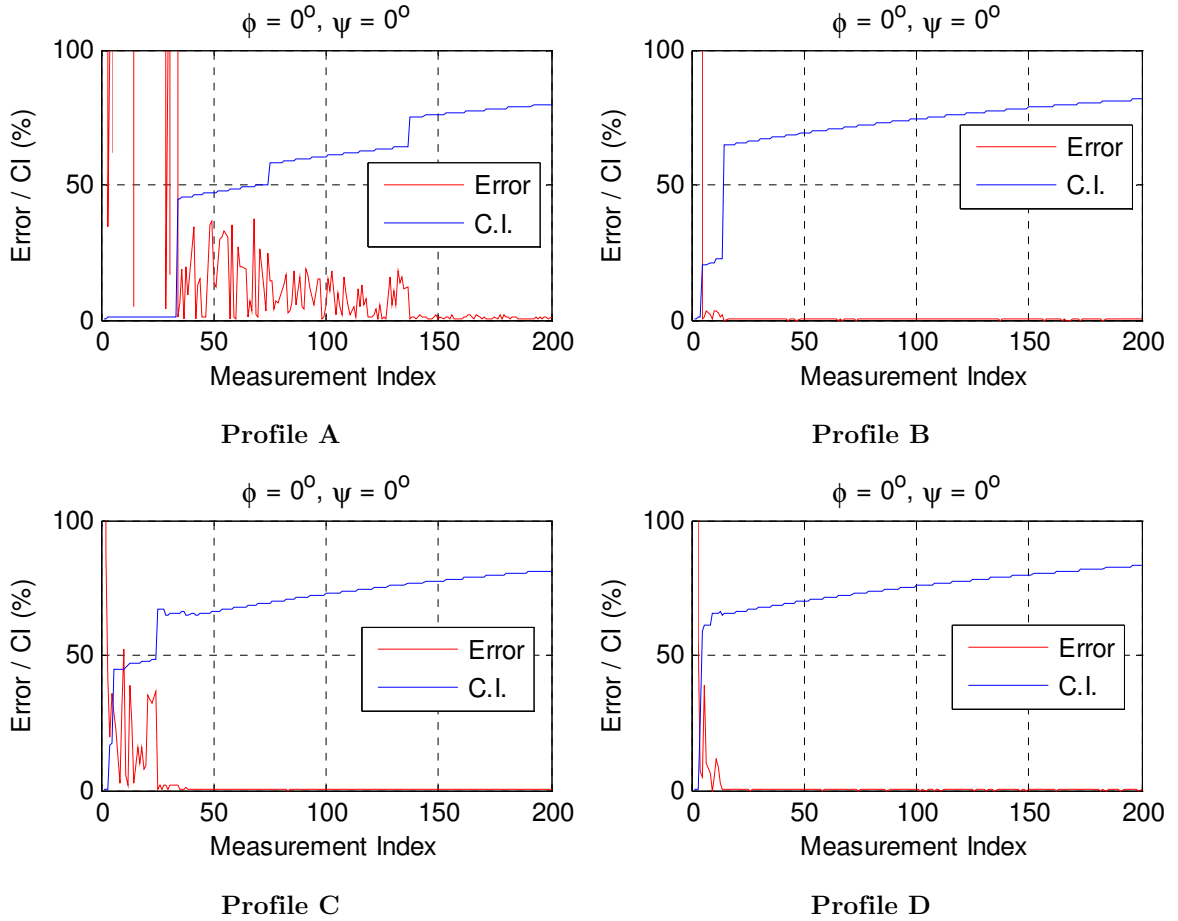


Figure 6.13: Simulation results for profile A, profile B, profile C and profile D, when  $D = 300$  mm,  $x = 20$  mm,  $d = 25$  mm.

### 6.5.3 Case Study III: Correlated Currents

Till now, the far-field and near-field producing currents were considered to be independent. However, there may be cases where there is a high correlation between far-fields and near-fields. The extreme case is when the same conductor loops around and acts as far-field to the sensor. If it was assumed that the currents in the two branches are exactly the same, the smart DCTM algorithm would fail to converge. The reason behind this failure is that the sensor would keep collecting the same data (only scaled by a constant factor) over time; and therefore, the sensor would have infinitely many solutions to choose from. However, in practice the two currents would still not be exactly the same.

Other far-assets would interact with the loop to create some variability. This variability could be enough for the smart DCTM algorithm to converge to the true solution.

In this simulation study, a minor variability in the two currents is created, such that

$$I_1 = I$$
$$I_2 = (I + \varepsilon)e^{j\pi}$$

Where

$$\varepsilon \in (-4, 4)$$

Note that,  $I_2$  has  $\pi$  phase difference as compared to  $I_1$  as the same conductor loops around, therefore, the direction of current reverses. The plot of variability between the RMS values of  $I_1$  and  $I_2$  is shown in Figure 6.14(a). It can be seen that the variability is never more than  $\pm 4$  A. Therefore, the currents are essentially of the same magnitude. Figure 6.14(b) shows the convergence of the smart DCTM algorithm in this case. In this simulation study, two more cases were simulated. These cases correspond to two conductors carrying currents of the same magnitude but  $2\pi/3$  and  $-2\pi/3$  phase apart. These specific phase angles are chosen as they are common in power systems. The results for this case are shown in Figure 6.14(b) and (c). Again, it can be seen that the sensed current computed by the algorithm is able to converge to the true solution.

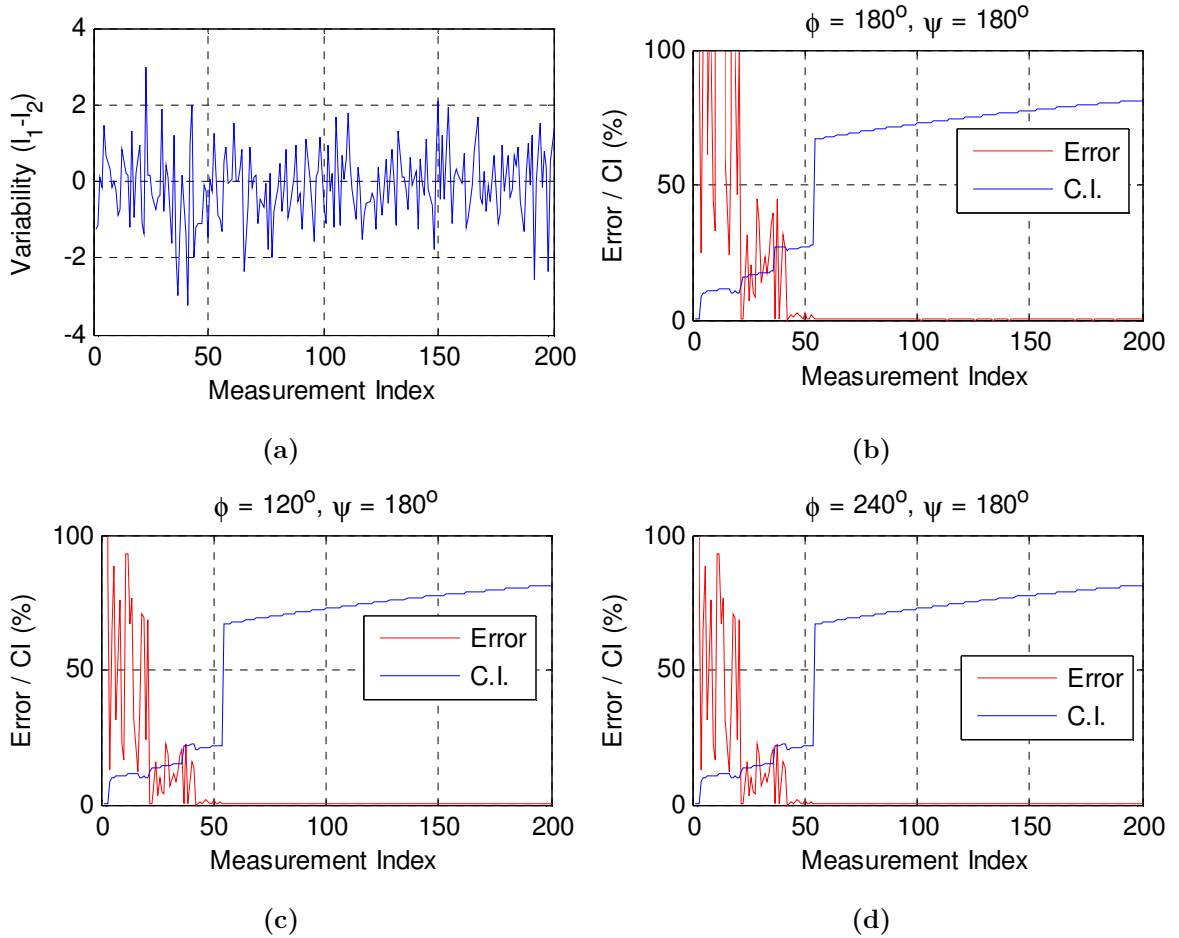


Figure 6.14: (a) Variability in current magnitudes of currents  $I_1$  and  $I_2$ , (b), (c) and (d) show simulation results for two conductors carrying same magnitude of current shifted by  $180^\circ$ ,  $120^\circ$  and  $240^\circ$  in phase, when  $D = 300$  mm,  $x = 20$  mm,  $d = 25$  mm.

#### 6.5.4 Case Study IV: Three-Phase Conductors

In a realistic system, such as a single circuit overhead distribution line, there are three conductors that ideally carry the same magnitude of current shifted by  $2\pi/3$  in phase. Assuming that the conductors have exactly the same current would be a misrepresentation of the practical system. Even in the case of three conductors carrying the same magnitude of current, it is perfectly valid to assume that there is some minor variability in the currents due to minor imbalances in the system. These imbalances are normally present in power systems. The variability may not be large, and yet, the

algorithm has the ability to self-calibrate, reject the effects of far-fields and find close to accurate results.

To show that the smart DCTM algorithm works even in a three phase system, a three phase system is considered, such that the distance between any two conductors is 300 mm and they are all in the same horizontal plane. The sensor is supposed to sense the current  $I_a$  in the A-phase conductor. The currents in B and C phases,  $I_b$  and  $I_c$  respectively, act as the far-field producing agents. The variability of currents is modeled similar to Case III, and the RMS value of current  $I_a$  is chosen to be the same as  $I_1$  in case III. The currents in phases B and C have some minor variability given by  $\varepsilon_1$  and  $\varepsilon_2$ .

$$\begin{aligned} I_a &= I \\ I_b &= (I + \varepsilon_1)e^{j2\pi/3} \\ I_c &= (I + \varepsilon_2)e^{-j2\pi/3} \end{aligned}$$

Such that,

$$\varepsilon_1, \varepsilon_2 \in (-4, 4)$$

The plots for  $\varepsilon_1$  and  $\varepsilon_2$  are given in Figure 6.15(a) and (b). It can be observed that both  $\varepsilon_1$  and  $\varepsilon_2$  are always limited between the  $\pm 4$  A.

The error between actual  $I_a$  and the value of  $I_a$  computed by the smart DCTM algorithm is presented in Figure 6.15(c). It can be seen that the algorithm performs well, and is not affected by the presence of multiple conductors in the vicinity. Further, the small variability in the three phase currents is enough for the algorithm to converge to the true solution of the currents.

Successful demonstration of the algorithm in a three phase system also proves that the two far conductors can be indeed considered as a single resultant conductor by the sensor for rejecting the far-fields. Therefore, even for a general n conductor case, the sensor would converge to the true solution.

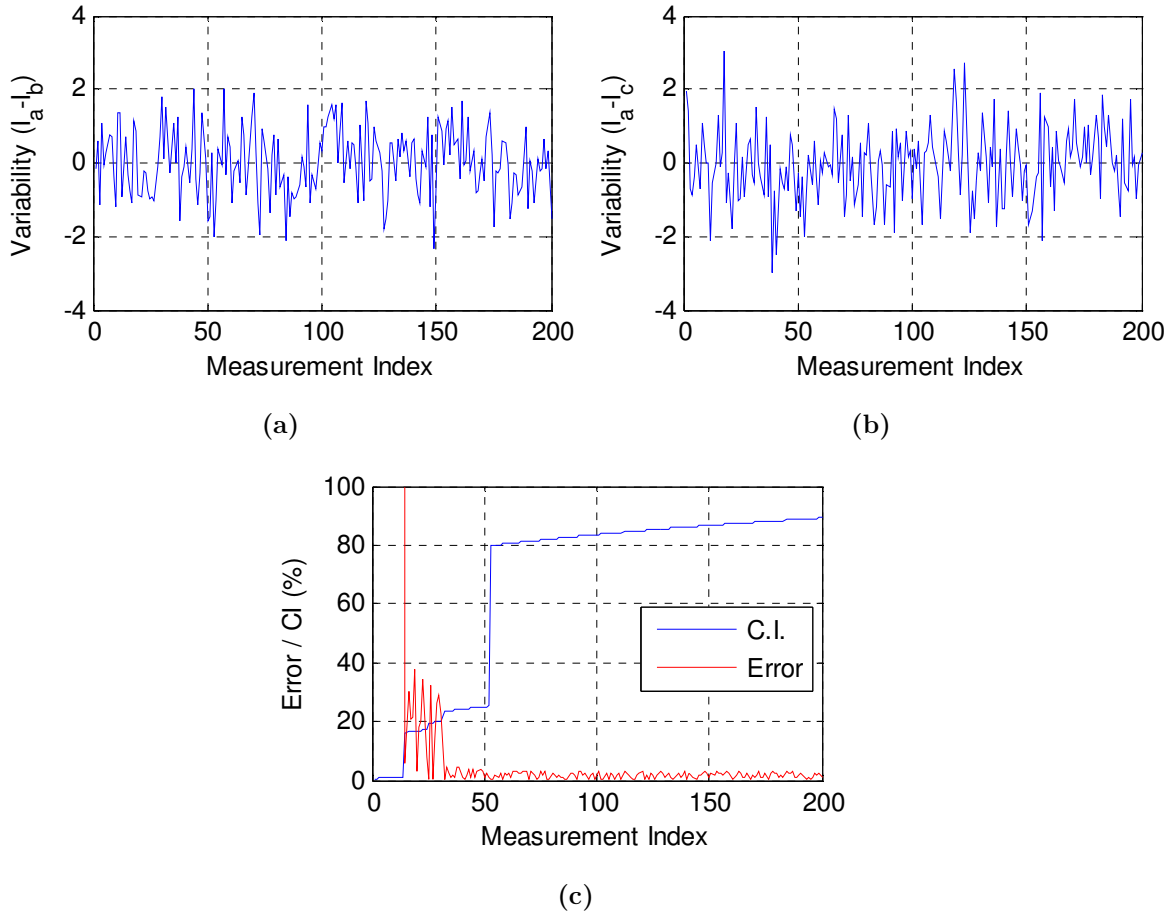


Figure 6.15: (a) and (b) show variability between magnitudes of  $I_a - I_b$  and  $I_a - I_c$  respectively, (c) simulation results in the case of a three-phase conductor system, when  $D = 300$  mm,  $x = 20$  mm,  $d = 25$  mm.

## 6.6 PROTOTYPE DEVELOPMENT AND EXPERIMENTAL TESTING

### 6.6.1 Prototype development

Successful results obtained in the simulation studies motivated the development of a prototype of the smart DCTM current sensor. The Stick-on sensor discussed and developed in Chapter 4 was modified to incorporate two sensor core-coil assemblies. The sensor core-coil assembly used for the experiment is shown in Figure 6.16(a) with its dimensions. It can be noticed that the size of the sensor core is quite small as compared to the energy harvester. Therefore, the addition of two sensor cores does not increase the

overall size and weight of the current sensor by a large percentage. Moreover, the use of small cores facilitate in keeping the cost of magnetic components low.

The cores were installed inside the Stick-on sensor with a 10 mm separation as shown in Figure 6.16(d). A signal conditioning circuit was used for converting the low-voltage AC signal developed across the sensor coil terminals to full-wave rectified signals that were read by the MCU. The signal conditioning circuit was built using micro-power operational amplifiers, and is shown in Figure 6.16(b). The algorithm given in Figure 6.7 was programmed on the TI-CC2530 that contains a ZigBee® transceiver and an industry enhanced 8051 MCU core. Further details on TI-CC2530 can be found in Chapter 4.

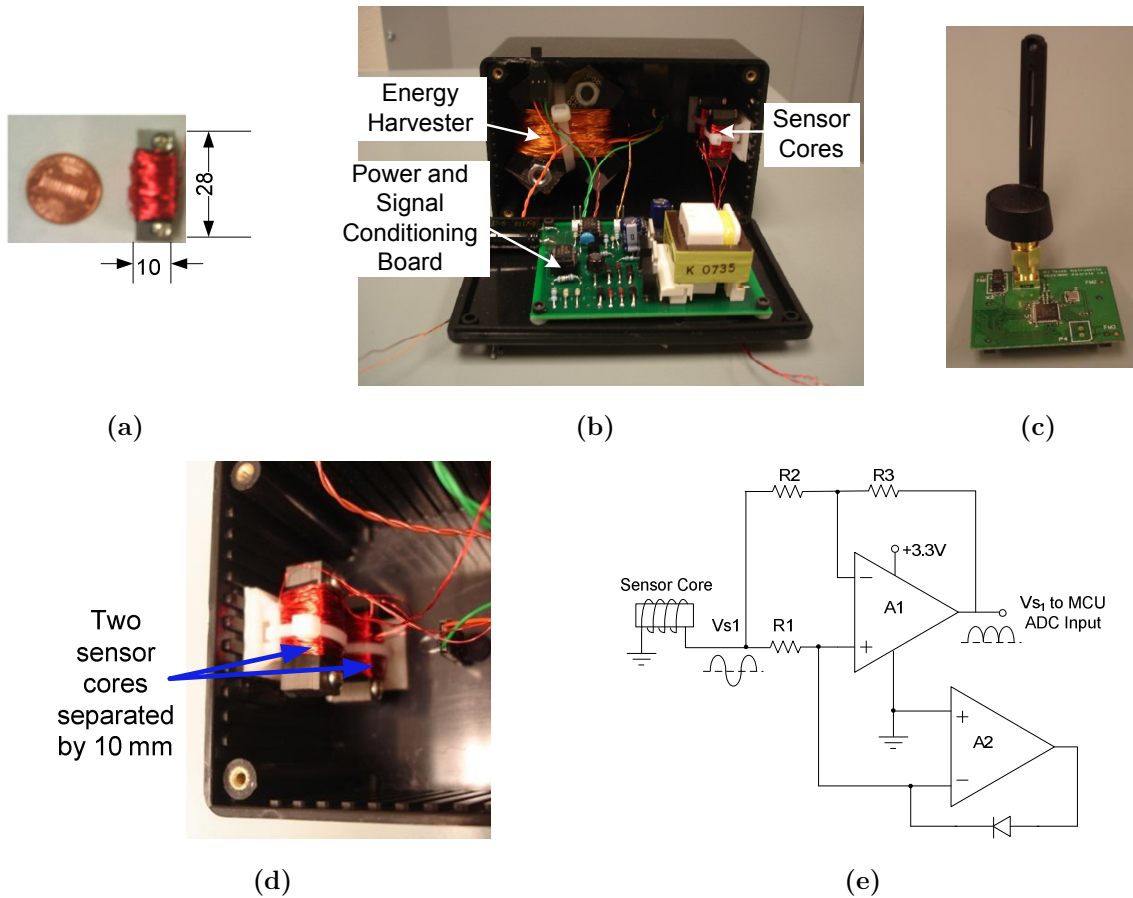


Figure 6.16: (a) Sensor core-coil assemble, (b) Stick-on sensor prototype containing the two sensor cores, (c) TI CC2530 microcontroller/ZigBee® transceiver used, (d) Zoomed in view of the sensor cores, (e) Signal conditioning circuit for sensor core signals.



## 6.6.2 Experimental Setup

An air-cored inductor that has the capability to carry variable current was used for creating far-fields. The air-cored inductor was developed using a 14 AWG wire wound around a spool. The air-cored inductor was connected to a variable AC voltage source through a resistor; this way the fields created by the air-cored inductor could be controlled by controlling the AC voltage. The far-field system was kept very close to the smart current sensor used for monitoring current in a main conductor. The air-cored inductor was designed such that in the worst case it could give rise to errors as high as 200 % in the current sensor measurements. A schematic of the far-field producing system kept close to the smart current sensor is shown in Figure 6.17.

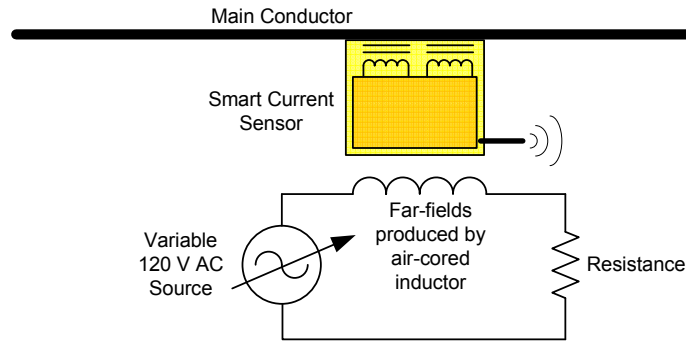


Figure 6.17: Circuit schematic of the setup for testing the smart DCTM algorithm

The smart DCTM algorithm was tested using two different experiments. In the two experiments, the position and variability of the far-fields producing air-cored inductor was chosen to be different. As before, the sensor sent the computed current values over ZigBee® to a remote coordinator. The remote coordinator was connected to a laptop through a serial-to-USB connector where the results were displayed.

### 6.6.2.1 *Experiment I*

The test system for the first test is shown in Figure 6.18. It can be seen that the sensor cores are very close to the far-field producing air-cored inductor to create the maximum disturbance. The sensor was programmed to record current measurements after every one minute. The results computed by the smart DCTM algorithm were sent to the

remote coordinator. To introduce variability in the system, the far-field and the main conductor currents were changed to follow the profile shown in Figure 6.19(a) and (b).

To begin with, the sensed current computed by the smart DCTM algorithm, shown in Figure 6.19 (b) and (c), had an error of close to 150%. Due to the variability present in the far-fields and the current in the main conductor, after a few samples, the error reduced to 7% and subsequently settled at around 2%. An important observation that needs emphasis is that once the sensor locks on to the correct solution for the sensed current, any further variation in far-fields does not affect the current computed by the sensor. Therefore, after around eight samples, the sensor became completely immune to the crosstalk created by the air-cored inductor. This experiment clearly validates the objective of far-field rejection and self-calibration by the smart DCTM algorithm.

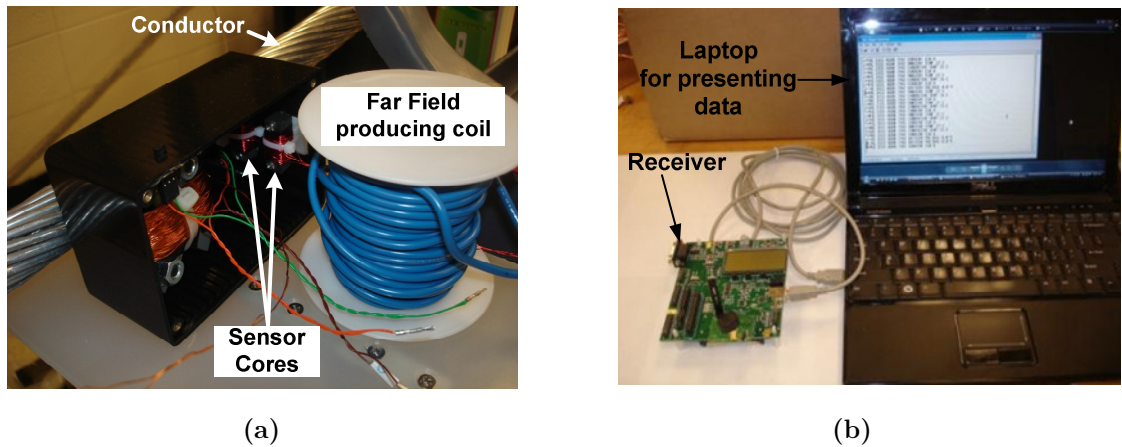


Figure 6.18: (a) Actual test setup for experiment I showing the air-cored inductor kept very close to the sensor cores to create maximum disturbance, (b) Coordinator connected to laptop

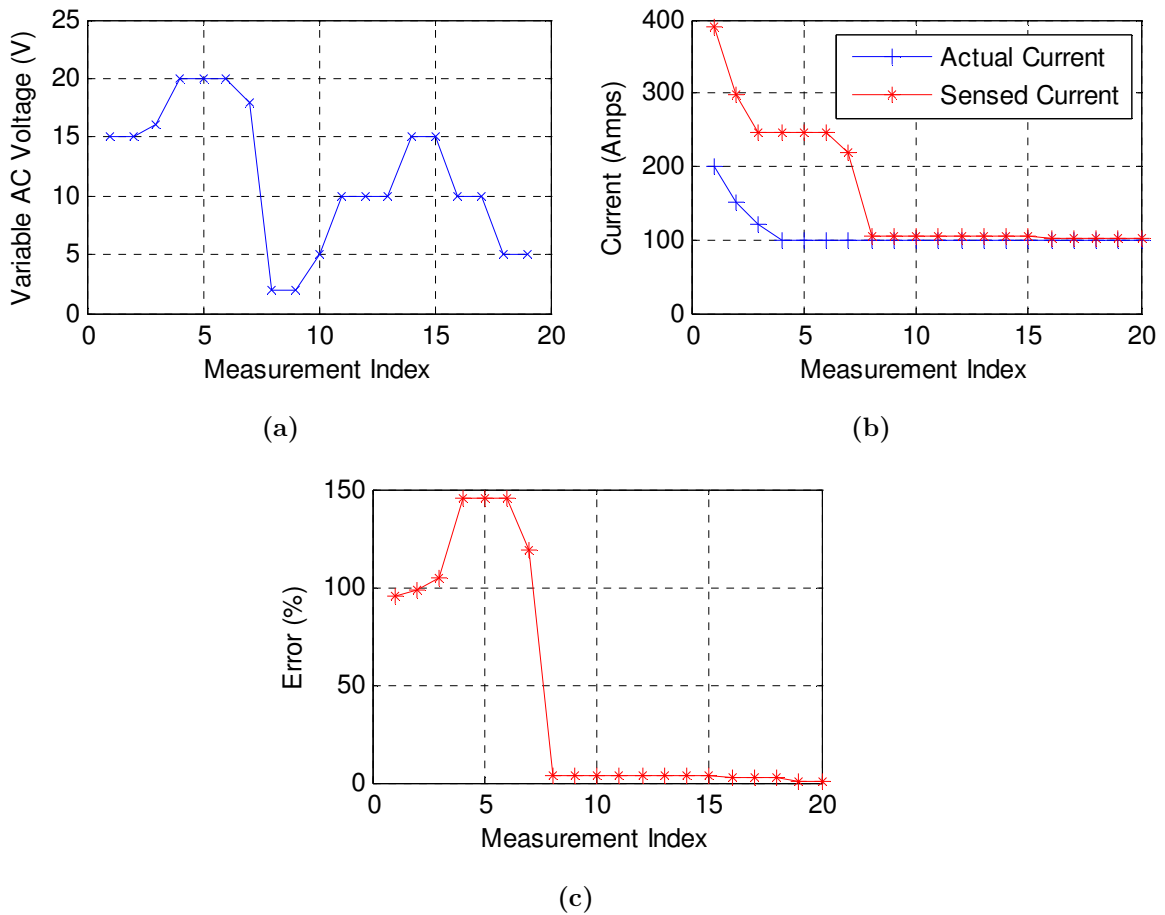
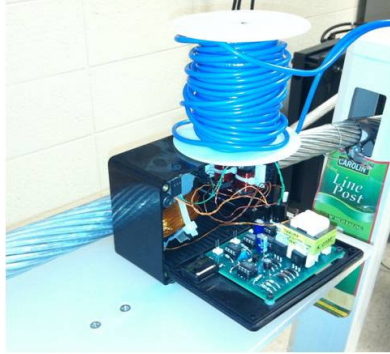


Figure 6.19: (a) Far-field profile, (b) actual current and sensed current profile, and (c) percentage error profile for experiment I.

### 6.6.2.2 *Experiment II*

In the second experiment, the position of the air-cored inductor was changed. Further, the variability in current and far-fields was also chosen to be different from experiment I. However, the experiment was conducted in a similar fashion as the first experiment, the relative position of the air-cored inductor with respect to the sensor cores is depicted in Figure 6.20. The variability of the far-fields and the main conductor current is shown in Figure 6.21(a) and (b). The error in the current computed by the smart DCTM algorithm is shown in Figure 6.21(c). It can be observed that initially, when the test started, errors on the order of 120% were present. However, again due to the variability in the main conductor current and far-fields, the error went down to 5%

ultimately. The tracking occurred at the 13<sup>th</sup> sample. Thereafter, the sensor became immune to any changes in the far-fields. An increase in the far-fields to their peak values that potentially caused a 120% error to begin with, caused little disturbance in the computed results after convergence was achieved. Further, after the 20<sup>th</sup> sample, a change in the actual current in the main conductor is tracked very well by the smart current sensor and is not affected by the far-fields.



**Figure 6.20: (a) Actual test setup for experiment II**

Successful results from both the experiments completely validate the concept of the smart DCTM algorithm.

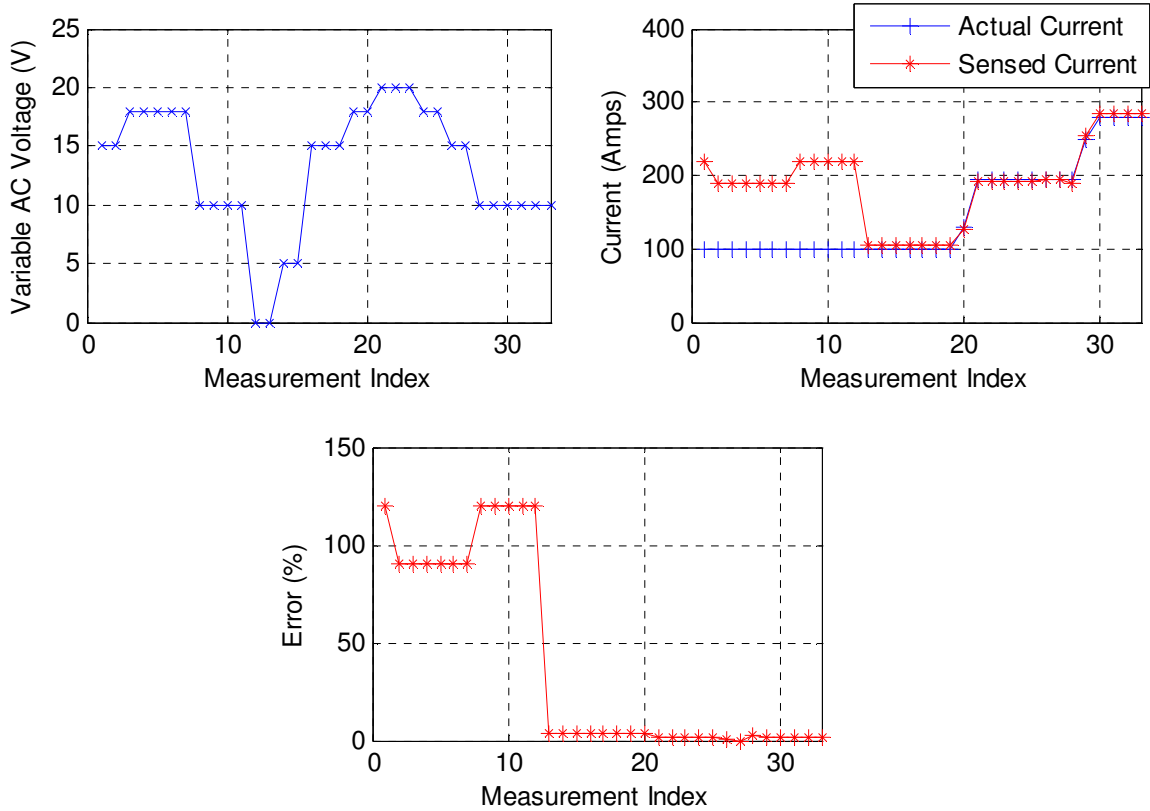


Figure 6.21: (a) Far-field profile, (b) actual current and sensed current profile, and (c) percentage error profile for experiment II. Here each data is separated by 5 sec duration. The algorithm itself does not require any specified time duration between measurements for proper functioning.

## 6.7 CONCLUSIONS

In this chapter, a modification to the MCTM algorithm for current sensing was proposed, called the smart DCTM. The DCTM approach uses two cores to reject the effects of far-fields by logging data over time and using the historical trends and variability in the near and far fields to estimate the present asset geometry and therefore current. The algorithm was developed using rigorous mathematical modeling concepts. Realistic issues such as 3-D geometries were considered, and it was shown that the DCTM algorithm can operate even in the most general scenario with multiple assets present in the vicinity of the sensor. The algorithm was tested through several simulation case studies, namely, general two independent conductor scenario, two correlated conductor scenario, and three phase conductor scenario. Various design constraints were also presented. Finally, the DCTM

method was implemented in the Stick-on sensor to demonstrate functionality. An artificial variable far-field was created using an air-cored inductor. With the help of two different experiments, successful operation of the algorithm was shown. In both the experiments, the algorithm was able to reduce errors as high as 150% to as low as 3 % over the first 10 measurements. Therefore, the proposed smart DCTM algorithm was able meet the expectations of autonomous calibration and rejection of errors due to far-fields. Consequently, the smart DCTM approach transforms the simple core-coil assembly based current sensor into a highly intelligent method, while maintaining the cost of the overall sensor low.

## CHAPTER 7

### SMART AND LOW-COST VOLTAGE SENSING

#### 7.1 INTRODUCTION

Apart from the information on current, the knowledge on voltage of a utility asset such as overhead conductors, transformer, and shunt capacitors also has high value for utilities. However, the term low-cost voltage sensing is an oxymoron in the utility domain. As discussed in Chapter 2, conventionally, potential transformers (PT) and capacitively coupled voltage transformers (CCVT) have been used for sensing voltage. However, PTs and CCVTs have high insulation requirements, usually require oil for cooling or insulation, and require regular maintenance, which makes them expensive. On the other hand, the optical voltage sensing techniques (EOVT) have been deployed by some utilities; however, due to their high costs, and limited life span, their acceptance has been limited.

The newer technologies presented in research that make use of a floating sensor on a high voltage asset look promising as they are free from high voltage insulation requirements. However, they suffer from the at least one of the following limitations:

- Most of the sensors require field calibration that are very expensive
- The construction of the sensor is challenging
- The algorithm used to compute the voltage is complex and requires a lot of computing power
- The implementation of the sensor in a low-power module is difficult
- The sensor is constrained in its application, for example, can work only in a three-phase system
- The sensor is sensitive to variations in distance to ground, nearby assets, electric fields from nearby assets, and changes in atmospheric conditions.

Moreover, most of the above solutions aim at developing voltage sensors for revenue grade metering applications. In such applications, the errors are required to be on the

orders of 0.1 - 1 %. Therefore, there exists a clear gap in the opportunity space for applications that require moderate accuracy of voltage sensing. Here, low-cost sensing solutions are required that can be deployed and scaled on the utility networks. A single solution that can be used on multiple voltage levels, medium (<35 kV), sub-transmission and transmission level (> 35 kV) voltages has significantly higher value than expensive single point solutions. Applications, such as use of sensors to find the energized-status of assets in a smart substation (finding whether a particular asset is energized or not), are of paramount importance to the utilities. In such applications, very high accuracy of measurement (up to 1%) is not relevant; in fact, if the sensor is able to monitor and track voltage changes with moderate (up to 5-10%) accuracy levels, the sensor will still have considerably larger acceptance by the utilities than conventional voltage sensors.

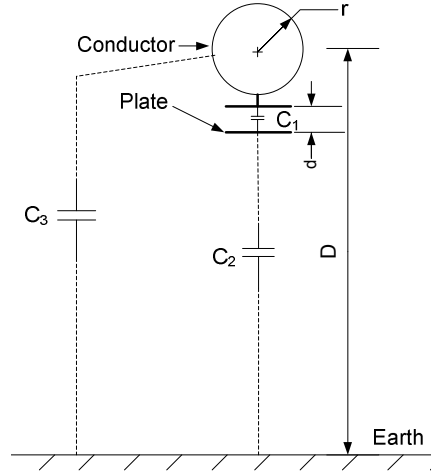
In this chapter, a novel low-cost voltage sensing solution is proposed. The chapter begins by introducing the challenges of voltage sensing, such as need for calibration, effects of far-fields, and effects of distance to ground. Subsequently, a mathematical model for a floating sensor is derived to better understand the factors that affect accuracy of the sensor and challenges with voltage sensing. Thereafter, using some valid assumptions a new algorithm for voltage sensing is proposed. Next, extensive simulation studies are presented to test the algorithm and proposed voltage sensing concept. Finally, the chapter is concluded with experimental results of the sensor operating at up to 35 kV voltage levels.

## **7.2 CHALLENGES WITH VOLTAGE SENSING**

It is evident that to reduce the cost by orders of magnitude as compared to conventional PTs and CCVTs, the use of floating sensors is necessary. Essentially, such a voltage sensor physically and electrically floats on the asset, which reduces its insulation requirements and therefore cost. However, many challenges need to be addressed before any meaningful voltage sensing can be performed using these floating sensors.



Consider an inexpensive voltage sensor floating from a conductor which has a configuration similar to that used for electric field energy harvesting in Section 3.2. Figure 7.1 shows the considered two-plate configuration for voltage sensing. In a typical transmission line,  $D$  will be much larger than  $d$ . This results in  $C_1$  being very large as compared to  $C_2$ .



**Figure 7.1: A simple two plate system of voltage sensing of a single overhead conductor**

Further, consider an RC filter used across the capacitor  $C_1$  for measuring the voltage across  $C_1$ . Then, the value of displacement current is given by

$$i_D = \frac{V_l}{\frac{1}{j\omega C_2} + \frac{1}{j\omega(C_1 + C)R}} \quad (169)$$

Given that  $\omega CR$  is designed to be much greater than 1,  $C \gg C_1$  and  $C_1 \gg C_2$ ,  $i_D$  simplifies to

$$i_D = j\omega C_2 V_l \quad (170)$$

The voltage measured across capacitor  $C_2$  becomes

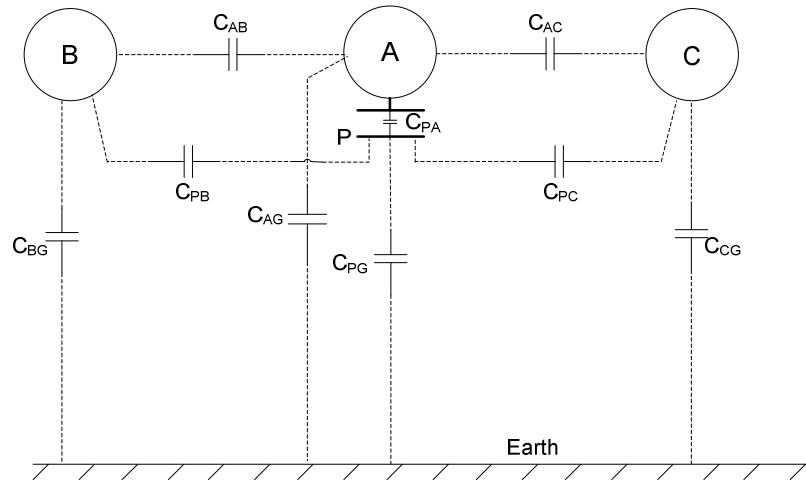
$$V_{c1} = i_D \frac{R}{1 + j\omega CR} \quad (171)$$

But,  $\omega CR \gg 1$ ,  $V_{c1}$  simplifies to

$$V_{c1} = \frac{C_2}{C} V_l \quad (172)$$

In the above equation, it can be seen that the voltage across capacitor  $V_{c1}$  is directly proportional to the line voltage  $V_l$  and capacitance  $C_2$ , between the lower plate and the earth. Further,  $C_2$  is a function of the distance of the conductor from the ground. A decrease (increase) in this distance is expected to increase (decrease) the capacitance; hence, change the voltage measured. Therefore, the information on sag of the conductor and its voltage is embedded in the measured voltage  $V_{c1}$ . However, the task of decoupling the voltage of the conductor from the capacitance  $C_2$  is not trivial.

In a realistic system, there are three conductors for the three phases, each carrying AC currents separated in phase by  $120^\circ$ . Therefore, the other conductors will also have an influence on the displacement current flowing through capacitor  $C_2$ . Modeling the effects of other conductors on the capacitor  $C_2$  can be quite complex. Figure 7.2 shows the configuration of the considered system and Figure 7.3 shows the electrical model of the system. A, B and C represents the three phase conductors, P represents the plate used to sense the voltage of conductor A.



**Figure 7.2: Voltage sensing using a floating two plate capacitor on a three phase overhead conductor system**

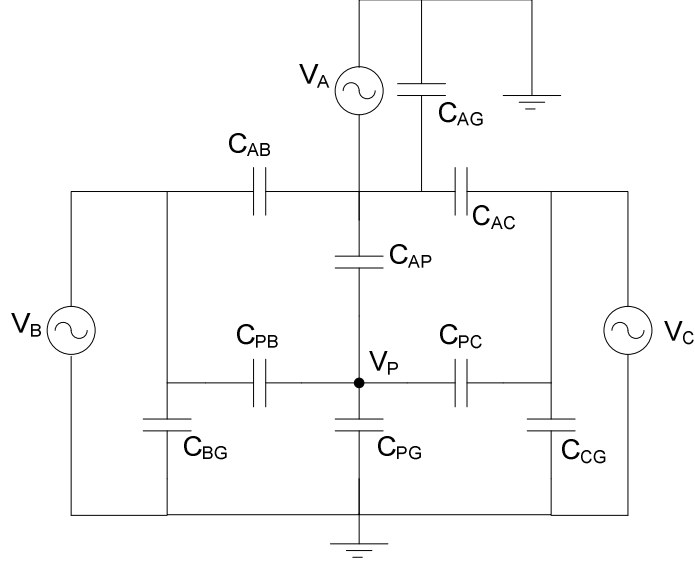


Figure 7.3: Electrical equivalent circuit of the system shown in Figure 7.2

Using nodal analysis, the voltage at P can be found and is given as

$$V_P = \frac{V_A C_{PA} + V_B C_{PB} + V_C C_{PC}}{C_{PA} + C_{PB} + C_{PC} + C_{PG}} \quad (173)$$

It should be noted that  $V_A$ ,  $V_B$  and  $V_C$  are phasor voltages given by

$$V_A = V, V_B = Ve^{-j120}, V_C = Ve^{j120}$$

Replacing the phasor values of  $V_A$ ,  $V_B$  and  $V_C$  in (173), we get

$$V_P = V \left[ \frac{(C_{PA} - (C_{PB} + C_{PC})/2) + j\sqrt{3}(C_{PB} + C_{PC})/2}{C_{PA} + C_{PB} + C_{PC} + C_{PG}} \right] \quad (174)$$

Another simplification that can be applied to the above equation is that  $C_{PA} \gg C_{PB}, C_{PC}, C_{PG}$ . Using this assumption, (174) reduces to

$$V_P \simeq V \quad (175)$$

The current in capacitor  $C_{PG}, C_{PB}, C_{PC}$  is found as

$$I_{PG} = j\omega C_{PG} V_P = j\omega C_{PG} V \quad (176)$$

$$I_{PB} = j\omega C_{PB} (V - Ve^{-j120}) = \sqrt{3}\omega C_{PB} Ve^{j120} \quad (177)$$

$$I_{PC} = j\omega C_{PC} (V - Ve^{j120}) = \sqrt{3}\omega C_{PC} Ve^{j60} \quad (178)$$

The current flowing from conductor A to plate P which charges the capacitor  $C_{AP}$  can be given as the sum of displacement currents flowing in the neighboring conductors and to the ground,

$$I_{PA} = I_{PG} + I_{PC} + I_{PB} \quad (179)$$

The use of (176) (177) (178) simplifies  $I_{PA}$  to

$$I_{PA} = \omega V \left( \frac{\sqrt{3}}{2} (C_{PC} - C_{PB}) + j \left( C_{PG} + \frac{3}{2} (C_{PC} + C_{PB}) \right) \right) \quad (180)$$

The voltage across the two plates of the capacitor can be found as

$$V_{AP} = \frac{I_{AP}}{j\omega C_{PA}} \quad (181)$$

Plugging the value of  $I_{AP}$  from (180) into (181) gives

$$V_{PA} = \frac{V}{C_{PA}} \left( C_{PG} + \frac{3}{2} (C_{PC} + C_{PB}) + j \frac{\sqrt{3}}{2} (C_{PB} - C_{PC}) \right) \quad (182)$$

$V_{PA}$  is the voltage across the plates being sensed to estimate the value of the voltage of the conductor A. In (182),  $C_{PG}$  is a function of the distance of the plate to ground, while,  $C_{PB}$  and  $C_{PC}$  is a function of distance of the plate from conductor B and C, respectively. As before, the voltage  $V_{PA}$  contains information on the voltage of the conductor and its distance from the ground with the additional information on its distance from the other conductors.

One way to compute the value of voltage is to calibrate the sensor at the time of installation. However, as the goal of this research is to develop low-cost sensing solutions, if the sensor were to be calibrated, the effective cost of the sensor would increase and the purpose of the research would be defeated. A similar issue for current sensing was elaborated in Chapter 5. Therefore, an approach has to be developed for voltage sensing which can assure self-calibration of the sensor. Such an approach is not found in the state-of-the-art discussed in Chapter 2.

Further, other challenges associated with sagging of the conductors, which effectively changes  $K$ , and introduce errors in measurements have to be investigated. Further, it is also of interest to make the technique independent of the system configuration. As is evident from the discussion in this section, voltage sensing using floating sensors is riddled with challenges. All these challenges have been addressed systematically in the sections to follow. A mathematical model of the relationship between the displacement current and the asset voltage can help to decode the problems, and consequently, solve them.

### 7.3 A MATHEMATICAL MODEL OF THE VOLTAGE SENSOR

Consider a simple case of a single conductor above the earth as seen in Figure 7.4. The sensor plate is in the form of a sector, having a sector-angle given by  $\psi_N$ , and the radial distance of the sectored sensor from the center of the conductor is  $r$ . Further, the value of  $r$  is very close to the radius of the conductor, and very small as compared to the distance of the conductor above the earth,  $R$ , i.e.  $R \gg r$ .

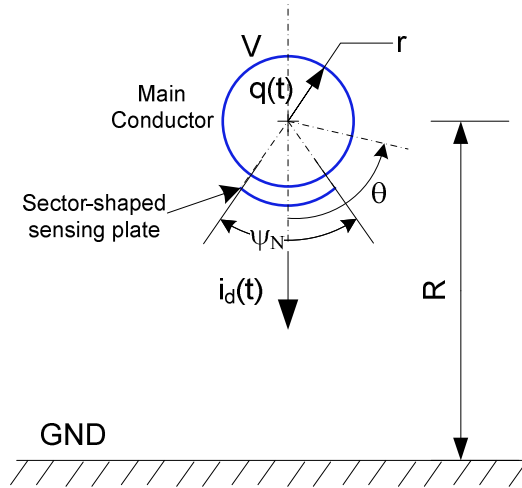


Figure 7.4: Single Conductor above the Earth

The objective is to find the displacement current produced by the conductor  $i_d(t)$  as a function of  $r$ ,  $R$ ,  $\psi_N$  and the voltage of the asset  $V$ . This requires solving the Laplace differential equation given by (183)

$$\frac{1}{\rho} \frac{\partial}{\partial \rho} \left( \rho \frac{\partial \Phi}{\partial \rho} \right) + \frac{1}{\rho^2} \frac{\partial^2 \Phi}{\partial \theta^2} = 0 \quad (183)$$

The particular solution to (184) has a general form given by

$$\Phi(\rho, \theta) = \left( A\rho^m + \frac{B}{\rho^m} \right) (C \cos(m\theta) + D \sin(m\theta)), m = 1, 2, 3... \quad (184)$$

An alternate approach is to use the method of images. Whereby, the earth is considered to be an infinite plane having an infinite conductance. Any charged surface above the earth will have an image having a negative charge below the earth at an equal distance from the earth's surface. The electric fields inside the earth are zero as it is a perfect conductor and exist only above the earth. The detailed derivation of the displacement current for such a case is given in Appendix E. The expression obtained for the displacement current is given by

$$i_d(t) = \frac{\psi_N l \epsilon d}{R \ln \left| \frac{R-r+d}{R-r-d} \right|} \left( 1 + \frac{r}{R} \cos \theta \right) \frac{dV}{dt} \quad (185)$$

where

$$d = \pm \sqrt{R^2 - r^2},$$

$\psi_N = 2\pi/N =$  Angular length of the voltage sensor plate,

$N =$  A number greater than 1,

$\theta =$  Angular displacement,

$l =$  Length of the sensor.

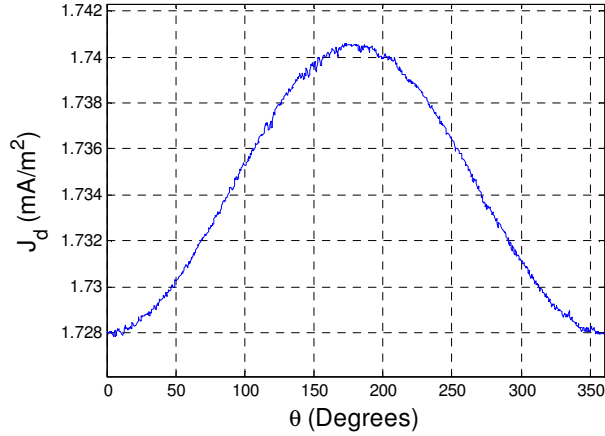
If  $V = V_m \sin(\omega t)$ , (185) can be written as

$$i_d = \frac{\psi_N l \epsilon d \omega}{R \ln \left| \frac{R-r+d}{R-r-d} \right|} \left( 1 + \frac{r}{R} \cos \theta \right) V_m \cos(\omega t) \quad (186)$$

In terms of phasor quantities,

$$\tilde{I}_d = \frac{j\psi_N l \varepsilon d \omega}{R \ln \left| \frac{R-r+d}{R-r-d} \right|} \left( 1 + \frac{r}{R} \cos \theta \right) \tilde{V} \quad (187)$$

The nature of displacement current variation with spatial angle around the conductor was validated using an FEA simulation through ANSYS® Maxwell, as shown in Figure 7.5.



**Figure 7.5: Variation of current density around a concentric circle with the conductor having radius 20 mm for a 115 kV line 30 m above the earth.**

The variation of displacement current with a change in the angular position  $\theta$  can be used to estimate the value of voltage and has been demonstrated in [29]. However, for a realistic application, this variation is very difficult to detect and implement. Take the example of Figure 7.5, the peak-to-peak variation of the displacement current density is on the order of  $10 \mu\text{A}/\text{m}^2$ , already extremely small to detect. Detecting a 10% variation in the displacement current density would imply detecting a change of  $1 \mu\text{A}/\text{m}^2$  of displacement current density, even more difficult to measure. Therefore, a prudent direction is the use of the average value of the displacement current than the variation. As a matter of fact, if the assumption that  $R \gg r$  is indeed true, (187) reduces to its average value

$$i_d \simeq \frac{\psi_N l \varepsilon \omega}{\ln \left| \frac{2R}{r} \right|} V_m \cos(\omega t) \quad (188)$$

In terms of phasor quantities

$$\tilde{I}_d = j \frac{\psi_N l \varepsilon \omega}{\ln \left| \frac{2R}{r} \right|} \tilde{V} \quad (189)$$

Equation (189) can be represented as

$$\tilde{I}_d = Y \tilde{V} \quad (190)$$

Equation (190) can be used to estimate the value of voltage on the conductor. However, this equation has essentially three variables, voltage, distance of the conductor from the earth, and electrical permittivity. Without any knowledge of two variables, it is not possible to estimate the third. If it was assumed that the electrical permittivity does not change dramatically, and it can be considered fairly constant over a given period of time. Even then, the equation has two unknowns and only one equation to solve for the unknowns; therefore, a solution is not possible. A similar problem of self-calibration was discussed in current sensing (Section 5.2). Therefore, possibly an approach similar to that used for smart current sensing can be used here; where historical data is saved over time in the sensor memory and is used to estimate the value of present voltage. However, unlike current, the voltage of an asset does not vary over a large range, and therefore, the problem can be simplified with the knowledge of typical profiles of voltage and distance over time.

## 7.4 ALGORITHM DEVELOPMENT

### 7.4.1 Information on Typical Profiles of Voltage and Distance

#### 7.4.1.1 *Voltage Profile*

For a given class of overhead conductor or a utility asset, the mean RMS voltage is constant over long periods of time. In reality, the RMS voltage has a maximum of  $\pm 5\%$  variation over time, but on a large time scale, the averaging of the RMS voltage gives a



fixed known value. Further, an inherent variability at any time is always present in the RMS voltage of the asset and is on the order of  $\pm 1\%$  -  $\pm 5\%$ .

#### *7.4.1.2 Distance Profile*

The variation in the distance of the conductor above the earth occurs due to either heating of the conductor or galloping in the presence of strong winds. Heating of the conductor is dependent on the loading of the line, ambient and conductor temperature and wind speed. The time constant of heating is large, and a considerable variation occurs only over longer durations. For instance, a variation of a few centimeters might occur over a period of several hours.

On the other hand, galloping of the conductor due to strong winds leads to fast changes in the distance of the conductor above ground. However, these changes are limited due to the tension on the conductor. Whereas, heating causes more pronounced changes in the distance of conductor to ground. Moreover, in other applications, such as voltages sensing in transformers, and capacitor banks, the changes in distance of the high voltage bushing may not be a prominent issue. Therefore, it is fair to assume that the change in distance occurs slowly as compared to the variability in voltage. Over the course of a day, this change could be linearly decreasing, linearly increasing or sinusoidally varying, depending on whether the temperature of the conductor is linearly increasing, decreasing or is a combination of both.

For a utility asset, such as a conductor, the information on the typical profiles of RMS voltage and distance from the earth was leveraged to formulate an algorithm.

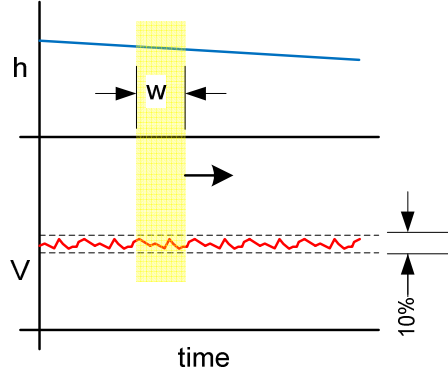
### **7.4.2 Single Phase Application**

In this section, an algorithm is proposed that uses a window of width  $w$ , which spans over the collected data points over time, and uses the averaged information over the window to compute the present results. A windowed average of size  $w$  taken at the  $n^{\text{th}}$  interval spanning all data points from  $(n-w+1)^{\text{th}}$  to  $n^{\text{th}}$  sample gives

$$\langle \tilde{I}_d \rangle_{n,w} = \langle Y \tilde{V} \rangle_{n,w} \quad (191)$$

where  $\langle p \rangle_{n,w} = \frac{\sum_{k=n-w+1}^n p_k}{w}$

The moving windowed averaging of data points is depicted in Figure 7.6.



**Figure 7.6: Comparison of the variation of voltage and height of an overhead conductor**

Over a relatively small window, the variation in  $Y$  is not large, and  $Y_n$  can be assumed constant over the window length, which gives

$$\langle \tilde{I}_d \rangle_{n,w} = Y_n \langle \tilde{V} \rangle_{n,w} \quad (192)$$

Inverting  $V$  gives the estimated value of  $Y_n$  as

$$Y_n = \langle \tilde{I}_d \rangle_{n,w} \langle \tilde{V} \rangle_{n,w}^{-1} \quad (193)$$

The average value of  $I_d$  over the specified window can be computed if the past data of  $I_d$  was saved. The realistic assumption that the average voltage of the line over a period of time remains constant can be used to get an estimate of  $Y$  as

$$\langle \tilde{V} \rangle_{n,w} = V_{class} \quad (194)$$

$$\hat{Y}_n = \frac{\langle \tilde{I}_d \rangle_{n,w}}{V_{class}} \quad (195)$$

Subsequently, at the  $(n+1)^{\text{th}}$  measurement index, the update-expressions for all the parameters are given by

$$\widehat{Y}_{n+1} = \widehat{Y}_n + \frac{\left( \frac{\tilde{I}_{d_{n+1}} - \tilde{I}_{d_{n-w+1}}}{w} \right)}{V_{class}} \quad (196)$$

$$\widehat{V}_{n+1} = \left( \frac{\tilde{I}_{d_{n+1}}}{\widehat{Y}_{n+1}} \right) \quad (197)$$

$$\widehat{R}_{n+1} = \frac{r}{2} \exp\left( \frac{\psi_N l \varepsilon \omega}{\widehat{Y}_{n+1}} \right) \quad (198)$$

The proposed moving average voltage sensing (MAVS) algorithm can be used to compute the value of voltage and distance from the earth for all possible measurement indices after the first window index. This implies that only after the first  $w$  measurements would the sensor be self-calibrated, and give meaningful results. To solve this problem, the sensor can be programmed to take multiple measurements at a relatively fast speed in the beginning, and thereafter, slow down. This strategy can help reduce the time for convergence to the true solution.

The flowchart for the algorithm is given in Figure 7.7.

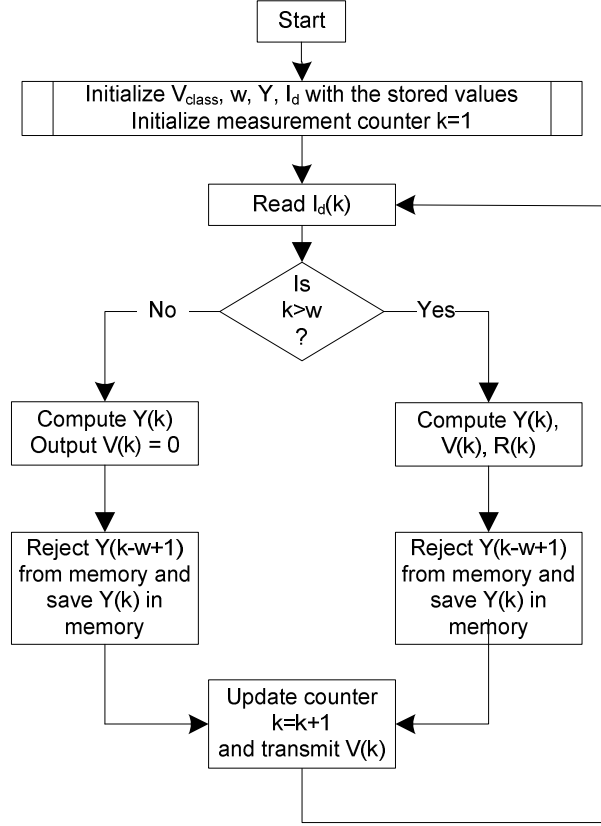


Figure 7.7: Flowchart for implementing the MAVS algorithm on a microcontroller

### 7.4.3 Three Phase Application

Many utility assets that require voltage sensing have three phases. As the goal of this research is to develop sensors on a per phase basis, the issue of electric field interaction from the other two phases also needs to be considered. A mathematical model of the voltage sensor for a multi-conductor case is derived in [113] and is given by

$$\frac{dV_i}{dt} = \frac{1}{2\pi\epsilon} \left[ \sum_{k=1}^n I_{d_k} \ln \left( \frac{1}{d_{ik}} \right) \right] \quad (199)$$

where

$I_{d_k}$  = Capacitive charging current flowing out of  $k^{\text{th}}$  conductor,

$d_{ii} = r_i =$  radius of  $i^{\text{th}}$  conductor,

$d_{ik} =$  distance between  $i^{\text{th}}$  and  $k^{\text{th}}$  conductor,

$V_i =$  Voltage of  $i^{\text{th}}$  conductor.

The derivation assumes that the charge distribution on the surface of the conductor is uniform, i.e.  $R \gg r$ . The expression given in (199) can be converted to phasors by assuming

$$V_i = \text{Re} \left\{ \sqrt{2} \tilde{V}_i e^{j\omega t} \right\} \quad (200)$$

$$I_{di} = \text{Re} \left\{ \sqrt{2} \tilde{I}_{di} e^{j\omega t} \right\} \quad (201)$$

$$\tilde{V}_i = \frac{1}{j\omega 2\pi\epsilon} \left[ \sum_{k=1}^n \tilde{I}_{dk} \ln \left( \frac{1}{d_{ik}} \right) \right] \quad (202)$$

The phasor equation can be written in the form of a matrix as

$$\begin{bmatrix} \tilde{V}_1 \\ \tilde{V}_2 \\ \vdots \\ \tilde{V}_n \end{bmatrix} = \begin{bmatrix} x_{11} & x_{12} & \cdots & x_{1n} \\ x_{21} & x_{22} & \cdots & x_{2n} \\ \vdots & \cdots & \ddots & \vdots \\ x_{n1} & x_{n2} & \cdots & x_{nn} \end{bmatrix} \begin{bmatrix} \tilde{I}_{d1} \\ \tilde{I}_{d2} \\ \vdots \\ \tilde{I}_{dn} \end{bmatrix} \quad (203)$$

$$V = XI_d \quad (204).$$

The intent is to find the displacement currents in terms of V. In typical cases, the value of n is three. For a balanced 3-phase system, the displacement currents are also expected to be balanced and are 120 degrees phase apart. The sequence component transformation can be used to simplify analysis. If a transformation T is defined as

$$T = \frac{1}{3} \begin{bmatrix} 1 & a & a^2 \\ 1 & a^2 & a \\ 1 & 1 & 1 \end{bmatrix} \quad (205)$$

where

$$a = e^{j\frac{2\pi}{3}} \quad (206)$$

such that

$$V_{120} = TV_{abc} \quad (207)$$

and

$$I_{120} = TI_{abc} \quad (208)$$

Then,

$$V_{120} = TXT^{-1}I_{120} \quad (209)$$

X is a symmetric matrix with,

$$x_{12} = x_{21}, \quad x_{32} = x_{23}, \quad x_{13} = x_{31} \quad (210)$$

To simplify computation of  $TXT^{-1}$ , it is assumed that,  $x_{11} = x_{22} = x_{33} = x_s$  i.e. the radius of all the conductors is the same (a good approximation). Further, it is assumed that  $x_{12} = x_{23} = x_{13} = x_m$  i.e. all the other conductors are considered to be at an equal distance  $d_{eq}$  from the conductor of interest. Using these simplifications,  $TXT^{-1}$  reduces to

$$TXT^{-1} = \begin{bmatrix} x_s - x_m & 0 & 0 \\ 0 & x_s - x_m & 0 \\ 0 & 0 & x_s - 2x_m \end{bmatrix} \quad (211)$$

Even if the assumptions were not considered, the off-diagonal elements of  $TXT^{-1}$  for almost any practical geometry of conductors are negligible as compared to the diagonal elements. This fact is used regularly in power systems research [113]. Therefore, the expressions of the decoupled sequence components are obtained as

$$V_1 = I_1(x_s - x_m) \quad (212)$$

$$V_2 = I_2(x_s - x_m) \quad (213)$$

$$V_0 = I_0(x_s - 2x_m) \quad (214)$$

Using the first equation,

$$I_1 = j \frac{2\pi\omega\epsilon V_1}{\left( \ln \frac{1}{r} - \ln \frac{1}{d_{eq}} \right)} = j \frac{2\pi\omega\epsilon V_1}{\ln \frac{d_{eq}}{r}} \quad (215)$$

Under balanced operation, the magnitude of positive sequence component is the same as the magnitude of the abc phase components, and is given by

$$I_{rms} = \frac{2\pi\omega\epsilon}{\ln \frac{d_{eq}}{r}} V_{rms} \quad (216)$$

It can be observed that the general form of (216) is the same as the expression for displacement current in a single conductor above the earth. Therefore, the algorithm designed for the single phase conductor system will work even with the three phase conductors. However, in the three phase analysis, the effect of the earth was not considered. If the effect of the earth is taken into account, the following relationship is obtained:

$$\tilde{V}_i = \frac{1}{j\omega 2\pi\epsilon} \left[ \sum_{k=1}^n \tilde{I}_k \ln \left( \frac{d'_{ik}}{d_{ik}} \right) \right] \quad (217)$$

Where,  $d'_{ik}$  = the distance of the  $i^{\text{th}}$  conductor from the image of the  $k^{\text{th}}$  conductor.

To simplify analysis, assume that the images of all the conductors are lumped together to get an equivalent image at a distance  $d'_{eqo}$  from all the other conductors. The equivalent distance of the conductor where the sensor is mounted from its own image is given by  $d'_{eqs}$ . The rest of the assumptions are the same as before. Performing a similar analysis as before gives

$$I_1 = j \frac{2\pi\omega\epsilon V_1}{\left( \ln \frac{d'_{eqs}}{r} - \ln \frac{d'_{eqo}}{d_{eq}} \right)} = j \frac{2\pi\omega\epsilon V_1}{\ln \frac{d'_{eqs} d_{eq}}{r d_{eqo}}} \quad (218)$$

If it was assumed that

$$D_{eq} = \frac{d'_{eqs} d_{eq}}{d_{eqo}}$$

Then

$$I_{rms} = \frac{2\pi\omega\epsilon}{\ln \frac{D_{eq}}{r}} V_{rms} \quad (219)$$

Evidently, the form of (219) is again the same as with the single conductor case. The difference in the three-phase and single-phase case is that the distance to ground in a single phase case has been replaced with some unknown equivalent distance in a three phase case. Therefore, in the case of a three-phase system, it is not possible to compute the distance of the conductor to ground. Nevertheless, the goal of this research is finding the voltage and not the equivalent distance or sag of the conductor.

Finally, the approach of lumping all the far-field producing conductors into one single far-field conductor can be used even in the case of multiple conductors in the vicinity. Therefore, the approach can be generalized for an n-conductor system. As the general form of the governing equation relating the displacement current to the voltage remains the same, the algorithm proposed for a single conductor case will also be applicable to an n-conductor scenario to compute voltage.

## **7.5 SIMULATION STUDIES**

Several simulation case studies were conducted to test the MAVS algorithm under various operating conditions. The case studies are given in the following sub-sections.

### **7.5.1 Case Study I: Single Phase Conductor – MATLAB® Simulations**

In this study, the geometry of a typical 115 kV overhead line was considered. Several cases were simulated with the RMS voltage profile varied to have either a normal distribution or a sinusoidal profile over time. Simultaneously, the distance of the conductor to ground was also varied over time either linearly or sinusoidally. The details of all the cases are given in Table 7.1. The variation in the RMS voltage is purposely kept small to mimic a real world scenario.



Table 7.1: Test Cases for Single Conductor Above the Earth

| Case | Voltage Profile     |  | Distance Profile |  | Window Size |
|------|---------------------|--|------------------|--|-------------|
|      | Nature              | Parameter                                      | Nature           | Parameter                              |             |
| 1    | Normal Distribution | $\mu = 115 \text{ kV}, \sigma = 10 \text{ kV}$ | Linear Drop      | 30 m to 20 m                           | 100         |
| 2    | Normal Distribution | $\mu = 115 \text{ kV}, \sigma = 10 \text{ kV}$ | Linear Drop      | 30 m to 10 m                           | 25          |
| 3    | Sinusoidal          | $\mu = 115 \text{ kV}, A = 10 \text{ kV}$      | Linear Drop      | 30 m to 10 m                           | 20          |
| 4    | Sinusoidal          | $\mu = 115 \text{ kV}, A = 10 \text{ kV}$      | Sinusoidal       | $\mu = 20 \text{ m}, A = 10 \text{ m}$ | 20          |

The simulation results for all the cases are shown in Figure 7.8 - Figure 7.12. In all the cases, it can be observed that the error in voltage goes down to below 2% after the window index. Further, the algorithm is able to provide a fairly good approximation of the distance to ground.

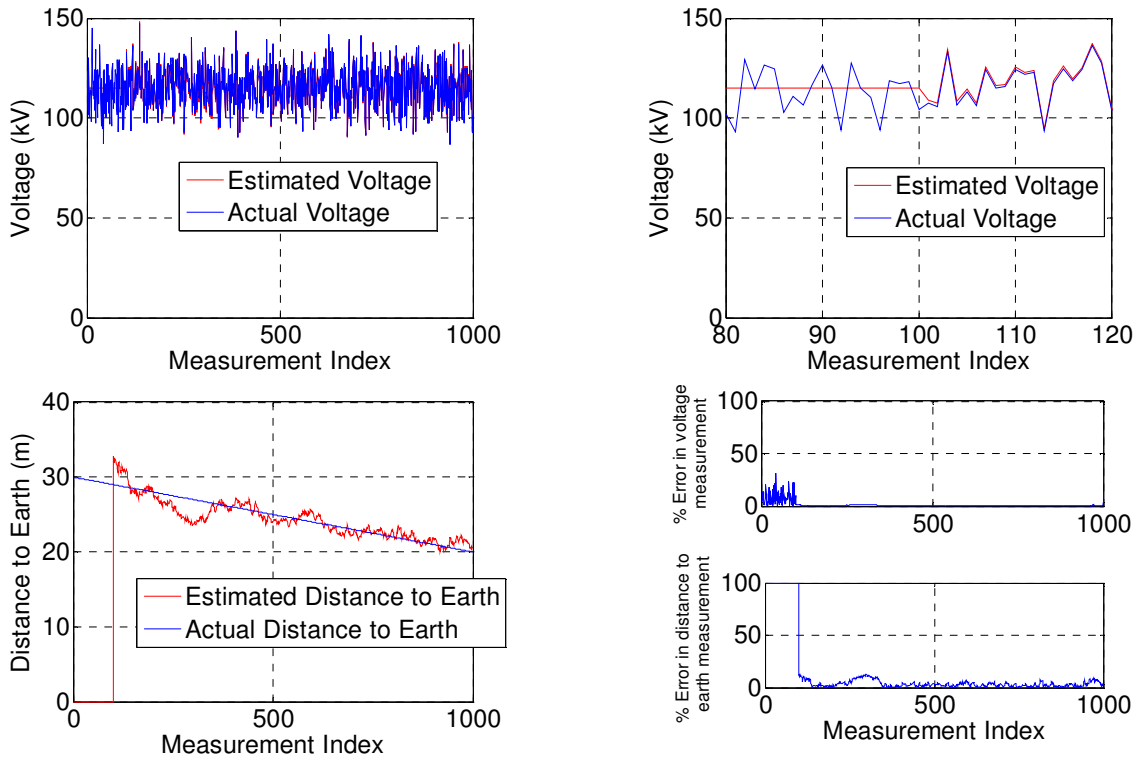


Figure 7.8: Case 1: Voltage is normally distributed with 115 kV mean and 10 kV std dev, Distance linearly drops from 30 m to 20m, algorithm window size is 100

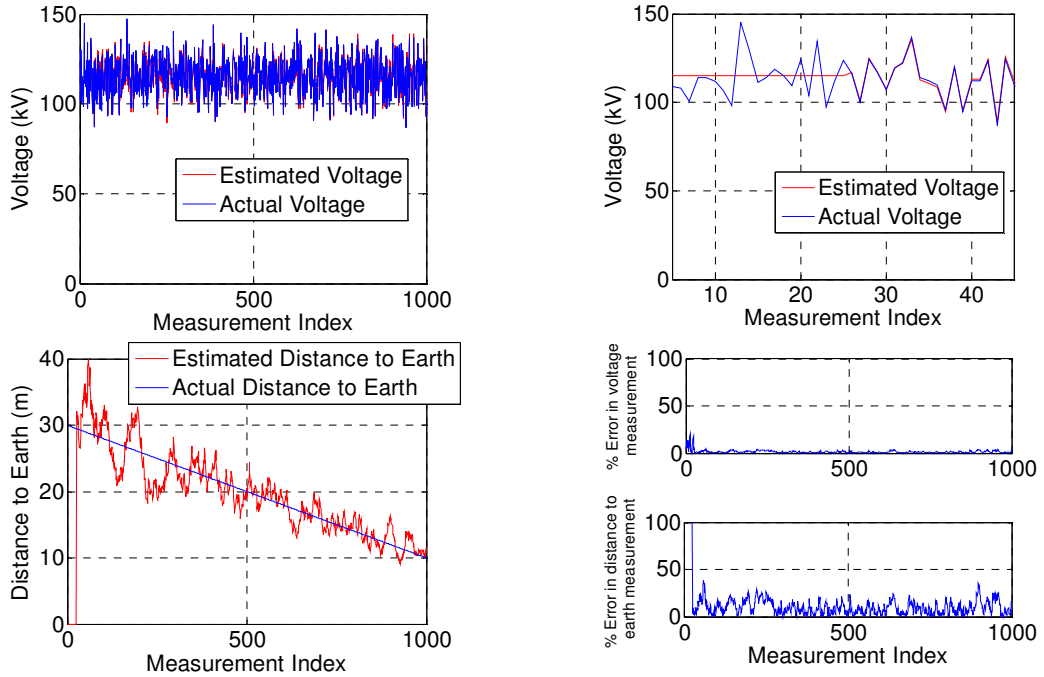


Figure 7.9: Case 2: Voltage is normally distributed with 115 kV mean and 10 kV std dev, distance linearly drops from 30 m to 10m, algorithm window size is 25

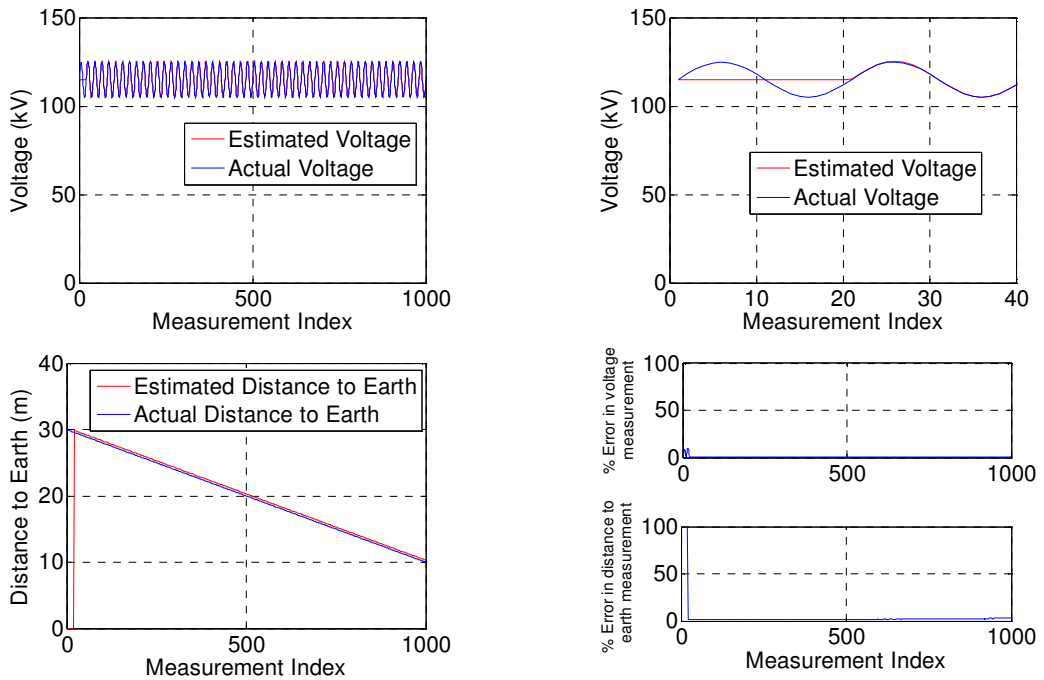


Figure 7.10: Case 3: Voltage has sinusoidal variation about a mean of 115 kV mean and 10 kV peak, distance linearly drops from 30 m to 10m, algorithm window size is 20

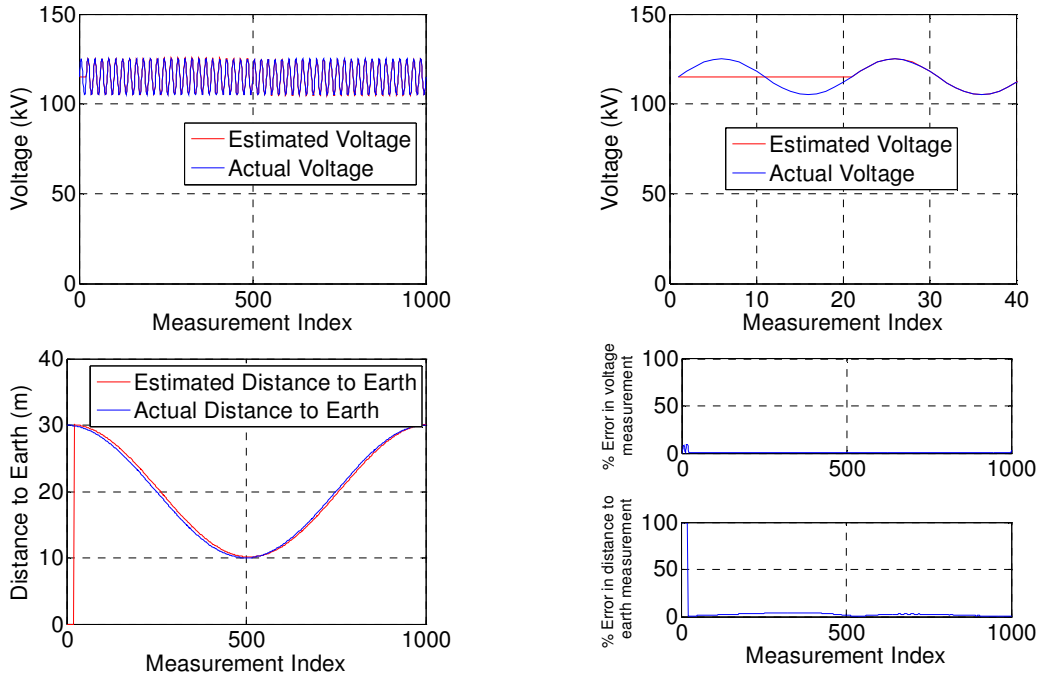


Figure 7.11: Case 4: Voltage has sinusoidal variation about a mean of 115 kV mean and 10 kV peak, distance also has a sinusoidal variation about a mean of 20 m and 10 m peak, algorithm window size is 20

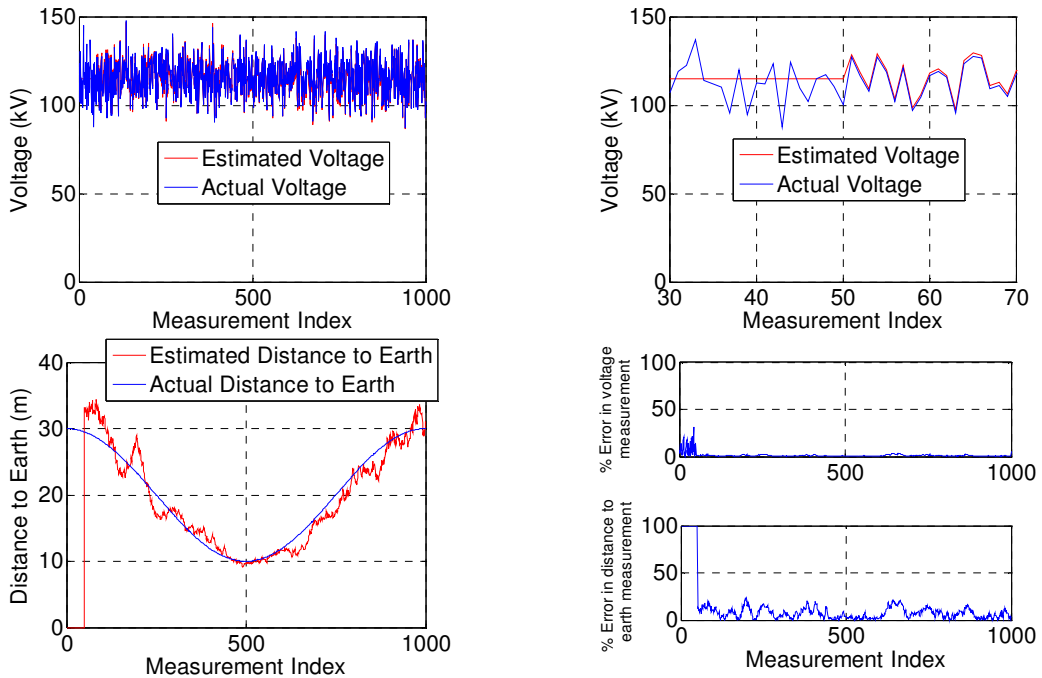


Figure 7.12: Case 5: Voltage is normally distributed with 115 kV mean and 10 kV std dev, distance also has a sinusoidal variation about a mean of 20 m and 10 m peak, algorithm window size is 50

## 7.5.2 Case Study II: Three Phase Conductors – MATLAB® Simulations

In this case study, a typical 345 kV transmission line was considered with a typical geometry given in Figure 7.13.

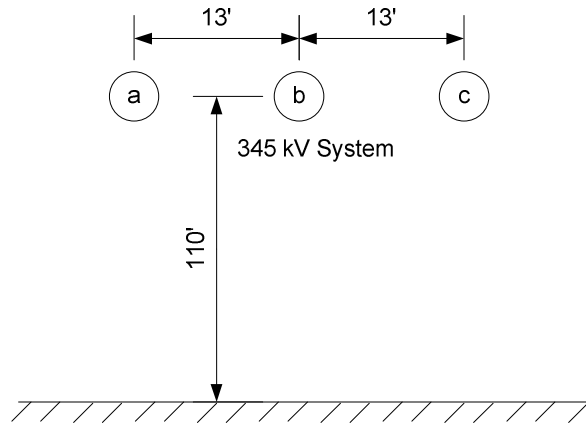


Figure 7.13. Typical 345 kV Line Geometry

As in case study I, different cases were simulated to validate the algorithm for voltage sensing in a three phase system. The parameters of variation in voltage and distance are given in Table 7.2 for all the simulated cases.

Table 7.2: Test Cases for Three Conductors Above the Earth

| Case | Voltage Profile     |   | Distance Profile |   | Window Size |
|------|---------------------|---|------------------|---|-------------|
|      | Nature              | Parameter   | Nature           | Parameter                                 |             |
| 6    | Normal Distribution | $\mu = 345 \text{ kV}$ , $\sigma = 34 \text{ kV}$ | Constant         | 34 m                                      | 100         |
| 7    | Normal Distribution | $\mu = 345 \text{ kV}$ , $\sigma = 34 \text{ kV}$ | Linear Drop      | 34 m to 14 m                              | 40          |
| 8    | Sinusoidal          | $\mu = 345 \text{ kV}$ , $A = 34 \text{ kV}$      | Linear Drop      | 30 m to 10 m                              | 40          |
| 9    | Sinusoidal          | $\mu = 345 \text{ kV}$ , $A = 34 \text{ kV}$      | Sinusoidal       | $\mu = 24 \text{ m}$ , $A = 10 \text{ m}$ | 40          |
| 10   | Normal Distribution | $\mu = 345 \text{ kV}$ , $\sigma = 34 \text{ kV}$ | Sinusoidal       | $\mu = 24 \text{ m}$ , $A = 10 \text{ m}$ | 100         |

The results of the simulation cases are given in Figure 7.14 - Figure 7.18. The results validate the efficacy of the algorithm in estimating the voltage of the conductor. In all

cases, the errors in voltage estimation after the window index are below 2%. As discussed in Section 7.4.3, for a multi-conductor system it is not possible for the algorithm to predict the distance to ground. Nevertheless, the algorithm does compute the effective distance to the resultant far-field producing asset.

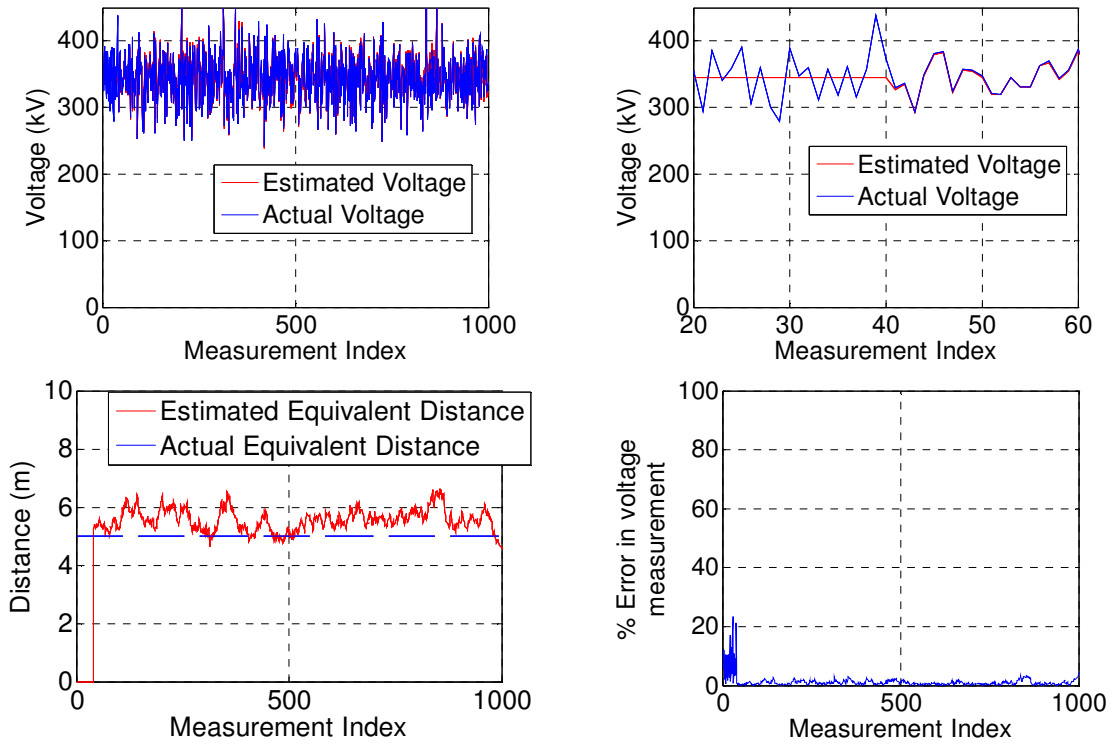


Figure 7.14: Case 6: Voltage is normally distributed with 345 kV mean and 34 kV std dev, distance remains a constant at 34 m, algorithm window size is 100

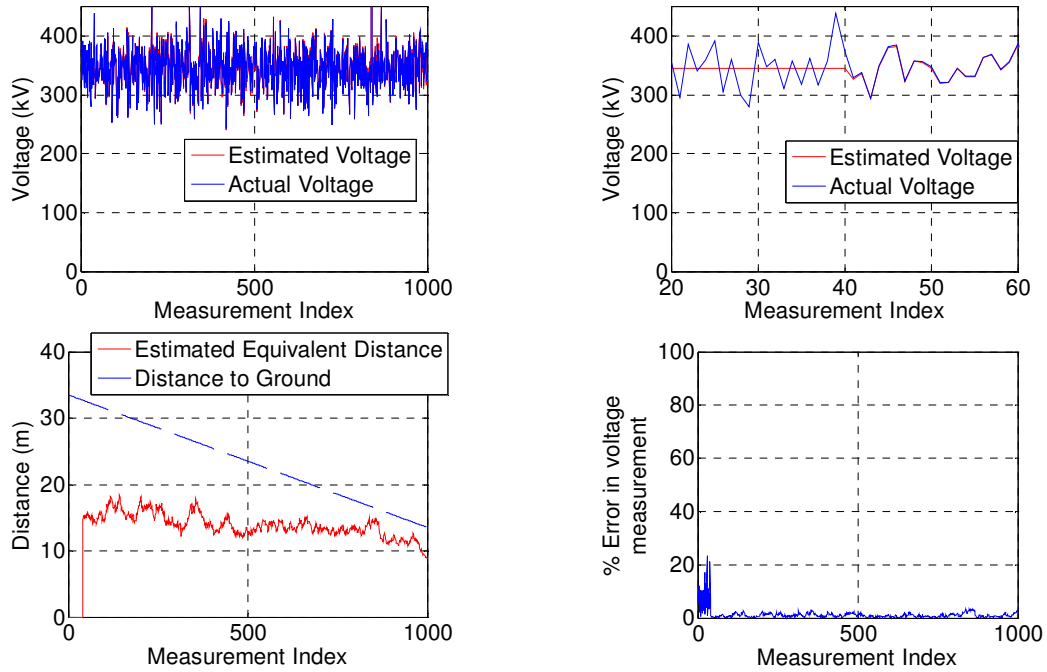


Figure 7.15: Case 7: Voltage is normally distributed with 345 kV mean and 34 kV std dev, distance linearly drops from 34 m to 14 m, algorithm window size is 40

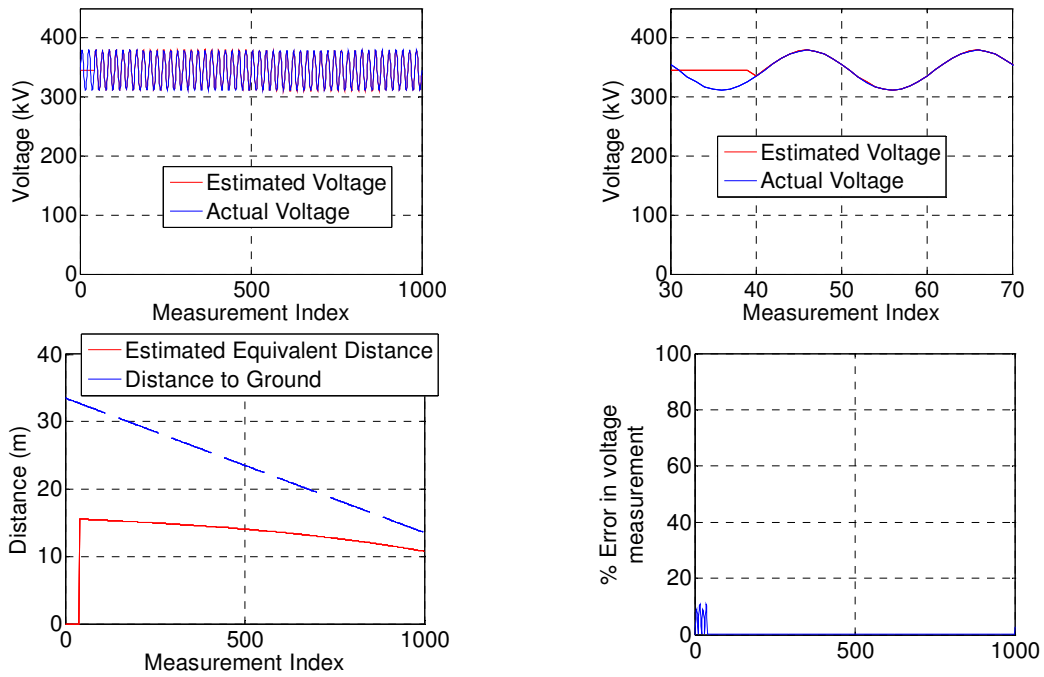


Figure 7.16: Case 8: Voltage has sinusoidal variation about a mean of 345 kV mean and 34 kV peak, distance linearly drops from 30 m to 10m, algorithm window size is 40

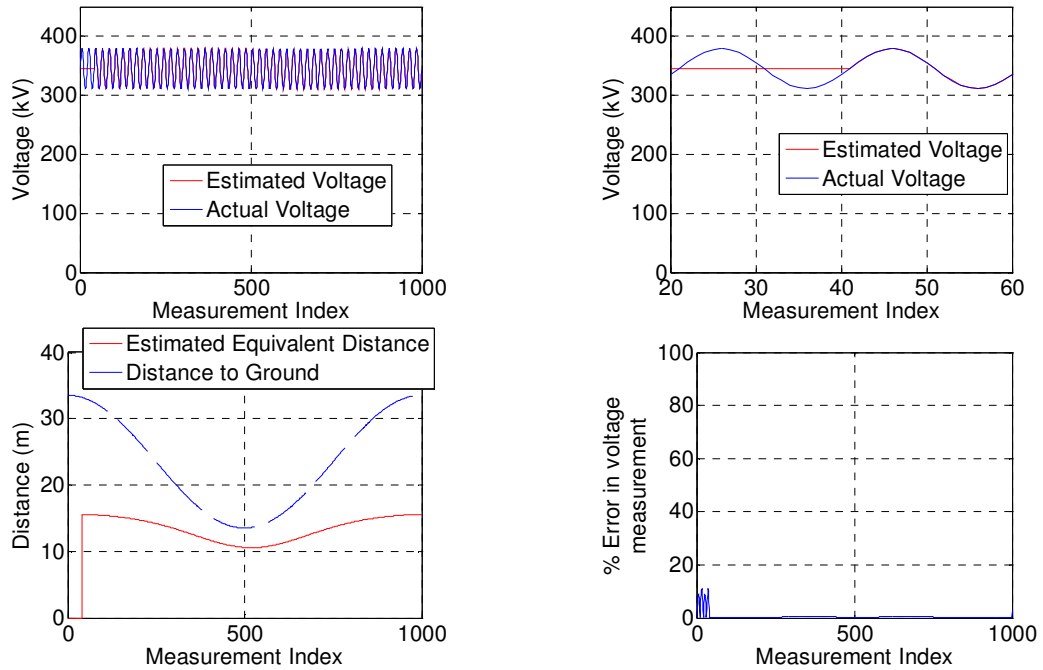


Figure 7.17: Case 9: Voltage has sinusoidal variation about a mean of 345 kV mean and 34 kV peak, distance also has a sinusoidal variation about a mean of 24 m and 10 m peak, algorithm window size is 40

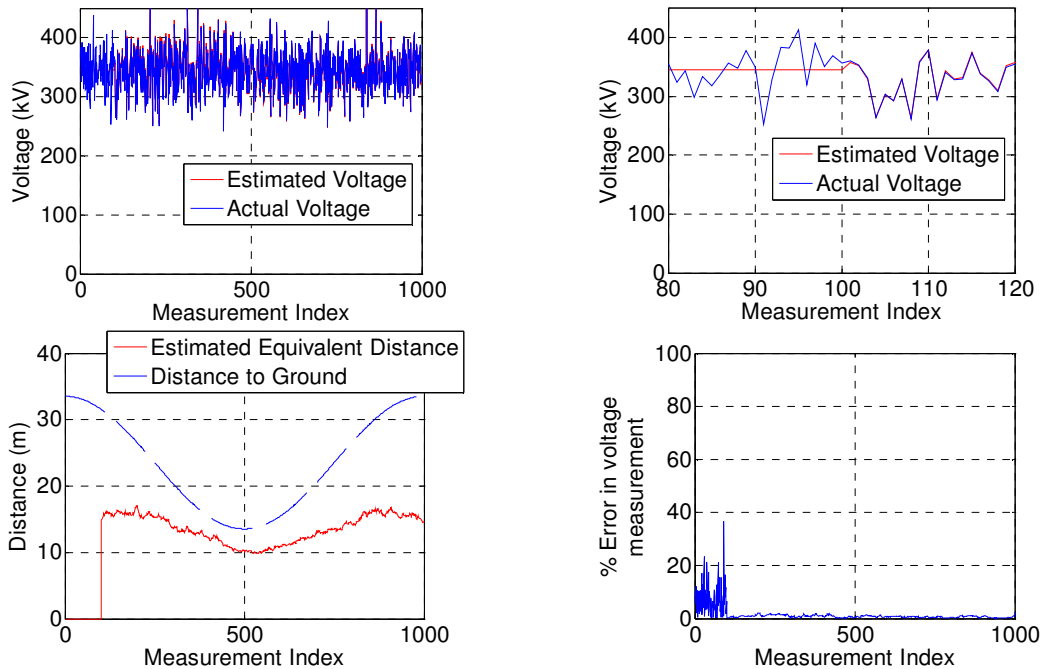


Figure 7.18: Case 10: Voltage is normally distributed with 345 kV mean and 34 kV std dev, distance has a sinusoidal variation about a mean of 24 m and 10 m peak, algorithm window size is 100

### 7.5.3 Case Study III: Validation of Concept through ANSYS® Maxwell

The previous two cases studies validate the efficacy of MAVS algorithm in providing an estimate of the voltage in MATLAB®. The algorithm was tested under the assumption that the model found mathematically (in Section 7.4) is indeed applicable to realistic situations. Therefore, to validate the developed mathematical model and MAVS algorithm simultaneously, FEA simulations were used.

The configuration considered in theory was translated to a simulation model and was applied a voltage and distance profile. The displacement current was measured through ANSYS® MAXWELL and was used as an input to the MAVS algorithm programmed in MATLAB®. The various simulation cases are given in Table 7.3.

**Table 7.3: Voltage Sensing Simulation Cases**

| Case | Configuration | Voltage Profile     |  | Distance Profile |              | Window Size |
|------|---------------|---------------------|--|------------------|--------------|-------------|
|      |               | Nature              | Parameter  | Nature           | Parameter    |             |
| 11   | Single Phase  | Normal Distribution | $\mu = 115 \text{ kV}$ ,<br>$\sigma = 12 \text{ kV}$ | Linear Drop      | 30 m to 10 m | 20          |
| 12   | Single Phase  | Normal Distribution | $\mu = 115 \text{ kV}$ ,<br>$\sigma = 12 \text{ kV}$ | Linear Drop      | 30 m to 10 m | 100         |
| 13   | Three Phase   | Normal Distribution | $\mu = 115 \text{ kV}$ ,<br>$\sigma = 12 \text{ kV}$ | Linear Drop      | 30 m to 20 m | 20          |
| 14   | Three Phase   | Normal Distribution | $\mu = 115 \text{ kV}$ ,<br>$\sigma = 12 \text{ kV}$ | Linear Drop      | 30 m to 20 m | 70          |

The successful results obtained from the ANSYS® MAXWELL-MATLAB® simulations are shown in Figure 7.19 - Figure 7.22. The errors in voltage measurement in all the cases are well below 2%. These simulation results show the efficacy of the MAVS algorithm in tracking the asset voltage and providing a close to accurate estimation.



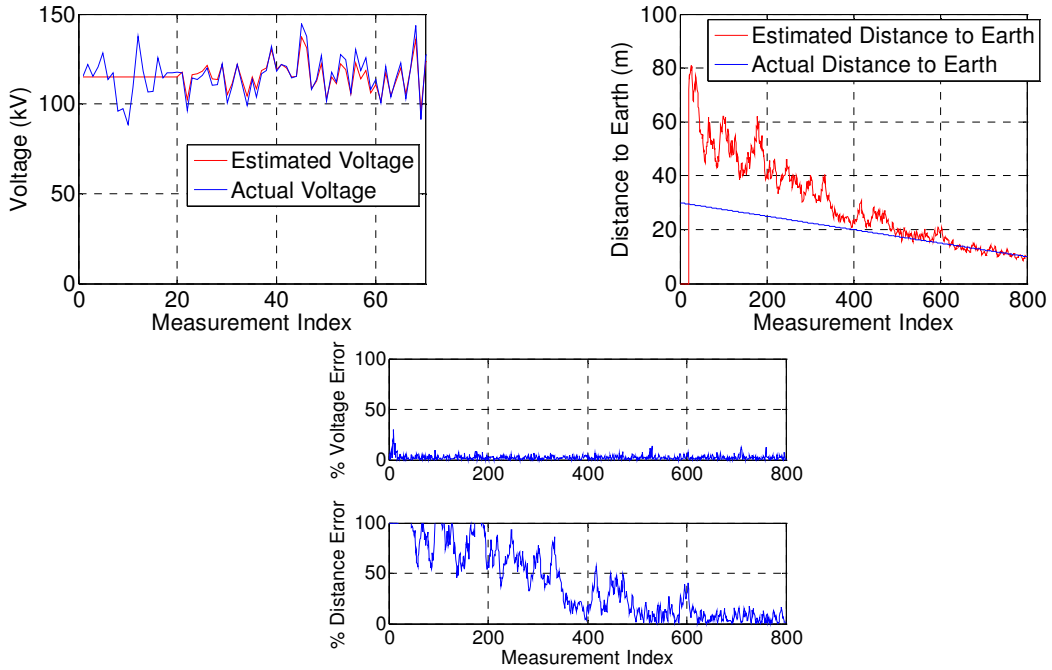


Figure 7.19: Case 11 Simulation results for a single conductor above the earth,  $w=20$

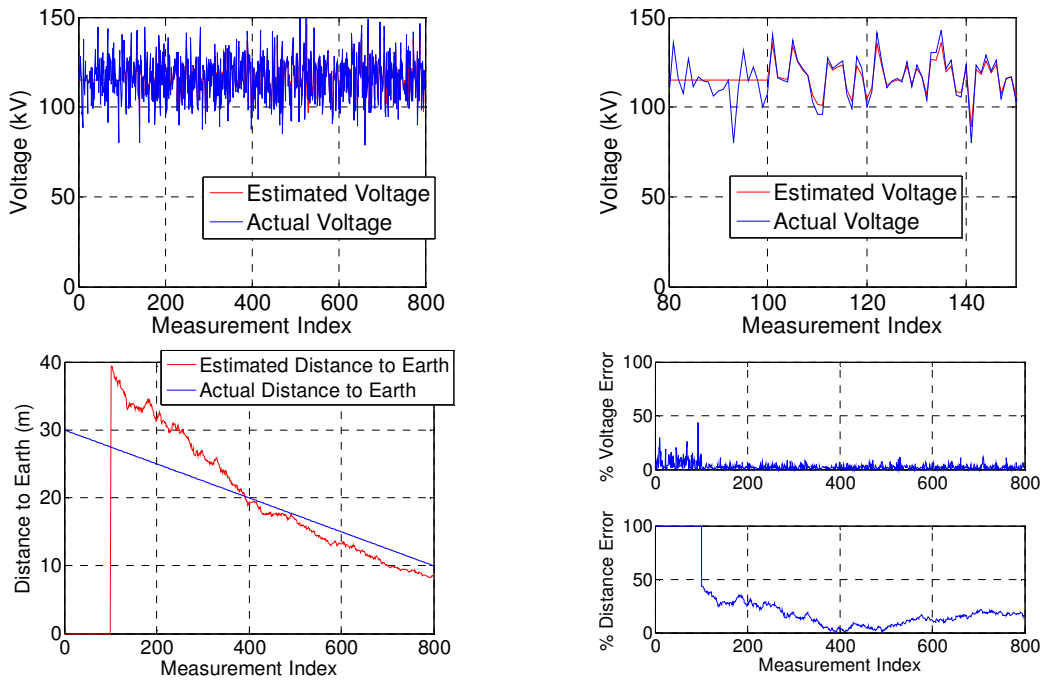


Figure 7.20: Case 12 Simulation results for a single conductor above the earth,  $w=100$

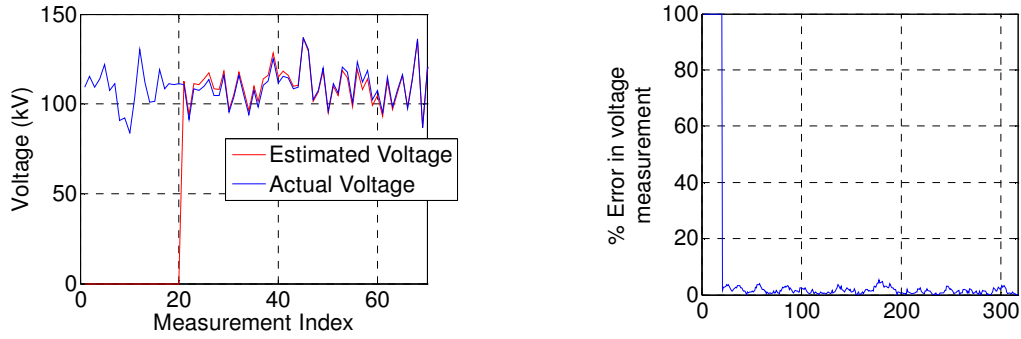


Figure 7.21: Case 13 Simulation results for three phase conductors above the earth,  $w=20$

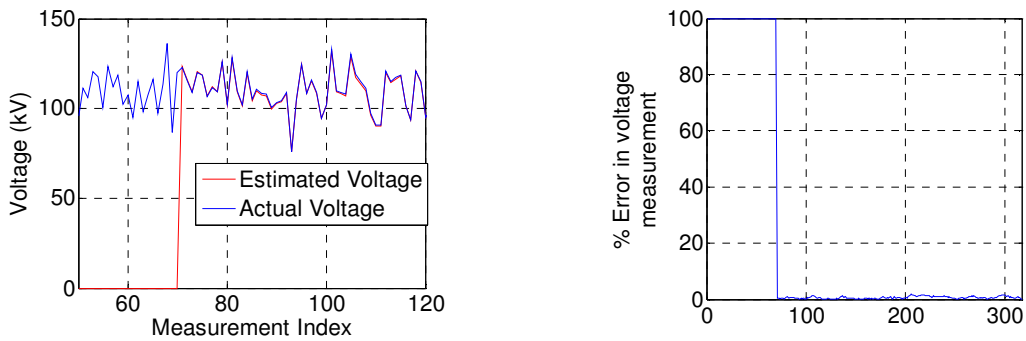


Figure 7.22: Case 14 Simulation results for three phase conductors above the earth.  $w=70$

## 7.6 PROTOTYPE DEVELOPMENT AND EXPERIMENTAL TESTING

### 7.6.1 Prototype Development

After successfully testing the MAVS algorithm under several operating conditions and configurations of overhead conductor systems, a prototype of the voltage sensor was built to test the algorithm in a real world application. The schematic of the self-contained voltage sensor prototype is shown in Figure 7.23. The voltage sensor prototype uses the metallic enclosure as one plate of the sensing capacitor. The metallic enclosure comes in contact with the high voltage asset and is naturally shorted to it at the time of installation. A slight modification to the enclosure is made in that another metallic plate is provided at the bottom of the enclosure separated by a small distance ( $\sim 1$  mm). A voltage

sensing plate integrated with the enclosure of the prototype is a novel concept that eliminates the need for extra sensing plates, and therefore, reduces size and cost of the sensor. Pictures of the actual prototype are shown in Figure 7.24.

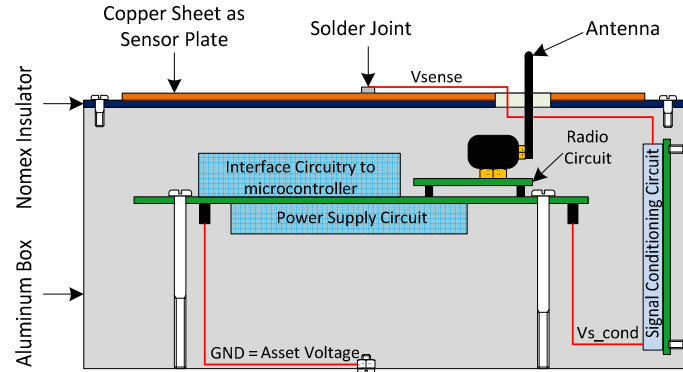


Figure 7.23: Final voltage sensor prototype schematic

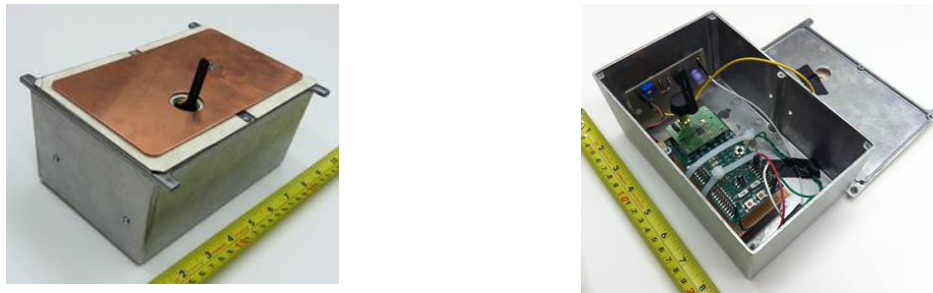


Figure 7.24. Voltage sensor prototype tested at NEETRAC

The circuit used to condition the AC voltage induced on the sensor plate is given in Figure 7.25. The ground reference of the circuit is equal to the asset potential, in other words, the sensor floats electrically at the asset potential. The circuit rectifies the AC voltage, as all the circuit components and chips work with positive voltage signals. The rectified signal is buffered using a voltage follower circuit and subsequently low-pass filtered. The signal is then fed into one of the ADC channels of the microcontroller of a TI-CC2430 module. Thereafter, the signal is processed, measured, and passed to the MAVS algorithm. The computed voltage values are sent to a remote coordinator over ZigBee®.

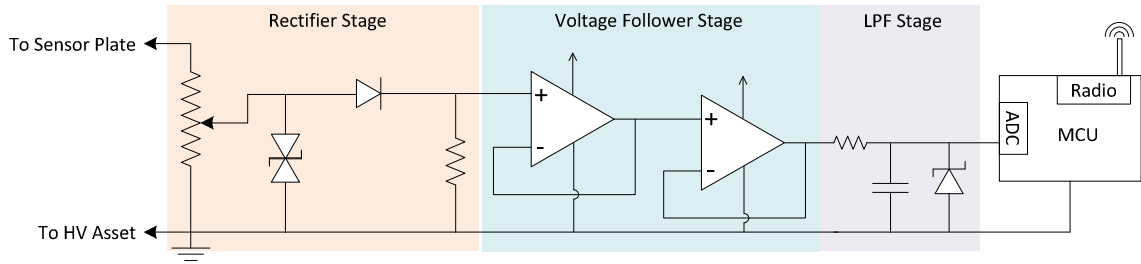


Figure 7.25: Signal conditioning circuit for the final voltage sensor prototype

## 7.6.2 Experimental Testing

### 7.6.2.1 *High Voltage Test Setup*

The test system used to validate the MAVS algorithm is shown in Figure 7.26. The setup uses a step-up transformer that can generate voltages up to 100 kV. To mimic a practical scenario of an overhead line, a voltage bus was connected to the transformer and the voltage sensor prototype was zip-tied to this high voltage (HV) bus. It should be noted that the box was also electrically shorted to the HV bus potential which is used as the ground of the electronic circuit. The antenna protrudes from the bottom. The HV bus was 1 m above the earth. In this setup, there are earth interactions from other directions also, such as, the side walls, and the faraday shield formed of a metallic mesh. These interactions tend to distort the fields emanating from the asset, and therefore introduce disturbance. Any results obtained under these conditions are prone to higher errors than under normal conditions. Therefore, if the algorithm works well under these conditions, it is expected to work well in a normal practical scenario.

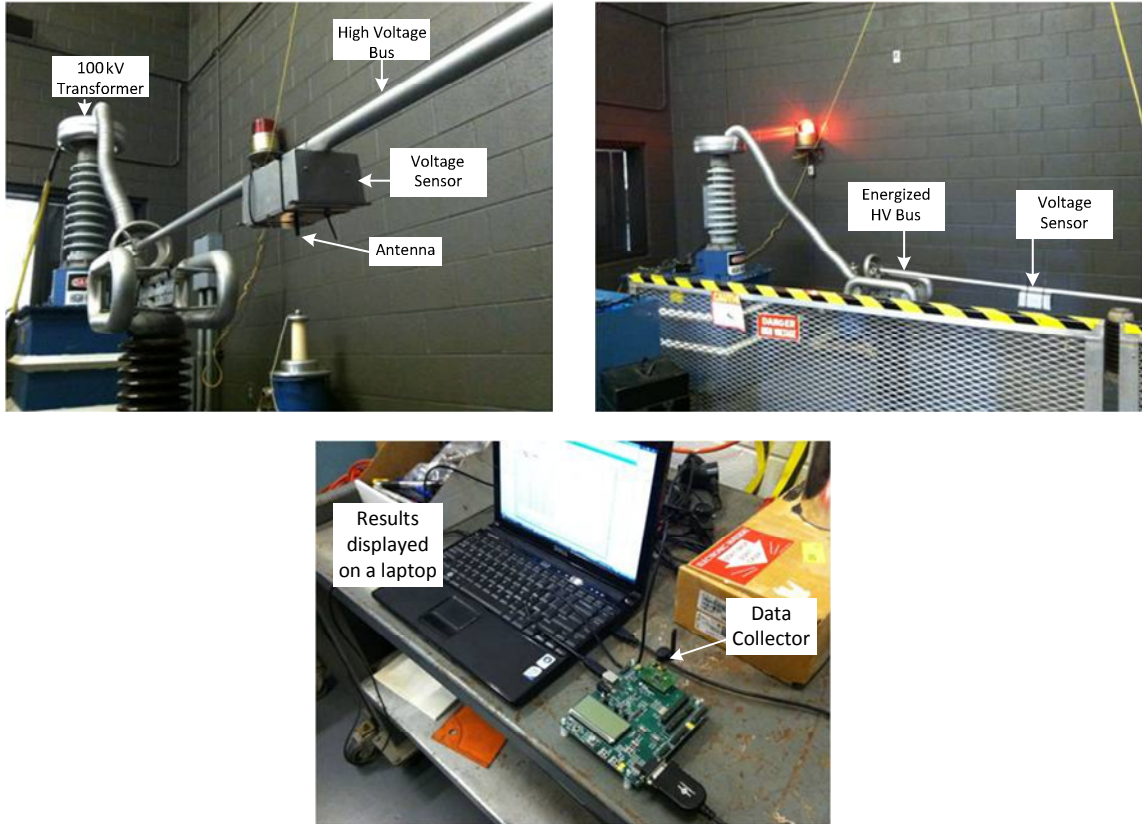


Figure 7.26: Actual test setup at NEETRAC for validating the MAVS algorithm

#### 7.6.2.2 *Test Methodology*

The voltage of the HV bus was variable with a least count of 500V. Two different datasets (HV1 and HV2) were used to perform the test. The statistics of the datasets are given in Table 7.4. The underlying assumption of the dataset is that the mean asset voltage is fairly constant, in this experiment, 25 kV. It can be observed that HV1 has a lower variance than HV2. Further, the variation in the RMS voltage is much larger in both the datasets than a realistic scenario where a  $\pm 5\%$  variation is expected. The reason behind using datasets with larger variation than a practical scenario is that if the sensor is able to detect large variations and track them effectively, it will perform well with a fairly stiff voltage source also.

Table 7.4: Voltage Profile Statistics used for Experimental Validation of MAVS

| Dataset No. | Sample Size | Mean (kV) | Standard Deviation (kV) | Minimum (kV) | Maximum (kV) |
|-------------|-------------|-----------|-------------------------|--------------|--------------|
| HV1         | 24          | 25.38     | 5.89                    | 15           | 35.5         |
| HV2         | 24          | 25.16     | 8.29                    | 5.5          | 36           |

During the experiment, the dataset voltage was impressed on the HV bus and was changed every minute. This voltage was sensed by the voltage sensor prototype connected to the HV bus. The sensed data was processed in the MAVS algorithm using the on-board microcontroller, and used to compute the estimated voltage on the HV bus. Finally, the estimated voltage was sent over ZigBee<sup>®</sup> to a remote data collector. The data collector was connected to a laptop through a serial-to-USB connector where it displayed the sensed results.

### 7.6.2.3 Results and Discussion

Figure 7.27 - Figure 7.28 show the results for dataset HV1 and HV2 respectively. It can be observed from both the figures that the MAVS algorithm based voltage sensor is able to track the asset voltage successfully.

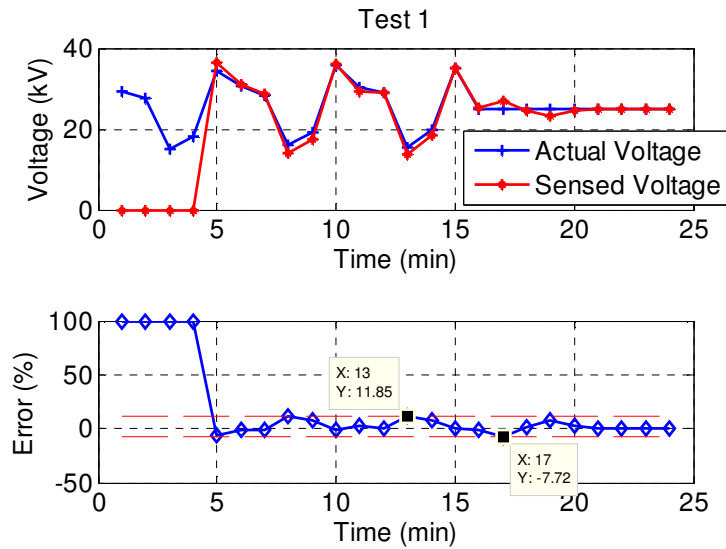
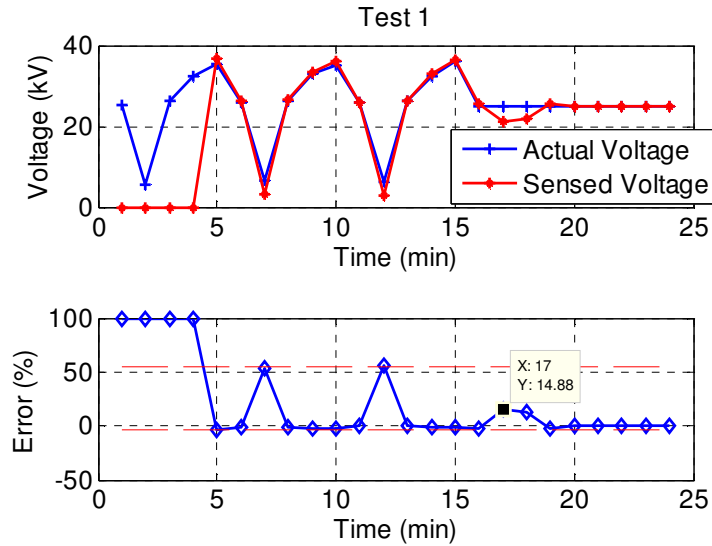


Figure 7.27: HV Test-I results



**Figure 7.28: HV Test-II results**

The error statistics for both the test cases are given in Table 7.5. It is evident that the voltage sensor shows the ability to track the variable voltage and is able to keep a mean error of  $< 2\%$  for the first test case. A maximum error of close to  $12\%$  is seen when there is a sudden decrease in the HV bus voltage.

In the case of test 2, as discussed above, the range of voltage variation on the HV bus was kept high (around  $30\text{ kV}$ ). Therefore, in this case a higher mean error is observed, close to  $6\%$ . However, one of the major reasons for the high mean error is that at lower voltages close to  $5\text{ kV}$  (for a  $25\text{ kV}$  nominal bus voltage), the sensor gives a relatively higher error. This may not be a big issue in a practical situation as if the voltage of a bus drops below a certain threshold the sensor can be used to send warning signals. For all other voltage levels, the sensor works perfectly well and if the two maxima points occurring at low voltages are removed, a mean error of  $2.5\%$  is obtained.

**Table 7.5: Error Statistics for Sensed Results in HV1 and HV2 Tests**

| Test No.                                      | Convergence Index               | Mean error (%) | Standard Deviation of error (%) | Minimum absolute error (%) | Maximum absolute error (%) |
|---|---------------------------------|----------------|---------------------------------|----------------------------|----------------------------|
| HV1   | 5 min (5 <sup>th</sup> reading) | 1.72           | 5.08                            | 0.1                        | 11.85                      |
| HV2   | 5 min (5 <sup>th</sup> reading) | 5.95           | 17.2                            | 0.1                        | 55                         |
| HV2 (not considering the low voltage results) | 5 min (5 <sup>th</sup> reading) | 2.5            | 4.2                             | 0.1                        | 14.8                       |

Overall, the performance of the voltage sensor met the expectations of

- low-cost
- tracking the voltage of the HV bus effectively
- self-calibrating using the MAVS algorithm
- keeping mean errors below 5%

In a nutshell, the technique can be considered to be an intelligent way of sensing voltage of assets at low-cost.

### 7.6.3 Electric-field Energy Harvesting using the Prototype

The concept introduced in Section 2.5.6 for electric-field energy harvesting can be used in the developed sensor. The range of power that can be harvested by the prototype was tested and is shown in Figure 7.29. It can be seen that at 35 kV, nearly 17 mW of continuous power was derived. Power on this order may be sufficient for operating sensors with lower duty cycles. Moreover, with further increase in voltage levels, the power harvested is expected to increase. Therefore, the proposed sensor can be used for the dual purpose of voltage sensing and energy harvesting with the same package.



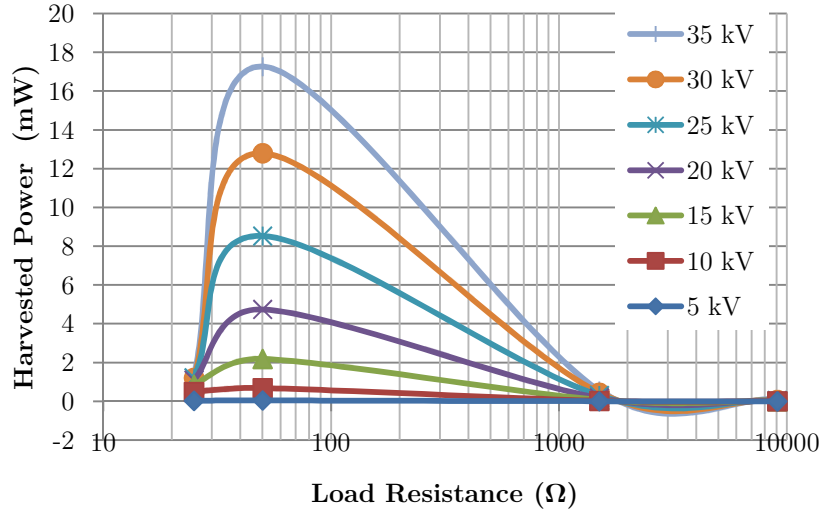


Figure 7.29: Power harvested from developed prototype at different output load levels and asset voltages

## 7.7 CONCLUSIONS

In this chapter, a new voltage sensing algorithm was also proposed, called the moving average voltage sensing (MAVS) algorithm. The major purpose of the proposed voltage sensor was to detect whether a particular asset is energized or not. In addition, the role of the sensor was to detect voltage sags and swells on the asset and to produce alarm signals under these conditions. Therefore, as compared to conventional voltage sensors used for energy metering purposes, the acceptable error bands on the proposed voltage sensor can be relatively high ( $< \pm 5\%$ ). The MAVS algorithm is a novel method that uses history of recorded measurements to estimate the present voltage of the asset, and therefore, the method is self-calibrating. Extensive simulation studies were performed to validate the algorithm under different operating conditions, such as changes in voltage of the conductor, distance of conductor from the earth and configuration of conductors. Finally, a voltage sensor prototype was built and tested on a high voltage bus up to 35 kV voltage levels. The self-calibration of the sensor was successfully demonstrated in these experiments. Further, the sensor tracked the voltage changes on the asset within an

average error band of  $\pm 5\%$ . Finally, the sensor can be used for the dual purpose of energy harvesting and voltage sensing using the same package.

## CHAPTER 8

### DESIGNING A ROBUST SENSOR

#### 8.1 INTRODUCTION

The smart current and voltage sensor prototypes developed in this research have been tested to operate over a wide range. Both the current and the voltage sensors have been tested to operate independently at currents up to 1000 A and voltages up to 35 kV respectively, yet many challenges need to be addressed.

- Presently, although the energy harvester provides sufficient power to the sensor, its design is sub-optimal. An optimal design of the energy harvester can lead to reduction in size and increase in energy density of the sensor system.
- Although, the prototype has been successfully demonstrated at currents up to 1000 A; however, protection of the sensor from high fault current, high di/dt conditions, and lightning strikes has to be performed. Further, a protection architecture that ensures reliable operation of the sensor under faulted conditions has to be developed.
- Operation of the communication link in high voltage and noisy environments in the presence of corona needs to be tested.
- Designing and packaging the sensor to prevent interference due to corona and other EMI sources also remains to be addressed.

This chapter looks at all of these issues and presents some interesting design concepts for low-cost smart sensors.

#### 8.2 OPTIMAL ENERGY HARVESTER DESIGN

The energy harvester (EH) used in the prototype of the smart Stick-on sensor is an X-shaped core (XEH), as shown in Figure 8.1(a). This prototype provides sufficient power at higher currents when close to the current carrying asset, but an increase in distance of

the XEH from the asset decreases the harvested power dramatically, as shown in Figure 8.1(b). Moreover, at lower current levels, the energy harvested is an order of magnitude smaller than at higher currents. Therefore, an optimal design of the EH is required. The design process consists of finding the optimal shape, size and winding of the harvester core and has been performed in the following sub-sections.

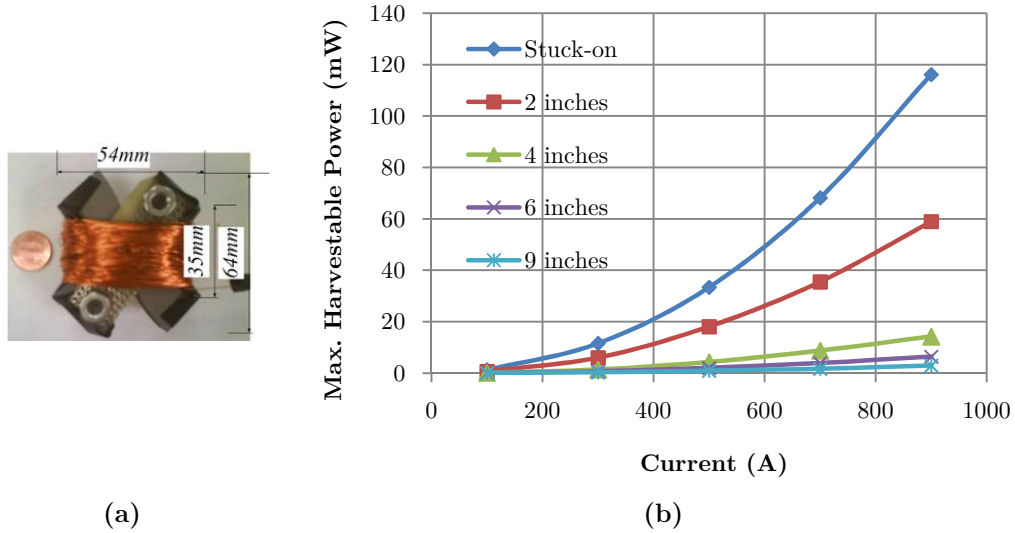


Figure 8.1: (a) XEH, (b) power harvested by XEH as a function of distance from and current in the conductor.

### 8.2.1 Shape

The role of the EH is to concentrate the flux lines and channel them through the energy harvester to form a flux concentrator. The X-shaped core performs this task very well due to the larger area of the core on top and bottom. If this philosophy is used for designing the flux concentrator, an even better design would be an H-shaped core, shown in Figure 8.2, which has maximum area on top and bottom, thereby, maximizing the amount of flux lines captured. Further, the H-shape can be easily mass produced to reduce cost.

### 8.2.2 Dimensions

A parametric search was performed using ANSYS® Maxwell to analyze the nature of variation in power harvested for a change in the different dimensions of the core.

In the software, the core was placed 60 mm (center to center) away from the conductor and a steady-state current in the conductor of 1000 A was chosen. The value of current and distance in the conductor does not have an effect on the selected dimensions as the power harvested scales as square of current and inversely with distance. The search space spanned for all of the dimensions are given in Table 8.1. The results of the simulations are shown in Figure 8.3. Apart from understanding the variation of harvested power with changes in dimensions of the core, the parametric search also helps in reducing the convergence time of the optimization by decreasing its trust region.

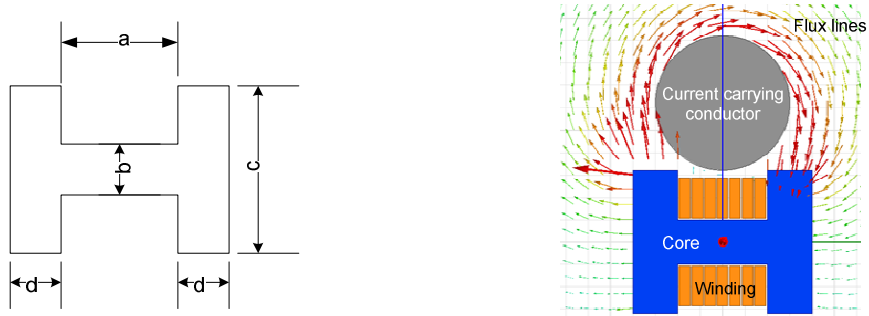
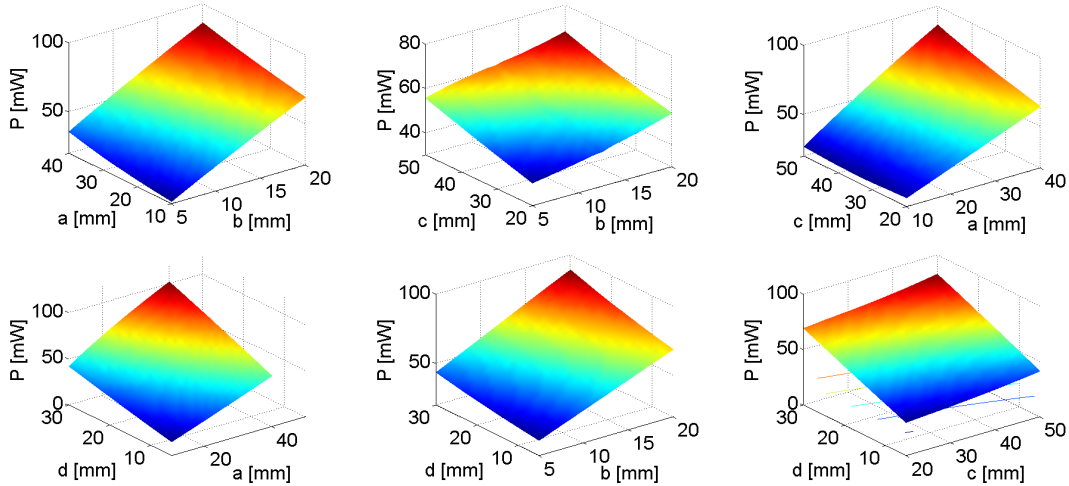


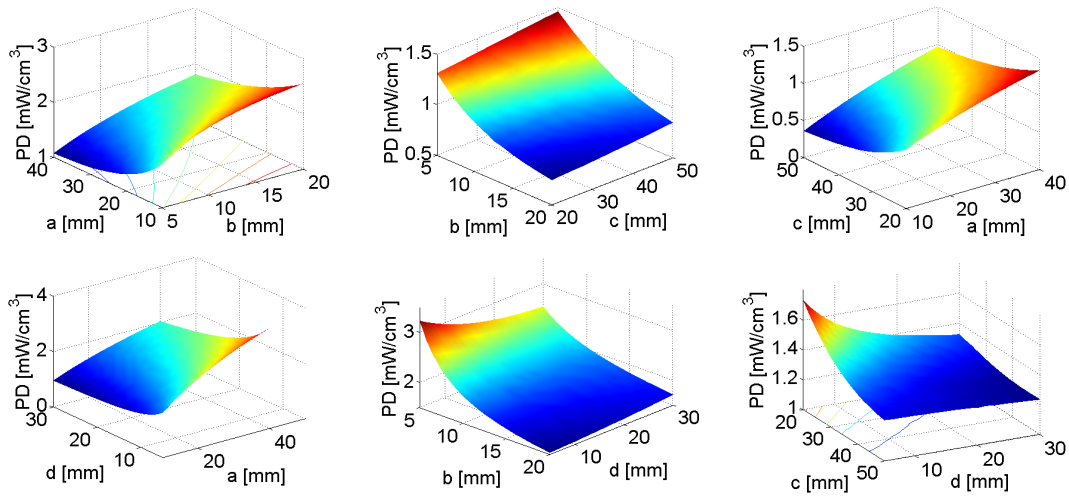
Figure 8.2: H-shaped geometry for the flux concentrator (left), Sample ANSYS® Maxwell simulation for finding the optimal geometry (right)

Table 8.1: Design Space for Parametric Search

| Dimension | Minimum Size Tested (mm) | Maximum Size Tested (mm) | Step-Size (mm) |
|-----------|--------------------------|--------------------------|----------------|
| a         | 10                       | 40                       | 1.5            |
| b         | 5                        | 20                       | 0.75           |
| c         | 20                       | 50                       | 1.5            |
| d         | 5                        | 30                       | 1.25           |



(a) Variation in power harvested with size of the flux concentrator



(b) Variation in power density with size of the flux concentrator

**Figure 8.3: Parametric search plots for designing an optimal energy harvester. There are a total of 6 ( ${}^4C_2$ ) cases. PD = power density, P = Power.**

Next, an optimization was performed. The objective of the optimization was to maximize power harvested and power density simultaneously. Apparently, power harvested increases (decreases) while power density reduces (increases) when the size of the core is increased (decreased). Therefore, the solution of the problem that maximizes power contradicts the solution that maximizes power density. To address this issue, a single objective function was computed that combines both the harvested power and power density for the optimizer. The objective function formed for the optimization is shown in (220) Further, boxed constraints were added on the dimensions of the core to limit any

one dimension to be above a maximum value and below a minimum value. In addition, a minimum constraint was added on both power and power density based on the minimum power required for the sensor to operate.

$$\max_{a,b,c,d} f(x) = w_1 \max(P) + w_2 \max(PD) \quad (220)$$

$$s.t. \ a_{\min} < a < a_{\max}$$

$$b_{\min} < b < b_{\max}$$

$$c_{\min} < c < c_{\max}$$

$$d_{\min} < d < d_{\max}$$

$$\max(P) > P_{\min}$$

$$\max(PD) > PD_{\min}$$

where

$$\max(PD) = \frac{\max(P)}{\nabla} \quad (221)$$

$$\max(P) = \frac{V_{oc} I_{sc}}{4} \quad (222)$$

$$\nabla = f(a, b, c, d) = Volume \quad (223)$$

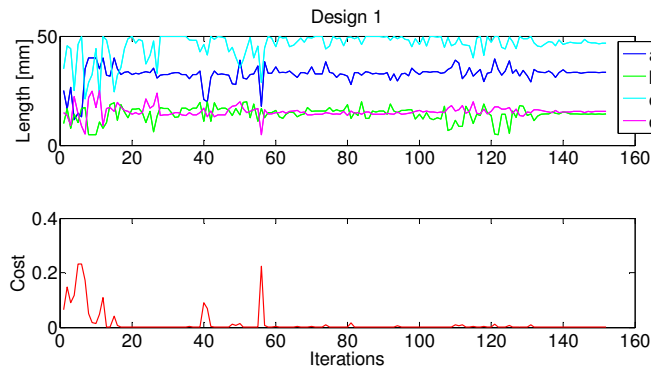
For every simulation step, the values of OCV and SCC were computed, and were used to calculate the value of cost function. A sequential non-linear programming (SNLP) technique that uses a response surface (RS) was utilized for the optimization. The SNLP is integrated into the FEA models through ANSYS® Maxwell's Optimetrics toolbox. The optimizer converged when either the maximum iterations were reached or the maxima condition (cost function is nearly zero) were satisfied.

Two different sets of constraints were applied on the dimensions of the core, and are given in Table 8.2.

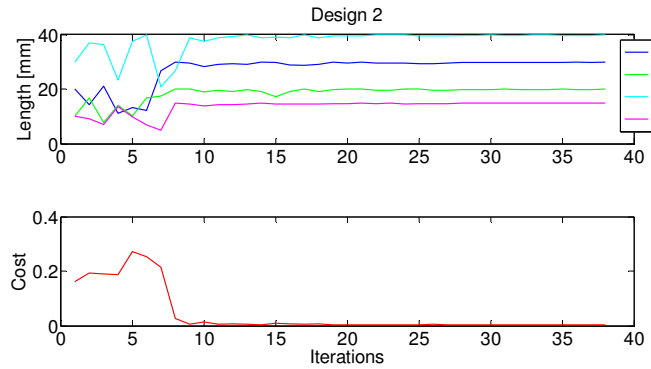
Table 8.2: Constraints on Dimensions of the Flux Concentrator

| Dimension | Step Size | Design 1 |         | Design 2 |         |
|-----------|-----------|----------|---------|----------|---------|
|           |           | Minimum  | Maximum | Minimum  | Maximum |
| a         | 0.5       | 10       | 40      | 10       | 30      |
| b         | 0.5       | 5        | 20      | 5        | 20      |
| c         | 0.5       | 20       | 50      | 20       | 40      |
| d         | 0.5       | 5        | 30      | 5        | 20      |

A plot showing the convergence of solution for the two designs is presented in Figure 8.4. This graph gives the optimal dimensions for the core for both the designs.



(a) Optimal flux concentrator size for Design 1



(b) Optimal flux concentrator size for Design 2

Figure 8.4: Plot showing convergence of solution

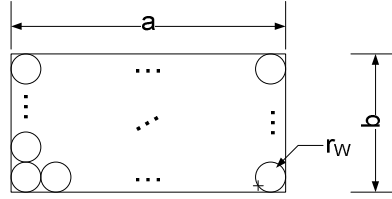
### 8.2.3 Optimal Winding Design

In this section, an optimal design of the flux concentrator and transformer windings is presented through detailed modeling of winding resistances and inductances.



### 8.2.3.1 Resistance computation

Consider a cross section of the EH winding as shown in Figure 8.5.



**Figure 8.5: Winding Geometry**

If this winding is wound on a core of width  $l_v$  and height  $l_h$ , then the resistance of the winding is given by

$$R = \frac{2\rho N^2 \left[ (l_h + l_v) + 4\sqrt{\frac{0.78A}{\pi n_a n_b}} (n_b - 1) \right]}{0.78A} \quad (224)$$

where,

$N = n_a n_b =$  Total number of turns,

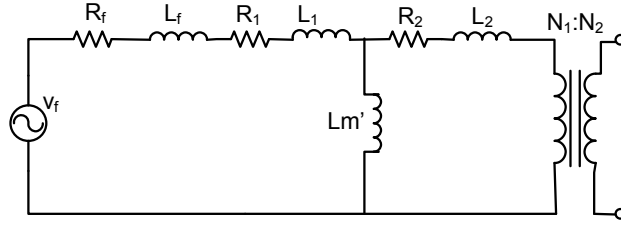
$n_a = a/2r_w$ ,  $n_b = b/2r_w$ ,  $r_w =$  radius of wire,

$A = ab =$  Cross sectional area of the winding.

The complete derivation of the winding resistance is given in Appendix F. It can be seen in (224) that the resistance is dependent on the number of turns for a given volume of winding. Equation (224) was used to compute the resistance of the EH and transformer windings for the different configurations that were analyzed.

### 8.2.3.2 Inductance Computation

The equivalent circuit of the flux concentrator along with the transformer is shown in Figure 8.6. Optimal design of the flux concentrator cannot be performed independently from the transformer as the two are electrically coupled. Therefore, it is necessary to compute the inductances for the entire equivalent circuit shown in Figure 8.6.



**Figure 8.6: Equivalent Circuit of flux-concentrator and transformer**

The expressions for the various inductances can be given by

$$L_f = k_f N_f^2 \quad (225)$$

$$L_1 = k_1 N_1^2 \quad (226)$$

$$L_2' = k_2 N_1^2 \quad (227)$$

$$L_m' = k_m N_1^2 \quad (228)$$

The values of  $k_f$ ,  $k_1$ ,  $k_2$ , and  $k_m$  are dependent on the structure of the core and windings. As the cores have an open structure, the values of  $k_f$ ,  $k_1$ ,  $k_2$ , and  $k_m$  cannot be analytically found. Thus, ANSYS<sup>®</sup> Maxwell 3D was used for this purpose.

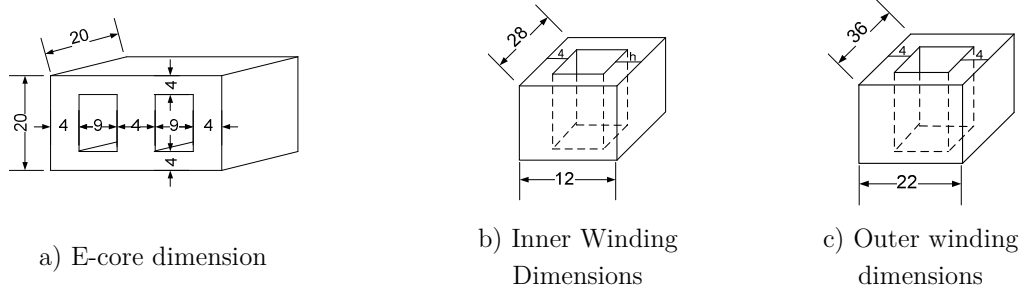
As an example, the optimal design 1 computed in Section 8.2.2 for the flux concentrator was considered to compute  $k_f$ . Further, the dimension of the transformer core and winding that were used for computing  $k_1$ ,  $k_2$ , and  $k_m$  are shown in Figure 8.7. The values computed for  $k_f$ ,  $k_1$ ,  $k_2$ , and  $k_m$  are given as

$$k_f = 186.4 \times 10^{-9} \quad (229)$$

$$k_1 = 8.4 \times 10^{-9} \quad (230)$$

$$k_2 = 17.7 \times 10^{-9} \quad (231)$$

$$k_m = 2158.6 \times 10^{-9} \quad (232)$$



**Figure 8.7. Transformer Core and Winding Geometries (all dimensions are in mm)**

### 8.2.3.3 Maximum Power Transfer

Finally, using the concept of maximum power transfer, the maximum power was computed for different EH and transformer winding configurations. The Thevenin equivalent of the circuit shown in Figure 8.6 was used for computation. Thevenin equivalent voltage and impedance are given by

$$V_{th} = V_f \left( \frac{j\omega L_M}{R_f + R_1 + j\omega(L_M + L_1 + L_f)} \right) \quad (233)$$

$$Z_{th} = R_2 + j\omega L_2 + (R_f + R_1 + j\omega(L_1 + L_f)) \parallel (j\omega L_M) \quad (234)$$

$$R_{th} = \text{Re}\{Z_{th}\} \quad (235)$$

$$X_{th} = \text{Im}\{Z_{th}\} \quad (236)$$

In (233) and (234)  $R_f$ ,  $R_1$ , and  $R_2$  are computed using (224) while,  $L_f$ ,  $L_1$ ,  $L_2$ , and  $L_m$  are computed using (225) - (228) If the load is purely resistive, the maximum power that is transferred to the load is given as

$$P_{\max}^R = \frac{|V_{th}|^2}{4R_{th}^2} \quad (237)$$

While, if the load is resistive and inductive, the maximum power is given as

$$P_{\max}^{RL} = \frac{|V_{th}|^2}{2\left(R_{th} + \sqrt{R_{th}^2 + X_{th}^2}\right)} \quad (238)$$

A locus of the maximum power at 100 A primary current for all the configurations,  $N_1 \in (1, 200)$ ,  $N_f \in (1, 600)$ , has been plotted in Figure 8.8(a). Further, the plots of OCV, radius of flux concentrator, transformer primary and secondary windings are given in Figure 8.8(b)-(e).

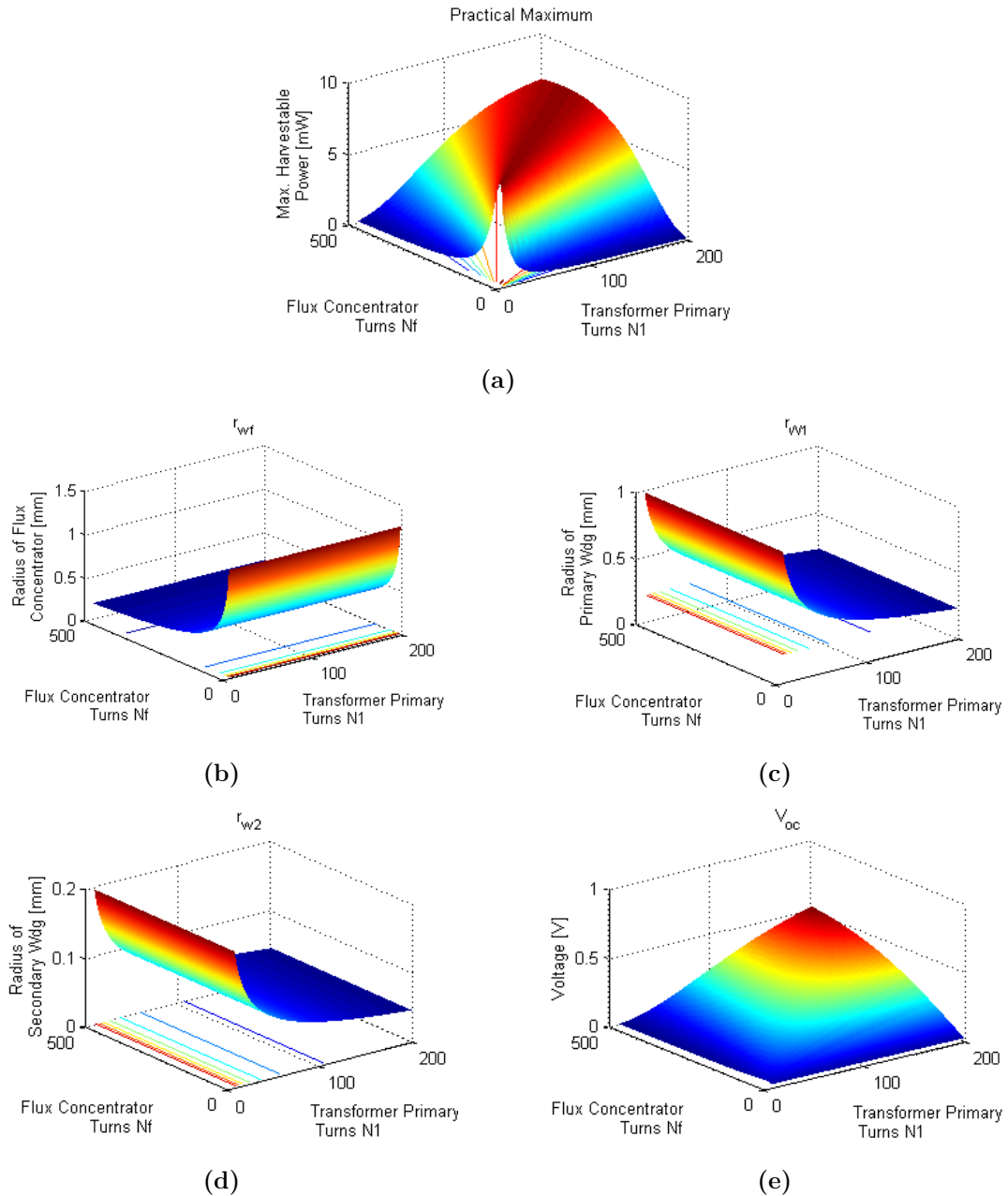


Figure 8.8. (a) Locus of maximum power for all configurations at  $I=100A$ , (b), (c) and (d) radius of various windings as a function of turns (e) Voltage at the flux concentrator winding as a function of  $N_f$  and  $N_1$

An interesting feature about Figure 8.8(a) is the presence of a region of maxima among all the maximums. This maxima region shows that there are many solutions to choose from, thereby giving enough design flexibility. For instance, the design corresponding to 1 turn would not be feasible as it would give a very low magnitude of voltage induced on the EH windings, so a design with more number of turns which also lies on the maxima region can be chosen. Further, it is required to simultaneously examine all the plots when selecting a particular combination for the number of turns ( $N_f$ ,  $N_1$  and  $N_2$ ), as other practical constraints such as ampacity and open circuit voltage also need to be considered.

The above analysis was performed at a fixed current. However, with increasing (decreasing) currents the harvested power for any configuration increases (decreases) monotonically. Thus, a design that is optimal at  $I_1$  amps is also optimal at  $I_2$  amps for all  $I_1 \neq I_2$ .

The flowchart shown in Figure 8.9 below summarizes the procedure used to find the optimal core designs.

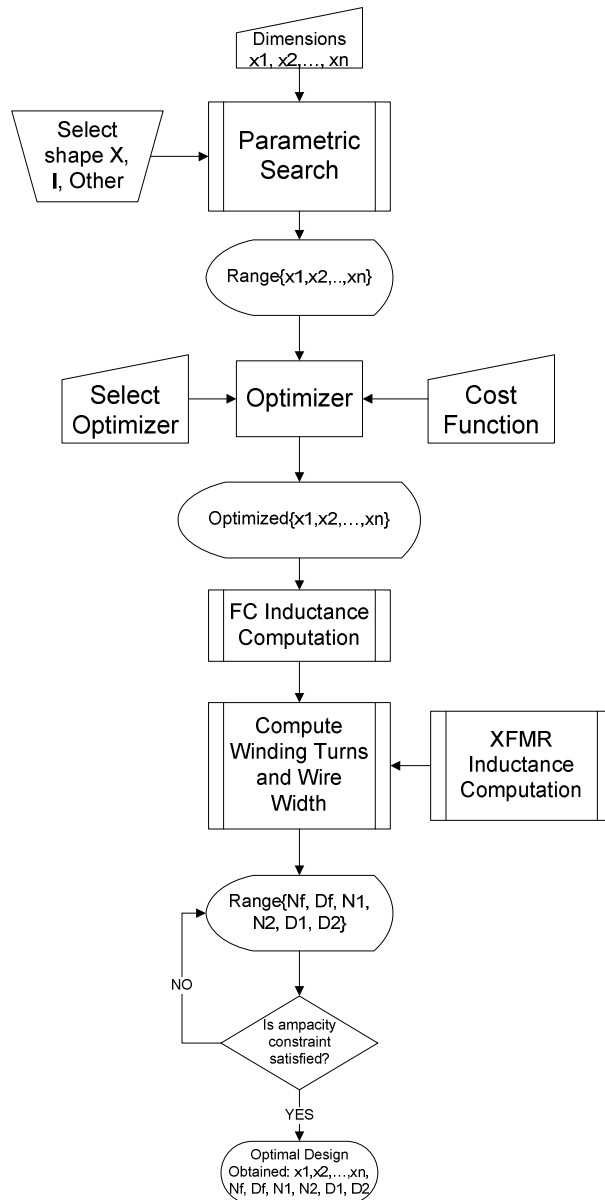


Figure 8.9. Flow Chart for Optimal Designs

### 8.3 FAULT ANALYSIS

As the smart sensor may be used in conjunction with assets that are likely to experience fault conditions, analysis has to be performed to understand the challenges of operating the sensor under scenarios such as high current impulses (high  $di/dt$ ) and lightning strikes or excessive voltage impulses on the asset. High current impulses give rise to high voltages induced on the flux concentrator terminals. Even if the aggregate induced

voltage across the flux concentrator winding is within the safe operating area of the semiconductor devices and the breakdown voltage of the windings, the voltage induced between individual windings may lead to inter-winding failure. Further, under faulted conditions, the core begins to saturate.

This section presents the simulation studies and experiments that were conducted to test the performance of the flux concentrator under different fault conditions. The focus is on investigating the maximum overvoltage (and short circuit current (SCC)) observed on the flux concentrator windings under various scenarios. The core selected for the simulation study is the optimal H-core obtained in Section 8.2. Finally, actual current impulse tests were performed on a set of scramble wound cores prepared in the lab.

#### **8.4 SIMULATION STUDIES**

To monitor the voltage across different sections of the windings, the core was divided into seven different sections, with each section having 50 turns. Therefore, the total number of turns is 350. The volume of each coil section is based on the average volume required for a 26-32 AWG wire with a reasonable stacking factor (0.5-0.7). The core material is selected as CRGO silicon steel.

Subsequently, ANSYS® Maxwell simulation studies were conducted to find the peak open circuit voltage (OCV) (and SCC) developed between any two sections of the winding and also on the entire winding for different faulted conditions.

A list of the different fault conditions that were simulated is given in Table 8.3 along with the results. The plots of developed over-voltages, short circuit currents and fault currents for all the cases are shown in Figure 8.10. Note that Case 1 is not a fault condition but a base case scenario.

Table 8.3: Design Space for Parametric Search

| Case No. | Source Nature                     | Peak Inter-winding (50 turn section) Voltage | Peak Open circuit voltage | Peak Short Circuit Current of Coil |
|----------|-----------------------------------|--|---------------------------|------------------------------------|
| Case 1   | $500\sin(377t)$                   | 159 mV                                       | 1.122 V                   | 305 mA                             |
| Case 2   | $20kA\sin(377t)+10kAe^{-t/0.032}$ | 6.618 V                                      | 46.6 V                    | 17.61 A                            |
| Case 3   | $60kA\sin(377t)$                  | 19.2 V                                       | 134.9 V                   | 36.68 A                            |
| Case 4   | 100 kA Lightning Strike           | 13.7 kV                                      | 95.8 kV                   | 61.6 A                             |

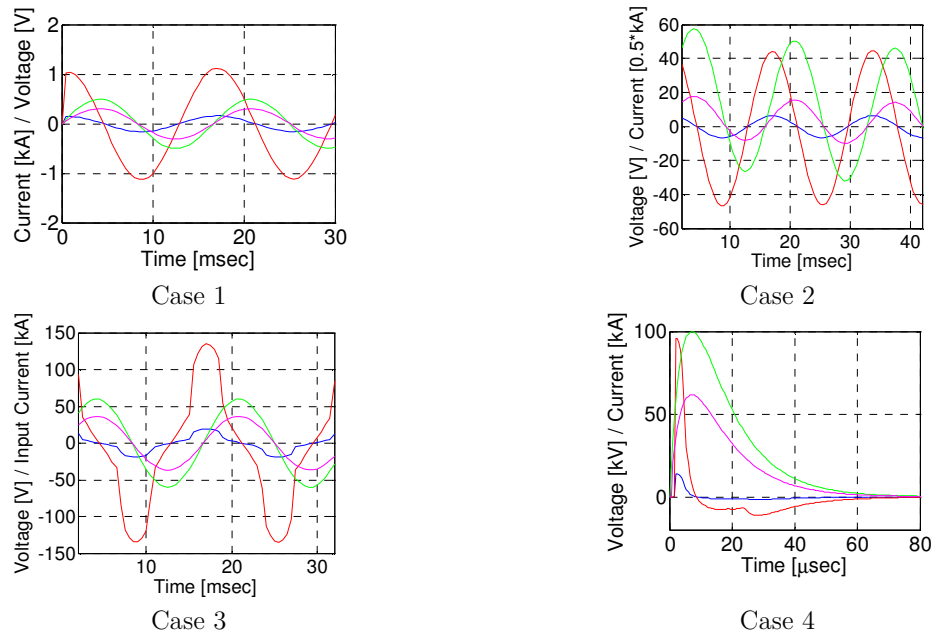


Figure 8.10: Parametric Simulation results depicting conductor current in green, inter-winding voltage in blue, total winding voltage in red, and winding SCC in blue. Note that the SCC is in amps.

The simulation results show that the voltage developed on the flux concentrator under faulted conditions is almost a 100 times more than nominal conditions. Moreover, under lightning strikes the voltage may increase to almost a million times more. Therefore, under fault conditions it is essential to limit the voltage developed on the flux concentrator to safeguard the sensitive sensor electronics.



## 8.5 EXPERIMENTAL RESULTS

To validate the simulation results, three different cores were designed and tested at NEETRAC under fault conditions. The cores designed in the lab are shown in Figure 8.11. All cores were wound with a 30 AWG magnetic wire. The I-core was wound with 150 turns, while the X-core and H-core were wound with 300 turns each. The cores were characterized in the lab under nominal conditions before and after the impulse test so that the performance of the cores could be compared to their nominal values.

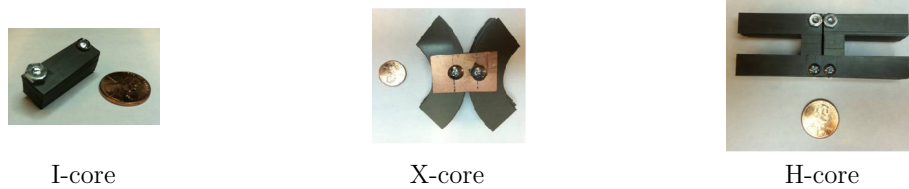


Figure 8.11: Different cores tested at NEETRAC

The test setup used at NEETRAC was capable of generating 20 kA (4/10  $\mu$ s and 8/20  $\mu$ s) of fault current with a di/dt of up to 2.5 kA/ $\mu$ s. A circuit diagram of the test setup is shown in Figure 8.12. The actual test setup is shown in Figure 8.13.

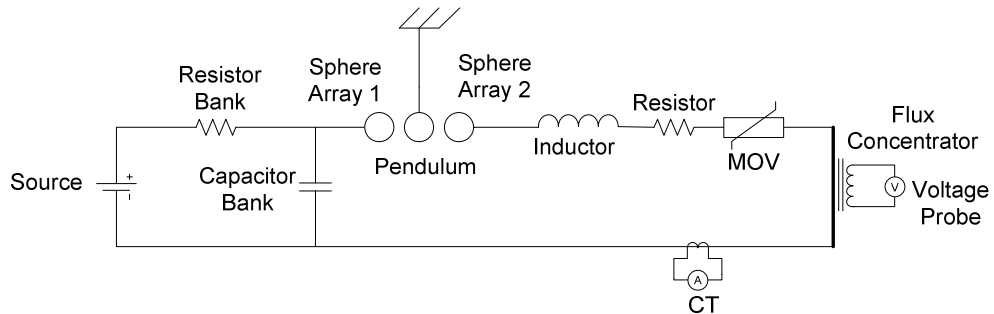


Figure 8.12: Circuit diagram of high impulse test facility in NEETRAC

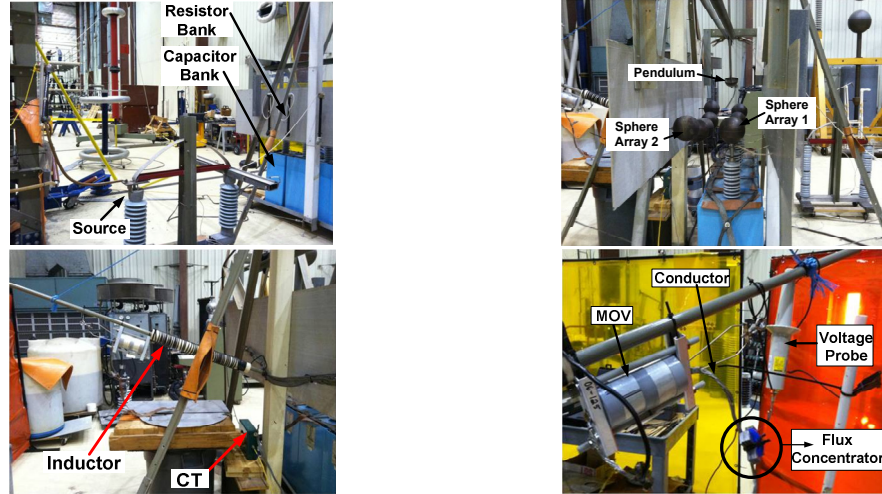


Figure 8.13: Experimental setup for impulse testing on the flux concentrators

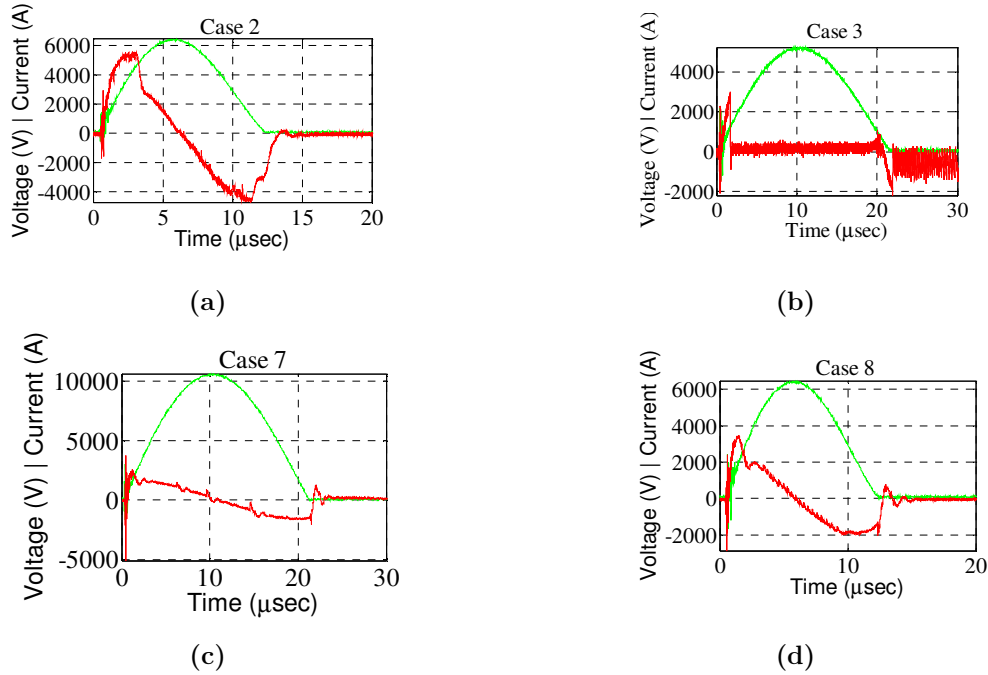
The hardware required for measurements are given in Table 8.4. A summary of the key results are presented in Table 8.5 and plots are shown in Figure 8.14.

Table 8.4: Measurement Equipment Used for the Impulse Test

| Part Number         | Feature  |
|---------------------|--|
| TDS 3014            | Battery operated oscilloscope, 100 MHz bandwidth                       |
| P5100 Voltage Probe | 250 MHz bandwidth, 2.5 kVdc + 1 kV Peak AC, 7-30 pF compensation range |
| P6015 Voltage Probe | 75 MHz bandwidth, 40 kV peak, 7-49 pF compensation range               |
| Current Transformer | Pearson Current Monitor Model 1330                                     |

Table 8.5: Experimental Results of Impulse Testing on Flux Concentrators

| Case | Core   | Test Condition    |                      |                      | Peak Voltage Induced (kV)<br>HF = High frequency, LF =<br>Low frequency |
|------|--------|-------------------|----------------------|----------------------|---|
|      |        | Current Peak (kA) | Rise Time ( $\mu$ s) | Fall Time ( $\mu$ s) |   |
| 1    | I-Core | 5.235             | 9.95                 | 11.7                 | 2.38  |
| 2    | I-Core | 6.45              | 5.36                 | 6.6                  | 5.6   |
| 3    | X-Core | 5.235             | 10                   | 11.71                | 3   |
| 4    | H-Core | 5.235             | 10                   | 11.7                 | 1.28 LF, 2.64 HF  |
| 5    | H-Core | 6.59              | 10.24                | 11.04                | 1.42 LF, 2.335 HF   |
| 6    | H-Core | 7.88              | 9.8                  | 11.4                 | 1.88 LF, 4.96 HF  |
| 7    | H-Core | 10.64             | 9.9                  | 11.2                 | 2.54 LF, 5.11 HF  |
| 8    | H-Core | 6.47              | 5.2                  | 7.1                  | 3.44 LF, 2.88 HF  |



**Figure 8.14:** Plots showing experimental results of impulse testing on the flux concentrators. The impulse currents are in green and the voltage induced on the flux concentrator is red.

Some interesting observations are as follows:

- In Case 2, the results show that on the small I-core, voltages on the order of 5.6 kV are developed at 6.45 kA of peak currents.
- In Case 3 (X-core), to begin with, the voltage starts building up but at around 2  $\mu$ s, shorting of windings occurs due to a possible discharge, which stays till 20  $\mu$ s. Thereafter, the discharge extinguishes and the core operates normally.
- In Case 7 (H-core), at multiple points on the voltage waveform, discharges are observed in the form of single cycle wavelets. However, the core performs well otherwise.

The cores were characterized under nominal conditions before and after the impulse tests were performed. The pre- and post-impulse test nominal characteristics of all the cores were compared. The results are given in Table 8.6.

**Table 8.6: Pre-Post Impulse Test Analysis**

| Primary Current | I-Core |        | X-Core |        | H-Core |        |
|-----------------|--------|--------|--------|--------|--------|--------|
|                 | Before | After  | Before | After  | Before | After  |
| 100             | 56 mV  | 55 mV  | 472 mV | 471 mV | 326 mV | 345 mV |
| 500             | 277 mV | 263 mV | 2.28 V | 2.3 V  | 1.63 V | 1.69 V |
| 900             | 497 mV | 480 mV | 4.13 V | 4.29 V | 2.94 V | 3.04 V |

For all of the cores, the RMS errors for the pre- and post- impulse results lie in the range (13 mV, 85 mV) for OCV and (4.35 mA, 6 mA) for SCC. The RMS errors are not large between the pre- and post- impulse results and can be attributed to measurement error, marginal changes in the operating conditions and minor changes in core position. During the impulse experiments a clear discharge was seen between some windings, evident in Figure 8.14(b)-(d). However, the damage to the windings was not permanent. These results are promising from the standpoint of using the smart sensor for utility assets. Nevertheless, even though the overvoltage do not permanently damage the flux concentrator, it is still necessary to protect the windings and more importantly the sensitive sensor electronics from these overvoltage conditions. The design of a robust protection circuit to prevent the sensor electronics from damage under faulted conditions is presented in the next section.

## 8.6 PROTECTION CIRCUIT DESIGN

It is evident from the simulation and experimental results that the voltage developed on the flux concentrator under faulted conditions can be many orders of magnitude larger than the nominal condition. Therefore, a circuit is designed for the windings of the flux concentrator core, the transformer, and the sensitive sensor electronics for protection against high current faults or lightning strikes. The protection circuit is designed for the worst case scenarios based on the simulation and experimental tests performed previously. Further, a general design methodology for the protection circuit is given the sub-sections to follow. The design-rules presented in this section can be used to design protection circuit for a similar smart-sensor under a different set of worst case conditions.

### 8.6.1 Protection of the Flux Concentrator

Suppose the worst case peak voltage produced at the flux concentrator terminals under a lightning strike or a high current fault is  $V_p$ . Further, assume that the worst case SCC of the flux concentrator is  $I_p$ . If there are  $N_f$  turns on the windings, the worst case peak voltage between any two adjacent windings is given by  $V_{pw}$  ( $V_{pw}=V_p/N_f$ ). Further, if there are  $l$  number of layers in the windings, the voltage developed between any two layers will be given by  $V_{pl}$  ( $V_{pl} = V_p/l$ ). It is vital to protect the different layers from arcing under a high voltage stress. For this purpose, insulation is required between any two layers, such that the peak voltage withstand  $V_{pt}$  of the insulation having thickness  $t$  should be greater than  $V_{pl}$  ( $V_{pt}>V_{pl}$ ). Further, the winding insulation can be selected to withstand the maximum voltage between any two windings ( $V_{Insulation}>V_{pw}$ ). The design equations are summarized in (239) and (240)

$$V_{pw} = \frac{V_p}{N_f} \qquad V_{pt} > V_{pl} \qquad (239)$$

$$V_{pl} > V_p / l \qquad V_{Insulation} > V_{pw} \qquad (240)$$

Apart from protecting the windings from flashovers and discharges, the sensor electronics also needs to be protected. The surge voltages are clamped using transient voltage suppressors. Two different technologies can be used for preventing electronics from high voltage surges, namely transient voltage suppressor diodes (TVS diodes) and metal oxide varistors (MOV). On the one hand, TVS diodes can provide a lower clamp voltage, as compared to MOVs. While on the other hand, the TVS diodes absorb less energy as compared to MOV. Therefore, it is recommended to use a hybrid protection scheme comprising both the TVS diodes and MOVs.

### 8.6.2 TVS Diodes for Winding Sections

As each winding section has to be protected from surge voltages, access to several taps on the windings is essential. A bi-directional TVS diode is provided between any two sections. The rating of the TVS diodes is selected in such a way that its clamping voltage

( $V_{cTVS}$ ) at  $I_p$  is less than  $V_{pl}$ . Further, the peak current carrying capacity of the TVS diodes ( $I_{pTVS}$ ) should be greater than  $I_p$ . The design equations are summarized in (241)

$$V_{cTVS} < V_{pl} \qquad I_{pTVS} > I_p \qquad (241)$$

### 8.6.3 MOV Design

As the energy dissipation capacity of an MOV is much higher than the TVS diode, it is recommended to provide an MOV in addition to the TVS diodes across the entire winding. The rating of the MOV is selected such that the MOV nominal voltage ( $V_{nMOV}$ ) is greater than the nominal operating voltage of the circuit. In addition, the clamp voltage of the MOV ( $V_{cMOV}$ ) is equal to the sum of the clamp voltages of all the TVS diodes at the peak current. Moreover, the energy dissipation rating of the MOV ( $E_{MOV}$ ) should be higher than the worst case energy dissipation ( $E_p$ ). The design equations are summarized in (242) and (243)

$$V_{nMOV} > V_{nom} \qquad V_{cMOV}(I_p) = \sum_{i=1}^n V_{cTVSi}(I_p) \qquad (242)$$

$$E_{MOV} > \frac{1}{2} I_p V_{cMOV} t_f = E_p \qquad (243)$$

### 8.6.4 Secondary Transformer TVS diode design

It should be noted that the clamp voltage of an MOV and the TVS diode increases with an increase in current. As there is a step-up transformer right after the TVS diode/MOV protection stage, the voltage is further stepped-up. In the worst case, the voltage at the output of the step-up transformer also needs to be clamped to prevent the AC/DC boost converter from experiencing over-voltages. A TVS diode is used for this purpose. The TVS diode is selected in such a way that the clamp voltage of the diode ( $V_c(I_{LP})$ ) at peak short circuit current is less than the breakdown voltages ( $V_{br}$ ) of any of the MOSFETs or diodes in the converter. Further, the reverse stand-off voltage ( $V_r$ )

should be greater than the nominal voltage of the circuit ( $V_{nom}$ ). The design equations are summarized in (244) - (246)

$$I_{LP} = \frac{N_2}{N_1} \frac{V_{cMOV} \Delta t_f}{L_T} \quad (244)$$

$$V_c(I_{LP}) > V_{br} \quad (245)$$

$$V_r > \frac{N_2}{N_1} V_{nom} \quad (246)$$

### 8.6.5 Zener Design

The AC/DC boost converter is connected to a voltage regulator and an ultra-capacitor. A uni-directional zener is designed in such a way that it can clamp the voltage at the peak of the capacitor ( $V_{pc}$ ) and the voltage regulator ( $V_{pr}$ ). The zener voltage ( $V_z$ ) also needs to be greater than the operating voltage of the sensor electronics ( $V_{snom}$ ) so that it doesn't draw a lot of quiescent current under nominal conditions.

$$V_{snom} < V_z < \min(V_{pc}, V_{pr}) \quad (247)$$

### 8.6.6 Design Example for Protecting the Optimal Core

If the optimal core design 1 is considered, with  $N_f = 350$ ,  $V_{pl} = 13$  kV,  $V_{pw} = 350$  V and  $I_p = 50$  A. The worst case voltage build-up across the entire winding for a 350 turn flux concentrator will give rise to a turn-to-turn voltage of 350 V. Based on the optimal design, on an average in one layer there are 40-50 turns. Between any two layers, the worst case voltage will be 13 kV. Nomex sheet by DuPont having thickness of 10-12 mils can handle voltages up to 17 kV/mm – 33 kV/mm, and therefore it is recommended to provide a Nomex sheet between any two layers. Further, with some additional margin, the magnet wires can be coated with insulation supporting 1 kV discharges.

For preventing each section of the flux concentrator winding, the TVS diode from Littelfuse, SMBJ7.0CA, capable of handling the full fault current of 50 A is chosen.

The clamp voltage of the MOV should be close to the sum of the clamp voltages of the TVS diodes. Further, the energy rating of the MOV should be more than the maximum energy dissipated,

$$E_{MOV} > \frac{1}{2} I_p V_{cMOV} t_f \simeq 30mJ \quad (248)$$

A TDK Corporation AVR-M1608C120M MOV is chosen that can be used to handle 90 mJ with a clamp voltage of 20V at 2A. This MOV is suitable for use at the primary winding of the transformer. The quiescent current requirement at lower voltages of the chosen MOV is quite low, thereby, not imposing a problem under nominal operation.

The leakage inductance of the transformer as per the optimal design is close to 0.6 mH, which gives the peak short circuit current over an 8  $\mu$ s period with transformer turns ratio of 1:20 to be 50 mA. Usually, the clamp voltage of TVS diodes that are rated for smaller peak currents increases dramatically with an increase in current. Therefore, it is advisable to select a TVS diode that has a clamp voltage equal to the breakdown voltage of the MOSFETs and diodes but at a much higher peak current. The TVS diode on the secondary side of the transformer is chosen as the SMAJ51CA from Littelfuse. In this design, the peak current is chosen as 5A and the clamp voltage at this current is around 82V. This way, at 0.05 A, the clamp voltage remains small.

The general circuit diagram of the overall protection scheme is shown in Figure 8.15.

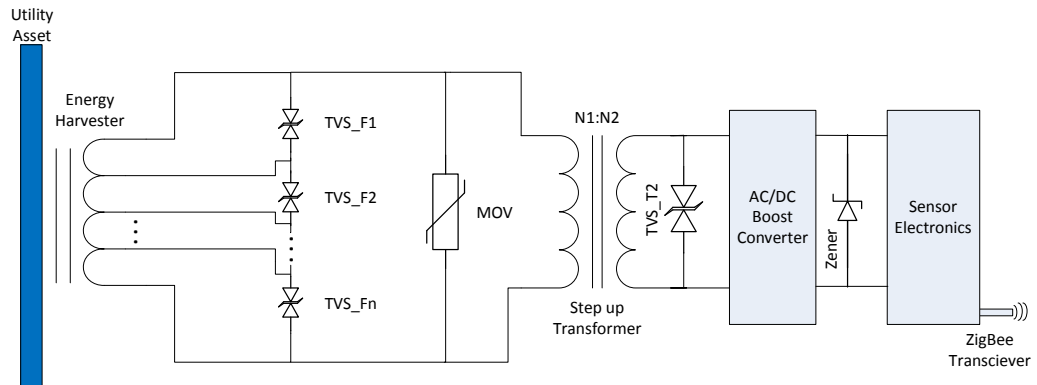
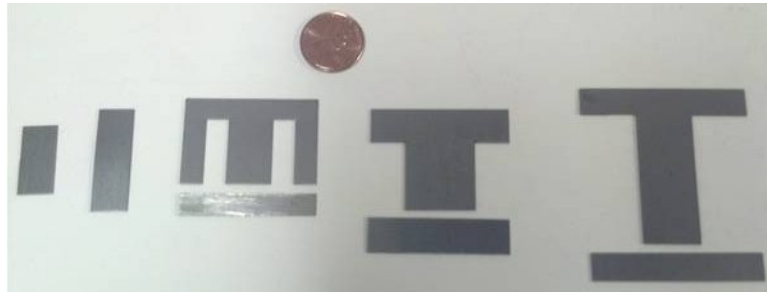


Figure 8.15: Proposed protection circuit for the optimal energy harvester.



Two different designs of optimal cores with the required protection were manufactured and are shown in Figures Figure 8.16 and Figure 8.17.



**Figure 8.16: Core laminations (Left to right: S1 - Sensor core design 1, S2 - sensor core design 1, TX - transformer, FC1 - flux concentrator design 1, FC2 - flux concentrator design 2)**



**Figure 8.17: Optimal flux concentrator and sensor cores with the required protection (Left to right: S1, S2, TX, FC1, FC2)**

## **8.7 ZIGBEE® COMMUNICATION LINK PERFORMANCE**

### **8.7.1 Distance Tests**

The performance of the ZigBee® transceiver system was tested in order to determine the maximum range and accuracy of the system. A transmitter was placed in a stationary position, in an open, flat field, and a receiver was moved from 2 m to 200 m away. This test was performed several times, with transmission power and channel frequency being varied.

The strength of signal at the receiver (RSSI) and the packet error ration (PER) were both recorded over five-thousand sample intervals, and are shown graphically in Figure 8.18 and Figure 8.19 below.

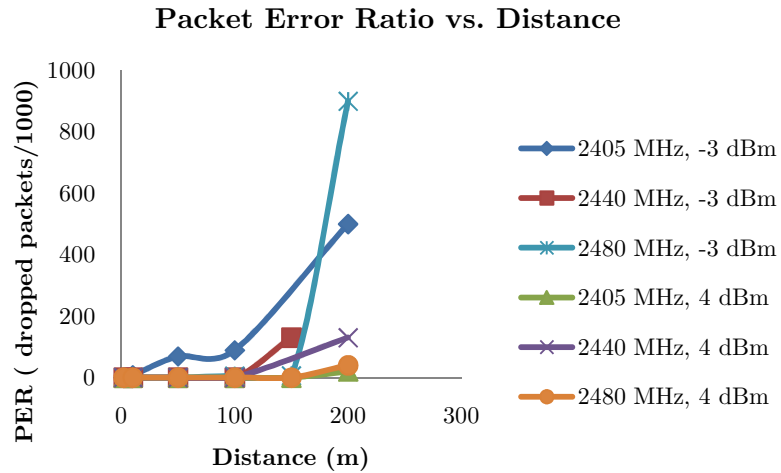


Figure 8.18: ZigBee® PER Variation with Distance

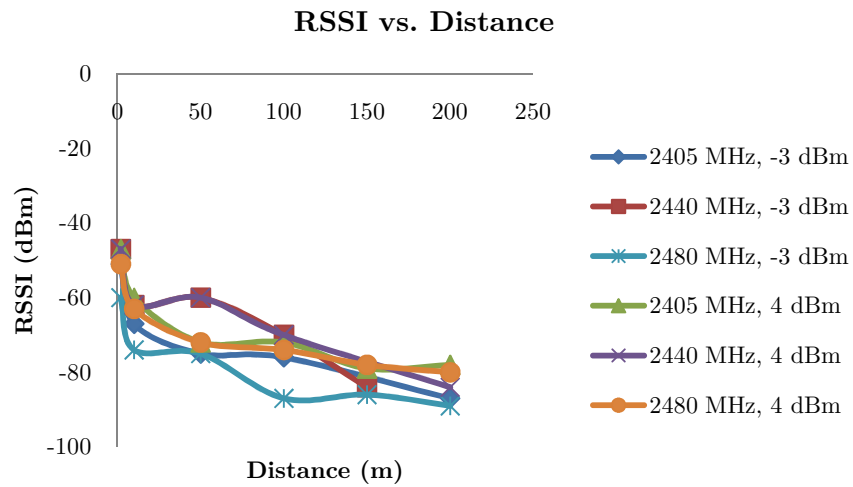


Figure 8.19: ZigBee® RSSI Variation with Distance

Studying the data it is seen that there is almost zero packet error at a transmission power level of 4 dBm, and at -3 dBm there is a tolerable level of loss up to distances ranging from 100 m to 150 m.

Regarding channel frequency, there was minimal difference between the channels, though the channel at 2440 MHz does perform slightly worse than 2405 MHz and 2480 MHz.

Tests were also performed indoors, as seen in Table 8.7. Indoor ZigBee® performance test results were comparable to those of the outdoor test. One interesting result however, was that a no-line-of-sight test was also performed, and it showed a significant decrease in RSSI.

### 8.7.2 High Voltage Interference Tests

In order to gauge the effects of high voltage environments on the performance of the ZigBee® communications system, a test environment capable of producing voltages as high as 80 kV was constructed at Georgia Tech's NEETRAC facility.

The setup, seen in Figure 8.20 shows a step-up transformer and suspended rod surrounded by a grounded cage. The sensor was tested in two situations, atop the step-up transformer to simulate a typical substation connection and directly attached to the rod to simulate a line connection. The ZigBee® receiver was placed outside the cage at a distance varying from 3.5 m to up to 10 m.

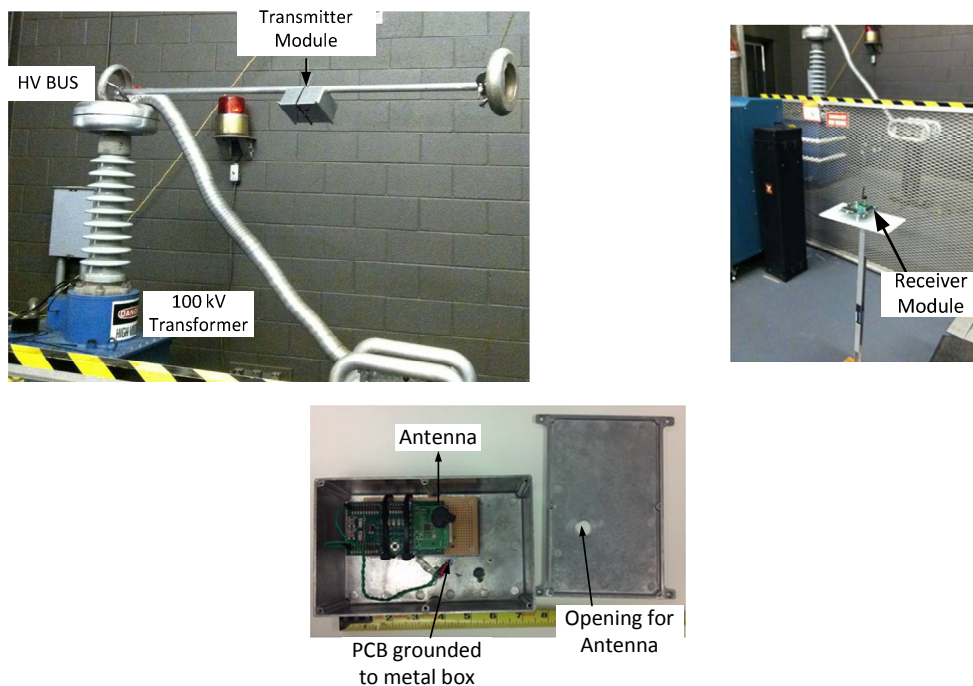
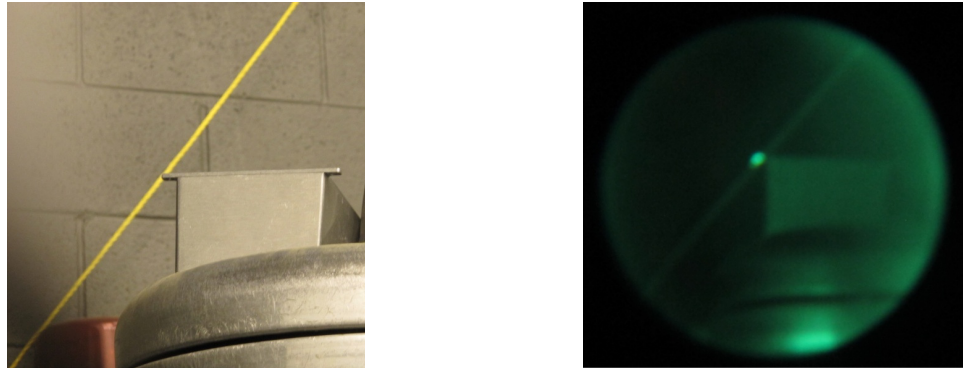


Figure 8.20: NEETRAC High Voltage Test Setup

In addition to creating high voltage conditions, at above 65 kV corona and partial discharge was seen to occur in the system, allowing gauging of the effect of this form of EMI on the ZigBee® communication's performance. Figure 8.21 below shows a camera photo capturing this corona phenomenon at 80 kV.



**Figure 8.21: Development of Corona at 80 kV**

Results of the test showed that the ZigBee® communication link performed extraordinarily well, and was unaffected by HV conditions and corona noise. Figure 8.22 and Table 8.7 below show that line voltage has no correlation with ZigBee® performance, having a correlation coefficient of nearly zero. Additionally, at ranges less than 10 m, distance and channel frequency also had little or no effect on performance. Transmission power, on the other hand, was greatly correlated with RSSI, as expected.

These results show that for substations or utility networks with a maximum length between any two sensors of around 200 m, it is expected that ZigBee® will perform very well, and that a transmission power level of -3 dBm will be possible to be used.

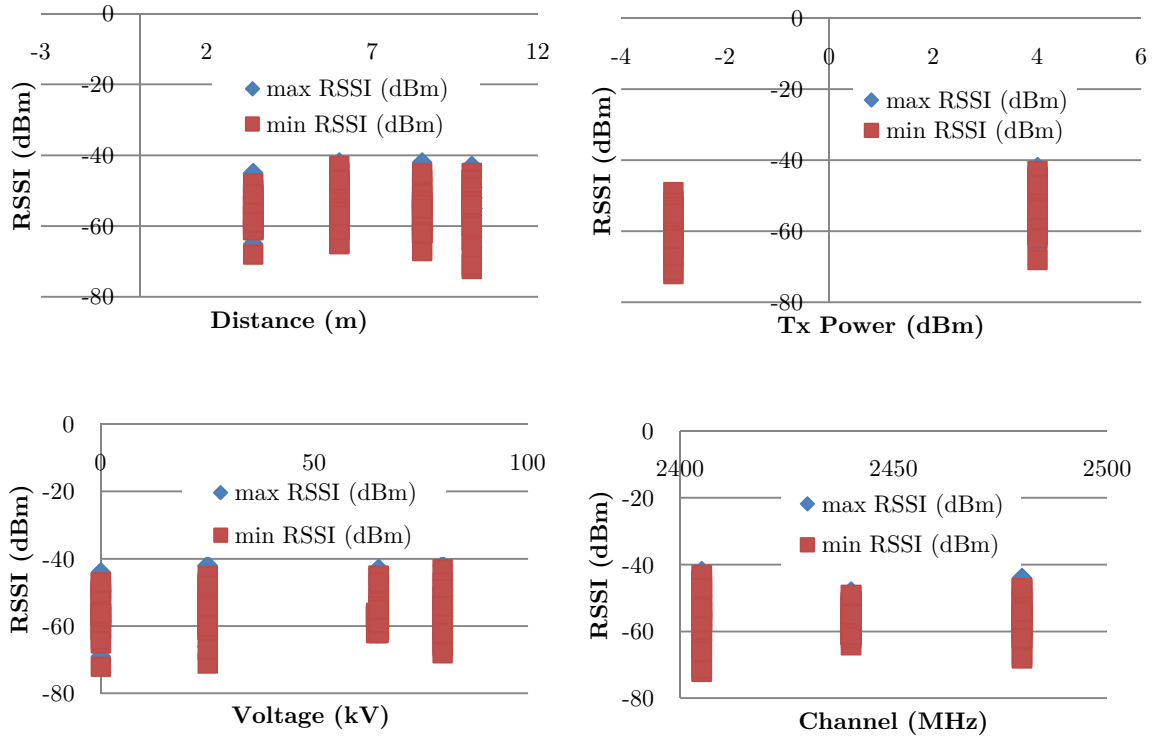


Figure 8.22: Relationship of Variables with ZigBee® RSSI

Table 8.7: Correlation of Variables with ZigBee® RSSI

| Variable                                    | Correlation with Maximum Observed RSSI |
|---|--|
| Voltage (0 V to 80 kV)                      | -0.03                                  |
| Transmission Channel (2405 MHz to 2480 MHz) | -0.16                                  |
| Transmission Power (-3 dBm to 4 dBm)        | 0.56                                   |
| Distance (3.4 m to 10 m)                    | 0.02                                   |

## 8.8 EMI/CORONA SUPPRESSION AND PACKAGE DESIGN

A conceptual diagram of the final smart current, temperature and voltage sensor with the integrated protection circuit is shown in Figure 8.23 along with a 3-D conceptualization of the sensor in Figure 8.24. Note that a partial dual-cage structure is used to house and protect the sensor.

The partial dual-cage structure is designed to be able to compactly house the sensor, while being able to segregate sensing and energy harvesting circuitry from the control, signal conditioning, and communications circuitry that need a higher degree of protection.

The outer case contains the energy harvester and sensors and is a partial Faraday cage with insulation on the face attached to the utility asset. The inner case is a completely enclosed Faraday cage to protect sensitive circuitry from low frequency electric field signals generated by normal line operation and high frequency signals due to corona, lightning, etc. There is also a single point electrical connection to the utility asset which is used to set the ground of the inner case to the same potential as the asset. A single point connection prevents current from flowing in the cage which would then effectively bypass the energy harvester and current sensor.

In both cages, all sharp edges have been filleted and a minimum number of openings are made in order to maximize each cage's effectiveness at rejecting noise. Small openings are provided in order to connect to the sensor cores, flux concentrator, and ZigBee<sup>®</sup> transceiver and they are placed on different faces of the cage to minimize their detrimental effect to the cage's performance.

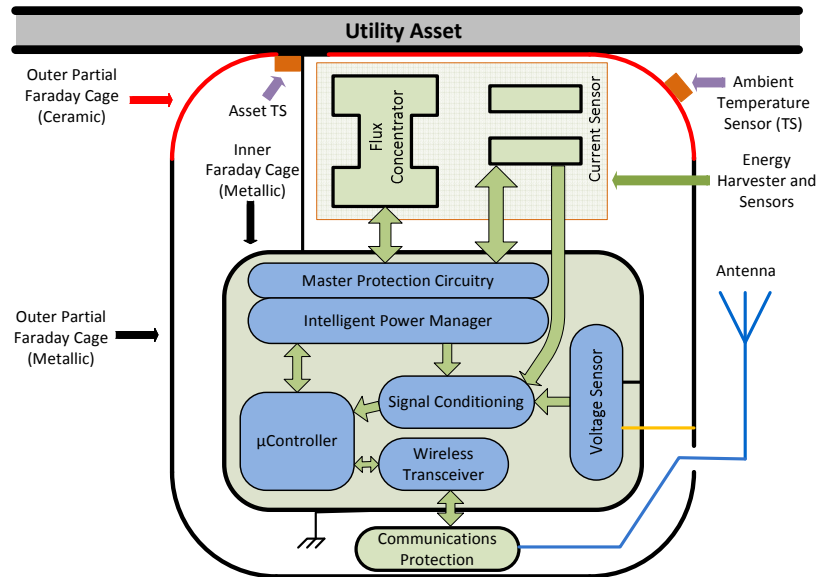


Figure 8.23: Conceptual diagram of sensor, including shielding scheme

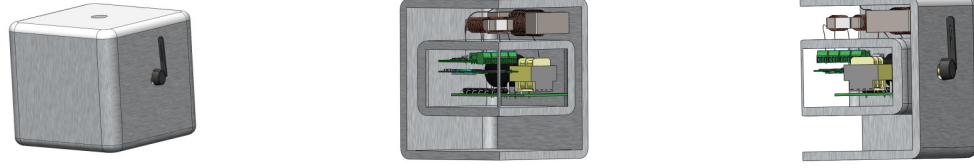


Figure 8.24: 3-D conceptualization of Stick-on sensor showing dual-cage design

$$A=3.34t\sqrt{f\mu_r\sigma_r} \quad (249)$$

$$R=322+10\log\left(\frac{\sigma_r}{\mu_r f^3 r^2}\right) \quad (250)$$

Corona and air gap discharge occur over frequency ranges of as low as 10 MHz to up-to 600 MHz, with power levels as high as -20 dBm [114]. Equations (249) and (250) show the near-field absorption loss and reflection loss of a full faraday cage, where A and R are absorption and reflection loss in dB, t is shield thickness in inches, f is noise frequency in MHz, r is the distance from the noise source in meters, and  $\sigma_r$  and  $\mu_r$  are electric conductivity and magnetic permeability relative to copper [115].

If copper is used as the shielding material, then a shielding thickness of only 0.2 mm will reduce a -20 dBm noise level from corona to -100 dBm, and provide more than adequate protection. Seams and apertures in the cage will reduce its shielding effectiveness from this level, as seen in (251) where S is the reduction in shielding effectiveness in dB,  $\lambda$  is the noise wavelength, l is the maximum aperture dimension, and n is the number of apertures in the case.

$$S = 20 \log\left(\frac{\lambda}{2l}\right) - 10 \log(n) \quad (251)$$

The reflection loss, however, will likely produce 100 dB of attenuation at typical noise frequencies and sensor distances. This is more than enough to counteract the non-idealities of the case.

To maintain mechanical integrity and ease of manufacturability, a thicker cage size of 2 mm is used in the conceptualization and should provide more than adequate protection to the sensor's circuitry from the high voltage environment.

## **8.9 CONCLUSIONS**

In conclusion, this chapter proposed a robust design for a low-cost, smart wireless sensor which can be stuck-on to a utility asset and operate autonomously. Challenges related to optimal design of the energy harvester were addressed and an example design was presented. Practical issues related to fault currents and lightning strikes were addressed through extensive simulation and experimental studies. It was found that the sensors could develop voltages a million times larger in faulted conditions as compared to nominal conditions. Therefore, a protection scheme was proposed to prevent the sensor from overvoltage conditions and large impulses. Finally, a novel partial dual faraday cage design was presented to prevent the sensor from EMI and other corona noise present near high voltage assets. The effects of high voltage noise such as corona on wireless communication and integration of low-cost voltage sensing were also addressed.



## CHAPTER 9

### CONCLUSIONS, CONTRIBUTIONS AND FUTURE

#### RESEARCH

##### 9.1 CONCLUSIONS

This work presented the concept of a small, low-cost, self-powered smart wireless sensor that can be used for monitoring current, temperature and voltage on a variety of utility assets. Wireless sensor network architecture for integrating these sensors to information systems, such as SCADA, was proposed. The role of these sensors is to provide real-time information and min-max history of asset parameters such as current, voltage and temperature. In addition, these sensors can be used to detect faults and absence of power on assets. The information collected by these sensors could be used by asset managers, system operators and planners to take informed decisions about maintenance, and replacement of utility assets. A meshed network of these sensors can also help in diagnosing failure on assets, reducing downtime during an outage, and minimizing truck-rolls by providing information of the particular asset that lost power. Therefore, these sensors have tremendous value for utilities.

The sensor developed in this research was designed to operate without batteries to have an expected life of 20-30 years. Energy harvesting techniques that could power the sensor from energy present in the ambient were explored. Particularly, electric field, magnetic field and solar energy were considered. All these sources of energy have use in a plethora of utility asset monitoring applications. Specifically, the flux concentrator based energy harvester that uses magnetic field for harvesting energy produced the maximum energy density of all the techniques. The flux concentrator is an open ferromagnetic core-coil assembly, which also gives information of the current flowing in the asset. Therefore, the flux concentrator was used for the dual purpose of energy harvesting and current

sensing. Another advantage of using the flux concentrator as the current sensor is that it has a wide linear range, up to 40 kA, unlike CTs that can easily saturate at higher current levels. Further, the flux concentrator approach for monitoring current reduces the size and cost of the sensor by an order of magnitude as compared to the existing current sensing solutions.

Moreover, it was found that one of the major challenges for self-powering the sensor is maintaining a regulated DC supply for the sensor electronics under all operating conditions. To address this problem, a novel 0.2V to 3.3 V AC/DC boost converter was proposed, designed and implemented. Subsequently, the energy harvester was integrated to the power circuit and was used to operate a stick-on current and temperature wireless sensor developed in this research. This research also presented an optimal design of the flux concentrator and the power circuit. A process for optimization of the core dimensions, and windings was provided, which can be used to design energy harvester and power circuit for any other application.

One of the applications of the sensor is to be used in a substation where multiple current carrying assets may interact with the sensor to produce errors in measurement. Moreover, as the flux concentrator is an open core-coil assembly, it needs expensive field calibration. Two different approaches to solve these issues were proposed, namely the MCTM and smart DCTM. The smart DCTM approach used two small sensor-cores for rejecting the effects of far-fields and other cross-talk. Furthermore, the memory present on the sensor along with the microcontroller was used to implement a novel algorithm which over time allowed the sensor to calibrate autonomously. Essentially, the sensor triangulates its position relative to the near asset, finds an effective far-field distance from a resultant far-off asset, and rejects the effects of far-fields. The proposed algorithms make the sensor immune from any cross-talk or other magnetic noise, and help the sensor to self-calibrate. Extensive simulation studies were performed to validate the smart DCTM algorithm for current sensing under various realistic scenarios. Finally, the smart DCTM approach was demonstrated in the lab on an ACSR conductor in the presence of far-field artificially

created using an air-cored inductor. Successful operation of the sensor was demonstrated under two different configurations of the air-cored inductor relative to the sensor. Using the proposed approach, the error in measurement was reduced from over 150% to less than 5 % after convergence. Consequently, the smart DCTM approach transforms the simple core-coil assembly based current sensor into a highly intelligent method, while maintaining the cost of the overall sensor low.

Further, a new voltage sensing algorithm was also proposed, called the moving average voltage sensing (MAVS) algorithm. The major purpose of the proposed voltage sensor is to detect whether a particular asset is energized or not. In addition, the role of the sensor is to detect voltage sags and swells on the asset and to produce alarm signals under these conditions. Therefore, as compared to conventional voltage sensors used for energy metering purposes, the acceptable error bands on the proposed voltage sensor can be relatively high ( $< \pm 5\%$ ). The MAVS algorithm is a novel method that uses history of recorded measurements to estimate the present voltage of the asset, and therefore, the method is self-calibrating. Extensive simulation studies were performed to test the algorithm under different operating conditions, such as changes in voltage of the conductor, distance of conductor from the earth and configuration of conductors. Finally, a voltage sensor prototype was built and tested on a high voltage bus up to 35 kV voltage levels. The self-calibration of the sensor was successfully demonstrated in these experiments. Further, the sensor tracked the voltage changes on the asset within an average error band of  $\pm 5\%$ .

The research presented in this dissertation was also focused at solving practical issues associated with utility assets when they are subjected with high current impulses during faults and lightning strikes. Simulation studies were presented to understand the peak voltages that could be induced under faulted conditions and novel protection circuit architecture was proposed. Package design of the sensor to withstand external noise, such as corona, was also presented.

This ultimate goal of this research was holistic development of a smart sensor for utility asset that can serve as a universal solution for multiple applications at a low price point. These sensors when operated in a meshed topology can help increase situational awareness, provide increased visibility of the grid parameters, and therefore, increase reliability of the grid. The techniques developed in this research have shown spectacular performance under different operating conditions. Hopefully, the developed low-cost smart sensor will be an integral part of the *smart grid* of the future.

## 9.2 SUMMARY OF CONTRIBUTIONS

To summarize, this work has made the following contributions:

1. Performed a scoping study through extensive simulations and experiments of energy harvesting techniques for powering utility sensors.
2. Developed a 0.2 V to 3.3 V AC/DC boost converter that could self-start at currents as low as 60 A.
3. Developed, and designed a self-powered stick-on current and temperature wireless sensor and demonstrated its operation in conjunction with an ACSR conductor.
4. Developed two novel current sensing algorithms, namely MCTM and smart DCTM. The smart DCTM algorithm was implemented on the stick-on current sensor and operation was successfully demonstrated in the lab at currents up to 1000 A.
5. Developed a novel voltage sensing algorithm called the moving average voltage sensing (MAVS) which was implemented in a stick-on voltage sensor built in this research. The voltage sensor was used to monitor a high voltage bus at 35 kV.
6. Developed a method to optimally design the energy harvester and power management circuit.
7. Developed a novel protection architecture that prevents permanent damage to the sensor electronics and cores from fault currents and lightning strikes.

## 9.3 RECOMMENDED FUTURE RESEARCH

The future work has been divided into several sections, namely, voltage sensing current sensing and design and testing.

### 9.3.1 Voltage Sensing

#### 9.3.1.1 *Relaxing the assumptions*

In this research, a new voltage sensing algorithm was developed called the moving average voltage sensing (MAVS) method. The MAVS method was used to estimate and track changes in the voltage of a conductor in any configuration, single phase or multi-conductor, by using the history of collected data. Thereby, allowing the sensor to self-calibrate.

As a part of future research, one assumption in the algorithm related to changes in electrical permittivity of air can be relaxed. The electrical permittivity of the air around the conductor was assumed to be constant over time. Further, it was assumed that the permittivity doesn't change dramatically in short periods of time. This assumption is valid in most cases; however, with changes in weather, the permittivity of the air around the utility asset can change by orders of magnitude. A variation in electrical permittivity of the air, for instance, due to increase in humidity, can alter the capacitance ( $C_2$ ) between the sensing plate and ground. As  $C_2$  is very small and forms the dominant impedance that determines the value of displacement current and the voltage between the sensor plates, any deviation in  $C_2$ , would cause large changes in the sensed voltage. A simple solution to this problem could be to use a relatively higher impedance capacitor between the sensing plates such that any variations in the external capacitance would not affect the displacement current by a large percentage, hence, keep the errors in measurement low. This concept was not tested in this research and forms an interesting study for future research.

### *9.3.1.2 Field Testing*

Another research effort could be to experimentally validate the MAVS method under changes in external conditions, such as variations in distance of the high voltage bus from ground, variation in air humidity, and in a general, testing the algorithm in a multi-conductor case.

### *9.3.1.3 Estimation of Distance to Ground*

In a single phase system, the MAVS method was used to estimate the distance of the conductor to ground in addition to the voltage. However, for complex systems, such as a three phase system, it is difficult to decouple the governing equations to find a closed form solution for the distance to ground. Nevertheless, it is still possible to compute an equivalent distance that is strongly correlated with the actual distance to ground.

As the ultimate goal is to integrate the voltage sensor with the current sensor in a single package, the loading on the line can be used as additional information for decoding the distance of the line to ground. The sag on an overhead conductor is a function of ambient temperature, conductor temperature, wind speed and thermal loading. The sensed temperature and current information can be leveraged to form a correlation model with sag of the conductor. Further, this model could be fine-tuned using the effective distance information obtained from the MAVS algorithm. Over time, a robust mathematical model for the sag of the conductor could be estimated. Estimation of sag using intelligent sensing and modeling techniques can be a significant future research work.

## **9.3.2 Current Sensing**

In this research, the smart DCTM current sensing algorithm was tested on an ACSR conductor having a circular cross-section. An interesting future research experiment would be to test the sensor on different irregular asset geometries, such as rectangular cross section of a busbar.

### 9.3.3 Design and Testing

#### 9.3.3.1 Testing the Protection Circuit

In this research, successful operation of the sensor under a wide range was demonstrated. Further, a protection circuit was proposed to prevent the sensor from permanent damage under faulted conditions, such as high fault currents and lightning strikes. However, the ability of the proposed protection circuit architecture has not been tested under actual faults. Therefore, an interesting study for future research would be to subject the sensor with 8/20  $\mu\text{s}$  and 4/10  $\mu\text{s}$  impulses of 10-20 kA peak current. Consequently, gauge the ability of the protection circuit to prevent the sensor core assemblies, flux concentrator, transformer, and electronics from damage.

#### 9.3.3.2 Designing a Robust Enclosure

In this research, a novel partial dual-cage package is proposed. The package does not attenuate energy harvested by the flux concentrator, and concurrently, prevents the sensor electronics from external noise. Further, the package itself acts as a voltage sensor, reducing extra hardware in the form of sensing plates. As future work, design and development of the enclosure to handle changes in temperature and weather conditions needs to be performed. The package should be designed for a 20 years expected life.

#### 9.3.3.3 Field Demonstration of a Sensor Network

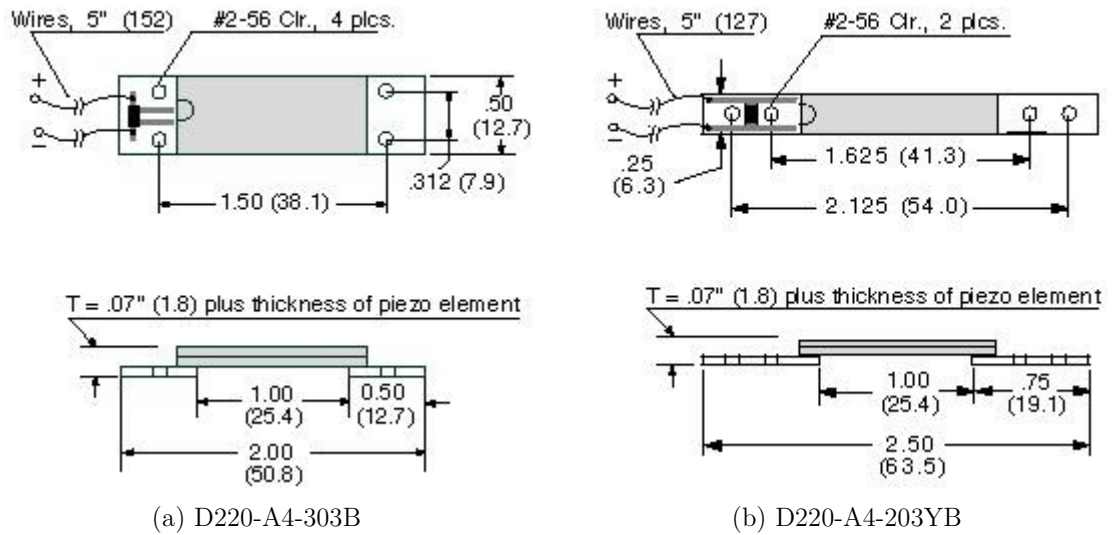
A field demonstration of a network of Stick-on sensors on multiple utility assets in a substation integrated to SCADA through a gateway can be an interesting experimental project. This effort can help validate the operation of the sensor in a practical scenario and test the communication architecture proposed in this research

## APPENDIX A

### PZB-MAGNET TECHNICAL SPECIFICATIONS



**Table A.1: Technical Specification of the Piezoelectric Bimorph bender**

| Part No.      | Piezo Material | Weight (grams) | Stiffness (N/m) | Capacitance (nF) | Rated Tip Deflection (mmpeak) | OC Voltage (Vpeak) | Rated Frequency (Hz) | SC Current ( $\mu$ Apeak/Hz) |
|---------------|----------------|----------------|-----------------|------------------|-------------------------------|--------------------|----------------------|------------------------------|
| D220-A4-203YB | 5A4E           | 1.7            | 120             | 23               | $\pm 1$                       | $\pm 14.9$         | 120                  | $\pm 3.9$                    |
| D220-A4-303YB | 5A4E           | 2.7            | 360             | 46               | $\pm 0.84$                    | $\pm 14.9$         | 145                  | $\pm 7.9$                    |



**Figure A.1: Dimensions of the Piezo bimorph bender**

**Table A.2: Technical Details of NdFeB Magnets**

| Part No. | Dimension (in x in x in)                             | Material  | Weight (gms) | Surface Field (T) | Picture   |
|----------|--|-----------|--------------|-------------------|---|
| B441     | $\frac{1}{4} \times \frac{1}{4} \times \frac{1}{16}$ | Grade N42 | 0.480        | 0.2305            |  |
| B442-N50 | $\frac{1}{4} \times \frac{1}{4} \times \frac{1}{8}$  | Grade N50 | 0.960        | 0.4215            |  |



## APPENDIX B

### BILL OF MATERIALS OF THE STICK-ON SENSOR

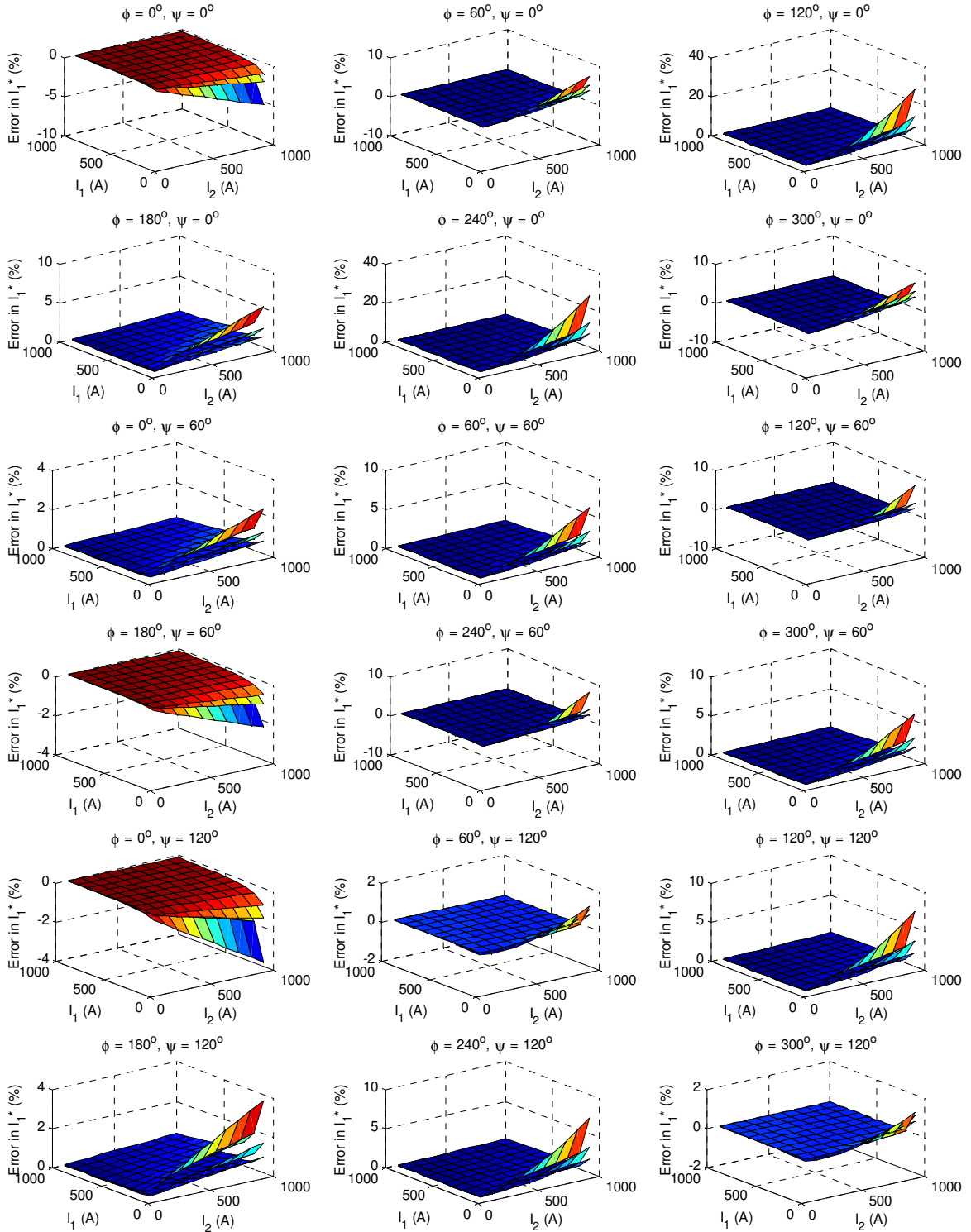
**Table B.1: Bill of Materials for the Stick-on sensor**

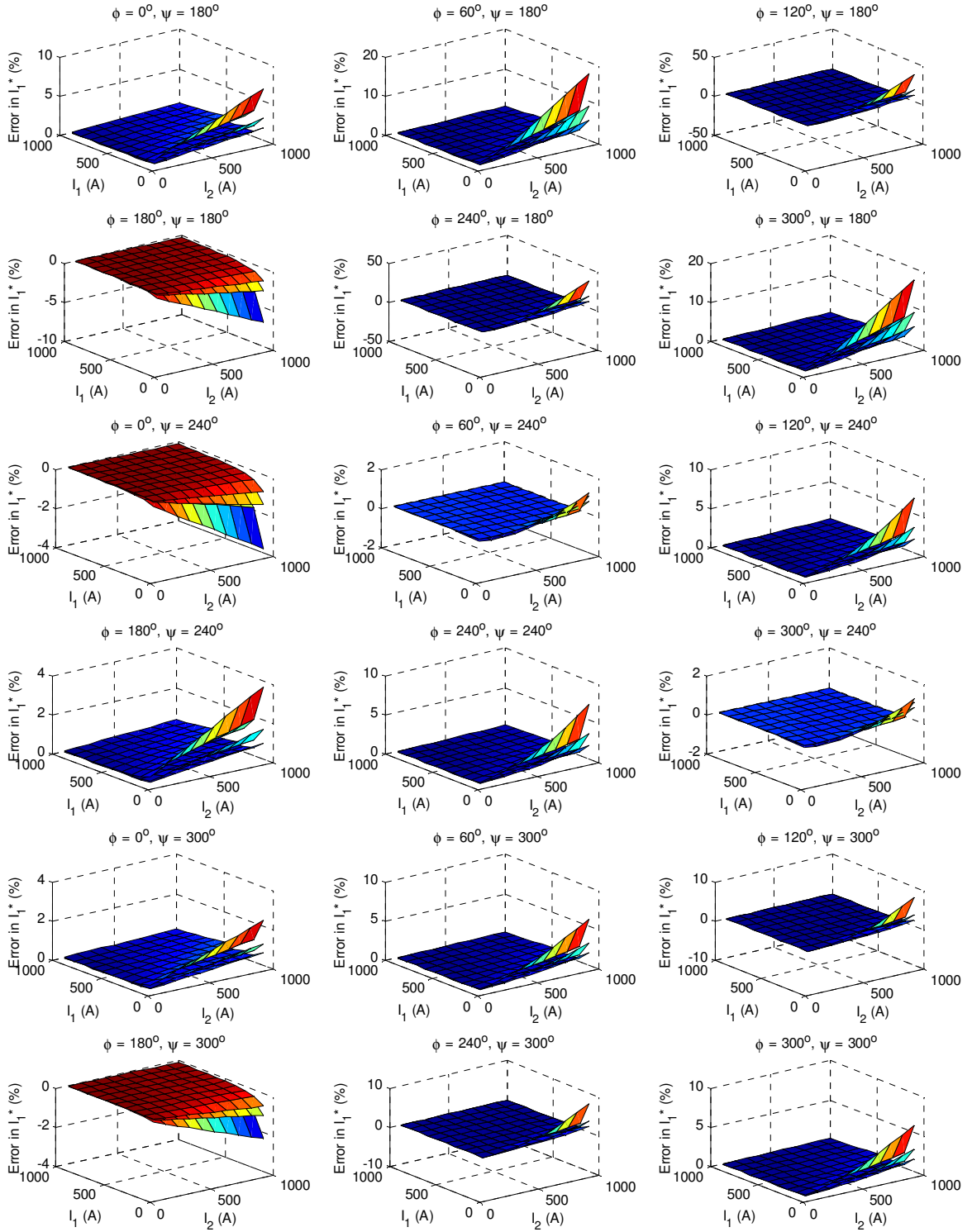
| Component                             | Company                     | Part No.          | Quantity | Per unit price | Price    |
|---------------------------------------|-----------------------------|-------------------|----------|----------------|----------|
| Energy Harvester                      | NA                          | NA                | 1        | \$ 2.50        | \$ 2.50  |
| Step-up Transformer                   | Tamura                      | SB2812-1204       | 1        | \$ 2.68        | \$ 2.68  |
| Schottky Diode                        | Vishay                      | 1N5818IR-ND       | 5        | \$ 0.38        | \$ 1.90  |
| Mosfet                                | Zetex Semiconductors        | ZXM64N035L3       | 2        | \$ 1.45        | \$ 2.90  |
| Regular Diodes                        | Diodes Inc                  | 1N4148            | 2        | \$ 0.26        | \$ 0.52  |
| Zener Diode                           | Diodes Inc                  | 1N5233BDICT-ND    | 1        | \$ 0.50        | \$ 0.50  |
| Transistor                            | PNP and NPN                 | 2N3906 / 2N3904   | 2        | \$ 0.40        | \$ 0.80  |
| Low Drop Out regulator                | Linear Technologies         | LT1121-3.3#PBF    | 1        | \$ 1.99        | \$ 1.99  |
| Resistance                            | Stackpole electronics       | RNF14FTD1M00CT-ND | 17       | \$ 0.05        | \$ 0.85  |
| Capacitor                             | Panasonic                   | ECE-A1AKS101      | 5        | \$ 0.10        | \$ 0.50  |
| Ultracapacitor                        | PowerStor                   | PB-5R0V105-R      | 1        | \$ 8.20        | \$ 8.20  |
| Low power comparator                  | Microchip                   | MCP6541           | 1        | \$ 0.38        | \$ 0.38  |
| Op amp                                | Microchip                   | TC1029EPA         | 3        | \$ 1.50        | \$ 4.50  |
| Temperature Sensor                    | Analog Devices              | TMP35             | 2        | \$ 1.35        | \$ 2.70  |
| Sensor Core                           | NA                          | NA                | 2        | \$ 0.75        | \$ 1.50  |
| Microcontroller and Zibee Transceiver | Texas Instruments           | CC2530            | 1        | \$ 6.65        | \$ 6.65  |
| Enclosure                             | -                           | -                 | 1        | \$ 2.50        | \$ 2.50  |
| Male Header Connectors                | FCI                         | 609-3239-ND       | 1        | \$ 0.52        | \$ 0.52  |
| Female Header                         | Molex Connector Corporation | 50-57-9010        | 4        | \$ 0.20        | \$ 0.80  |
| Printed Circuit Board                 | -                           | -                 | 1        | \$ 5.00        | \$ 5.00  |
| Antenna                               | Antenova                    | Titanis           | 1        | \$ 5.00        | \$ 5.00  |
| Total cost of the Stick-on sensor     |                             |                   |          |                | \$ 52.89 |

**Note:** Most of the above prices are single quantity Digikey prices and do not reflect high volume pricing.

# APPENDIX C

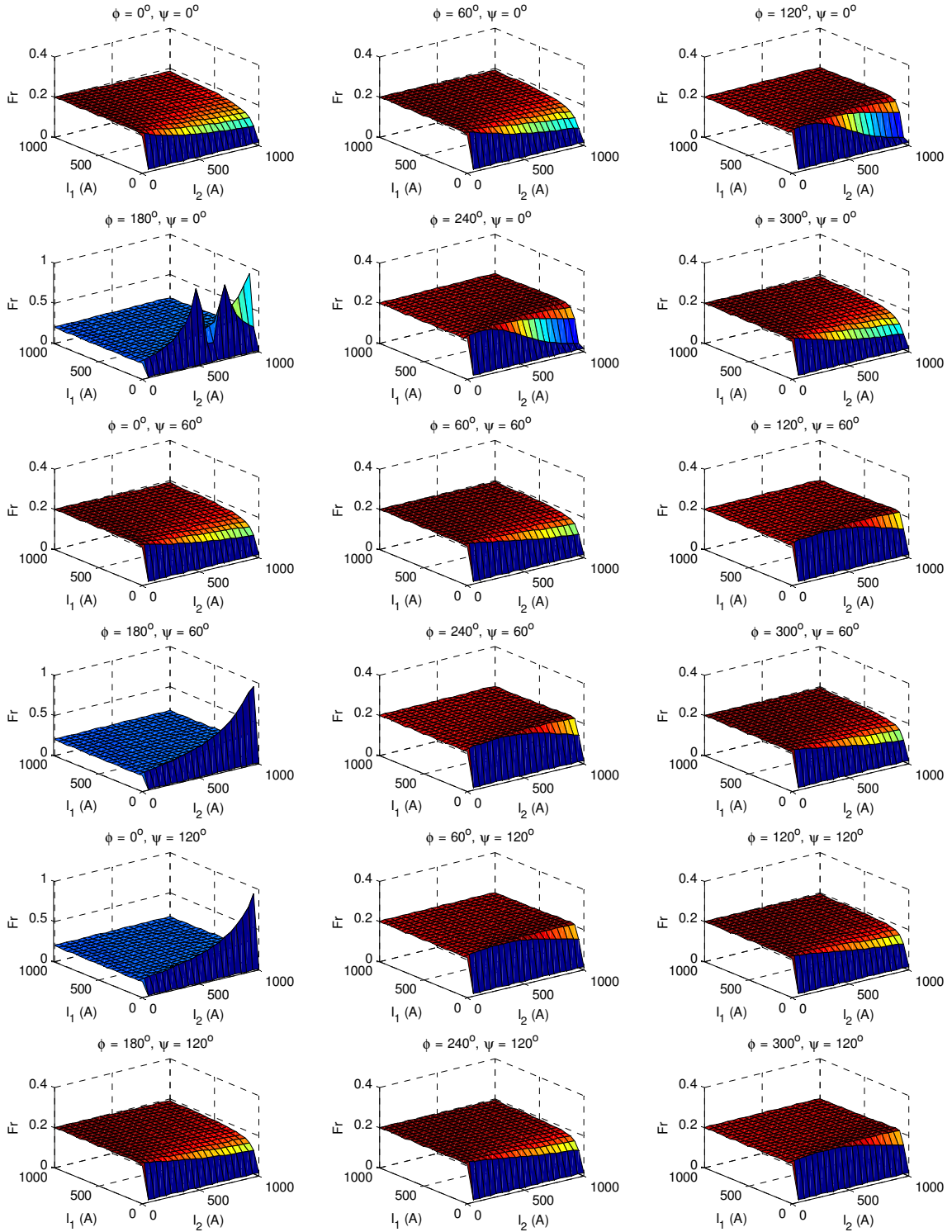
## ERROR PLOTS FOR MCTM ALGORITHM

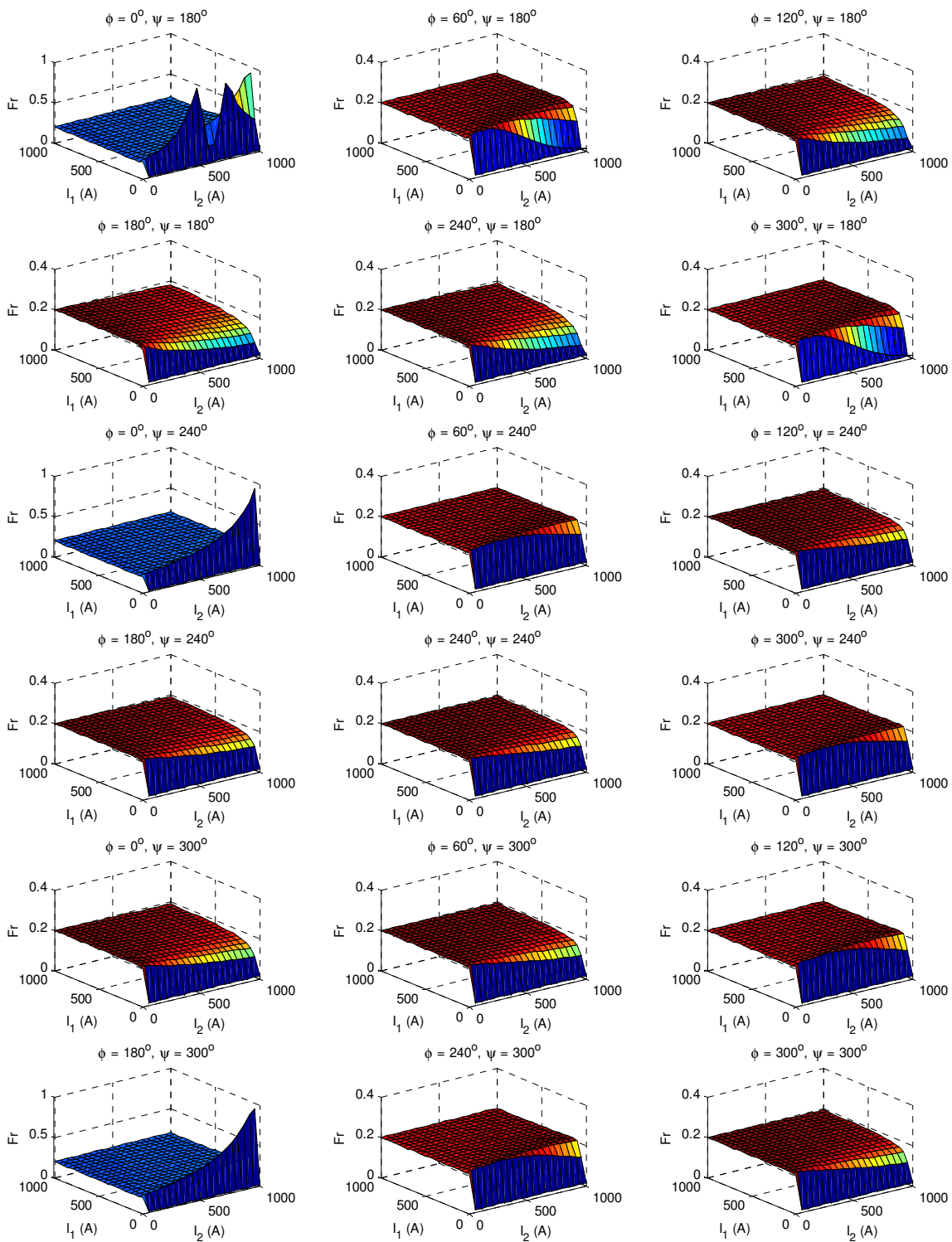




# APPENDIX D

## F<sub>R</sub> PLOTS FOR SMART DCTM ALGORITHM

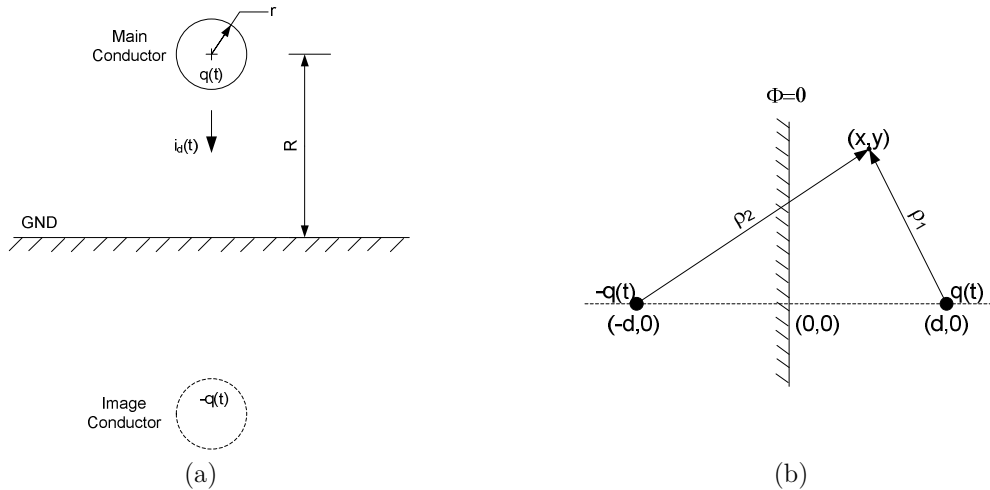




## APPENDIX E

### VOLTAGE SENSOR MODEL DERIVATION

The simple case of a single conductor above the earth is considered as seen in Figure 7.4. The earth is considered to be an infinite plane perfect conductor. Any charged surface above the earth will have an image having a negative charge below the earth at an equal distance from the earth's surface. The electric fields inside the earth are zero as it is a perfect conductor and exist only above the earth. To simplify the approach, consider a line charge having  $q$  coulombs per unit length. Although, the charge per unit length is a function of time, for simplicity, the variation in time is not represented in the symbol while performing the derivation.



**Figure E.1: (a) Single Conductor above the Earth, (b) Depiction of Method of Images**

Given that the potential at the origin is 0, the total potential at any point  $P(x,y)$  is given by,

$$\Phi(\rho, \theta) = \frac{q}{2\pi\epsilon} \ln\left(\frac{\rho_2}{\rho_1}\right) \quad (252)$$

In the Cartesian coordinate system the potential is given by,

$$\Phi(x, y) = \frac{q}{2\pi\epsilon} \ln \left( \frac{(x+d)^2 + y^2}{(x-d)^2 + y^2} \right)^{1/2} \quad (253)$$

It is of interest to find the equipotential planes in this system. The equipotential planes exist at location where the ratio of distances is a constant,

$$\frac{(x+d)^2 + y^2}{(x-d)^2 + y^2} = k^2 \quad (254)$$

Where, k is an arbitrary constant having defined values for different equipotential planes.

Simplifying the above equation gives,

$$\left( x - \left( \frac{k^2 + 1}{k^2 - 1} \right) d \right)^2 + y^2 = \left( \frac{2kd}{k^2 - 1} \right)^2 \quad (255)$$

The above equation represents a locus of equipotential planes which is a cylinder having

$$Radius = \frac{2kd}{k^2 - 1} \quad (256)$$

$$Center : \left( \left( \frac{k^2 + 1}{k^2 - 1} \right) d, 0 \right) \quad (257)$$

If the actual case of a conductor is considered, the conductor can be placed on this equipotential surface such that the radius of the conductor matches with the radius of the equipotential plane, and the distance of the conductor from the origin is equal to the abscissa of the plane,

$$r = \frac{2kd}{k^2 - 1} \quad (258)$$

$$R = \left( \frac{k^2 + 1}{k^2 - 1} \right) d \quad (259)$$

If  $k \neq 1$

$$\frac{R}{r} = \frac{k^2 + 1}{2k} \quad (260)$$

Solving the above gives k and d,

$$k = \frac{R}{r} \pm \sqrt{\left(\frac{R}{r}\right)^2 - 1} \quad (261)$$

$$d = \pm\sqrt{R^2 - r^2} \quad (262)$$

To compute the value of q in terms of the known quantities, from the boundary conditions, it is known that  $\Phi(0,0) = 0$  and  $\Phi(R-r,0) = V$ , where V is the voltage of the conductor. The potential around a conductor in terms of known quantities is given by,

$$\Phi(x,y) = \lambda \ln \left( \frac{(x+d)^2 + y^2}{(x-d)^2 + y^2} \right)^{1/2} \quad (263)$$

In cylindrical coordinates system,

$$\Phi(x,y) = \lambda \ln \left( \frac{\rho^2 + d^2 + 2\rho d \cos \theta}{\rho^2 + d^2 - 2\rho d \cos \theta} \right)^{1/2} \quad (264)$$

Where

$$\lambda = \frac{V}{2 \ln \left| \frac{R-r+d}{R-r-d} \right|} \quad (265)$$

For further computation, it will be convenient to shift the origin to the center of the actual conductor.

$$x_{new} = x - R \quad y_{new} = y \quad (266)$$

For simplicity of reading, represent the new coordinate system with the same symbols as before, x and y.

$$\Phi(x,y) = \lambda \ln \left( \frac{(x+R+d)^2 + y^2}{(x+R-d)^2 + y^2} \right) \quad (267)$$

In cylindrical coordinates,



$$\Phi(\rho, \theta) = \lambda \ln \left( \frac{\rho^2 + (R + d)^2 + 2\rho(R + d) \cos \theta}{\rho^2 + (R - d)^2 + 2\rho(R - d) \cos \theta} \right) \quad (268)$$

To compute the equation for electric field at any point around the conductor, use the following equation,

$$E(\rho, \theta) = -\nabla\Phi = -\left[ \frac{\partial\Phi}{\partial\rho} \hat{\rho} + \frac{\partial\Phi}{\partial\theta} \hat{\theta} \right] \quad (269)$$

As equipotential planes are circular, the variation of potential with  $\theta$  is 0. This reduces the above equation to,

$$E(\rho, \theta) = -\frac{\partial\Phi}{\partial\rho} \hat{\rho} \quad (270)$$

$$E(\rho, \theta) = \frac{4\lambda d}{\beta(\rho, \theta)} [2R\rho + (\rho^2 + r^2) \cos \theta] \hat{\rho} \quad (271)$$

Where,

$$\beta(\rho, \theta) = (\rho^2 + (R + d)^2 + 2\rho(R + d) \cos \theta)(\rho^2 + (R - d)^2 + 2\rho(R - d) \cos \theta) \quad (272)$$

At the surface of the conductor,

$$\beta(r, \theta) = 4r^2 (R + r \cos \theta)(R - r \cos \theta) \quad (273)$$

$$E(r, \theta) = \frac{2\lambda d}{r(R - r \cos \theta)} \quad (274)$$

If the charge enclosed by a surface S is Q

$$\oint E \cdot dS = \frac{Q}{\epsilon} \quad (275)$$

The surface charge density can thus be defined as,

$$\Delta_q = \epsilon E \quad (276)$$

$$\Delta_q = \frac{2\epsilon \lambda d}{Rr \left( 1 - \frac{r}{R} \cos \theta \right)} \quad (277)$$

$$\Delta_q = \frac{2\varepsilon\lambda d}{Rr} \left(1 - \frac{r}{R} \cos\theta\right)^{-1} \quad (278)$$

$$\Delta_q = \frac{2\varepsilon\lambda d}{Rr} \left(1 + \frac{r}{R} \cos\theta + \dots + h.o.t\right) \quad (279)$$

Neglecting the higher order terms gives,

$$\Delta_q = \frac{2\varepsilon\lambda d}{Rr} \left(1 + \frac{r}{R} \cos\theta\right) \quad (280)$$

Until now the analysis used a complete cylinder as shown in Figure 7.4. If only a section of the cylinder is used,

$$\psi_N = \frac{2\pi}{N} \quad (281)$$

Where N is the equal number of parts the cylinder is cut into.

$$Area = r\psi_N l \quad (282)$$

Where, l is the length of the cylinder.

$$\text{Total Charge} = \Delta_q r\psi_N l \quad (283)$$

The displacement current will then be found by,

$$\frac{dQ}{dt} = i_d \quad (284)$$

$$i_d = \frac{2\psi_N l \varepsilon d}{R} \left(1 + \frac{r}{R} \cos\theta\right) \frac{d\lambda}{dt} \quad (285)$$

$$i_d = \frac{\psi_N l \varepsilon d}{R \ln \left| \frac{R-r+d}{R-r-d} \right|} \left(1 + \frac{r}{R} \cos\theta\right) \frac{dV}{dt} \quad (286)$$

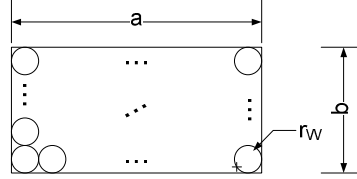
If  $V = V_m \sin(\omega t)$

$$i_d = \frac{\psi_N l \varepsilon d \omega}{R \ln \left| \frac{R-r+d}{R-r-d} \right|} \left(1 + \frac{r}{R} \cos\theta\right) V_m \cos(\omega t) \quad (287)$$

## APPENDIX F

### WINDING RESISTANCE MODEL DERIVATION

Consider a cross section of the EH winding as shown in Fig. 10.



**Figure F.1. Winding geometry**

Let the turns along length  $a$  be  $n_a$ , and turns along length  $b$  be  $n_b$ . Then, total turns are given by

$$N = n_a n_b \quad (288)$$

Given that radius of the wire is  $r_w$ ,  $a$  and  $b$  can be expressed as

$$2r_w n_a = a \qquad 2r_w n_b = b \quad (289)$$

Using (288) and (289), values of  $n_a$  and  $n_b$  in terms of  $N$ ,  $a$  and  $b$  can be obtained as

$$n_a = \sqrt{\frac{a}{b} N} \qquad n_b = \sqrt{\frac{b}{a} N} \quad (290)$$

The areas of cross section of various elements in the winding are shown in Table F.1.

**TABLE F.1: Cross Section Areas**

| Area of Cross section | Representation | Value               |
|-----------------------|----------------|---------------------|
| One Wire              | $A_w$          | $\pi r_w^2$         |
| All Wires             | $A_w$          | $\pi r_w^2 n_a n_b$ |
| Winding               | $A$            | $ab$                |

Also, Fill factor =  $\frac{A_w}{A}$

The fill factor can be simplified using (288)-(290) and Table F.1, to obtain a fixed value 0.78. Further, resistance of the winding is given by (4).

$$R_w = \frac{\rho l_w}{A_w} \quad (291)$$

In (4),  $l_w$  needs to be computed to calculate the value of resistance of the winding. Consider the winding to be cuboidal as shown in F.1 with horizontal inner length  $l_h$  and vertical inner length  $l_v$  with filleted edges. The length of the winding is given by

$$l_w = n_a(2l_h + 2l_v + 2(l_h + 2(2r)) + 2(l_v + 2(2r)) + \dots) \quad (292)$$

Equation (292) can be compactly expressed as

$$l_w = n_a \left[ \sum_{i=0}^{n_b-1} 2(l_h + l_v) + \sum_{i=0}^{n_b-1} (2(2^{i-1}r_w + 2^{i-1}r_w)) \right] \quad (293)$$

On computation of the summations in (293), the value of  $l_w$  is given by

$$l_w = 2n_a \left[ n_b(l_h + l_v) + r_w(2^{n_b} - 1) \right] \quad (294)$$

Using (288)-(290) and Table F.1,  $r_w$  can be expressed in terms of  $A$ ,  $n_a$  and  $n_b$  as

$$r_w = \sqrt{\frac{0.78A}{\pi n_a n_b}} \quad (295)$$

Finally, using (291) (294) and (295), the resistance can be expressed as

$$R_w = \frac{2\rho n_a^2 n_b \left[ n_b(l_h + l_v) + \sqrt{\frac{0.78A}{\pi n_a n_b}}(2^{n_b} - 1) \right]}{0.78A} \quad (296)$$

## BIBLIOGRAPHY

- [1] U.S. Department of Energy, *Annual Energy Outlook 2010 with Projections to 2035* [Online]. Available: <http://www.eia.doe.gov/oiaf/aeo/pdf/0383%282010%29.pdf>.
- [2] The Brattle Group, *The power of five percent: How dynamic pricing can save \$35 billion in electricity costs* [Online]. Available: <http://sites.energetics.com/MADRI/pdfs/ArticleReport2441.pdf>.
- [3] Reliable Plant, *Maintenance solutions for Power T&D market driven by rising energy demand* [Online]. Available: <http://www.reliableplant.com/Read/23696/Maintenance-solutions-energy-demand>.
- [4] R. Moghe, et al., "Mitigating distribution transformer lifetime degradation caused by grid-enabled vehicle (GEV) charging," in *Proc. of IEEE Energy Conversion Congress and Exposition (ECCE)*, Sep. 2011.
- [5] R. R. Hoffman and B. Moon, "Knowledge capture for the Utilities," in *Proc. of seventh American Nuclear Society International Topical Meeting on Nuclear Plant Instrumentation, Control and Human-Machine Interface Technologies*, November 2010.
- [6] John McDonald, *Recent Trends in Substation Automation and Enterprise Data Management, IEEE Educational Course*. [Online] <http://ieeexplore.ieee.org/servlet/opac?mdnumber=EW1161>.
- [7] Y. Yang, et al., "A Survey on Technologies for Implementing Sensor Networks for Power Delivery Systems," in *IEEE Power Engineering Society General Meeting (PES-GM)*, Jun. 2007, pp. 1-8.
- [8] U.S. Department of Energy, *A Policy Framework for the 21<sup>st</sup> Century Grid: Enabling Our Secure Energy Future* [Online]. Available: <http://www.doe.energy.gov/DocumentsandMedia/nstc-smart-grid-june2011.pdf>.
- [9] Onramp Wireless, *Ultra Link Processing* [Online]. Available: <http://onrampwireless.com/technology/ulp/>
- [10] GridSense, *Line Tracker charger user manual* [Online]. Available: <http://www.gridsense.com/linetracker-support.html>

- [11] Onramp Wireless, *Smart grid applications* [Online]. Available: <http://onrampwireless.com/applications/electricity/>
- [12] Trench, *Instrument transformers* [Online]. Available: [http://www.trenchgroup.com/Produkte/Instrument\\_Transformers/Current\\_Transformer/-8254-104-104-en-com/cms,em\\_url,internal.html](http://www.trenchgroup.com/Produkte/Instrument_Transformers/Current_Transformer/-8254-104-104-en-com/cms,em_url,internal.html).
- [13] ABB, *Instrument transformers and Sensors* [Online]. Available: <http://www.abb.com/product/us/9AAC720011.aspx?country=US>.
- [14] S. Tumanski, "A review of induction coil sensors," in *Journal of Measurement Science and Technology*, vol. 8, pp. R31- R46.
- [15] *Flexible Rogowski coils by Rocoil* [Online]. Available: <http://homepage.ntlworld.com/rocoil/products.htm#Flexible%20CoilsRocoil>.
- [16] Y. Didosyan and H. Huaser, "Magneto-optic sensors," in *Magnetic Sensors and Magnetometers*, 1<sup>st</sup> ed., P. Ripka, Massachusetts: Artech House Inc., 2000, pp. 243-264.
- [17] J. Song, et. al., "A prototype clamp-on magneto-optical current transducer for power system metering and relaying," in *IEEE Transactions on Power Delivery*, vol. 10, pp. 1764-1770, 1995.
- [18] *ABB Magneto-optic current transducer (MOCT)* [Online]. Available: <http://www.abb.com/product/db0003db002618/c12573e7003302adc1256eaf002cc96f.aspx>.
- [19] P. Ripka, "Current sensors using magnetic materials," in *Journal of Optoelectronics Advanced Material*, vol. 6, no. 2, pp. 587–592, 2004.
- [20] H. Blanchard, et al., "Highly sensitive Hall sensor in CMOS technology," in *Proc. of the 10th International Conference on Solid-State Sensors and Actuators*, pp.164-167, 1999.
- [21] *GW Associates Hall-effect sensors* [Online]. Available: [http://www.gmw.com/electric\\_current/LEM/hall-transducers.html](http://www.gmw.com/electric_current/LEM/hall-transducers.html).
- [22] P. E. Schneider, M. Horio and R. D. Lorenz, "Integrating giant magneto-resistive (GMR) field detectors for high bandwidth current sensing in power electronics modules," in *Proc. of IEEE Energy Conversion Congress and Exposition*, pp. 1260-1267, 2010.

- [23] R. D. Lorenz, "Key technologies for future motor drives," in *Proc. of Eighth International conference on IEEE Electric Machines and Systems*, pp. 1-6, 2005.
- [24] S. J. Syracuse, et al., "Sensor, method and system of monitoring transmission lines," E.U. Patent 2,059,823 B1, May 12, 2010.
- [25] L. D. Rienzo, et al., "Circular arrays of magnetic sensors for current measurement," in *IEEE Transactions on Instrumentation and Measurement*, vol. 50, no. 5, Oct. 2001.
- [26] R. Bazzocchi and L. D. Rienzo, "Interference rejection algorithm for current measurement using magnetic sensor arrays," in *Journal of Sensors and Actuators*, vol. 85, no. 1, Aug. 2000.
- [27] W. R. Vaniz and R. L. Sieron, "Apparatus for measuring the voltage of a transmission line conductor," U.S. Patent 4,714,893, Dec 22, 1987.
- [28] T. Sorensen, "Voltage measuring device," U.S. Patent 7,397,233, Jul 8, 2008.
- [29] Y. Yang, "Power line sensor networks for enhancing power line reliability and utilization," Ph.D. Dissertation, Elect. and Comp. Engg., Georgia Tech, Atlanta, GA, 2011.
- [30] F. Cleveland, "Use of Wireless Data Communications in Power System Operations," in *Proc. Power System Conf. and Expo.*, pp. 631-640, Mar. 2006.
- [31] *Protura Powerline Sensor by Protura* [Online]. Available: <http://www.protura.no/images/files /PLS.pdf>.
- [32] *Power Donut by USi* [Online]. Available: <http://www.usi-power.com/>.
- [33] *GridSync Wireless Sensor by ABB* [Online]. Available: <http://www.abb.com/product/db0003db004279/39766f868d8c677c8525772f0050ba11.aspx?productlanguage=us&country=us>.
- [34] *VaultSense Wireless Current Sensor by Eaton* [Online]. Available: <http://www.eaton.com/ecm/groups/public/@pub/@eaton/@ee/documents/content/sa02400005e.pdf>.
- [35] *WSO Wireless Sensor for Overhead Lines by Schweitzer Engineering Laboratory (SEL)* [Online]. Available: <http://www.selinc.com/FCI/Overhead /WirelessSensor>.
- [36] *LightHouse MV Sensors Brochure by Tollgrade*, [Online]. Available: <http://www.tollgrade.com/lighthouse/index.html>.

- [37] *RT-LMS System Brochure by Promethean Devices* [Online]. Available: <http://www.prometheandevices.com/index.html?reload>.
- [38] J. Mark Major, "Ensuring the Health of our Power Lines," [Online]. Available: <http://www.swri.org/3pubs/ttoday/summer06/PDFs/PowerLines.pdf>.
- [39] A. Nasipuri, et al., "Wireless Sensor Network for Substation Monitoring: Design and Deployment," in *Proc. of 6<sup>th</sup> ACM Conference on Embedded Network Sensor Systems*, pp. 365-366, 2008.
- [40] GridSense, *LineTracker* [Online]. Available: <http://www.gridsense.com/linetracker.html>.
- [41] Grid Sentry, *Load Sentry, Line Sentry and PQ Sentry* [Online]. Available: [http://gridsentry.us/index.php?option=com\\_content&view=article&id=6&Itemid=6](http://gridsentry.us/index.php?option=com_content&view=article&id=6&Itemid=6).
- [42] Cooper Power Systems, *OutageAdvisor Sensor* [Online]. Available: [http://www.cooperindustries.com/content/public/en/power\\_systems/products/automation\\_and\\_control/reliability-optimization/outage\\_detection/outageadvisor\\_sensor.html](http://www.cooperindustries.com/content/public/en/power_systems/products/automation_and_control/reliability-optimization/outage_detection/outageadvisor_sensor.html)
- [43] Sentient Energy, *AMP Master Monitor 2* [Online]. Available: <http://www.sentient-energy.com/product/amp-master-monitor-2/>
- [44] Y. Yang, F. Lambert and D. Divan, "Potential Applications for Sensor Networks in Power Delivery," NEETRAC Baseline Project Number 05-100, June 2006.
- [45] C. B. Williams and R. B. Yates, "Analysis of a Micro-Electric Generator for Microsystems," in *Proc. of The 8th International Conference on Solid-state Sensors and Actuators*, vol. 1, pp 369-372, Jun. 1995.
- [46] S. Meninger, et. al., "Vibration-to-Electric Energy Conversion," in *IEEE Transactions on VLSI systems*, vol. 9, no. 1, pp 64-76, Feb 2001.
- [47] M. Goldfarb and L. D. Jones, "On the Efficiency of Electric Power Generation with Piezoelectric Ceramic," in *Transactions of the ASME*, vol. 121, pp 566-571, Sep. 1999.
- [48] N. Elvin, A. Elvin and, M. Spector, "A Self Powered Mechanical Strain Energy Sensor," in *Journal of Smart Materials and Structures*, vol. 10, pp 293-299, Apr. 2001.



- [49] R. Amirtharajah and A. P. Chandrakasan, "Self-Powered Signal Processing Using Vibration-Based Power Generation," in *IEEE Journal of Solid State Circuits*, vol. 33, no. 5, pp 687-695, May 1998.
- [50] H. A. Sodano, et. al., "Use of piezoelectric energy harvesting devices for charging batteries," in *Proc. of SPIE*, vol. 5050, pp. 101-108, July 2003.
- [51] S. Roundy and P. K. Wright, "A piezoelectric vibration based generator for wireless electronics," in *Proc. of Smart Materials and Structures*, vol. 13, no. 5, pp. 1131-1142, 2004.
- [52] E. Leland, R White and, P. Wright, "Energy scavenging power sources for household electrical monitoring," presented at The 6th International Workshop on Micro and Nanotechnology, Berkeley, California, USA, 2006.
- [53] S. Roundy, et. al., "Improving Power Output for Vibration-based Energy Scavengers," in *IEEE Journal of Pervasive Computing*, vol. 4, issue 1, pp. 28-36, Mar 2005.
- [54] *Mide Engineering Smart Technologies* [Online]. Available: <http://www.mide.com/index.php>
- [55] *AdaptivEnergy* [Online]. Available: <http://www.adaptivenergy.com/>.
- [56] *Cedrat* [Online]. Available: <http://www.cedrat.com/>.
- [57] *Perpetuum* [Online]. Available: <http://www.perpetuum.co.uk/>.
- [58] *Ferro Solutions* [Online]. Available: <http://www.ferrosi.com/>.
- [59] J. A. Paradiso and T. Starner, "Energy Scavenging for Mobile and Wireless Electronics," in *IEEE Journal of Pervasive Computing*, vol. 4, issue 1, pp. 18-27, Mar 2005.
- [60] J. H. Kiely, D.V. Morgan and, D. M. Rowe, "The Design and Fabrication of a Miniature Thermoelectric Generator using MOS Processing Technique," in *Measurement Science and Technology*, vol. 5, no. 2, pp. 182-189, Feb. 1994.
- [61] M. Stordeur and I. Stark, "Low Power Thermoelectric Generator- Self Sufficient Energy Supply for Micro Systems," in *Proc. ICT 1997 International Conference on Thermoelectrics*, pp. 575-577.
- [62] I. Stark and M. Stordeur, "New Micro Thermoelectric Devices based on Bismuth Telluride-Type Thin Solid Films," in *Proc. ICT 2000 18<sup>th</sup> International Conference on Thermoelectrics*, pp. 465-472.

- [63] L. Mateu, et. al., "Energy Harvesting for Wireless Communication Systems Using Thermogenerators," in *Proc. of DCIS, 2006*.
- [64] G. Savelli, et. al., "Energy Conversion Using New Thermoelectric Generator," in *Proc. of Dans Symposium on Design, Test, Integration and Packaging of MEMS/MOEMS*, Apr. 2006.
- [65] L. Mateu, et. al., "Human Body Energy Harvesting Thermogenerator for Sensing Application," in *Proc. of International Conference on Sensor Technologies and Applications*, pp. 366-372, Oct. 2007.
- [66] H. Sodano, et. al., "Recharging Batteries using Energy Harvested from Thermal Gradient," in *Journal of Intelligent Material Systems and Structures*, vol. 18, no. 1, pp. 3-10, Jan 2007.
- [67] I. Stark, "Thermal Energy Harvesting with Thermo Life," in *IEEE International Workshop on Wearable and Implantable Body Sensor Networks*, pp. 19-22, 2006.
- [68] *Thermo Life Energy Corp.* [Online]. Available: <http://www.poweredbythermolife.com/>.
- [69] *Kryotherm* [Online]. Available: <http://www.kryotherm.ru/>.
- [70] *Seiko Watch Corporation* [Online]. Available: <http://www.seikousa.com/#>.
- [71] *Tellurex Corporation* [Online]. Available: <http://www.tellurex.com/>
- [72] V. Rangunathan, et. al., "Design Considerations for Solar Energy Harvesting Wireless Embedded Systems," in *The Fourth International Symposium on Information Processing in Sensor Networks*, pp. 457-462, Apr. 2005.
- [73] B. A. Warneke, et. al., "An Autonomous 16 mm<sup>3</sup> Solar-Powered Node for Distributed Wireless Sensor Networks," in *Proc. of IEEE Sensors*, vol. 2, pp. 1510-1515, 2002.
- [74] S. Roundy, et. al., "A 1.9GHz RF Transmit Beacon using Environmentally Scavenged Energy," in *IEEE International Symposium on Low Power Electronics and Devices*, Feb 2003.
- [75] T. Voigt, H. Ritter and J. Schiller, "Utilizing Solar Power in Wireless Sensor Networks," in *Proc. of IEEE International Conference on Local Computer Networks*, pp. 416-422, 2003.
- [76] *Enocean* [Online]. Available: <http://www.enocean.com/en/>.
- [77] *ICP Solar* [Online]. Available: <http://www.icpsolar.com/>

- [78] *Solio* [Online]. Available: <http://www.solio.com/charger/>.
- [79] R. Want, "An Introduction to RFID Technology," in *IEEE Journal of Pervasive Computing*, vol. 5, issue 1, Mar. 2006.
- [80] *Powercast* [Online]. Available: <http://powercastco.com/>.
- [81] M. Zhu, et. al., "Alternative Power Sources for Autonomous Sensors in High Voltage Plant," in *Proc. of IEEE Electrical Insulation Conference*, pp. 36-40, 2009.
- [82] M. Zhu, M. D. Judd, and P. J. Moore, "Energy Harvesting in Substations for Powering Autonomous Sensors," in *Proc. of IEEE Sensor Technologies and Applications*, pp. 246-251, 2009.
- [83] M. Zhu, et. al., "Energy Harvesting Technique for Powering Autonomous Sensors within Substations," in *Proc. of IEEE Sustainable Power Generation and Supply*, pp. 1-5, 2009.
- [84] S. Roundy and P. K. Wright, "A piezoelectric vibration based generator for wireless electronics," *Smart Materials and Structures*, vol. 13, no. 5, pp. 1131-1142, 2004.
- [85] N. N. Ching, et al., "A laser-micromachined multi-modal resonating power transducer for wireless sensing systems," in *Sensors and Actuators A: Physical*, vol. 97-98, pp. 685-690, April 2002.
- [86] B. A. Warneke, et. al., "An Autonomous 16 mm<sup>3</sup> Solar-Powered Node for Distributed Wireless Sensor Networks," in *Proc. of IEEE Sensors*, vol. 2, pp. 1510-1515, 2002.
- [87] I. Stark and M. Stordeur, "New Micro Thermoelectric Devices based on Bismuth Telluride-Type Thin Solid Films," in *Proc. of ICT 2000 18th International Conference on Thermoelectrics*, pp. 465-472.
- [88] *Kyocera* [Online]. Available: <http://global.kyocera.com/>
- [89] R. Dayal, S. Dwari, and L. Parsa, "Design and implementation of direct ac-dc boost converter for low voltage energy harvesting," in *IEEE Transactions on Industrial Electronics*, early access document, 2010.
- [90] J. W. Kimball, T. L. Flowers, and P. L. Chapman, "Low-input-voltage, Low-power Boost Converter Design Issues," in *IEEE Power Electronics Letters*, vol. 2, issue 3, pp 96-99, 2004.

- [91] J. S. Brugler, "Theoretical Performance of Voltage Multiplier Circuits," in *IEEE Journal of Solid-State Circuits*, vol.6, issue 3, pp 132-135, 1971.
- [92] J. F. Dickson, "On-chip High-voltage Generation in MNOS Integrated Circuits Using an Improved Voltage Multiplier Technique," in *IEEE Journal of Solid-State Circuits*, vol. 11, issue 3, pp. 374-378, 1976.
- [93] R. Pelliconi, et. al., "Power efficiency charge pump in deep submicron standard CMOS technology," *IEEE Journal of Solid-State Circuits*, vol. 38, no. 6, pp. 1068–1071, Jun. 2003.
- [94] A. Richelli, et. al., "A 1.2 to 8V charge pump with improved power efficiency for non-volatile memories," in *Proc. ISSCC*, Feb. 2007, pp. 522–619.
- [95] J. T. Wu and K. L. Chang, "Low supply CMOS charge pump," in *Symp. VLSI*, Hsin-Chu, Taiwan, 1997, pp. 522–619.
- [96] K. H. Cheng, C. Y. Chang, and C. H. Wei, "A CMOS charge pump for sub-2.0V operation," in *Proc. ISCAS*, May 2003, pp. V-89–V-92.
- [97] J. Shin, et. al., "A new charge pump without degradation in threshold voltage due to body effect," in *IEEE Journal of Solid-State Circuits*, vol. 35, no. 8, pp. 1227–1230, Aug. 2000.
- [98] L. Mensi, et. al., "A new integrated charge pump architecture using dynamic biasing of pass transistors," in *Proc. ESSCIRC 2005*, Sep., pp. 85–88.
- [99] A. Richelli, et. al., "A 0.2-1.2 V DC/DC Boost Converter for Power Harvesting Applications," in *IEEE Transactions on Power Electronics*, vol. 24, issue 6, 2009.
- [100] J. Che, et. al., "Ultra-low-voltage Low-power Charge Pump for Solar Energy Harvesting Systems," in *Proc. of IEEE Communications, Circuits and Systems*, pp. 674-677, 2009.
- [101] S. Amini, and C. Plett, "Design and Analysis of Very Low Voltage Charge Pumps for RFID Tags," in *Proc. of IEEE Microsystems and Nanoelectronics Research*, pp. 9-12, 2008.
- [102] P. D. Mitcheson, T. C. Green, and E. M. Yeatman, "Power Processing Circuits for Electromagnetic, Electrostatic and Piezoelectric Inertial Energy Scavengers," in *Journal of Microsystem Technologies*, vol. 13, no. 11-12, pp 1629-1635, 2007.
- [103] R. Dayal, S. Dwari, and L. Parsa, "A new design for vibration-based electromagnetic energy harvesting systems using coil inductance of

- microgenerator,” in *IEEE Transactions on Industrial Electronics*, vol. 37, issue 2, pp. 820-830, 2011.
- [104] S. Dwari, et. al., “Efficient direct ac-to-dc converters for vibration-based low voltage energy harvesting,” in *Proc. of 34<sup>th</sup> Annual conference of IEEE Industrial Electronics*, pp. 2320-2325, 2008.
- [105] S. Roundy, et. al., “Improving Power Output for Vibration-based Energy Scavengers,” in *IEEE Journal of Pervasive Computing*, vol. 4, issue 1, pp. 28-36, Mar 2005.
- [106] M. A. Green, “Efficiency limits, losses and measurements,” in *Solar Cells*, 1st Ed., Australia, Bookworks, 1998, pp. 85-98.
- [107] M. A. Green, “Accuracy of analytical expressions for solar cell fill factors,” in *Journal of Solar Cells*, vol. 7, issue 3, 1982.
- [108] Zigbee® Alliance, *ZigBee*® [Online]. Available: <http://www.zigbee.org/>
- [109] SmartSynch, *GridRouter*, [Online]. Available: <http://smartsynch.com/products/gridrouter/benefits.php>.
- [110] Patrick Kinney, Gateways: Beyond sensor networks, [Online]. Available: <http://www.zigbee.org/zigbee/en/events/documents/SensorsExpo/7-Sensors-Expo-kinney.pdf>
- [111] Zigbee Scada Gateway by OEM Technology solutions, [Online]. Available <http://www.oem.net.au/index.php?a=31&b=109>
- [112] Smart Grid System Report [Online]. Available: [http://www.oe.energy.gov/DocumentsandMedia/SGSRMain\\_090707\\_lowres.pdf](http://www.oe.energy.gov/DocumentsandMedia/SGSRMain_090707_lowres.pdf)
- [113] A.P. Meliopoulos and G. J. Cokkinides, “Chapter 3: Modeling for Power Quality Analysis,” in *Electric Power Quality*.
- [114] Z. Li, Y. Huang, X. Wang, R. Zeng, L. Yao, C. Sasse, “Immunity research of wireless communication in switch cabinet monitoring and control,” *Electromagnetic Compatibility*, 2006. EMC 2006. 2006 IEEE International Symposium on , vol.2, no., pp.351-355, 14-18 Aug. 2006.
- [115] H. Ott, *Noise Reduction Techniques in Electronic Systems*, 2nd Edition, New York: John Wiley & Sons, 1988.

## VITA

Rohit Moghe was born in the small historic town of Indore, India, on December 7<sup>th</sup> 1985. After he was born, he moved with his family to New Delhi. As a four year old he wanted to be an engineer when he grew up due, in part, to his attraction towards railway engines, and also due to the fact that his father was a mechanical engineer in the automotive sector. He was fascinated by electricity, magnetism and physics in general during his high school years, which made him choose electrical engineering at IIT Roorkee in 2003. He completed the B.Tech in Electrical Engineering in 2007 as a silver medalist and was also awarded the prize for “best undergraduate research award” from IIT Roorkee. Subsequently, he joined Georgia Tech in 2007 and started working under the guidance of Dr. Deepak Divan towards his PhD. He completed his MS in Electrical and Computer Engineering in 2010 from Georgia Tech. At Georgia Tech, he was one of the founding members of the Energy Club and also served as the President of the club during 2010-11. His academic interests are in the area of smart grid, sensors, energy harvesting, high power converters and power flow controllers. He likes spending his free time reading novels related to philosophy, science, biographies, classics and business, watching TED talks, playing guitar and hiking.